NON-LINEAR FINITE ELEMENT ANALYSIS OF FLEXIBLE PIPES FOR DEEP-WATER APPLICATIONS

A thesis submitted for the degree of
Doctor of Philosophy

by
Ben Edmans

School of Engineering and Design
Brunel University

March 2013

Dedicated to

Monika, my wife and best friend

A very large oak was uprooted by the wind and thrown across a stream. It fell among some reeds, which it thus addressed: "I wonder how you, who are so light and weak, are not entirely crushed by these strong winds." They replied, "You fight and contend with the wind, and consequently you are destroyed; while we on the contrary bend before the least breath of air, and therefore remain unbroken, and escape."

- *The Oak and the Reeds*, Aesop's Fables

Non-Linear Finite Element Analysis of Flexible Pipes for Deep-Water Applications

Ben Edmans

Submitted for the degree of Doctor of Philosophy

March 10, 2013

Abstract

Flexible pipes are essential components in the subsea oil and gas industry, where they are used to convey fluids under conditions of extreme external pressure and (often) axial load, while retaining low bending stiffness. This is made possible by their complex internal structure, consisting of unbonded components that are, to a certain extent, free to move internally relative to each other. Due to the product's high value and high cost of testing facilities, much effort has been invested in the development of analytical and numerical models for simulating flexible pipe behaviour, which includes bulk response to various loading actions, calculation of component stresses and use of this data for component fatigue calculations.

In this work, it is proposed that the multi-scale methods currently in widespread use for the modelling of composite materials can be applied to the modelling of flexible pipe. This allows the large-scale dynamics of an installed pipe (often several kilometers in length) to be related to the behaviour of its internal components (with characteristic lengths in millimeters). To do this, a formal framework is developed for an extension of the computational homogenisation procedure that allows multi-scale models to be constructed in which models at both the large and small scales are composed of different structural elements. Within this framework, a large-scale flexible pipe model is created, using a two-dimensional corotational beam formulation with a constitutive model representative of flexible pipe bulk behaviour, which was obtained by further development of a recently proposed formulation inspired by the analogy between the flexible pipe structural behaviour and that of plastic materials with non-associative flow rules. A three-dimensional corotational formulation is also developed. The model is shown to perform adequately for practical analyses.

Next, a detailed finite element (FE) model of a flexible pipe was created, using shell finite elements, generalised periodic boundary conditions and an implicit solution method. This model is tested against two analytical flexible pipe models for several basic load cases.

Finally, the two models are used to carry out a sequential multi-scale analysis, in which a set of simulations using the detailed FE model is carried out in order to find the most appropriate coefficients for the large-scale model.

Declaration

The work in this thesis is based on research carried out at the Brunel University, United Kingdom. No part of this thesis has been submitted elsewhere for any other degree or qualification and it all my own work unless referenced to the contrary in the text.

Acknowledgements

I would like to thank my supervisor, Dr Giulio Alfano, for constant support and suggestions throughout the project. I could not have done this work without him. I am very grateful for his explanations of mechanical theory and personal attention to this project. I would also like to thank my second supervisor, Professor Hamid Bahai for managing the project and much strategic guidance.

This project is a continuation of the work of Dr Bahtui, whose research and models were of key importance (Bahtui, 2008). He helpfully provided data and advice on the operation of his model.

This project was made possible by an EPSRC CASE studentship, with Lloyd's Register EMEA as the industrial partner providing funding, calculations for model verification purposes and technical information. Thanks are due to Dr Lakis Andronicou, as industrial supervisor for this project for managing the project and sharing his extensive industrial experience. The contribution and technical advice provided by Dr Andronicou and Dr Bahtui were greatly appreciated and were essential for the validation work presented in Chapter 5.

Finally, I wish to thank my parents. I hope to act in my life with the kindness, humanity and wisdom they have shown to me in my upbringing.

Contents

List of Figures

List of Tables

Chapter 1

Introduction

1.1 Flexible pipes: Structure, applications, capabilities

In recent decades, the depletion of accessible oilfields and continued demand for crude oil has led to the rapid development of the subsea oil and gas industry. Oil prices have been sufficiently high to justify the capital expense required to install production systems that profitably operate in waters now often exceeding 3000m below sea-level. The development of physical systems and components capable of functioning in such extreme conditions, combined with demanding operating requirements and acceptable reliability and operating life has been the result of these trends.

One key development has been the unbonded flexible pipe. Consisting of a number of interlocking metal and polymer components, flexible pipes can fulfill the requirement to be able to transport oil and gas at high internal and external pressures for a wide range of applications, including production risers between the seabed and surface, jumpers between FPSOs (Floating Production, Storage and Offloading units), FSUs (Floating Storage units) and platforms, connections between subsea wellheads and manifolds on the seabed, in conjunction with rigid pipelines. Other uses include test lines and chemical injection lines. Advantages gained in using flexible, rather than rigid, connectors include ease of installation, operational

flexibility (flowlines on the seabed are often repositioned as an oilfield is developed), and suitability for dynamic applications , such as risers, where waves, currents and FPSO drift would otherwise cause high and fluctuating stresses in the pipe. As the cost of flexible pipes is five to six times the cost of an equivalent rigid pipe (though they are cheaper and faster to lay), they are only installed where their advantages are manifest (Palmer and King, 2008). Comprehensive modern reference works for pipeline and riser engineering are given by Bai and Bai (2005) and Palmer and King (2008).

The complex internal dynamics of a flexible pipe means that established stress prediction and fatigue analysis tools are inadequate for accurate analysis. In response, equipment designers have come to adopt a number of analysis tools, including traditional finite element methods and analytical models based on established structural theories.

Accurate modelling requires detailed knowledge of material and geometrical properties of flexible pipe. A schematic of a typical flexible pipe assembly, including layer profile shapes and layer designations, is shown in Figure 1.1. The components of a typical flexible pipe include, but are not limited to, the following:

- A "carcass" consisting of a helically wound metal strip wound at an angle approximately 85 degrees from the pipe axis. Adjacent turns interlock tightly (see Figure 1.2 (bottom profile)). The primary purpose of the carcass is to provide collapse resistance to external pressure. The carcass is not present in all flexible pipe designs. The carcass is permeable to gas and liquid.

- A "pressure armour" layer consisting of interlocking z-shaped wires wound at close to 90 degrees to the pipe axis. Its purpose is to withstand radial loads from internal fluid pressure.

- "Tensile armour wires/tendons", which are helically wound steel strips that can be flat (rectangular), round or shaped. Wires are wound at lay angles between 20 and 60 degrees to the pipe axis. These wires provide the dominant part of the tensile strength and stiffness of the pipe.

- "Anti-wear layers" consisting of polymer sheaths, which extend pipe lifespan by protecting adjacent helical armour layers from rubbing together.

- "Internal(pressure)/external sheaths", which are extruded polymer sheaths that provide fluid integrity.

- "High strength tapes", which provide resistance to bird-caging effects under high axial compression or internal pressure. They induce a degree of initial hoop stress in the outermost layer, as it is recommended that they are applied with sufficient tightness to limit the gap between tensile armour and next innermost layer to half the wire thickness (API, 1998).

Flexible pipes are connected to other components by integrated end fittings, which secure the terminations of all layers such that forces are transmitted to the end fitting flange or other interface and fluid integrity is maintained. An example of a typical end-fitting design is shown in Figure 1.3.

The tensile armour wires, the anti-wear layers and the internal/external pressure sheaths are used in all unbonded flexible pipes. Different flexible pipe designs use different numbers of layers; additional layers may be used to reduce gas permeability, provide thermal insulation or to increase flexibliity (by separating two steel layers with a polymer layer). Pipe internal diameters for single-bore flexible range from 25 to 400mm with current manufacturing capabilities (Palmer and King, 2008). The smallest pipes can withstand internal pressures of up to about 140 MPa and the largest up to about 20 MPa. Multiple tensile armour layers are usually used (2 or 4 layers is typical). Alternate tensile armour layers are wound in opposite directions to obtain torsional balance under load, and also to balance hoop and axial loads. Pipe mass varies considerably for a given diameter: the empty mass varies from about 11 to about 420 kg per metre length.

Material selection is influenced by the need for resistance to chemical corrosion (more important for "sour service" applications), weldability and fatigue characteristics. Carcass layers may be fabricated using carbon steel (with carbon content up to AISI 4130), austentitic stainless steels up to AISI 304, 304L, 316, 316L, duplex stainless steel up to UNS S31803. Polymer sheaths may be made of HDPE, XLPE

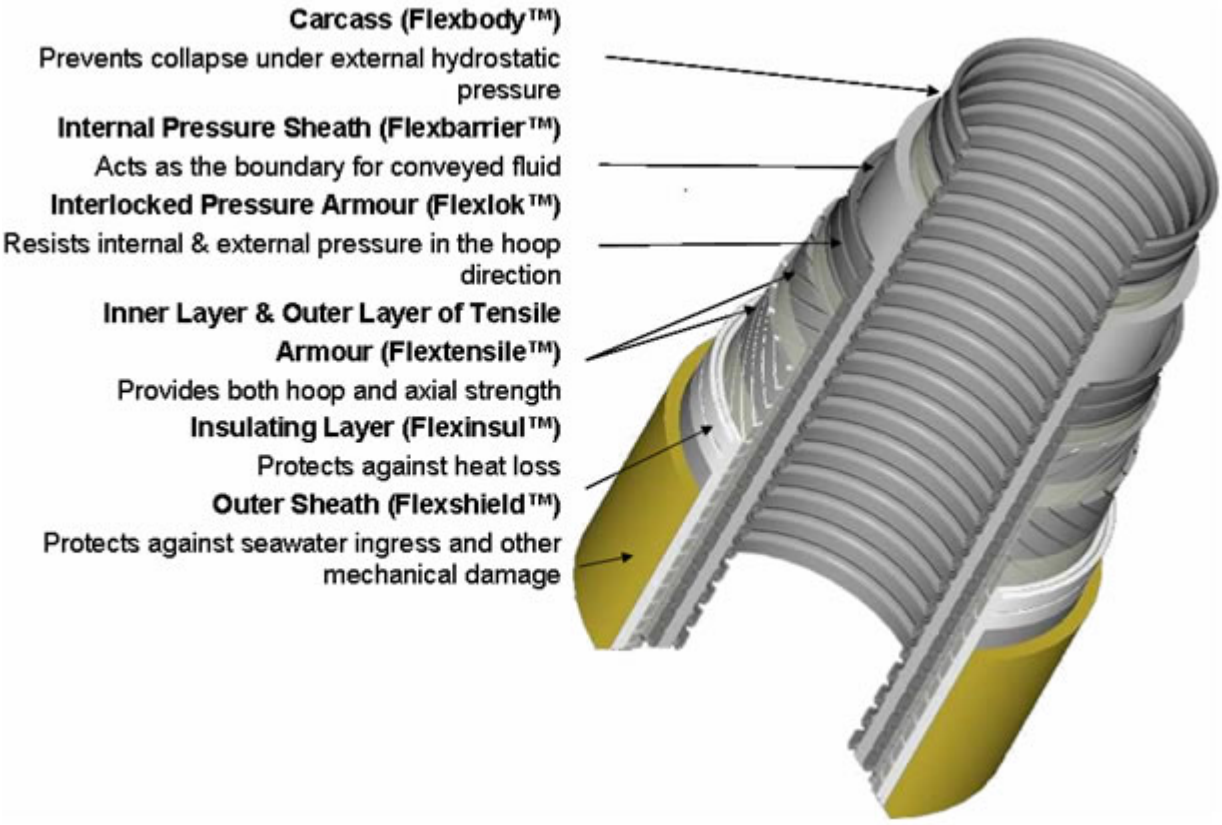

Figure 1.1: Schematic of typical flexible riser cross-sections. Image courtesy Wellstream International Limited

(a form of PE with cross-links between the polymer chains), polyamide (PA-11, PA-12), Nylon 11, Fluorocarbon or PVDF, a thermoplastic fluoropolymer. This choice is largely dependent on the operating temperature. Tensile armour wires are made from high-strength carbon steels.

Typical causes of failure for unbonded flexible pipes are from fretting and wear of internal components, corrosion failures and fatigue failures. The design life of a flexible riser is typically 25 years.

Flexible pipe is a specialised product with three main manufacturers: Coflexip (now part of Technip group), Wellstream and NKT Flexibles.

1.2 Objectives and scope of research

The objectives of this project were

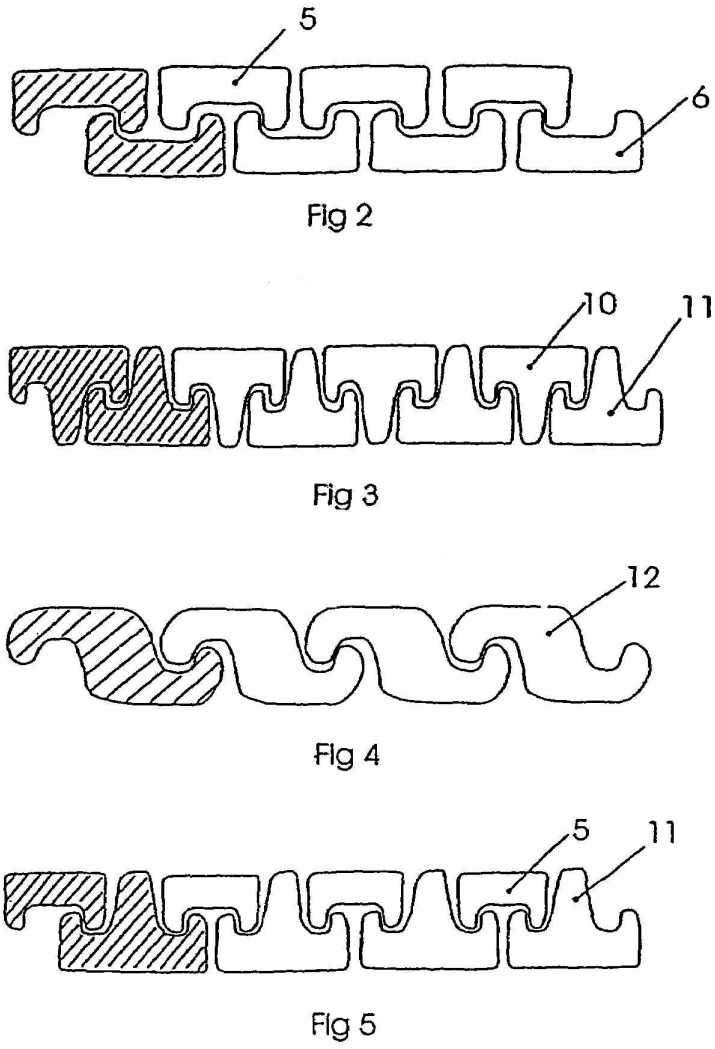

Figure 1.2: Pressure armour and carcass interlock profiles. Source: NKT Flexibles, US Patent No. 06981526

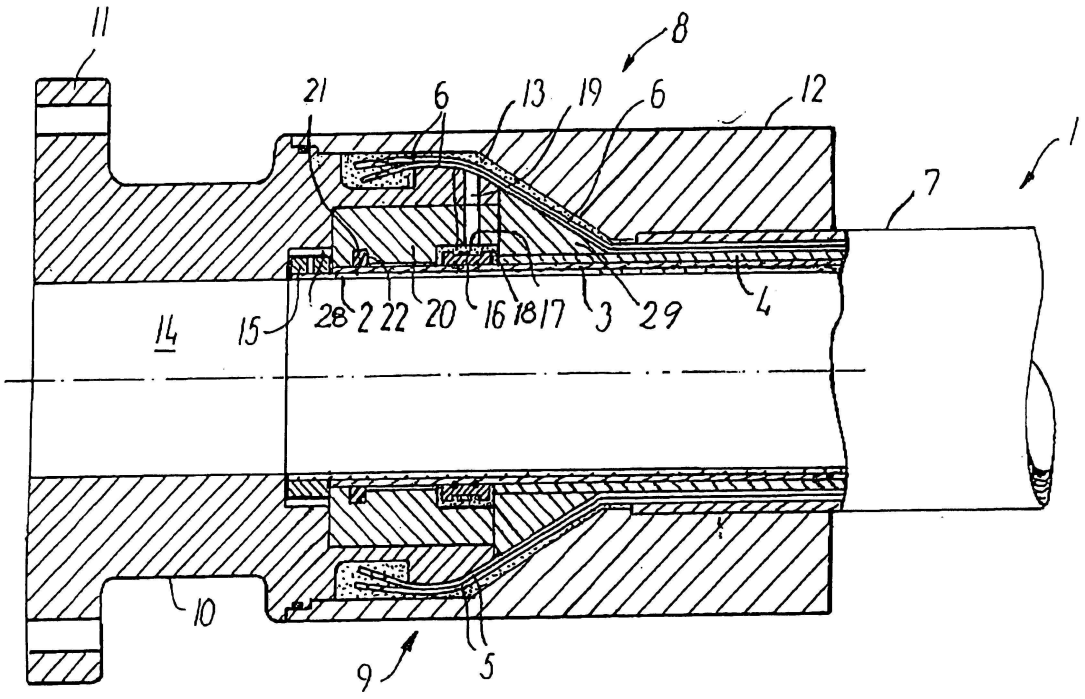

Figure 1.3: Example of an unbonded flexible pipe end fitting. Source: NKT Flexibles, US Patent No. 06360781

1. To develop a theoretically justified numerical multiscale analysis procedure suitable for the structural analysis of flexible pipes.

2. To develop and implement a robust beam-like finite element accounting for large displacements and rotations suitable for large-scale analyses of flexible pipes and to derive and implement an appropriate constitutive model for use with this element.

3. To develop a detailed finite element model for the stress analysis of flexible pipes, accounting for contact-friction interactions of internal components accurately, and accurately representing the behaviour of internal components by appropriate modelling choices.

4. To demonstrate the multiscale analysis procedure by using the beam-like finite element model as the large-scale model and the detailed finite element model as the small scale model.

The scope of the work was restricted to the unbonded, single-bored flexible pipe. The focus in on the nonlinear structural response; problems of characterising and implementing external loading conditions, including vortex induced vibration (VIV) effects and seabed interaction are not considered. Issues surrounding end fittings, connectors and bend limiters are also not considered. Therefore, the predicted pipe behaviour is considered accurate only at reasonable distances from such restrictions. Boundary conditions are discussed in the context of scale-linking (see Section 3.1).

The focus of this work is the creation of models which can accurately predict component stresses and displacements when the flexible pipe is subject to various combined loading actions. However, the design and analysis of flexible pipes also considers specific failure modes such as collapse and "bird-caging" (a phenomenon in which armour wires lose stability under axial compression and develop excessive radial or lateral displacements, see Section 2.2.1), which are associated with highly nonlinear structural behavior of flexible pipes and their internal components. Analysis of these failure modes require that structural limit states can be determined. Although the detailed finite element model developed in the current work is not designed to be able to predict these failure modes, it is anticipated that such a model will also be valuable for investigating these phenomena. This is because the model developed is designed to represent all components and interlayer interactions, and the implicit solution procedure allows the identification of limit states. The analysis of such failure modes would require additional attention to the solution convergence controls, contact enforcement methods and numerical damping.

In this work, multi-scale homogenisation techniques will be applied to the analysis of flexible pipes. It is noted that, in the context of this work, the term "large-scale" refers to phenomena and analyses in which the characteristic length scale is the length of an installed riser, which ranges from around 100m to 2-3 km, while the term "small scale" refers to phenomena and analyses of the pipe and internal components where characteristic length scales are around 0.1mm to 100mm. This contrasts with standard usage in research multiscale modelling of materials, in which the terms "small-scale" or "microscale" refer to phenomena occurring at length scales invisible to the naked eye ($\sim$1-100μm). Furthermore, it is necessary to distinguish

sequential and nested homogenisation approaches. In sequential approaches, a sufficient number of simulations are carried out on a detailed (or small-scale) model of a structure such that the parameters of a large-scale homogenised representation of it may be determined. Once these parameters have are known, large-scale simulations may be carried out using a number of such homogenised elements, without further reference to the detailed model being required to predict the large-scale behaviour. In contrast, the nested homogenisation approach involves the solution of the large- and small-scale problems in parallel. In this arrangement, real-time simulations are carried out using the detailed model for points in the large-scale model as a more accurate alternative to using a constitutive model relating stress, strain and history variables. In this work, the application of homogenisation techniques to flexible pipes will use the sequential approach, although the theoretical developments in Chapter 3 apply to both approaches, and a nested homogenisation is demonstrated in that Chapter.

1.3 Outline of thesis

A survey of the relevant literature is presented in Chapter 2, discussing analytical and numerical approaches to flexible pipe modelling, and also covering homogenisation techniques used for a variety of engineering problems.

In Chapter 3, a formal framework for multi-scale analysis is developed, in which computational homogenisation techniques are extended to deal with situations where both the large-scale and small-scale models are comprised of structural elements, and where different structural models are used at the different scales. In this Section, a "control node" approach for applying boundary conditions and transferring quantities between scales is introduced. An application of the approach is demonstrated in a fully-nested multi-scale analysis of a nonlinear periodic truss structure. Multi-scale convergence of the method is shown for several situations.

In Chapter 4, the large-scale model used in the multi-scale method is described, using a corotational beam element and a non-linear constitutive model. The constitutive model relates generalised stresses and strains with a non-associative plasticity

model with kinematic hardening that captures the hysteretic bending-moment curvature behaviour displayed by flexible pipes and the influence of internal end external pressure on this behaviour.

In Chapter 5, the detailed finite element model used for the small-scale analysis is described. In distinction to earlier work on finite element modelling of flexible pipes (Bahtui, 2008; Bahtui et al., 2009, 2010), in which an explicit dynamics approach was used, all models used in this work are solved using a nonlinear implicit static solution procedure. Special attention is paid to modifications used for modelling contact (Section 5.2.1) and practical implementation of the "control node" method (Section 5.2.2). In this Chapter, verification and parameter studies on this model are described. Comparisons are presented for overall response to axial and pressure loading (Section 5.3.1) and for component stresses when the pipe is subjected to load cases of practical interest (Section 5.3.3), including axial loading, pressure loading and bending. Qualitative comparisons of the stress and slip fields resulting from the use of periodic and "fixed-in-plane" boundary conditions are also shown in Section 5.3.2.

A modification to the constitutive model of the large-scale model is developed in Chapter 6 in order to account for the carcass separation phenomenon noted in the results of the detailed model presented in Chapter 5.

Chapter 7 deals with the implementation of the scale-linking procedure in a sequential multi-scale approach. The determination of large-scale model parameters from simulations using the detailed model is described. In Chapter 8, overall conclusions from this work are presented.

Chapter 2

Literature review

In this Chapter, a survey and critique of the relevant published literature is presented. The purpose of reviewing different modelling methods is to gain understanding about the types of models currently used: their assumptions, level of complexity, modelling procedures and predictive capability. Secondly, through modelling and experiments, a great deal of understanding has been gained about the kinematic and dynamic phenomena and behaviour exhibited by flexible pipes. Such understanding is apparent in the literature in the modelling decisions and predictive scope as revealed by verification testing. No attempt is made to fully evaluate and compare all the work presented in this Chapter.

This Chapter begins with some definitions and explanations in Section 2.1, followed by an overview of the few test data in the public domain in Section 2.2. In Section 2.3, a description of various analytical models used for flexible pipes is provided, covering the basic formulation and solution of the models, commenting on assumptions made and the mechanical phenomena incorporated. Such models are characterised by varying descriptions or approximations of flexible pipe kinematics, which are then used to derive linear or non-linear equations which are solved by computational techniques. Despite the name of this class of models, numerical solution of these equations is often required in practice.

In Section 2.4, detailed modelling methods using finite element software are reviewed. Such models avoid some of the explicit assumptions made by analytical models, but require various modelling choices instead, such as element type and

contact modelling techniques.

In Section 2.5, relevant publications on material and structural homogenisation techniques are reviewed. These techniques are used to formulate and derive model coefficients for "large scale" response models for materials and structures with complex but predictable small-scale structures. These approaches are of particular interest to this project, given the objective of developing multiscale models.

Finally, a survey of other notable models and modelling issues not falling into the above categories is presented (Section 2.6).

Although the capability to predict fatigue endurance in flexible pipe components is a key concern of the current work, the existing literature on flexible pipe fatigue testing and modelling will not be reviewed here, other than to briefly describe the types of structural model that are currently considered to have adequate stress-prediction capabilities. The specific application of the model to the fatigue problem (and empirical tools used in the industry) will not be covered. Similarly, coverage of investigations into limit-state loading (such as birdcaging or collapse prediction) will be restricted to coverage of the models used.

2.1 Common definitions and classifications

Before describing the models, some common definitions and model classifiers are given in this Section.

2.1.1 Bird-caging

"Bird-caging" indicates a failure mode of flexible pipes characterised by local buckling of the tensile armour wires such that the wires undergo significant radial expansion. Bird-caging is usually caused by high axial compression. Bird-caging modes can be predicted by linear elastic pre-buckling analysis using finite element software. A finite element based study of wire instability modes is presented by Vaz and Rizzo (2011).

2.1.2 End-fittings

Flexible pipe end-fittings connect and secure the individual pipe components at their termination for connecting the pipe to the end connector equipment, transmitting loads and ensuring fluid integrity. End-fittings may be built into the pipe during manufacture, or attached during installation. The presence of end-fitting introduces complicated global and local structural effects. An important global effect is the so-called end-cap effect, which occurs when internal pressure, acting on pipe terminating surfaces in the cross-sectional plane, causes additional axial stress and strain in the pipe.

2.1.3 Ovalisation

The term "ovalisation" indicates the out-of-roundness of the pipe, quantified by the expression $(D_{max} - D_{min})/(D_{max} + D_{min})$, where D_{max} and D_{min} are the maximum and minimum pipe diameter respectively (API, 1998). Ovalisation causes stress concentrations at points of high curvature and can lead to collapse of the carcass and/or pressure armour at lower pressures that if it were not present. For this reason, design recommendations require that ovalisation is taken into account when analysing collapse resistance of a flexible pipe (API, 1998).

2.1.4 Single bore vs. multibore

A pipe with a single central core in which all layers are concentric is called single-bore. Multi-bore pipes, also called umbilicals, include several core components with different functions, including tubes supplying chemicals for injection into a flowline, bundles of electrical conductors and hydraulic fluids.

2.1.5 Axisymmetric models vs. flexural models

Axisymmetric loading involves tension, internal/external pressure or torsional loads on the pipe, or a combination of these. In general, axisymmetric modelling methods are fairly well established and reliable, whereas models capable of dealing with bending are not. Popular approaches to detailed modelling (Witz and Tan, 1992a,b;

Witz, 1996) derive axisymmetric and bending formulations separately and superimpose displacement and stress results. This modelling superposition is used because combining axisymmetric and bending load causes complex three-dimensional deformations that are very difficult to analyse.

2.1.6 Layer separation vs constant contact and interlayer slip

For modelling multi-layer pipes, some models require that all layers have the same radial deformation and are constantly in contact with each other with no tangential slipping; others allow layer separation and differential radial displacements.

2.1.7 Interlayer slip

Interlayer slip is the phenomenon of relative motion between pipe internal components, especially between helical armour wires and adjacent layers. This capability is a key design feature of flexible pipes as it allows the pipe to assume large curvature configurations as the outer layers can slide over the inner ones to relieve the high bending stresses that would otherwise be induced.

2.1.8 Radial constriction with empirical coefficients vs. radial constriction in formulation

Some early methods for calculating the axial strength and axial and torsional stiffness accounted for radial constriction by means of experimentally-determined values or empirical formulae (Goto et al., 1987; de Oliveira et al., 1985). More precise ways of representing interlaminar effects include one or more independent variables that are solved for in the model. An example of the former option is the constitutive model developed by Bahtui (2008). The latter is employed in multi-layer models where each layer may take a different radial displacement.

2.1.9 Serret-Frenet frame

The Serret-Frenet frame is a non-homogeneous (spatially varying) orthonormal frame commonly used for describing parameterised space curves. For a given space curve, the Serret-Frenet triad consists of 1) the tangent vector to the curve, 2) the normal vector, defined as the rate of change of the tangent vector with respect to the curve parameter, and 3) the binormal vector mutually perpendicular to the other two. The curve may then be characterised by the coefficients of the matrix mapping the three vectors to their derivatives with respect to the curve parameter. These coefficients consist of two curvature parameters and a torsion parameter. This last parameter is sometimes referred to as the mathematical torsion or tortuosity of the curve, to emphasize that it is a geometrical measure that is not necessarily associated with mechanical stress. This frame is often used for describing the geometry of deformation of the helical armour wires of a flexible pipe. In this context, the normal vector (in the undeformed configuration) points towards the pipe's central axis.

2.1.10 Bent helix slip assumption vs. geodesic slip assumption

The problem of finding the final deformed configuration of an (initially helical) flexible pipe armour wire that is in potential contact with, but is not bonded to an underlying or enclosing layer, is difficult, if not impossible to solve, unless simplifying assumptions are made (Out and von Morgen, 1997). For flexural analytical models, the helical components are supposed to slip relative to internal or external layers along their own axes. This means that the helix stretched such that it attempts to fill the "groove" traced out by the helix in its undeformed configuration. This is referred to as the bent helix assumption or loxodromic curve (see, for example, Sævik (2010))

In contrast, the geodesic assumption assumes that the component will deform to follow the shortest distance on the curved surface of a hypothetical underlying cylinder, which deforms uniformly. This results in zero normal curvature[1]. In phys-

[1]Normal curvature acts against the wire thickness, rather than against its (radial) depth.

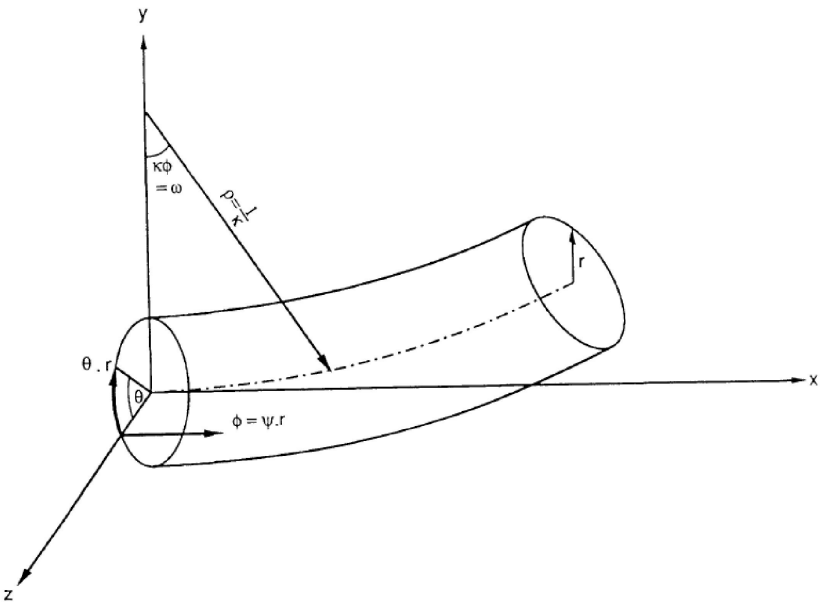

Figure 2.1: Parameterisation of a bent cylindrical surface (Out and von Morgen, 1997)

ical terms, this condition is associated with high normal bending stiffnesses of the armour wire; for this reason it is considered the most appropriate assumption to use for wide tensile armour wires (Tan et al., 2005).

Given a cylinder bent with uniform curvature around one transverse axis (Figure 2.1.10), positions on the cylinder's surface can be described by the coordinates θ, the angular coordinate in the cylinder cross-section and ω, the angular coordinate in the plane of the resulting torus. The position vector is

$$R = \begin{pmatrix} x \\ y \\ z \end{pmatrix} = \begin{pmatrix} (\rho - r\sin\theta)\sin\kappa\phi \\ \rho - (\rho - r\sin\theta)\cos\kappa\phi \\ r\cos\theta \end{pmatrix} \tag{2.1.1}$$

where ρ is the radius of the toroid, r is the radius of the toroid cross-section, κ is the toroid curvature and ϕ is the arc length such that $\kappa\phi = \omega$. The length of a line segment on the surface of infinitesimal length is $dL = \sqrt{dR \cdot dR}$ (Out and von Morgen, 1997). A line drawn on this surface can be described as the function $\theta = \theta(\phi)$, which has the total length between the two positions ϕ_1 and ϕ_2.

$$s = \int_{\phi_1}^{\phi_2} L(\phi, r)\, d\phi \tag{2.1.2}$$

The geodesic (the curve between two given points with minimum length) can be found by solving the Euler-Lagrange equation associated with the minimisation problem.

This can be solved numerically (von Morgen), or an approximate (linearised) analytical solution can be found (Out and von Morgen, 1997). The slip predicted using the geodesic slip assumption may be considered the upper-bound estimate for the slip that occurs during pipe deformation, as it represents the lowest-energy configuration of a stressed armour wire modelled using the wire bar assumption, if zero friction is assumed.

2.1.11 Wire bar assumption vs. wire beam assumption vs. wire shell assumption

A typical way of representing the helical armour wires is to consider them as simplified structural elements in the shape of a helix, so that established structural theories can be used. When using the wire bar assumption, wires have only axial stiffness. This assumption is less useful for predicting stress and fatigue of the armour wires because bending stress resulting from changes in pipe curvature are important factors in assessing serviceable life of the wire (Out and von Morgen, 1997) and this is not accounted for in the bar formulation.

As an alternative to the wire bar assumption, wires can be modelled as helical beams that have axial stiffness and two bending stiffnesses. The appropriate equilibrium equations for these elements are Love's equations (see below). It is noted that the basic beam formulation excludes the torsional, shear and transverse normal stiffness components of the wire, which may influence the accuracy of the model's radial deformation predictions.

A third option is to model the wire as a helical shell strip, with the shell normals aligned with the local radius. This method has the advantage that surface-to-surface

contact discretisation may be used to compute the principal contact interactions i.e. the interactions between the wire and the layers positioned radially outwards or inwards. This is more accurate than the standard node-to-surface discretisation that must be used if the wire is represented as a bar or beam because contact forces are applied to the wire based on the averaged contact separation or penetration of the wire surface, whose position is defined by several nodes, rather than one. This minimises the contact overpenetration error that may occur and hence improves the accuracy of radial displacement predictions. However, using this option is more computationally expensive.

2.1.12 Love's equations

Love's equations are a set of 6 nonlinear differential equations describing the equilibrium of a beam with initial curvature in terms of section force and moment resultants (Love, 1944, pp. 371–372). These equation are difficult to solve, and numerical procedures often leads to bifurcations or no solution (Tan et al., 2005).

$$\begin{aligned}
&\frac{dN}{ds} - S_x\chi_y + S_y\chi_x + q_z = 0\\
&\frac{dS_x}{ds} + N\chi_y - S_y\tau + q_x = 0\\
&\frac{dS_y}{ds} - N\chi_x + S_x\tau + q_y = 0\\
&\frac{dM_x}{ds} - M_y\tau + T\chi_y - S_y + m_x = 0\\
&\frac{dM_y}{ds} + M_x\tau - T\chi_x + S_x + m_y = 0\\
&\frac{dT}{ds} - M_x\chi_y + M_y\chi_x + \theta = 0
\end{aligned} \tag{2.1.3}$$

where s is the distance along the curve, χ_x and χ_y are the components of the final curvature, τ is the final twist (tortuosity), q_x, q_y, q_z, m_x, m_y and θ are the component of the force and couple-resultants per unit length along the curve and N, S_x, S_y, M_x, M_y and T are the components of the force and couple-resultants acting on a cross-section (Costello, 1977). Specifically, N is the axial force, S_x and S_y are the shear force resultants, M_x and M_y are the bending moments and T is the torque

couple.

2.1.13 Equivalent layer

An equivalent layer is a homogenous pipe layer that is used as a substitute for a complex nonhomogenous layer. To ensure equivalence of the two layers, some form of justified averaging or homogenisation procedure must be used. Such procedures typically assume that no friction occurs between the components in the original layer. An example of this procedure is described by Merino et al. (2010), who derive the orthotropic material parameters of the carcass and pressure armour using an analytical calculation assuming these layers could be considered as consisting of helical beam with a modified moment of area. Alternatively, detailed finite element models of these layers may be used to derive the properties of these layers.

2.1.14 Other model features

Other features to be be noted when classifying and evaluating models include the number of degrees of freedom in the model and the extent to which coupling effects are allowed or accounted for between loading and response types. An example of a coupling effect would be an axial load that causes a twisting effect on the pipe. A final factor could be whether the model accounts for residual stresses and strains present in the pipe, although, to the best of the author's knowledge, this is currently not considered in any model due to the difficulty in obtaining the relevant data.

2.2 Test data

The utility of an engineering model intended for practical use, regardless of its theoretical soundness, sophistication or explanatory power, lies in its ability to make accurate predictions that can be verified by experiment. In the case of flexible pipe modelling, desirable predictive capabilities include the ability to predict the response of a pipe as a whole under a range of loading conditions including axial tension, bending, torsion, internal and external pressure, and combinations of these loads. This enables the global response of an installed pipeline to be calculated. Secondly,

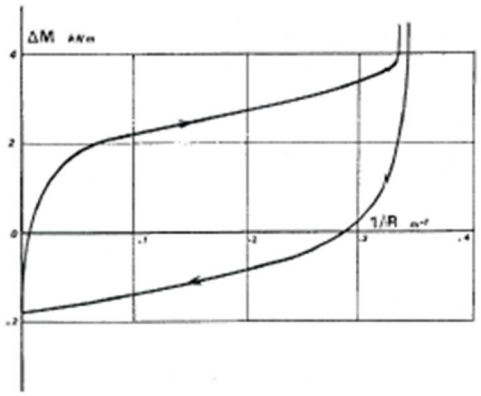

Figure 2.2: Experimental hysteresis curve for bending (Féret and Bournazel, 1987)

it is desirable to calculate the magnitude and range of stresses in pipe components, in order that possible yield points may be identified and fatigue lifespan may be estimated. Thirdly, given a knowledge of likely failure modes, a model can be used to carry out parametric studies under a range of loading conditions to determine the permissible operational envelope for each failure mode.

An obstacle to progress in the development of accurate models of flexible pipes lies in the lack of experimental data in the public domain. Such data that do exist are generally provided with pipe data insufficient to allow the creation of a comparable analytical or numerical model. However, often experimental data provides useful information on the qualitative behaviour of flexible pipes, challenging the analyst to explain and reproduce new phenomena.

Féret and Bournazel (1987) present experimental bending moment-curvature data for a 4 inch diameter flexible pipe designed for a working pressure of 69 MPa under a three-point bending test. The results showing a hysteresis curve (Figure 2.2). These data are reproduced in a report by the oil company Shell (Royal Dutch Shell plc, 1976). It is notable that the hysteresis loop shows very high bending stiffness just before the maximum curvature is obtained, which significantly increases the maximum bending moment.

Leroy et al. (2010) present the results of a high-pressure (50 MPa), high curvature (0.2 to 0.3 m^{-1}) cyclic bending test on an 8m flexible pipe. In this test, a horizontal flexible pipe is anchored at one end (with an end connection) while the other end

is raised and lowered cyclically with a crane. This causes the pipe to experience a curvature that varies along the pipe length and reaches up to 0.5 m^{-1} locally. Strain gauges were attached along one helical wire, along the neutral axis of the pipe and around the circumference of two pipe cross-sections. 10 loading cycles were carried out and strain results were averaged over the cycles. This arrangement seems more convenient than carrying out a four-point bending test, but the non-constant curvature makes it difficult to replicate the conditions in some models.

Sævik (2010) describes a bending test with internal pressure carried out on a 300mm OD flexible pipe of 14.5m length. Full geometric data of the pipe are provided. In the bending test described, the pipe curvature is precisely controlled by a bellmouth, a guide tube formed in a special shape that is used to restrict excessive pipe curvature in operation. The imposed curvature varied linearly along the pipe length. Strain sensors using fibre-optic technology were installed on both sides of several helical wires in the pipe. The testing procedure involved imposing internal pressure of 34 MPa, followed by axial tension of 750kN, followed by imposed cyclic curvature.

Tan et al. (2007) make use of bending hysteresis test data from the SINTEF report, 'Structural Damping in a Wellstream Pipe", FPS200/Flexible Risers and Pipes, STF71 F91059, Dec. 20, 1991. The report provides bending moment-curvature data for a 4 inch ID flexible pipe with internal pressures of 0.7, 10 and 20 MPa. The curves are reproduced by Tan et al. (2007) without numerical axis data.

Two articles compare experimental studies with analytical predictions from different models. The first, presented by Witz (1996), provides flexural and axial-torsional results predicted by the cross-sectional models used by 10 different institutions, including universities, manufacturers, consultancies and specialised research institutes for a single 100mm internal diameter flexible pipe. Good agreement is found between the models for axial-torsional response prediction; however, agreement for flexural results is less good. This study is particularly interesting because the simulations were carried out by the institutions themselves (including Wellstream, Coflexip, SINTEF and Lloyd's Register), and many of the models discussed above were compared, including McIver (1992), Féret and Bournazel (1987), Witz

and Tan (1992a,b) and Løtveit and Often (1990). Data and parameters other than material and geometrical quantities were chosen by the institutions; for example, inter-layer friction coefficients were chosen by the institutions separately.

The second comparison article, by Ramos et al. (2008), presents an experimental study of the axial-torsional behaviour of a flexible riser, which is compared with analytical results calculated by 10 different institutions using different software, including software based on the models of McIver (1995) and Witz and Tan (1992a) described earlier in this Chapter. Full geometric and material data is provided for the 8-layer flexible pipe with 2.5 inch internal diameter, as well as simplified diagrams of the section profiles of the carcass and pressure armour layers. Test data is presented for the axial reaction force resulting from imposed axial extension with ends free to rotate, and for imposed axial extension with ends prevented from rotating, torque-torsion response with no axial force or pressure, and bending-moment curvature data for zero internal pressure and 30 MPa internal pressure. Several comments may be made concerning the experimental results. Firstly, hysteresis loops were observed in the axial strain-axial force response; the axial reaction force is lower on unloading. Secondly, a hysteresis loop is also evident in the torque-torsion response. Thirdly, torsional stiffness is markedly different for torque loading in the anticlockwise direction as compared to the clockwise direction. Finally, the hysteresis loop under flexural loading is much wider when internal pressure is present in the pipe. Bending stiffness also appears to be lower in this condition.

For the purposes of the current work, the published experimental data provides qualitative data on the nonlinear behaviour exhibited by flexible pipes. In particular, the bending hysteresis data presented by Tan et al. (2007) were valuable in demonstrating the dependence of bending behaviour on pipe internal pressure. In previous work, (Bahtui, 2008), this phenomenon led to consideration of the local mechanism responsible for this behaviour and formulation of the constitutive model, which is used in this work.

2.3 Analytical formulations for flexible pipes

In the analytical modelling of flexible pipes, a common approach uses a composite or cross-sectional model. These models develop the global load-displacements relation for pipes based on summing the contributions of the individual layers; i.e. interlaminar effects (contact, friction, radial contraction, delamination, etc.) are ignored. In distinction, multi-layer formulations model the layers separately, with their own degrees of freedom. Next, some stress-prediction models based on the analysis of a single armour wire in a flexible pipe are considered.

Models can be focused on obtaining the response of the pipe in bulk, or also involve the calculation of stress and strain in the constituent components of the pipe. Accurate prediction of the latter puts higher demands on the accuracy, appropriateness and sophistication of the analytical equations developed.

2.3.1 Cross-section models

One of the most straightforward, intuitively understandable and computationally tractable approaches to flexible pipe modelling is to assume linearity of response, in that the response of a pipe composed of many independent parts is predictable by summing or superimposing the characteristic responses ("stiffnesses") of the component parts. Several authors apply this method to the analysis of steel cables and similar structures, which share many characteristics and structural components with flexible pipes with helical armour wires. The primary difference is that interwire contact in flexible pipes generally does not occur, and as a result, there is no hoop stress developed in helical armour layers. Secondly, component strands in such cables are usually circular in section, whereas in flexible pipes they are typically rectangular in section.

Cross-section models represent axial-torsional pipe behaviour by relationships between stress resultants and generalised strain measures considered at a pipe longitudinal cross-section, where all sections are considered identical. It is frequently assumed that plane sections remain plane throughout the analysis. Linear behaviour (with coupling between the loading actions) is assumed, as frictional and contact

phenomena are not revealed in the plane of the sections. These are models are used in the inital stages of pipe design to size components. The sectional properties that must be evaluated are:

- Axial stiffness (EA) [N]
- Bending stiffness (EI)[Nm^2]
- Torsional stiffness under clockwise torsion (GJ) [Nm^2]
- Torsional stiffness under anticlockwise clockwise torsion (GJ) [Nm^2]
- Torsion resulting from tension[m]
- Clockwise torsion resulting from tension [m^{-1}]
- Anticlockwise torsion resulting from tension [m^{-1}]

An early example of this approach is given by Knapp (1979). In this work, a derivation of a new stiffness matrix is given for helically armoured cables considering tension and torsion of the cable. Expressions are developed for strain along wire axes resulting from cable axial extension, twist, bending and radial contraction of the layer, from which an internal strain energy expression can be calculated. The wire bar assumption is used in these calculations. An expression for wire strain under bending is taken from a solution of Love's equations (Love, 1944) without derivation. This analysis is limited by the fact that the radial contraction is given from an independent analysis considering the underlying layer as an elastic thick cylinder, and thus contact between components is not handled directly. The geometrical restrictions on the method are that expressions are valid for initially straight wire sections only. A linearised version of the equations is also presented that neglects higher-order terms in the strain expressions.

A more extensive and discursive treatment of helically armoured cables is given by Lanteigne (1985), in a formulation that includes bending. The work focusses on aluminium conductor steel-reinforced (ACSR), in which the central core component may be assumed to be rigid.

The wire bar assumption is used to model component wires. Linearised expressions for wire strain due to cable axial strain, twist and bending are developed. The contribution from bending is derived using the assumption that plane sections remain plane during bending. A global stiffness matrix is then assembled. The author then extends the analysis of Knapp (1979) by considering cables comprised of multiple layers of helically wound wires.

The bent helix assumption is used for wire deformation under bending. This is considered appropriate for the application because the high fill-factor and associated high frictional forces between wires prevent the wires from assuming the "natural" geodesic configuration. The author discusses the case in which differing axial force between adjacent layers may cause one layer to slide over the other, and derives an expression predicting when this will occur, based on the radial force and a friction coefficient. In the context of cables consisting of multiple layers of helically wound wires, the axial force carried by layers when the conductor is bent will be greatest in the outer layers. The author accounts for this by assuming that, if the slip condition is met, the axial force carried by the outer layer is reduced to that carried by the layer directly underneath it. Expressions are then developed for the radial force exerted by each layer.

Unlike the development of Knapp (1979), the variation of the lay angle of a wire after deformation is ignored in this analysis, as the author observes that this does not influence results for torsional problems.

The discussion of the reduction of flexural stiffness with increasing cable curvature is of interest for the purposes of this project because the same phenomena occurs in flexible pipes, and due to the same mechanism: slippage of wires. The author discusses the effects of radial stresses and cable tension in enabling frictional forces to develop that resist wire slip, and develops an expression to predict the onset of slip similar to that used by Kraincanic and Kebadze (2001), but, instead of considering individual wires, the expression considers each layer in aggregate, in terms of the axial loads carried by each layer. Calculations for radial forces are also presented, but these are less applicable to flexible pipes.

2.3.2 Multi-layer models

Flexible pipes are always constructed of multiple concentric layers. Capturing the interactions between layers in terms of radial displacement constraints and normal and friction forces is key to predicting behavior.

In a relatively straightforward approach to multi-layer modelling, Harte and McNamara (1989, 1993) and McNamara and Lane (1984) develop layer stiffness matrices relating external actions on each layer (axial force, bending, torsion, internal and external pressure) with deformation parameters (axial strain, curvature, torsion and radial displacement of the inner and outer surfaces). The wire bar assumption is used for helical armour layers. The layer matrices are then assembled into a global stiffness matrix. Due to the presence of initially unknown interlaminar contact pressures in the global load vector, a set of radial compatibility constraints are introduced that force all layers to remain in contact. The equations are then solved iteratively. In Harte and McNamara (1993), comparison is made with a axisymmetric finite element model, perfectly bonded, using a layer of rebar elements (designed for modelling reinforced concrete) to model the helical armour layers. Good agreement between the methods is found, but no comparison with experimental results is attempted. The simplicity of inter-layer interactions in this model means that is can be considered almost as a cross-section model with the equations assembled using a different approach. The limitations of such a model become clear when large deformations are considered. Accurate modelling in these situations require components to be able to deform nonlinearly and interact realistically.

An analytical model for the axisymmetric loading of unbonded umbilicals and flexible pipes is presented by Custódio and Vaz (2002). This model incorporates nonlinear material behaviour, computes the occurrence and effects of interlaminar gaps and inter-wire contact. Instead of using Love's equations to model the equilibrium conditions of the helical wires, the simplified Clebsch-Kirchoff equations are used, which assume the wires are structural bars rather than beams.

Féret and Bournazel (1987) develop a multi-layer model used for axisymmetrical loading and bending predictions. This model includes variables for the change in radius and thickness of each layer. The wire bar assumption is used. The full model

is implemented in the program EFLEX; only simplified and approximate equations are presented in this paper, using the assumption that all layers remain in contact. Equations are presented for wire stresses, interlayer pressures and changes in radius and pipe length.

The authors identify three distinct regions in the bending moment curvature response: an initial very stiff section where a "frictional moment" prevents any significant bending. The magnitude of the frictional moment is described as increasing linearly with internal pressure. This is followed by an elastic section (approximated as linear) in which the stiffness of the plastic sheaths are largely responsible for determining the pipe bending stiffness, and the stiffness is only weakly dependent on the pressure. The model predicts a much stiffer final interval in the bending response, which is demarcated by a "contact radius" on the lower curvature side, when armour wires within a layer come into contact with each other and are required to change their lay angles in order to deform further, and a blocking radius on the higher curvature side, where the bending stiffness increases sharply. The reason for this is that the pressure armour is comprised of a single self-interlocking wire. The interlock is fairly loose such that some motion between the adjacent "hoops" is possible. When the pipe curvature is very high, the raised sections of the adjacent "hoops" are foced into contact with each other, causing high resistance to further bending. Finally, data is presented from a bending test that shows the pattern of bending behaviour predicted by the authors' model.

The initial stiff response is not reproduced by the works of other authors reviewed here. Instead, a centred, symmetrical hysteresis curve is obtained in some articles (see, for example, Kraincanic and Kebadze (2001) and Witz and Tan (1992b)). It is notable that this response is obtained using a three-point bending test, which would cause a linearly varying bending moment distribution along the pipe, with a maximum at the midpoint. Other investigators (for example, Witz and Tan (1992b)) use a two-point rotary bending test, which produces a bending moment that is constant along the pipe length. Also, relatively high curvatures are used ($\sim 0.35 m^{-1}$). To model this, the geodesic slip assumption is used. Expressions are given for the slip magnitudes of tendons according to this assumption, separated into components

along the length of the tendon and perpendicular to it. Equations are also given for calculation of the contact radius, post-slip bending stresses and post-slip frictional stresses. Again, derivations are not presented in this article.

Out and von Morgen (1997) derive exact and approximate expressions for the deformed shape of an initially helical armour wire of a flexible pipe using the geodesic slip assumption. The slip, normal curvature and binormal curvature are then calculated by finding the difference between the geodesic solution and the bent helix configuration. The aim of the analysis is to determine slip and curvature change in the wire, described as important for fatigue assessment.

Kraincanic and Kebadze (2001) develop a model for predicting the onset of wire slippage during bending. The model predicts a gradual, nonlinear transition region between high stiffness (at small curvatures) and low stiffness (at large curvatures) parts of the pipe's bending moment-curvature response due to the fact that different parts of the helical wires start to slip at different points. The model predicts that, upon increasing pipe curvature, wire segments start to slip at the neutral axis of the pipe. The zone of slippage increases gradually until all the wire segments on the pipe cross-section are in this state. The authors develop expressions for the curvature that will cause slippage in a single wire, expressions for the force that can be carried by wires in the slipped and, by summing these forces, a model capable of predicting the bending moment-curvature response of a complete flexible pipe. Simulation results obtained using this model are shown to correspond closely to experimental results.

Witz and Tan present pipe analyses for bending (Witz and Tan, 1992b) as well as analyses for the axial-torsional case (Witz and Tan, 1992a), using the wire beam assumption. The authors use analytical expressions for the axial strain, local change of curvature and twist of a helical wire based on the deformation of the pipe as a whole. Variation of stress and strain over the wire cross-section is ignored. A reduced version of Love's equilibrium equations for a helical element is employed, using the assumption that all external forces and moments acting on the wire and all the section force/moment resultants of the wire are constant along the strip. It is assumed that the only distributed force is towards the pipe axis (interlayer

pressure). The constitutive relation connecting stress resultants and curvatures takes the geometric section properties of the wire as constants. The authors note that local bending and twisting of the wire may be restricted due to friction of structural restraint of the surrounding components. The mechanisms and onset of axial and twisting slip of wires over the pipe is discussed. A combined equation is written for each layer, whether cylindrical or composed of helical wires, that relates interlayer contact pressures (constant over the surface) with a nonlinear function of the layer's change in radius and change of thickness. Interlayer compatibility conditions are introduced that reduced the number of degrees of freedom. If negative pressure (and hence layer separation) is detected at an interlayer interface, the model is split into two substructures, which are solved for separately. Substituting for the "change in thickness" variables leads to a single nonlinear equation for the pipe which is solved using the Newton-Raphson method. Using this model, predictions of the axial-torsional behaviour of an unbonded flexible pipe, an umbilical and a marine cable are made and compared with test data (except in the case of the flexible pipe). The model predicts a bilinear response to axial loading, with initially compliant behaviour changing abruptly to a much stiffer response when the small gap (0.25mm) included between inner armour layer and inner polymer layer is closed. A linear response is predicted in torsion, with a different stiffness depending on whether the applied torque is in the clockwise or anti-clockwise direction. The authors highlight the sensitivity of response to the presence or absence of interlayer gaps and note that if pipe ends are prevented from rotating in a tensile simulation, or prevented from extending axially in a torsional simulation, the response will be much stiffer. The authors note that this is also observed in tests and attribute the proximate cause to the interlayer gap formation process.

From consideration of the axial strain in helical wires under bending, it is predicted that, under increasing bending curvature, slip will first occur at the pipe's neutral axis and, secondarily, on the inside of the pipe bend, on the plane of curvature. The same expression for critical pipe curvature for slip onset at the neutral axis as Kraincanic and Kebadze (2001) is presented. The contribution of the bending and torsional stiffnesses of each individual wire to the bending stiffness of a heli-

cal armour layer is calculated. From these theoretical considerations, 3 regions in bending are predicted: an initial high stiffness region (with linear response), a transition region (with a nonlinear softening response) and a final lower stiffness region, again with linear response. However, in bending tests of unpressurised pipes, the transition points were not observed and it was found that slip onset occurs at very small curvatures under these conditions. Experimental bending stiffnesses matched well with analytical predictions, if expressions for post-slip behaviour are used. It is stated that the contribution to pipe bending stiffness from the axial stiffness of the wires is in many cases the main contribution.

In a later article (Witz and Tan, 1995), the analytical model is extended for predicting the stresses and strains arising in the helical wires of a flexible pipe under bending. This is achieved by differentiating the expressions developed for the deformed configuration of the wires developed in the previous articles (Witz and Tan, 1992a,b). In this model, the configuration of helical wires following slip is derived using the bent helix assumption and uses a linearised expression for the deformed configuration. The authors note that, when the ends of a flexible pipe are constrained, the main direction of wire slip is in the lateral direction and the axial strain in the wires following slip is in general nonzero. The model is compared with rotary bending test of an umbilical. Close agreement in the final global configuration of the umbilical is shown, but a comparison of stress data is not presented.

A very detailed analytical model for flexible pipes is presented by McIver (1995) Distinguishing features of this model include modelling of armour wires as helical beams with torsional stiffnesses and inclusion of interlaminar friction and separation. Imposed deformations or applied forces may be used as input data. Equations of equilibrium are based on Love's equations. The accuracy of the model is based on the accuracy of the kinematic description of the helical armour wires. Starting with the Serret-Frenet equations relating the derivatives of the Serret-Frenel vectors to the vectors themselves, a second pair of axes are introduced in the principal directions of the wire section, passing through the wire shear centre. Together with the wire tangent vector, these axes form the local (undeformed) basis. The curvature in the Serret-Frenet relations is split into two components relative to these axes. This

results in a set of equations, similar in form to the Serret-Frenet relations, that describe the change in the local basis vectors with respect to the curve parameter, valid for the initial undeformed helical configuration.

The next step is to express the wire displacement and rotation variables that arise under a given deformation (which are functions of the wire parameter) using the local basis vectors. The current basis vectors are related to the initial basis vectors using a rotation matrix containing the rotation variables.

Expressions for axial strain, local curvature vector, and local torsion are written as dot and cross products of the wire displacement vector, initial tangent vector, the current basis vectors and derivatives thereof with respect to the wire parameter, and expanded in terms of the initial basis vectors. From this, local expressions for the wire axial strain, curvature and torsion can be written in terms of the local displacement in the local system, with the parameters being the initial components of curvature and initial geometrical torsion, and the variables being the three components of displacement and axial twist. Thermal effects are also included in the model.

McIver's formulation is more sophisticated than the model of Witz and Tan (1992a) chiefly due to consideration of the rotation of principle axes of the sections of the helical wires. Witz and Tan assumed that the principal axes maintain their initial orientation with respect to the normal, binormal and tangent axes of the deformed helix representing the wire centroidal axis, such that the normal and binormal stiffnesses, as well as torsional rigidity of the wire is not affected by the deformation of the centroidal axis. This would clearly not capture stresses induced in helical wires due to, for example, twisting of the wire around its own centroidal axis. This modification greatly increases the complexity of the governing equations. Only a limited selection of results obtained using the proposed model are presented in McIver's article. It is interesting that his model predicts compression of the carcass layer under combined axial tension and internal pressure loading, whereas internal pressure alone causes the outer layers to separate from the carcass because internal pressure is applied to the pressure sheath and not on the carcass. When tested under tensile loads, the model predicts a much lower axial stiffness under

compressive loads due to layer separation. In bending simulations, the response is investigated using different values of static and dynamic friction. Again, a bilinear moment-curvature results. Initial bending stiffness using a coefficient of friction of 0.2 is approximately double the stiffness of a model without friction. The author suggests that friction coefficients should be varied depending on the degree of wear accumulated by the polymer layers.

2.3.3 Single-wire analysis models

One interesting approach to flexible pipe modelling that has been developed in recent years involves representing only a single helical armour wire, without necessarily modelling other layers. This allows the effects of wire fatigue under cyclic loading to be calculated efficiently, without the complications of determining interlaminar contact pressures or deformation and equilibrium of other pipe components. This strategy, developed and described by Féret et al. (1995), Leroy and Estrier (2001) and Leroy et al. (2010), takes maximal advantage of the symmetry and structural periodicity of the helical component. It is therefore highly efficient at obtaining the wire stresses required for fatigue calculations, especially for bending, but is not suitable for local or limit-state analyses, due to the assumption of identical conditions in all armour wires and requirement of constant curvature.

The models based on this approach assume that the behaviour of all armour wires of a given layer is the same. The geometrical description of a point on a deformed tensile armour wire is described with the Serret-Frenet relationships (here referred to as Darboux-Ribeaucourt axes). The curvatures and (mathematical) torsion parameters used in these relationships are found by parameterising the curve with two coordinates, φ and θ (see Figure 2.3), and writing expressions for the position vector of a point on the wire in terms of these coordinates and the global Cartesian unit vectors , as well as the pipe radius and curvature (assumed constant in this formulation). An expression relating the rate of change of the φ coordinate with the θ coordinate for points lying on the bent helix of the armour wire completes the geometrical description of the wires and their deformation.

The equilibrium equations are developed for a single wire on each armour layer

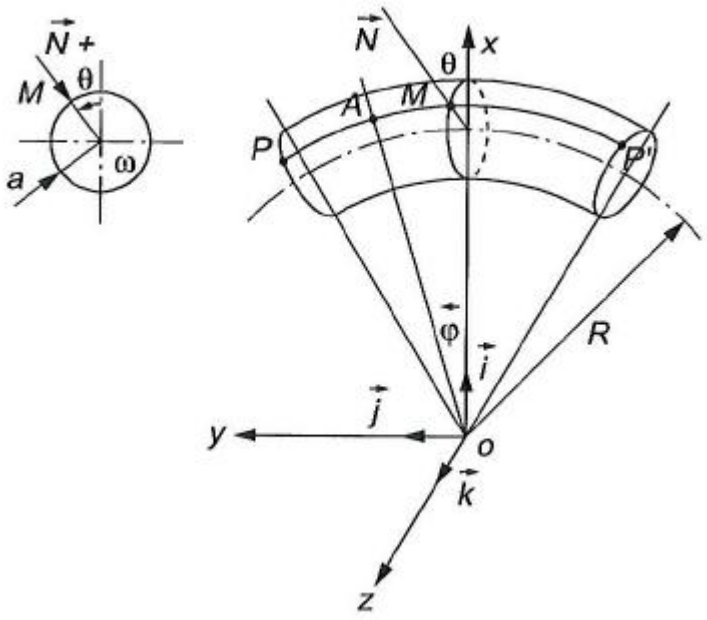

Figure 2.3: Idealised bent pipe geometry (Féret et al., 1995)

from this geometrical description assumes constant (but not uniform) interlaminar friction vectors, described as forces per unit length of the tendon. Shear stresses in the armour wire are neglected. Equations for interlaminar friction are developed. Tangential and binormal slip rates are defined as rates of increase of the respective slips with the pipe curvature. The assumption is made that the ratio between the tangential and binormal slip rates is equal to the ratio of the respective friction forces, that is, the friction is dynamically isotropic.

Solution of the equations proceeds in two steps: Firstly, the analysis is conducted assuming any axial deformation caused by friction is zero (only effects due to pressure are considered). This results in sinusoidally varying solutions for the slip. Secondly, friction forces are calculated from the equilibrium equations. With this information, axial stresses and strains in the wires can be calculated.

Further details of the finite-difference algorithm are given by Leroy and Estrier (2001). It is noted that the model neglects torsion and provides stress predictions only under conditions of constant pipe curvature. Periodicity in the displacement solution is assumed, corresponding to the helical periodicity of the armour layer. This model does not consider the global equilibrium of the pipe and does not compute

interactions between the components, instead relying on the kinematic assumptions of the wire deformation.

In a later publication (Leroy et al., 2010), three models for component stress prediction in flexible pipes are compared. The three models considered are an single-wire analytical model developed from the earlier model (Leroy and Estrier, 2001), and two finite element models, referred to as a 3D periodic model and a 3D explicit model. The 3D periodic model consisted of a single layer of helical wires, with all internal and external layers represented by rigid kernels. The length of this model was equal to the pitch length of the wires divided by the number of wires and periodic boundary conditions were applied to the ends of the model. The 3D explicit model was a detailed finite element model in which all layers were represented and a full pitch length of the structure was modelled (see Section 2.4.2). This model used end constraints such that all nodes on an end plane were linked to a reference node in the centre of the plane by a kinematic coupling constraint.

The single-wire model used is an extended version of that presented by Leroy and Estrier (2001), now including lateral contact between adjacent armour wires. Computations are still carried out on a single wire, assuming that all wires behave similarly. A contact detection and enforcement algorithm (penalty enforcement method) is incorporated into the finite difference solver. Frictional effects between the wires are ignored. The inclusion of inter-wire contact influences the transverse curvature of the wire.

Cross-validation between the models was carried out for cyclic bending. Inter-model comparisons of the variation of axial stress with circumferential angle showed good correspondence for the inner armour layer and poorer for the external layer. For the external layer, the stresses predicted by the 3D explicit model were greater than those predicted by the other models, by an amount that was both significant and roughly constant in magnitude over the pipe circumference. This difference was attributed to the effects of the end constraint in the 3D explicit model, which is not manifest in the inner armour layer because higher frictional loads localise this effect such that they are closer to the end fittings.

Secondly, the variation of transverse curvature with the angle around the cir-

cumference was plotted and compared between the models. The results are in fairly close agreement. Two reasons advanced for the differences were the greater degree of inter-wire contact within each layer present in the analytical model and, again, the presence or absence of end-fitting effects.

The 3D explicit model was then compared to experimental results (see Section 2.2). The model predictions are good, but fairly conservative in terms of stresses. The other two models were not compared because they were not able to simulate the varying curvature and end-fitting effects present in the physical test.

Sævik (1993) developed a curved beam finite element base on the differential geometry of thin curved beams and a wire-pipe interaction model. The element displacement formulation uses the kinematic constraint that the wire upper and lower surface conform to the bent cylindrical surfaces which the inner and outer restraining sheaths are assumed to take. The wire-pipe interaction model applies elasto-plastic springs to the wire nodes. Comparison of wire stresses at end restrictions were made with experimental data under conditions of high internal pressure (25 MPa), tension and varying curvature. A good approximation to experimental stresses was achieved, though results were less accurate for cases of large tension and curvature.

2.3.4 Summary

Although the purpose of the current work was to develop finite element-based, rather than analytical, models of flexible pipes, the examination of analytical models was an important preliminary step to the development of the models described in later Chapters. Examination of the capabilities, theoretical basis and validation status of these models was highly useful in choosing element types to use in the detailed finite element model and the contact-friction model. Examination of the limitations of the models due to simplifying assumptions highlighted areas in which finite element-based models could offer increased accuracy in local stress prediction and estimating global response; however, the robustness and speed of computation of analytical models provides a benchmark and challenge for developers of finite element models. A significant area of discrepancy between recent analytical developments is

determination of the deformed shape of the tensile armour wire under pipe bending. To the best of the author's knowledge, no experimental data has been published confirming or disproving the various assumptions made in different models, although the bent helix and geodesic assumption provide theoretic upper and lower bounds for the wires' motion. As this deformation directly influences the local bending stresses and fatigue life of components, accurate computation of this deformation has been identified as a key capability in the detailed finite model developed in this work.

2.4 FE-based models for flexible pipes

2.4.1 Commercial software and line models

Routine design and analysis of flexible pipes and installations is carried out by consultants and specialists using dedicated commercial software. A summary of commercial software for flexible pipes, together with general capabilities and literature references, is given in Table A.1 of the Appendix. Much of the power and convenience of such packages lies in the automated application of a wide range of environment effects and boundary conditions. In this Section, only the core structural models used in such packages, and their predictive capabilities, will be discussed. Models are designed to address questions of global configuration and mean section stress, and therefore represent pipelines as parameterised curved lines in three-dimensional space. For this reason, they are designated here as *line models*.

An early version of such types of model is described by Felippa and Chung (1981), who present a formulation and algorithmic implementation of a geometrically nonlinear beam model. Displacements and strains for each element are considered in a "convected" coordinate system that moves with the element. Axial strain is calculated using the formula $\epsilon_x = u_{,x} + 1/2(u_{,x}^2 + v_{,x}^2 + w_{,x}^2)$ where $(x,\ y,\ z)$ is the convected coordinate system with the corresponding displacements denoted by $(u,\ v,\ w)$, indicating that an extensional component due to bending is considered when calculating the axial strain. This geometric nonlinearity causes the element stiffness matrix to have a complex form, which is dependent on the displacement. Simple expressions for loading due to weight, external pressure and internal fluid flow.

The leading commercial software package for dynamic analysis of offshore systems is Orcaflex, produced by Orcina Ltd. The core structural model of Orcaflex avoids the difficulties of beam element representations of flexible pipes (in handling large displacements and rotations and in applying distributed external loading and weight and inertia loading consistently) in favour of a lumped mass and lumped stiffness approach, effectively representing pipelines as linear assemblies of axial and rotational springs, damper elements and lumped masses. Non-linear and hysteretic relationships can be included by specifying the relevant curves. Additional packages can extend functionality (Tan et al., 2007). Several verification studies have been published[2], comparing the predictions of Orcaflex with both competing software and other formulations. Of particular interest are comparisons with the lumped mass model of Low and Langley (2006) and the more complex model of da Silveira and de Arruda Martins (2005) for touchdown modelling. The former comparison shows how the core lumped model used in Orcaflex can be easily and accurately reproduced, while the latter uses Orcaflex to benchmark a numerical method solving the differential equations describing a flexible pipe (with bending stiffness) in three-dimensional space. Very little discrepancy was found when comparing results from both models for a test case. These validation show the good predictive capabilities of Orcaflex even compared to mathematically more sophisticated approaches.

The Flexcom package, produced by MCS Kenny, is a also a line-based flexible pipe simulator, based on 3D hybrid beam-column elements with fully coupled axial, bending and torque forces incorporated into the formulation. The axial force is treated as an independent solution variable, interpolated independently from the axial strain. This modification avoids numerical difficulties caused by the axial stiffness being much greater than the bending stiffness. The beam element used has 2 nodes and 14 degrees of freedom, including two Lagrange multipliers (Flexcom, 2011; O'Brien et al., 1991). Nonlinear kinematic modelling capabilities include large displacement, large rotations, but not large strains. Recent versions include frequency domain analysis and a fatigue analysis postprocessor.

[2]Available at *http://www.orcina.com/SoftwareProducts/Validation/index.php*

Tan et al. (2007) present and describe programs for three-dimensional time-domain analysis of the bending hysteresis phenomenon. In this paper, two models for nonlinear global analysis of flexible pipes are presented. Both programs are implemented as add-ins to Orcaflex.

The first model, developed by Orcina Ltd. provides a means for Orcaflex to apply appropriate 3D increments of bending moment to the inter-node rotational springs for given curvature increments and curvatures, when the user can only supply a moment-curvature relationship for single-plane bending (which is usual, because obtaining data for combined bending is much more expensive). The model uses the single-plane bending-moment curvature data (which must be supplied as input data) to provide appropriate scalar stiffnesses to multiply three dimensional curvature increments in the pipe model and obtain the associated bending moment increments. Upon monotonic loading, the total curvature of an inter-nodal interval is represented as the sum of curvature increments, each with an associated bending moment increment, with each curvature increment that is added later being associated with a progressively smaller increase in bending moment The model allows hysteresis behaviour to be simulated in any cycle of combined bending loading, because when the curvature is reduced, curvature increments are removed in the same order they were applied i.e. the ones associated with larger bending moment increments are removed first.

The second model, developed by Wellstream International Ltd., calculates the extent of the slip region in a pipe element using the current curvature data and internal history variables recording the element's previous curvature and slip states. This enables section moments to be calculated and returned to the main model. Stresses in individual tendon wires are calculated in a subsequent postprocessing operation. Details of the relevant equations are not given in the article.

For both of the above-mentioned models, the authors present pipe bending test data used for model calibration and a simple global dynamic analysis demonstration.

2.4.2 Detailed finite element models

De Sousa (2010) and Merino et al. (2010) describe a model composed wholly of structural elements. Using the commercial FE package ANSYS, a model is constructed with concentric solid layers discretised with thin-walled (shear-flexible), 4-noded shells. Helical armour wires are modelled individually as three-dimensional beams. The carcass and pressure armour layers are modelled as equivalent (cylindrical) layers with orthotropic properties, for which analytical derivations are presented. High-strength tapes may be included in the model by interpreting them as a layer of shells that are unable to resist compressive membrane loads. Tendons are modelled as Euler-Bernoulli beams, with principle axes (for moment calculations) in the pipe radial direction.

The authors use a penalty method for contact constraint enforcement. Although they do not provide details of the formula used to determine the penalty stiffness, it will be shown later in Section 5.2.1 that the penalty value is chosen to correspond to the physical normal stiffness of two plates in contact to compensate for the infinite normal stiffness inherent in standard beam and shell elements.

A Ramberg-Osgood material model is used for the steel wires and linear hardening plasticity is assumed for polymer layers. Derivation of the parameters of the equivalent layers is included. The article also describes a simple method to back-calculate stresses in individual components of equivalent layers once the analysis is complete. When carrying out simulations, all nodes in the two end planes of the pipe are constrained to move together.

A similar approach using a general-purpose FE program is adopted by Le Corre and Probyn (2009), in this case using the FE package ABAQUS. In this model of a single-core umbilical, three concentric sheaths are modelled as cylindrical shells. The annulus between each pair of sheaths contains helically wound tubes, cables and fillers, modelled as circular-section beams. Simulations are carried out using the explicit solver, using the general contact algorithm with a friction coefficient derived from tests. The discretisation of cylindrical layers is fairly coarse. When beams interact with surfaces in the ABAQUS general contact algorithm, they are assigned an effective contact surface in the form of a cylinder with the beam as

its axis. This surface is used to implement the contact constraint. The beam has then effectively a circular cross-sectional area (for the purpose of computing contact interactions) equal in area to the assigned beam cross-section, regardless of the actual shape of the beam cross section. The radius of the cylindrical contact surface is referred to as the "contact radius". The discretisation of beams is limited by requirement for the contact radius to be less than 0.3 times the length of the beam elements.

A detailed finite element model of an umbilical was created by Risa (2011) using ABAQUS. This model consists of two layers of helical conductors wrapped around a central core. The conductors are circular in cross-section and tightly packed. The conductors are discretised using three-dimensional finite elements. The general contact algorithm is used to compute contact interactions, and analysis are carried out using the explicit dynamics approach. Kinematic constraints are used to enforce fixed-in-plane conditions at the end sections. The model uses 261 000 elements and was solved using 128 or 320 processors running in parallel. It is notable that the contact causes "hot spots" in the conductor stress that are repeated periodically along the conductor length, although the model geometry and loading are uniform along the length. This pattern of stresses is very similar to that reported by Bahtui (2008), who used a similar approach for modelling flexible pipes.

In the work by Sævik (2010), bending stresses generated in finite element models of flexible pipes are compared with experimental results. Two different FE models are used. The first is a cross-section stress-resultant method (moment-based model) based on a similar approach as used by Kraincanic and Kebadze. Based on the local friction conditions at different parts of the armour wires, the three regions of possible slip states for a tensile armour layer identified by Kraincanic and Kebadze (2001) are recognised. The critical conditions delimiting these states are formulated in terms of local section curvature relative to a constant critical curvature that is a function of the number, material and cross-sectional properties of the helical wires and on the friction coefficient. This leads to expressions for the frictional moment developed by each layer. It is recognised that different layers may have different geometrical and material properties; for this reason, the section frictional moment

is obtained by summing the contributions from each of the constituent layers.

The author then formulates a constitutive relation for each armour layer in terms of the moment resultants and the wire slips. In this formulation, an associative plasticity relation is developed using the two applied moments as generalised stresses, the aforementioned friction moment as the slip-onset/yield surface and the elastic and plastic "slip curvatures" as generalised strains. In summary, this is a plastic beam model with coefficients derived from an analytical model, similar in principle to the plastic beam described by Bahtui (2008) and the current work, where "friction moments" correspond to the "generalised back-stresses ($\boldsymbol{\beta}$)" for the moments.

The appropriate incremental form of the constitutive relation is also derived and is equivalent to the "consistent tangent matrix" used in this work and discussed in Section 4.3.1.

The second model considered by Sævik (2010) is a sandwich beam formulation: this is a multi-layer finite element model in which all components and armour wires are modelled separately, but in constant contact, such that the whole structure forms a type of composite beam. The wires are allowed to deform along their own axes (bent helix assumption). The potential energy of each tendon is assumed to consist of a part resulting from strain along the helix path, and a part representing the slip along the helix path. The latter is considered purely elastic, so the energy contribution is $E_{Slip} = 1/2k(v_s - v_p)^2$ where v_s is the actual displacement along the helix axis, and v_p is the displacement that would result if plane sections of the pipe remained plane during deformation. Thus, the stick-slip behaviour of the wires is handled, not by a discontinuous Coulomb-type friction interaction governed by interlaminar normal pressure, but by enforcing the stick condition using a weak penalty spring with a constant stiffness (a chosen shear stiffness parameter).

The author explains the importance of evaluating high-cycle fatigue associated with low-magnitude loading because, combined with corrosion effect, it can be the cause of significant damage. End effects are dealt with in the model. Verification tests were also performed, detecting wire stresses by lacing the test specimen with fibre-optic sensors. The author finds good agreement between both models and test data for low magnitude curvatures.

Based on earlier work it is reported that, for multiple cycle analyses, transverse slip sums to zero and, hence, the bent helix slip assumption can be used.

Tan et al. (2005) conduct a finite element study on the validity of the bent helix and geodesic assumptions for slipped wires. The effects of wire thickness and height on the appropriate choice of slip assumption to be used is also investigated by a parametric study because, by assuming the deformed wire stays flat on the surface on the underlying cylinder, the influence of the wire cross-section is neglected in both assumptions. An analytical strain energy model and a finite element model are used to evaluate these effects. The finite element model consists of a cylinder and a helical wire modelled with 3D continuum elements. The wire is pinned at the ends to the cylinder. Pressure is applied to force the parts together.

The description of the deformed wire state is expressed as a relationship between the wire parameters θ and ϕ (see Figure 2.3). The authors show that if the exact solutions for the deformed configurations of slipped wires are calculated for either of the two assumptions, the result will be that the length of the helical wires (and therefore the axial strain) will not be same before and after slip, and will in fact be a function of the pipe length modelled. This result uses the assumption that end restrictions do not allow the ends of the helical wires to move out of plane, so this is consistent with experimental tests, but not necessarily with the condition of a flexible pipe segment in operation, which may be kilometres distant from end connectors. It is noted that the linearised approximation to the geodesic slip assumption introduces spurious non-zero normal bending stresses as the final configuration no longer has uniformly zero curvature in the wire normal direction.

In the same paper it is noted that using expressions for deformation without simplification leads to axial-bending coupling, and the nature of the coupling is shown by the higher-order effects. In this case, the geodesic slip assumption predicts a contraction of the wire of 0.2% and a very slight increase in length for the bent helix assumption. These observations are interesting when considering the appropriate boundary conditions to apply to a detailed flexible pipe model (see also Section 5.2.2).

The authors also speculate that in a combined bending-tension case with con-

stant tension, the tension stress in the wires drives them to follow the geodesic path more closely.

Comparing the analytical and FE models used in this article, it can be seen that the analytical model forces the wires to stay flat on the cylinder surface while the FE model does not. This means that, in the analytical model, the wire normal curvature cannot change to relieve stresses, forcing the binormal curvature to change instead such that the normal bending stress is overestimated. This can also be true for some multi-layer analytical models that allow layer separation.

Further examples of detailed finite element models can be found in the work of Leroy et al. (2010). Two finite element models are employed in this work: a "3D periodic model" of very short axial length and a larger "3D explicit model". Both models were implemented using the commercial FE code ABAQUS.

The 3D periodic model includes all the wires in a layer. The length of the model was equal to the pitch length of the wires divided by the number of wires in the layer. This is justified by the observation that the structure will appear the same this distance along the pipe, even though the identity of wires that fill the positions will be different at each periodic section. This is effectively an assumption that the local wire behaviour is dependent on the position of the point in circumferential-axial coordinates, rather than on the particular wire the point is on. This assumption is weaker than the previously used assumption (in the analytical model) of equivalent behaviour regardless of the circumferential placement of the wire. A 3D implicit finite element model of this segment was built using linear reduced-integration continuum elements and the appropriate periodic boundary conditions applied in a user subroutine written in FORTRAN code. Equivalent layers were used to model the non-helical layers. All contact interactions between components were computed (details not specified). Loads are imposed on a floating "control node" which is attached to the rest of the model via the boundary condition constraints.

The 3D explicit model is a detailed finite element model using equivalent layers for the carcass and pressure armour layer, with all tendons being modelled as seperate geometric components. 3D linear continuum elements were used throughout. Flexible pipe lengths of up to 10m were simulated. Boundary conditions at

the end of the pipe were enforced with kinematic coupling constraints, forcing all nodes in the end planes to remain in plane during the analysis. Equivalent layers and universal contact were used as for the 3D periodic model. This model was finely discretised (4 elements were used across the width of the armour wire) resulting in a model with approximately 2.5 billion degrees of freedom. This model was analysed using explicit dynamics.

A similar explicit model was developed by Bahtui (2008) using the ABAQUS package. This model was also comprised of 3D linear continuum elements, in this case for all layers, helical or cylindrical. The carcass layer is modelled as a homogeneous equivalent layer with orthotropic material properties. The simulation was carried out using explicit dynamics and a time increment of $5x10^{-7}$ s, on a 16 processor cluster. The model approximated the bending hysteresis curves produced by analytical models well, but was less accurate at predicting stresses in individual wires. The model has approximately 120 000 nodes.

2.4.3 Corotational formulations

Corotational formulations are frequently used in computational mechanics where model parts undergo large rotations relative to the problem reference coordinate systems, yet the displacement gradients remain small, such that small-strain constitutive relations and tangent operators are applicable. As such they fill an intermediate role between small strain formulations and fully geometrically nonlinear formulations. The formulation involves embedding a coordinate system either at a point on the element or at the element's integration points that rotate with the material. Expressing stress and strain measures in these coordinate systems can mean that geometrically linear strains (and hence, geometrically linear constitutive relations) can be used in calculating the element's response. This is particularly convenient for use with structural elements, where constitutive relations are expressed relative to the geometrical features (planes, axes, etc) of the undeformed body. Simple demonstrations of the corotational approach are given in Belytschko et al. (2000, Ch. 4.6).

Crisfield (1997) describes a corotational framework suitable for use with any two-noded, three-dimensional beam element with six degrees of freedom at each node, whether linear or nonlinear. A direction triad attached to each of the beam's nodes is defined in the element's initial configuration and updated as the nodes rotate. A direction triad for the deformed element is established that represents the rigid-body rototranslational part of the element deformation, such that the local 1-axis points from the final position of the first node to the final position of the second node. The other two axes are established by finding a rotation matrix that would transform the first coordinate system into the second. This is computed by dividing the pseudo-vector associated with this rotation matrix by two. Then the rotation matrix equivalent to this pseudo-vector is found (using the Rodrigues formula). Then the vectors of the first nodal triad are multiplied by this matrix to obtain unit vectors "interpolated" between the nodal basis vectors.

A relation between variations of the global displacements and rotations and the global forces is written in terms of the local stiffness matrix, the transformation matrix that relates global and local coordinate systems, and an "initial stress" matrix found by computing the variations of the transformation matrix.

In this formulation, local displacements are (arbitrarily) taken to be measured relative to the displacement of the first node. As a consequence as the local translational displacements at the first node are always zero, and all translational local displacements that are not in the direction of the local 1-axis at the second node are also zero.

Other corotational formulations have been developed by Hsiao et al. (1987), Crisfield and Moita (1996) and Urthaler and Reddy (2005).

2.4.4 Summary

Research carried out into finite element models in use and described in the published literature has provided the starting point for developing the models described in this work, for both large-scale representations of flexible pipes and detailed finite element models. Investigations into commercial software and line models suggests beam models or lumped-stiffness models are common numerical representations of

flexible pipes, capable of simulating the range of applied loads and large displacements experienced by flexible pipes in operation. However it is not clear that these representations are sufficiently accurate for use as part of a multi-scale analysis in which component stresses are to be determined. The large-scale finite element model developed in Chapter 4 will be developed with these models in mind. Investigation of the detailed finite element models revealed modelling techniques such as use of orthotropic material models with homogeneous cylinders to represent the carcass and pressure armour layer and insights into the benefits and limitations of using explicit analysis methods for the finite element solution. Finally, as mentioned for the research on analytical models, investigation into models focusing on pipe bending and slip of the tensile armour wire led to consideration of appropriate finite element modelling choices, such as element type and contact algorithm, which were incorporated into the detailed finite element mode developed in this work.

2.5 Linear and nonlinear homogenisation and multiscale analysis

2.5.1 Survey of homogenisation methods

Multi-scale methods are an increasingly used approach in a wide range of applications in computational mechanics thanks to the continuous increase in computer memory, speed and power, the impressive advances of hardware, software and algorithms for parallel computing and the further developments of the underlying multi-scale homogenisation theories of the last decade, particularly for non-linear problems.

Many basic multi-scale methods have found their earliest expression in composites modelling and associated statistical averaging techniques (for a survey of such techniques, see, for example, Hashin (1983)). Representative Volume Element (RVE) -based methods, first proposed by Hill (1963), involve the creation of a single representative model of a portion of a complex material or structure, chosen or constructed such that its analysis yields accurate estimates of the large-scale stress-

strain behavioural parameters in the vicinity of any given point in the large-scale model. RVEs are required to be large enough that they incorporate the heterogeneities (inclusions, voids, etc.) on the scale at which they occur, but small enough that the 'coarse-graining' of the material response does not lead to significant inaccuracies in the predicted behaviour of the large-scale model.

A widely-used development from RVE techniques leads to computational homogenisation methods. In a finite-element-based parallel or nested computational homogenisation procedure, strains resulting from an attempted displacement increment are calculated at each integration point in the large-scale model. Each set of strains at each integration point is imposed on a separate RVE model and the resulting stresses are averaged over the RVE and returned to the integration point in the large-scale model for calculation of residuals. Such methods are conceptually straightforward and can be applied to nonlinear problems (Matsui et al., 2004; Yuan and Fish, 2007), though their efficiency in calculating local stresses is variable and the computational expense of the nested solution procedure can be considerable.

The displacement field in the RVE is typically decomposed into a smooth part and a locally fluctuating part. A key aspect of the formulation is that the smooth part is directly linked to the macro-strain, while boundary conditions are applied to the fluctuating part. Common boundary conditions choices include the so-called Taylor assumption of zero fluctuations, uniform displacement, periodic displacement, uniform traction and mixed traction-displacement boundary conditions (Perić et al., 2011; Terada et al., 2000). For typical applications, it has been shown that periodic boundary conditions are more accurate for predicting bulk material behaviour than the uniform types (Amieur et al., 1995; Hazanov and Huet, 1994; Terada et al., 2000; Van Der Sluis et al., 2000).

One of the first descriptions a nested computational homogenisation is given byFeyel and Chaboche (2000), who use this approach (referred to an FE^2 approach) for the modelling of a periodic long-fibre composite material. For this application, each RVE contains a single circular fibre section. Periodic boundary conditions are used. To improve convergence of the large scale solver, the calculation of the effective current tangent matrix for each RVE is suggested. This can be computed

numerically using perturbations of the RVE model. The RVE uses nonlinear material models (elastoviscoplastic with hardening) for the matrix, but fibre debonding is not accounted for in the work presented in this article.

A nested computational homogenisation is a computationally expensive procedure, a feature that is often aggravated by lack of convergence of the iterative procedure used at the small-scale model, especially if the small-scale model incorporates nonlinear behaviour. For this reason, a sub-stepping approach has been suggested by Perić et al. (2009) to provide better estimates of the RVE configuration.

Applications of computational homogenisation in the literature mostly involve transfer of field quantities between scales where continuum models are used. In the so-called first-order framework, Cauchy models are used at all scales and averaging principles are used to transfer field quantities from one scale to the other. In particular, the macro-strain and macro-stresses are assumed to be the average (on the RVE) of the corresponding micro-strain and micro-stresses.

A limitation of the first-order computational homogenisation method lies in the enforcement of a uniform macro-strain across the RVE which may not be an adequate representation in situations where strain localisation or fracture occurs. To remedy this, non-local continuum models such as Cosserat or strain-gradient models may be used. Examples of such procedures are given in the papers by Geers et al. (2002) and Kaczmarczyk et al. (2010), who use second-order macro-continua and first-order micro-continua to investigate the effect of the micro-structure size, and by Addessi et al. (2010) and Marfia and Sacco (2012) who analyse masonry walls in the framework of transformation field analysis using two-dimensional Cosserat continuum models for large-scale modelling, while the small-scale model of masonry incorporates a nonlinear damage contact-friction model for the mortar joint.

In these cases, the models used at either scale are not the same. Hence, to relate the deformation at the micro-scale to the first and second order strain measure at the large scale, suitable extensions of the averaging principle are formulated by Geers et al. (2002) and Kaczmarczyk et al. (2010) whereas Adessi and Sacco used a least-square optimisation procedure to minimise the difference between macro-displacement and the smooth field at the small scale. To recover the stress measures

at the large scale, the Hill-Mandel condition, which states that the corresponding micro- and macro- virtual works should be the same, is used. Since the models at both scales are different but still both continuum, they are able to ultimately compute the stress tensors at the macro-scale through integral expressions of the micro-stress field, either over the RVE volume or on its boundary.

Examples of non-linear computational homogenisation in which a continuum model is used at the small scale while a structural model is used at the large scale are contributed by Geers et al. (2007) and Coenen et al. (2010) who develop a formulation for heterogeneous thin sheets using continuum shell elements at the macro-level and continuum elements at the micro-level. In this approach, a second order approximation to the nonlinear deformation map is used, with components of the deformation gradient and second deformation gradient identified as shell generalised strain measures. Stress resultants are recovered from the detailed model by integration of the continuum strains over the RVE transverse faces, equivalent to a form of volumetric averaging.

Multi-scale techniques have been developed to bridge atomic- and microscopic-scale representations of materials. This requires linking continuum and atomistic models and therefore also represents an example in which different types of model are used at different length scales. Computational homogenisation principles can also be applied here. An example of this is demonstrated by Samadikhah et al. (2012) in the modelling of graphene membranes. In this article, computational homogenisation relations were used to express atomic displacements as a function of the macro-scale displacement field and deformation gradient. A total potential energy functional is calculated by summing interatomic potentials calculated using the local displacement fluctuation field. The sum of energy-conjugated atomic forces is used to calculate the microscopic stress, via the principle of equivalence of micro- and atomic-scale internal work. This approach clearly can only be used for problems where an energy functional exists.

An alternative approach to computational homogenisation, described by Oliveira et al. (2009), Hassani and Hinton (1998), Guedes and Kikuchi (1990) and others, is the asymptotic expansion method. The two-scale asymptotic method expresses the

displacement field as a power series expansion with coefficients that are increasing powers of the scaling parameter (a constant representing the ratio between characteristic length scales of the microscopic and macroscopic problems), multiplying component displacement functions that are periodic with a period equal to the RVE length. This converts the original boundary value problem into a pair of closed-form boundary value problems to be solved sequentially for the first-order solution. Higher order periodic components of the displacement may be calculated up to an arbitrary level of accuracy using higher order equation sets resulting from the original BVP expansion. For linear problems (used by, for example, Guedes and Kikuchi (1990)), only one boundary value problem needs to be solved at each scale (for a first order approximation): a small-scale simulation to determine the homogenised elastic operator which completely characterises its behaviour, and a large-scale simulation to address the problem of interest. RVE geometries, as for other homogenisation methods, are usually parallelepipeds, though Ghosh et al. (1995) adapts the technique to the Voronoi cell finite element method, which uses an irregular polygonal tessellation of the plane, such that each macro-scale contains at most one single secondary-phase inclusion.

The asymptotic expansion method has also been extended to solve nonlinear problems. This requires a nested solution scheme. Fish and Shek (2000) present a three-scale non-linear asymptotic method solved using a specialised multi-scale Newton-Raphson solution algorithm, along with a derivation of the associated error estimators.

Most of the work done on asymptotic expansion techniques expand the governing (continuum) PDE(s) and express the resulting equation sets in continuum form. In this way, as in the case of computational homogenisation, homogenisation between the same continuum models, rather than different continuum or structural models, is dominant. One extension using a large-scale structural model is the development for general linear periodic beams in bending by Buannic and Cartraud (2001). Multi-scale algorithms for general (linear and nonlinear) RVEs may also be developed using variational formulations by using the concept of two-scale convergence. This approach has been explored by Terada and Kikuchi (2001).

Research into homogenisation methods described in the published literature was important for the current project because it revealed the theoretical basis and implementation procedures involved in computational homogenisation, one of the most common methods used for multi-scale analysis of materials and structures, which is a key part of the multi-scale procedure presented in this work. Futhermore, developments of computational homogenisation, such as second-order methods and applications to non-continuum models such as shells and atomistic models, provided inspiration and motivation to develop the general homogenisation approach described in Chapter 3. Investigation of the boundary condition choices used for carrying out simulations on RVEs and their theoretical justification led to the formulation of the boundary conditions used for the detailed model.

2.6 Other approaches and extensions

An alternative finite-element based approach to flexible pipe modelling used elbow elements. Elbow elements are designed to model pipes undergoing large bending deformations.

The use of elbow elements for flexible pipe modelling has been explored by Bathe and Almeida (1980), Bathe et al. (1983), Hosseini-Khordkheili and Bahai (2008) and Bahai and Hosseini-Khordkheili (2008). A four-noded elbow element with three translational and three rotational degrees of freedom at each node is described by Hosseini-Khordkheili and Bahai (2008) and Bahai and Hosseini-Khordkheili (2008), who express displacements as cubic functions of nodal displacements and rotations. Consistent force vectors for buoyancy, current and seabed interaction forces are developed. This fully (geometrically) nonlinear formulation is shown to be of equivalent or slightly improved accuracy when compared to the two-dimensional corotational formulation used by Yazdchi and Crisfield (2002a). The element developed by Hosseini-Khordkheili and Bahai was validated with a realistic test case for flexible risers also used by Yazdchi and Crisfield (2002b).

Provasi and de Arruda Martins (2010), present a novel approach for the formulation of equivalent layers. It is proposed that a single “macro-element”, or

generalised finite element can represent an entire equivalent layer, or, for computations involving tensile armour, an entire helical wire. In this way, nonlinearities due to contact, separation and friction can be "internalised" in the element formulation. A formulation for a cylindrical macro element in presented in 2010, while a later publication (Provasi and de Arruda Martins, 2011) gives the formulation for a helical macro-element.

The basis of the finite element formulation is the expression of the displacement fields as Fourier series in cylindrical coordinates. It is assumed that the fields solutions permit variable separation; they can be expressed as sums of products of functions in the axial-radial plane with functions of the cylindrical coordinate.

The authors show how such an element can be less computationally expensive than a traditional finite-element discretisation of a thin cylinder under a range of axisymmetric and non-axisymmetric loading conditions.

2.7 Concluding remarks

From the survey of techniques presented above, it can be seen that that there are relatively few models that combine both global and local analysis. Examining the issues addressed by the analytical methods show the standards that an accurate model should achieve.

It seems that homogenisation techniques could provide a consistent, justified procedure for dealing with flexible pipe complexity, and possible also provide a framework for approaching the end-effects problem. This has inspired research work recently conducted at the Brunel University. Bahtui et al. (2009) propose a sequential multiscale framework for flexible pipe modelling. A specialised constitutive model is proposed to represent the large-scale behaviour of a flexible pipe, intended for use with a representation of a flexible pipe composed of Euler-Bernoulli beam elements. The form of the constitutive model is a generalised plasticity model based on the analogy between interlaminar slip in a flexible pipe under bending and the microscopic model of metal plasticity in which layers of atoms slip over each other, which allows the hysteresis loops observed in tests to reproduced. The authors de-

scribe a method for carrying out out a limited number of tests on a detailed finite element model of the flexible pipe in order to determine the parameters of the constitutive model. This procedure provides a consistent way for using the detailed information provided by the detailed finite element model (which are obtained using almost no assumptions about the deformation of pipe components) for a simple one-dimensional representation of a pipeline suitable for global dynamic analyses of installed pipelines. Further development of the model (Bahtui et al., 2010) describes the formulation of an extended Euler-Bernoulli beam element to implement the constitutive model and derive the consistent tangent matrix for the constitutive model. Edmans et al., (2010a) use the same principle but introduces a new detailed finite element model, as described in Chapter 5.

An important issue addressed by computational homogenisation theory concerns the choice of boundary conditions to be applied to the RVE. The arguments concerning boundary conditions in the literature on homogenisation have direct relevance for the creation of finite element models of flexible pipes, if they are intended for use in a multiscale analysis as described above. From the survey of analytical and finite element models in this Chapter, it is notable that almost all models (with the exception of one the finite element models described by Leroy et al. (2010)) use the assumption that all points on the end planes of a flexible pipe remain in plane during the deformation. Stresses are typically evaluated at distances far from the end in order to use these results for predicting stresses in a pipe in operational situations. Although the use of this end restriction is a realistic representation of the constraints induced by a flexible pipe end connection, it is the current author's contention that this method does not represent bending behaviour accurately, locally or globally, as interlaminar slip is prevented at the end sections. The findings of researchers investigating computational homogenisation techniques (Section 2.5) for nonlinear materials suggests that periodic displacement boundary conditions are preferable for carrying out simulations on an RVE. For this reason, the detailed finite element model described in Chapter 5 and Edmans et al., (2010b) implement a form of periodic displacement boundary conditions.

However, direct application of the computational homogenisation procedure for

flexible pipes is not possible, because the proposed detailed model uses structural, rather than continuum finite elements. This requires the development of a general computational homogenisation theory which extends the extant theory such that it can deal with these cases. Such a development is presented in Chapter 3.

Chapter 3

Structural-to-structural multi-scale analysis

In this Chapter a general theory is presented to extend the conventional multi-scale homogenisation theory, developed for the case when the same, typically continuum, models are used at either scale, to the general case when different and arbitrary structural models are used at each scale.

This theory is necessary in order to construct a multi-scale analysis of flexible pipes to ensure that the transfer of quantities at different length scales is valid. It is desirable to use structural elements at both scales because of the relative slenderness of flexible pipes at the large scale and the slenderness of its internal components. Furthermore, as it is known that significant non-conservative forces are present at the level of the internal components, the use of an energy potential to determine response at the small scale is not realistic.

The proposed formulation provides a general framework which can be applied to a wide range of cases, including, among others, the cases of 2D or 3D truss structures that at a very large scale can be modelled as beams or shells, but also problems where higher-order continua are used at the macro-scale and a Cauchy continuum model is used at the micro-scale, such as for second-order computational homogenisation. In all these cases, the conventional theory based on strain and stress averaging is not applicable, at least, not directly, because its implicit requirement is that the same formal model is used at both length scales, or, at least, that it is possible to

compute some local value that represents the macro-generalised-strain or the macro-stress resultants on the RVE, that can be integrated over the remaining dimensions of the RVE.

It is emphasised that the approach presented in this Chapter does not propose a fundamental modification to computational homogenisation procedures nor does it enable multiscale analyses which would otherwise be impossible - the conventional procedure could be used for flexible pipe analysis. However, use of the extension presented here is more convenient for this application, due to the aspect ratios, geometric complexity and contact nonlinearities involved.

The theoretical justification of how the micro-scale boundary value problem (BVP) is defined starting from the macro-strain is also revisited. This is because the conventional point of departure that the RVE average of the micro-strains has to be equal to the macro-strain is not applicable.

An application of this extended theory is presented for the fully nested (FE^2) multi-scale non-linear analysis of a truss for which each member is treated as elasto-plastic. The relative simplicity of this problem allows the fundamental theoretical contributions of the paper to be highlighted and makes it possible to assess the effectiveness of the proposed approach by comparison of the results of the multi-scale method with those of direct numerical simulations. A similar problem has previously been studied by Tollenaere (1998). An application of such a model could be in modelling auxetic foams, where analytical calculations are often used to determine unit cell behaviour (see e.g. Smith et al. (2000)), but a multi-scale approach could bring benefits.

An outline of this Chapter is as follows: firstly, the theory of the first-order computational homogenisation method is extended to a more general structural-structural procedure in a general form (Section 3.1). This is followed in Section 3.2 by descriptions of the form of the large-scale (Section 3.2.1) and small-scale (Section 3.2.2) models chosen for our specific application, the latter including details of the implementation of the homogenisation procedure derived from theoretical considerations. Numerical results and the validation of the multi-scale model predictions against the results of direct numerical simulations are reported and discussed in

Section 3.3. Finally, summarising remarks on the method and its application are made, with a view to future further developments.

3.1 Structural-structural homogenisation

3.1.1 Conventional computational homogenisation procedure

In this Section we review the conventional two-scale computational homogenisation procedure developed for the case where the same continuum-based model is used at both scales, using the same continuum stress and strain measures. We conclude the Section by explaining why the formulation cannot be directly applied to the more general case when different models are used at different scales, and by making a number of remarks which suggest and justify the generalisation proposed in Section 3.1.2.

For simplicity, this review is limited to the case of the first-order homogenisation and small strains and displacements. Higher-order and/or geometrically nonlinear formulations can be obtained using similar arguments.

The starting point is the assumption of 'separation of scales', whereby at each point x_M of the macro-domain Ω under consideration a representative volume element (RVE) is postulated to exist and to occupy a domain Ω_{RVE} centred on x_M, such that the RVEs associated with two points with arbitrary separation are treated as independent (even if they overlap). The microscopic displacement u_m in the RVE is expressed as the sum of a smooth component v_m and a fluctuating component w_m:

$$u_m(x_m, x_M) = v_m(x_m, x_M) + w_m(x_m, x_M) \tag{3.1.1}$$

where $x_m \in \Omega_{RVE}$. The smooth component describes a displacement field in the RVE which is linear in x_m so that its associated strain is constant within Ω_{RVE} and is equal to the macroscopic strain $\varepsilon_M(x_M)$:

$$\varepsilon_M(x_M) = \nabla_s v_m(x_M) \tag{3.1.2}$$

where ∇_s is the symmetric part of the gradient. Therefore, the microscopic strain ε_m can also be decomposed as follows:

$$\begin{aligned}\varepsilon_m(x_m, x_M) &= \nabla_s v_m(x_M) + \nabla_s w_m(x_m, x_M) \\ &= \varepsilon_M(x_M) + \nabla_s w_m(x_m, x_M)\end{aligned} \tag{3.1.3}$$

The constitutive law and the equilibrium differential equations are then imposed on the RVE:

$$\begin{cases}\sigma_m(x_m, x_M) = \sigma_m[\varepsilon_m(x_m, x_M)] \\ \operatorname{div} \sigma_m(x_m, x_M) = 0\end{cases} \tag{3.1.4}$$

where for simplicity (and without loss of generality) the body forces are neglected.

The following assumption is then made:

$$\varepsilon_M(x_M) = \overline{\varepsilon_m}(x_M) \tag{3.1.5}$$

where the bar indicates the average over the RVE, defined such that:

$$\overline{(\bullet)_m}(x_M) = \frac{1}{\Omega_{RVE}} \int_{\Omega_{RVE}} (\bullet)_m(x_m, x_M) \, \mathrm{d}\Omega_{RVE} \tag{3.1.6}$$

Integrating the microscopic strain ε_m over the RVE and using Equations (3.1.3) and (3.1.6) and the Green theorem, the following relation is obtained:

$$\oint_{\partial\Omega_{RVE}} w_m(x_m, x_M) \otimes N(x_m) \, \mathrm{d}\partial\Omega_{RVE} = 0 \qquad \forall \, x_M \in \Omega \tag{3.1.7}$$

N denoting the normal to the boundary of the RVE.

The above equations provide a method to determine a micro-displacement field on the RVE starting from a known deformation at the macro-scale (so-called "down-scaling" procedure (Kaczmarczyk et al., 2010)): Given a macro-strain field ε_M, a micro-displacement field u_m can be determined by solving, in each RVE, the boundary value problem (BVP) represented by Equations (3.1.1)-(3.1.4) and a suitable set of boundary conditions respecting Equation (3.1.7). It has been shown that boundary conditions which comply with Equation (3.1.7) include zero fluctuations over the whole RVE (Taylor assumption), uniform displacement, uniform traction and periodic boundary conditions (see, for example, Larsson et al. (2011) and Perić et al. (2011)). The latter have been found to be the most effective for most cases involving a periodic microstructure or when the microstructure is not periodic but the RVE is sufficiently statistically representative ((Amieur et al., 1995) (Hazanov and Amieur, 1995)).

Once the above BVP is solved for each RVE, the macro-stress field is recovered by averaging the micro-stress field over the RVE (the so-called "up-scaling" procedure described by Kaczmarczyk et al. (2010)):

$$\sigma_M(x_M) = \overline{\sigma_m}(x_M) \tag{3.1.8}$$

This stress-averaging procedure is related to Hill's condition, which, in one of its forms, states that the local macroscopic virtual work done by the macroscopic stress for any macroscopic strain variation must be equal to the average over the RVE of the microscopic virtual work done by the microscopic stress for the corresponding microscopic strain variation (Geers et al., 2002; Michel et al., 1999):

$$\sigma_M \cdot \delta\varepsilon_M = \overline{\sigma_m \cdot \delta\varepsilon_m(\delta\varepsilon_M)} \qquad \forall \delta\varepsilon_M \tag{3.1.9}$$

where dependence on the local and global position will henceforth be omitted in the notation for simplicity. The notation $\delta\varepsilon_m(\delta\varepsilon_M)$ highlights that the microscopic strain variation $\delta\varepsilon_m$ is the variation of the solution to the BVP (given in terms of the microscopic strain) corresponding to a variation $\delta\varepsilon_M$ of the macroscopic strain

ε_M. From Equations (3.1.2) and (3.1.3):

$$\delta\varepsilon_m(\delta\varepsilon_M) = \delta\varepsilon_{mv} + \delta\varepsilon_{mw} = \delta\varepsilon_M + \delta\varepsilon_{mw} \tag{3.1.10}$$

where $\delta\varepsilon_{mv} = \delta\nabla_s v_m$ and $\delta\varepsilon_{mw} = \delta\nabla_s w_m(\delta\varepsilon_M)$. In the absence of body forces the self-equilibrated microscopic stress field on the RVE is orthogonal to the field $\delta\varepsilon_{mw}$, i.e. it results that

$$\int_{\Omega_{RVE}} \sigma_m \cdot \delta\varepsilon_{mw}\, d\Omega = 0 \tag{3.1.11}$$

which leads to:

$$\begin{aligned} &\overline{\sigma_m \cdot \delta\varepsilon_m(\delta\varepsilon_M)} = \frac{1}{\Omega_{RVE}} \int_{\Omega_{RVE}} \sigma_m \,\mathrm{d}\Omega \cdot \delta\varepsilon_M = \\ &= \overline{\sigma_m} \cdot \delta\varepsilon_M \qquad \forall\delta\varepsilon_M \end{aligned} \tag{3.1.12}$$

Hence, assuming that Relation (3.1.8) holds true, then from Equation (3.1.12), Hill's condition, i.e. Equation (3.1.9), is obtained. Vice versa, if it is assumed that Hill's condition holds true, the stress-averaging formula (3.1.8) is obtained.

The following remarks can be made:

1. Equations (3.1.5) and (3.1.8), i.e. the equality between macroscopic strain or stress and the average on the RVE of the microscopic strain or stress do not make sense when different models are used because the strain and stress measures typically have different meaning and often even different dimensions at the macroscale and the microscale.

2. Equation (3.1.2) is meaningless too, in the general case of two different models used at the two scales. This implies that the definition of the smooth displacement field on the RVE is not necessarily a straightforward issue.

3. Relation (3.1.5) certainly applies when uniform boundary conditions are pre-

scribed, see Michel et al. (1999). Otherwise it simply becomes an *a priori* assumption which results in restriction (3.1.7) for the boundary conditions to be applied on the fluctuating field w. To the authors' knowledge no specific physical or mathematical justification has ever been provided for such assumption in a case different from uniform boundary conditions. However, such an assumption is still not sufficient to fully define the BVP as it is still necessary to make a choice among all possible boundary conditions which satisfy Equation (3.1.7), which is typically done on the basis of experience and engineering judgment. Hence, the question arises whether assumption (3.1.5) is really necessary to develop a computational homogenisation theory or it is possible to use experience and engineering judgment directly to determine an effective set of boundary conditions for the BVP on the RVE.

4. Unlike Equations (3.1.5) and (3.1.8), Equation (3.1.9) is also meaningful for the general case in which two different models are used at the two scales. This equation can be seen as a scale-bridging variational condition and, if the equations governing the problem at the small scale are the stationary conditions for an energy potential, it becomes a condition of energy equivalence between the micro- and macro-models. On the other hand, Equation (3.1.3) can be written also when a potential energy cannot be defined at the small scale, and is therefore more general.

5. Hill's condition (i.e. Equation 3.1.9) was originally derived in the case of uniform displacement or uniform traction boundary conditions (Hill, 1963, 1972) (see also Michel *et al.* 1999) and later in the case of periodic boundary conditions by Suquet et al. (1987). However, this equation is normally invoked as an a priori assumption of energy equivalence.

These four remarks form a point of departure from which a more general theory in the next Section is developed.

3.1.2 A general framework for homogenisation

In this Section we develop a theory to provide and justify the extension of the multi-scale procedure to the case where two different models are used at either scale and no potential energy can be introduced at the small scale. We are particularly interested in the analysis of unbonded flexible risers using the approach described in Edmans et al., (2010a), in which a co-rotational beam model is used at the macro-scale, while at the small-scale a geometrically linear multi-layered model is used in which each layer is modelled with shell elements and adjacent layers are in potential frictional contact. Therefore, here we consider a two-scale formulation in which a geometrically nonlinear model is used at the macro-scale and a geometrically linear model is adopted at the micro-scale. The extension to the case where geometric nonlinear models are used at both scales is possible within the proposed generalised framework, but it also requires addressing some nontrivial issues regarding the micro-scale formulation, including how to apply and update the boundary conditions, which we prefer to leave for future developments. We also make the hypothesis that body forces are absent.

Apart from the above assumptions, we also wish to make the treatment general enough to be applicable to any other case of computational two-scale homogenisation, when the models used at the two scales are not necessarily continuum models and are generally different from each other. To this end, we use the abstract notation of operators, vector spaces and bilinear forms. In particular, we will indicate the argument of a linear operator without parenthesis, while the argument of a nonlinear operator will be included in parentheses. For example, $b = A(a)$ will be used if operator A is nonlinear, while $b = A\,a$ will be used if A is linear. For a nonlinear operator A, the symbol dA will indicate its derivative, which is always assumed to be properly defined. Furthermore, the adjoint of an operator A will be denoted by A^*.

We consider a macro-scale structural model defined by a vector space $\mathcal{V}_M$ of admissible macro-displacements, a vector space $\mathcal{D}_M$ of admissible macro-strains, and a macro-scale nonlinear strain operator $B_M : \mathcal{V}_M \to \mathcal{D}_M$. We then define

a micro-scale structural model defined by vector spaces $\mathcal{V}_m$ and $\mathcal{D}_m$ of admissible micro-displacements and micro-strains, respectively, and a linear strain operator $B_m : \mathcal{V}_m \to \mathcal{D}_m$. For the purposes of this work, there is no need to specify the functional nature of $\mathcal{V}_M$, $\mathcal{D}_M$, $\mathcal{V}_m$ and $\mathcal{D}_m$, because the determination of mathematical conditions for the existence and uniqueness of the solution, as well as for finite-element convergence and multi-scale convergence, are left for future developments. It is therefore sufficient to assume the elements of $\mathcal{V}_M$ and $\mathcal{D}_M$ are displacement and strain fields (u_M, ε_M) defined in the macro-structural domain Ω, while the elements of $\mathcal{V}_m$ and $\mathcal{D}_m$ are displacement and strain fields (u_m, ε_m) defined in $\Omega \times \Omega_{RDE}$, where Ω_{RDE} is the "representative domain element" independently associated with each point of the macro domain due to the assumption of scale separation, that is carried over into the generalised formulation. The change in terminology from the conventional "Representative Volume Element" (RVE) to the "Representative Domain Element" (RDE) is made to recognise the fact that the small-scale model does not necessarily represent a physical volume, but instead it represents a general domain, defined in a suitable space, where displacements, strains and stresses of the small-scale structural model are defined. An example of an RDE that is not an RVE is the truss structure described in Section 3.2.2 as part of the demonstration of the proposed general framework for homogenisation. We also assume that the elements of $\mathcal{V}_M$, $\mathcal{D}_M$, $\mathcal{V}_m$ and $\mathcal{D}_m$ and all the required derivatives are sufficiently regular.

Spaces $\mathcal{V}_M, \mathcal{V}_m$ are associated with the dual spaces $\mathcal{F}_M$, $\mathcal{F}_m$, whose elements are external macro- and micro-forces, respectively. These pairs of spaces are related by non-degenerate bilinear forms that have the physical meaning of macroscopic and microscopic external virtual work. Analogously, spaces $\mathcal{D}_M$ and $\mathcal{D}_m$ are associated with dual spaces $\mathcal{S}_M$ and $\mathcal{S}_m$, whose elements represent the macro- and micro-generalised stresses (or stress resultants), respectively. To simplify the notation, the same symbol $(\!(\bullet, \bullet)\!)$ will be used to denote the bilinear forms in $\mathcal{F}_M \times \mathcal{V}_M$, $\mathcal{F}_m \times \mathcal{V}_m$, $\mathcal{S}_M \times \mathcal{D}_M$ and $\mathcal{S}_m \times \mathcal{D}_m$, as the difference in meaning will be clear from the context.

A generally nonlinear constitutive law, $\sigma_m = \sigma_m(\varepsilon_m)$, is defined for the micro-scale structural model. In this context, for simplicity, we assume only that the law is one-to-one and both itself and its derivative are sufficiently regular.

To link the two scales we assume that a displacement-based formulation is used at both scales. An appropriate operator $P : \mathcal{D}_M \rightarrow \mathcal{V}_m$ is defined to map microscopic displacements to macroscopic strains. The following restrictions apply to the operator:

1. If $u_m \in \mathrm{Ker}(B_m)$ and $u_m = P(\varepsilon_M)$ then $\varepsilon_M = 0$.
2. The compound operator $B_m P$ must map one (and only one) micro-strain ε_m to each macro-strain ε_M.

The operator P, i.e. the down-scaling procedure, is defined by the solution to the following problem:

Given $\varepsilon_M \in \mathcal{D}_M$, find $u_m \in \mathcal{V}_m$ such that:

$$\begin{cases} u_m = P(\varepsilon_M) = v_m + w_m \\ v_m = \overline{P}\,\varepsilon_M \\ Q_{bc}\, w_m = 0 \\ (\!(\sigma_m(B_m\, u_m), B_m\, \delta w_m)\!) = 0 \qquad \forall \delta w_m :\ Q_{bc}\, \delta w_m = 0 \end{cases} \tag{3.1.13}$$

Once u_m has been found, $u_m = P(\varepsilon_M)$. In this system of equations $\overline{P}$ defines a linear operator (normally, but not necessarily, in closed form) which "translates" the macro-scale strain ε_M into a corresponding, "smooth" micro-displacement field v_m. Q_{bc} is a suitably defined trace operator, such that Equation $(3.1.13)_3$ represents a suitably chosen set of linear boundary conditions for the fluctuating displacement field w_m.

Combining operators B_m, P and B_M the compound "multi-scale" strain operator $B_{MS} = B_m\, P\, B_M$ is obtained, as described schematically in Figure 3.1. B_{MS} is generally nonlinear, because the constitutive law and operator B_M are generally nonlinear.

B_{MS} and the constitutive law at the small scale fully define a multi-scale structural model, in which $\mathcal{V}_M$ is the vector space of displacements, $\mathcal{D}_m$ is the vector space of strains and $\mathcal{S}_m$ and $\mathcal{F}_M$ are the spaces of generalised stresses and external forces associated with $\mathcal{D}_m$ and $\mathcal{V}_M$ through the appropriate bilinear forms. In theory, the

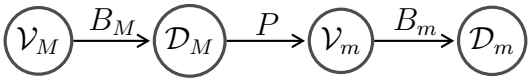

Figure 3.1: Schematic description of the compound "multi-scale" strain operator B_{MS}.

details of the up-scaling procedure could be ignored because what matters is the "multi-scale'' operator B_{MS}, the bilinear forms defined in $\mathcal{F}_M \times \mathcal{V}_M$ and $\mathcal{S}_m \times \mathcal{D}_m$ and the micro-scale constitutive law. Defined in this form, the multi-scale structural model is schematised in Figure 3.2, where dB^*_{MS} is the adjoint operator to dB_{MS}.

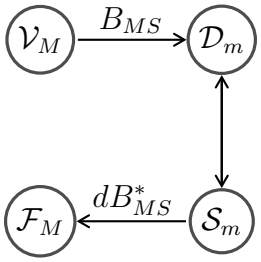

Figure 3.2: Multi-scale model.

In practice, in many cases it is useful or necessary to consider the spaces $\mathcal{D}_M$ and $\mathcal{S}_M$ explicitly and use an up-scaling procedure to determine the macro-stress field σ_M of $\mathcal{S}_M$ associated with the micro-stress field σ_m.

The up-scaling procedure can be formally obtained from the adjoint operators to B_m and dP as follows:

$$\sigma_M = [dP(\varepsilon_M)]^* \, B^*_m \, \sigma_m \tag{3.1.14}$$

This is equivalent to the following variational definition of σ_M:

$$(\!(\sigma_M, \delta\varepsilon_M)\!) = (\!(\sigma_m, B_m \, dP(\varepsilon_M) \, \delta\varepsilon_M)\!) \qquad \forall \delta\varepsilon_M \in \mathcal{D}_M \tag{3.1.15}$$

which represents a generalised Hill's condition (GHC). The up-scaling procedure is schematised below in Figure 3.3.

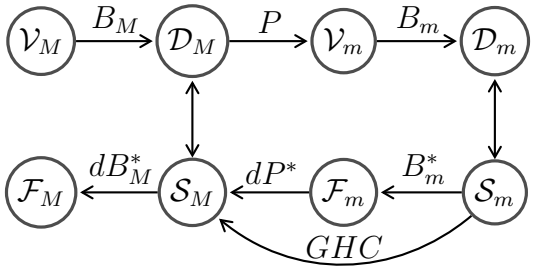

Figure 3.3: Schematic description of the up-scaling procedure.

The differential $dP(\varepsilon_M)d\varepsilon_M$ of P can be expressed with the aid of Equations $(3.1.13)_{1-3}$ as:

$$dP(\varepsilon_M)d\varepsilon_M = \overline{P}\,\delta\varepsilon_M + \delta w_m \tag{3.1.16}$$

where $Q_{bc}\,\delta w_m = 0$. Substituting into Equation (3.1.15) and noting that Equation $(3.1.13)_4$ holds for the variation of the displacement fluctuation field, the following relation is obtained:

$$(\!(\sigma_M, \delta\varepsilon_M)\!) = \big((\sigma_m, B_m\,\overline{P}\,\delta\varepsilon_M)\big) \qquad \forall\delta\varepsilon_M \in \mathcal{D}_M \tag{3.1.17}$$

Both Equations (3.1.15) and (3.1.17) define σ_M, but applying them in practice is different: Equation (3.1.15) requires the linearisation of the operator P, i.e. of the solution of the micro-problem in the RDE. When such solution is obtained numerically, its linearisation can only be obtained through perturbations, which can be computationally very expensive. Conversely, applying Equation (3.1.17) requires only the operators B_m and $\overline{P}$ which are predefined and therefore leads to a direct computation of σ_M.

Furthermore, if problem (3.1.13) is practically solved for each RDE using the finite-element method and by introducing ε_M in the micro-problem in the form of degrees of freedom of a dummy control node (see, for example, Michel et al. (1999)), then Equation (3.1.17) is equivalent to recovering σ_M as the reaction of the constraint imposed on this dummy control node.

It is worth noting that the generalised Hill's condition (3.1.15) and its simplified form (3.1.17), which fully define σ_M and therefore the up-scaling procedure, are not invoked as an *a priori* assumption of the theory. Instead, they are simply derived from the definition of σ_M in terms of duality.

Solution of the micro-problem in terms of u_m

In the above formulation, the total micro-displacement field is found from the sum of $v_m = \overline{P}\,\varepsilon_M$ and the fluctuating field w_m. From the practical point of view this implies assuming w_m as the field variable to be solved for. In a finite-element implementation this implies assuming that the nodal degrees of freedom in the micro-problem represent the nodal values of w_m.

It may be practically convenient, for example when using commercial software packages, to solve the problem directly in terms of u_m, so that in a finite-element implementation the nodal degrees of freedom correspond to the nodal values of u_m. To this end, substituting the relation $w_m = u_m - \overline{P}\,\varepsilon_M$ into Equations (3.1.13), and noting that, for a given ε_M, $\delta w_m = \delta u_m$, the micro-problem can be rewritten as follows:

Given $\varepsilon_M \in \mathcal{D}_M$, find $u_m \in \mathcal{V}_m$ such that

$$\begin{cases} Q_{bc}\, u_m = Q_{bc}\, \overline{P}\, \varepsilon_M \\ (\!(\sigma_m(B_m\, u_m), B_m\, \delta u_m)\!) = 0 \\ \qquad\qquad \forall \delta u_m : \; Q_{bc}\, \delta u_m = 0 \end{cases} \tag{3.1.18}$$

As mentioned above, in practice dummy control nodes C can be introduced whose degrees of freedom are the components of ε_M for each RDE. This is effectively equivalent to having the micro-problem defined in the product space $\mathcal{V}_m \times \mathcal{D}_M$. Let us denote by $\eta_{MC} \in \mathcal{D}_M$ a vector containing the new degrees of freedom associated with these control nodes, which may be unknown or prescribed. The problem can then be restated as follows:

Given $\varepsilon_M \in \mathcal{D}_M$, find $(u_m,\, \eta_{MC}) \in \mathcal{V}_m \times \mathcal{D}_M$ such that:

$$\begin{cases} Q_{bc}\, u_m - Q_{bc}\, \overline{P}\, \eta_{MC} = 0 \\ \eta_{MC} = \varepsilon_M \\ (\!(\sigma_m(B_m\, u_m), B_m\, \delta u_m)\!) = 0 \\ \qquad\qquad \forall \delta u_m : Q_{bc}\, \delta u_m = 0 \end{cases} \tag{3.1.19}$$

The fact that the macro-scale stress σ_M is the reaction of the constraint on the control node can be expressed in a variational way as follows:

$$\begin{aligned} (\!(\sigma_M, \delta\eta_{MC})\!) = (\!(\sigma_m, B_m\, \delta u_m)\!) \qquad & \forall \delta\eta_{MC} \in \mathcal{D}_M \\ \forall \delta u_m : Q_{bc}\, \delta u_m = Q_{bc}\, \overline{P}\, \delta\eta_{MC} & \end{aligned} \tag{3.1.20}$$

The choice of variation δu_m in the above equation is immaterial because, if δu_{m1} and δu_{m2} are two variations such that $Q_{bc}\, \delta u_{m1} = Q_{bc}\, \overline{P}\, \delta\eta_{MC}$ and $Q_{bc}\, \delta u_{m2} = Q_{bc}\, \overline{P}\, \delta\eta_{MC}$, then it results that $Q_{bc}\, \delta(u_{m2} - u_{m1}) = 0$. From Equation (3.1.18) this yields $(\!(\sigma_m(B_m\, u_m), B_m\, \delta(u_{m2} - u_{m1}))\!) = 0$, which finally leads to

$$(\!(\sigma_m(B_m\, u_m), B_m\, \delta u_{m1})\!) = (\!(\sigma_m(B_m\, u_m), B_m\, \delta u_{m2})\!) \tag{3.1.21}$$

In a finite-element implementation these considerations are purely theoretical, because from the practical point of view σ_M is provided simply by the reactions at the control nodes C, which is typically given by the program as part of the standard output.

3.2 Specialisation to a multi-scale analysis of a truss structure

In this Section, an application of the extended multi-scale theory is demonstrated and can be regarded as a template for the application of the extended theory to a wider range of problems. A two-scale model of a slender periodic two-dimensional truss structure is created, using one repeating truss unit as the RDE and employing an Euler-Bernoulli beam model as the large-scale model.

This problem has been chosen to emphasize the generality of the derivation of the extended multiscale homogenisation theory provided above in Section 3.1.2. In

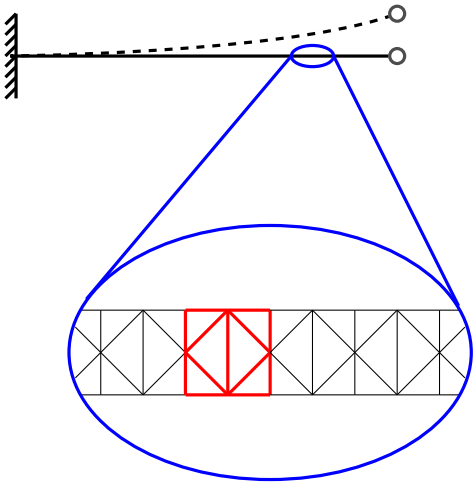

Figure 3.4: Beam-truss multi-scale model

particular, our formulation is not restricted to structural models obtainable from a continuum model with some kinematic hypotheses. Although each member of a truss structure is a rod and can be derived from a continuum model using some kinematic assumptions, the truss unit forming the RDE used in numerical demonstrations in the following Section, shown in Figure 3.4, is an assembly of rods and therefore cannot be derived in any of the usual ways from a continuum model.

3.2.1 Large-scale model and definition of $\mathcal{V}_M$, $\mathcal{D}_M$ and B_M

Since, the large-scale model is a slender structure, its kinematic response is modelled using the Euler-Bernoulli beam model. Thus the large-scale domain is

$$\Omega := \{x \in \mathbb{R} : 0 \leq x \leq L\}$$

where L is the model length. The structure is discretised with two-node beam elements with two planar displacements and one rotation as the degrees of freedom of each node. To describe how the extended theory of Section 3.1 specialises to this specific example we prefer to refer directly to the discretised problem. Hence, the space of displacements is defined as $\mathcal{V}_M := \mathbb{R}^{3N_M}$, where N_M is the number of (macroscopic) nodes. Given a displacement $u_M \in \mathcal{V}_M$, u^i_{Mj} will denote the j^{th} component of the i^{th} node. Axial strain and curvature are defined for each element,

whereby the strain space is defined as $\mathcal{D}_M := \mathbb{R}^{2N_g E_M}$, where E_M is the number of macroscopic elements and N_g is the number of integration points per element. Given a strain $\varepsilon_M \in \mathcal{D}_M$, ε_{Mj}^{ip} will indicate the j^{th} component of the p^{th} integration point of the i^{th} element. The macroscopic strain-displacement operator $B_M : \mathcal{V}_M \to \mathcal{D}_M$ is the nonlinear mapping

$$\begin{aligned} \varepsilon_{Mq}^{ip} = (\hat{B}_M^i)_{qh}(\xi_p)\hat{v}_h^i(\Lambda_{kn}^i v_n) \qquad & i = 1, 2, \dots E_M \qquad n = 1, 2, \dots 3N_M \\ & h, k = 1, 2, \dots 6 \qquad 0 \leq \xi_p \leq 1 \\ & p = 1, 2, \dots N_g \qquad q = 1, 2 \end{aligned} \tag{3.2.22}$$

where v_n is the vector of assembled global displacements such that, when $n = 3(i-1)+j$, $v_n = u_j^i$ $(j = 1, 2, 3)$, Λ_{kn}^i is the incidence matrix and $\hat{v}_h^i$ is the hth component of the local displacements for element i, which is a non-linear function of the global element displacement components $v_k^i = \Lambda_{kn}^i v_n$. The non-linear mapping $\hat{v}_h^i = \hat{v}_h^i(v_k^i)$ is defined in the corotational formulation developed by Urthaler and Reddy (2005) that is adopted here. Furthermore, $\hat{B}_M^i$ is the strain-displacement matrix

$$\hat{B}_M^i(\xi) = \frac{1}{l_i^2}\begin{bmatrix} -l_i & 0 & 0 & l_i & 0 & 0 \\ 0 & 12\xi - 6 & (6\xi - 4)l_i & 0 & -12\xi + 6 & (6\xi - 2)l_i \end{bmatrix}$$

where l_i is the length of beam element i. The incidence matrix is defined as

$$\Lambda_{kn}^i = \begin{cases} 1 & \text{if global DOF } n \text{ corresponds to element DOF } k \text{ of element } i \\ 0 & \text{otherwise} \end{cases},$$

noting that element DOFs represent the planar translational displacements and rotation of the nodes of the element using the ordering $(u_1^1, u_2^1, u_3^1, u_1^2, u_2^2, u_3^2)$, as

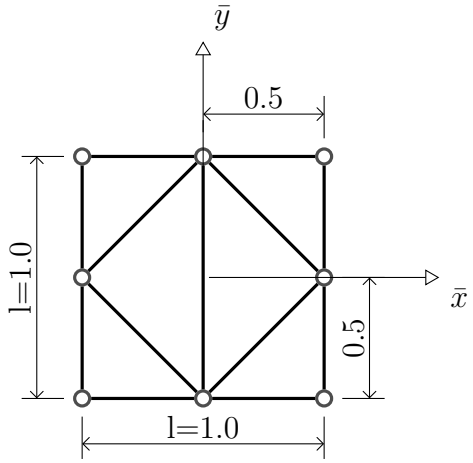

Figure 3.5: Geometry of the RDE (dimensions in m)

does the global displacement vector v_n.

3.2.2 Small-scale model and definition of $\mathcal{V}_m$, $\mathcal{D}_m$ and B_m

The small-scale model consists of 2-noded planar truss elements. Elastoplastic material behaviour with linear kinematic hardening is chosen for the constitutive relation of the members.

No finite-element approximation is required because the small-scale model is already finite-dimensional in nature and consists of N_m nodes and E_m elements. The space of displacements is defined as $\mathcal{V}_m := \mathbb{R}^{2N_g E_M 2N_m}$. Focusing on a single integration point, given a displacement u_m, u^i_{mj} will denote the j^{th} component of the i^{th} node. The space of strains is defined as $\mathcal{D}_m := \mathbb{R}^{2N_g E_M E_m}$. Focusing on a single integration point, given a strain $\varepsilon_m \in \mathcal{D}_m$, ε^i_m is the axial strain of the i^{th} element.

$B_m : \mathcal{V}_m \to \mathcal{D}_m$ is the linear mapping that, for each RDE, is defined as follows:

$$\varepsilon^i_m = \hat{B}^i_{mh} T^i_{hk} \Lambda^i_{kn} v_n \qquad i = 1, 2, \ldots E_m \qquad n = 1, 2, \ldots 2N_m$$
$$h, k = 1, 2, \ldots 4 \tag{3.2.23}$$

where v_n is the vector of assembled global displacements such that, when $n =$

$2(i-1)+j$, $v_n = u_j^i$ $(j = 1, 2)$, Λ_{kn}^i is the incidence matrix, l_i is the length of truss element i and T_{hk}^i is the 2D coordinate transformation matrix for element i.

The strain-displacement matrix is:

$$\hat{B}_m^i = \frac{1}{l_i}\begin{bmatrix} -1 & 0 & 1 & 0 \end{bmatrix}$$

The incidence matrix is as defined in Section 3.2.1, noting that element DOFs represent the planar translational displacements of the nodes of the element using the ordering $(u_1^1, u_2^1, u_1^2, u_2^2)$, as does the assembled displacement vector.

3.2.3 Scale bridging and definition of $\bar{P}$ and Q_{bc}

For these models, the operator $\bar{P} : \mathbb{R}^{2N_g E_M} \to \mathbb{R}^{2N_g E_M 2N_m}$ is defined in accordance with the Euler-Bernoulli kinematic assumptions as follows:

Given a node n of the small-scale truss model, the two components of the displacement of node n in the local directions $\bar{x}$ and $\bar{y}$ (see Figure 3.5) are given by:

$$\begin{aligned} v_{n\bar{x}} &= \alpha_M^{ip}\bar{x}_n + \chi_M^{ip}\bar{x}_n\bar{y}_n \\ v_{n\bar{y}} &= 0.5\chi_M^{ip}\bar{x}_n^2 \end{aligned} \tag{3.2.24}$$

where $\bar{x}_n$ and $\bar{y}_n$ are the local coordinates of n, while α_M^{ip} and χ_M^{ip} are the axial strain and curvature at the corresponding integration point p of element i.

Denoting by N_b the number of nodes on the small-scale model's left boundary, which is equal to the number of nodes on the right boundary, the restriction $Q_{bc}^* : \mathbb{R}^{2N_m} \to \mathbb{R}^{2N_b}$ of operator Q_{bc} in Equations (3.1.18), (3.1.19), (3.1.20) and (3.1.21) to a single RDE is defined as follows:

$$(Q^*_{bc})_{ij} = \begin{cases} 1 & \text{if degree of freedom } j \text{ corresponds to degree of freedom } i \\ & \quad \text{on right boundary} \\ -1 & \text{if degree of freedom } j \text{ corresponds to degree of freedom } i \\ & \quad \text{on left boundary} \\ 0 & \text{otherwise} \end{cases} \tag{3.2.25}$$

$$i = 1, 2, \ldots 2N_b \qquad j = 1, 2, \ldots 2N_m$$

We choose to apply the macroscopic strains to the microscopic model by means of a dummy control node, as described in Equation (3.1.19).

3.2.4 Multi-scale implementation

The large-scale model was implemented in the finite-element package Abaqus using user-defined elements to calculate the response of the small-scale model. The small-scale model and the scale bridging procedure were implemented as the material model used within the UEL subroutine. Three integration points were used for each large-scale element. For each integration point three simulations were carried out for each iteration of each increment of a full Newton-Raphson solution procedure. The macro-strain was passed in the first simulation to compute the macro-stress and perturbations of each of the two macro-strain components were passed in the remaining two simulations to compute the associated macro-stress variation and establish the consistent material tangent.

3.3 Numerical results

3.3.1 Test case

In this Section we numerically test convergence of the multi-scale procedure, or, in short, multi-scale convergence. By multi-scale convergence, we mean that the

difference between the multi-scale solution and direct numerical simulation (DNS) results tends to zero as the ratio ϵ between the characteristic lengths of the unit cell and the large-scale model tends to zero. This is investigated for the case of a truss structure created using a periodic array (Figure 3.4) of the unit cell truss structure shown in Figure 3.5. For the small-scale model the characteristic length is 1m. For the large-scale model it is the total length of the structure L.

To separate multi-scale convergence from FE convergence, for each case analysed we present results for increasing numbers of elements of the large-scale model. For the small-scale model this is not necessary because it is already discrete in nature.

Model parameters (with reference to Section 3.2) are presented in Table 3.1.

Three cases were studied for this type of structure. For case 1, a cantilever truss with an axial point load at the end of the structure was considered (Figure 3.6). For case 2, a transverse point load was applied to the same cantilever truss (Figure 3.7). For case 3, two unequal point loads were applied to a truss beam with three simple supports (Figure 3.8).

Figures 3.6-3.8 show geometry and loading for the three cases, referring to the multi-scale analysis, whereby the structure is modelled as a beam.

Each of these cases was modelled by both direct numerical simulation (DNS) and the fully nested (FE^2) multi-scale procedure. For the latter, the multi-scale procedure described in Section 3.2 was used. For each case, four values of the length L have been considered: 20, 60, 100 and 400m. Since the length of the RDE is 1m (Figure 3.5), the four different lengths correspond to four values of the scaling parameter $\epsilon = l/L$, equal to 0.05, 0.016667, 0.01 and 0.0025.

For each study, multi-scale convergence was evaluated by comparing the DNS results with those of the multi-scale analysis for each value of ϵ. For each value of ϵ, finite-element convergence of the multi-scale model with increasing number of elements was also examined.

3.3.2 Results

Convergence results for case 1 are shown in Figures 3.9 and 3.10. Results for case 2 are shown in Figures 3.11 and 3.12. Results for the case 3 are shown in Figures

Model parameters	
Load magnitude F (for axial loading)	2×10^7 N
Load magnitude F (for transverse loading)	$4 \times 10^5 \times \left(\frac{L}{20}\right)$ N
Load magnitude for non-proportional load case	$F_1 = 5\times 10^6 \times \left(\frac{L}{20}\right)$ N
	$F_2 = 2.5\times 10^6 \times \left(\frac{L}{20}\right)$ N
Young's modulus	200×10^9 Nm^{-2}
Yield limit	400×10^6 Nm^{-2}
Kinematic hardening constant	100×10^9 Nm^{-2}
Member cross-sectional area	0.01 m^2

Table 3.1: Material parameters

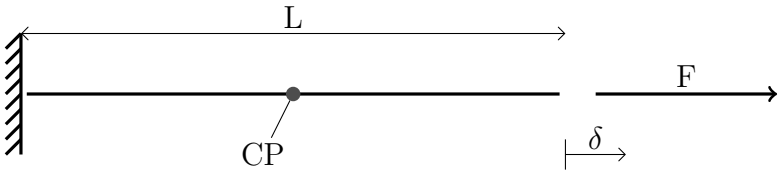

Figure 3.6: Case 1: Macro-geometry and loading. Comparison point (CP) located at distance 0.5L from support.

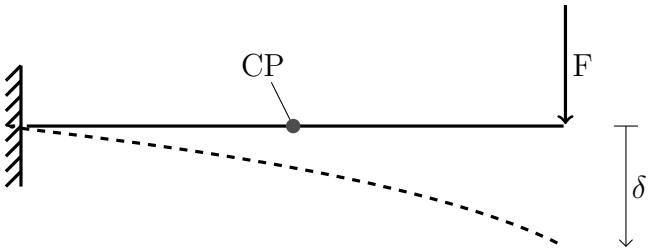

Figure 3.7: Case 2: Macro-geometry and loading. Comparison point (CP) located at distance 0.5L from support.

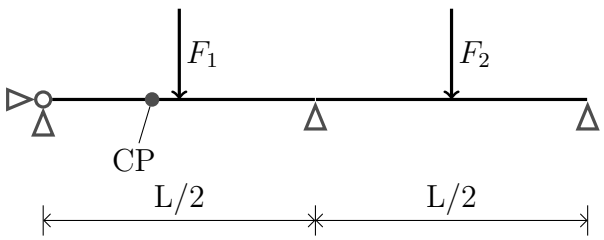

Figure 3.8: Case 3: Macro-geometry and loading. Comparison point (CP) located at distance 0.2L from pin joint; Applied loads located at distances 0.25L and 0.75L from pin joint.

3.13 and 3.14.

Displacement results were evaluated at the node corresponding to the comparison point (shown in Figures 3.6-3.8). For the DNS, stress results were obtained by averaging stresses in the two horizontal members on either side of the comparison point on the underside of the truss. For the multi-scale simulations, the comparison point is a node, and stress results are the average of the two integration points in the large-scale model on either side of the comparison point. For each integration point, the stresses in the horizontal truss members on the lower side of the RDE were evaluated. Due to the symmetry of the RDE problem, both lower horizontal members show the same stress.

Tolerances of 10^{-8}, 10^{-5} and 10^{-5} for the relative residual norm error were used for the DNS solver, the large-scale solver and the small-scale solver, respectively. The minimum error that can be achieved in these simulations is closely linked with the maximum tolerance used of 10^{-5}.

For case 1, Figures 3.9 and 3.10 show that both displacement and stress in the multi-scale model do not depend on the number of elements, whereby FE convergence is not an issue. Displacement results become increasingly accurate as the scaling parameter ϵ decreases, showing multi-scale convergence. Stress results do not change as the error is already as low as the numerical tolerance will allow.

For case 2 (Figures 3.11 and 3.12) displacement results from the multi-scale analysis are not significantly affected by number of elements. FE convergence appears to be achieved for L=60m and L=100m, which are more important to assess for multi-scale convergence. With decreasing ϵ multi-scale convergence can be observed for displacement results. For stresses the error for the multi-scale analysis is already below 0.2% for L=20m and only slightly reduces from L=60m to L=100m because the numerical tolerance has been reached. Increasing the number of elements does not significantly reduce error if more than 40 elements are used, showing that finite element convergence has occurred. For L=400, the Newton-Raphson procedure used did not converge.

For case 3, which has non-proportional loading (Figures 3.13 and 3.14), neither displacement nor stress results are significantly affected by the number of elements.

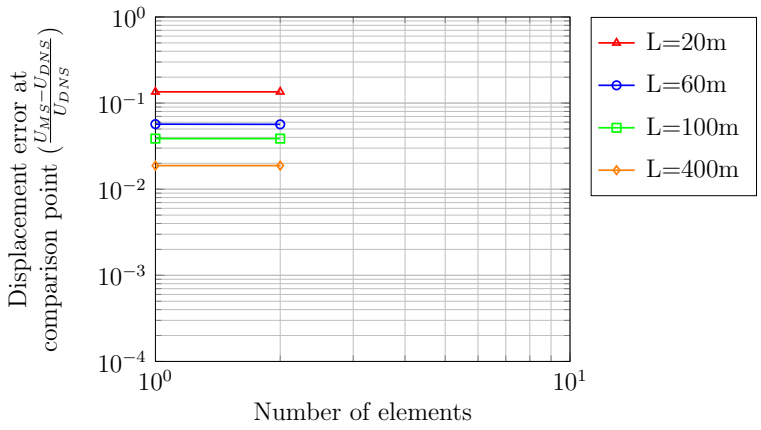

Figure 3.9: Multi-scale and FE displacement convergence at the comparison point for the axially loaded cantilever (case 1)

Both stress and displacement results converge as ϵ is decreased. The displacement error for the multi-scale procedure decreases from about 9% for L=20m to less that 0.5% for L=100m.

Deformed figures for transverse loading and the non-proportional load cases are shown in Figures 3.15, 3.16, 3.17 and 3.18, highlighting that the extent of plastic zones is constant with varying model length. In these figures, the annotation "plastic region" indicates regions in which the axial stress in some truss elements has exceeded the material yield limit, that is, plastic strain is occurring within the relevant RDEs. The truss elements where this is the case are coloured black instead of grey.

3.4 Concluding remarks

In this Chapter, a theoretical framework for the development of multi-scale models has been presented as an extension of the first-order computational homogenisation technique to the case in which different structural models are used at different length scales and where the lower-scale problem is not necessarily governed by an energy potential. It has been shown that volumetric averaging principles, which in general

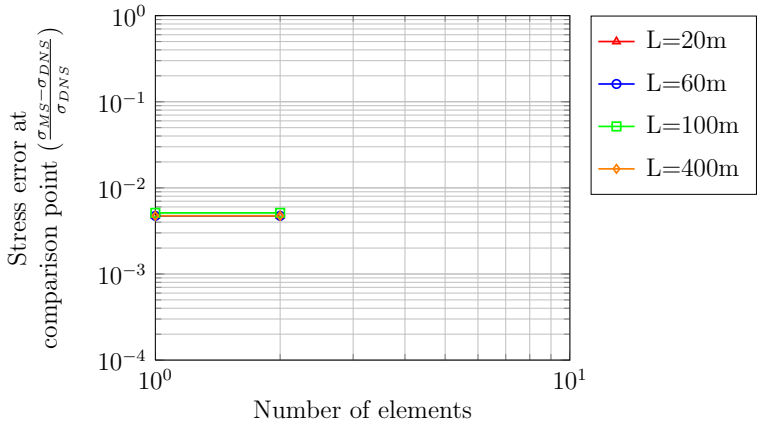

Figure 3.10: Multi-scale and FE stress convergence at the comparison point for the axially loaded cantilever (case 1)

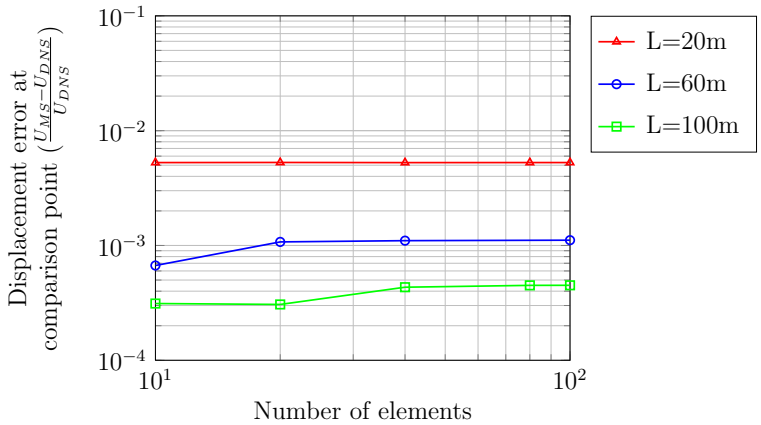

Figure 3.11: Multi-scale and FE displacement convergence at the comparison point for the transversally loaded cantilever (case 2)

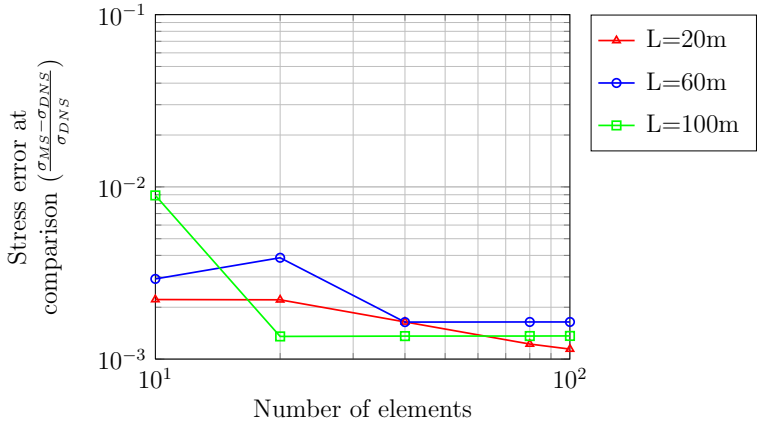

Figure 3.12: Multi-scale and FE stress convergence at the comparison point for the transversally loaded cantilever (case 2)

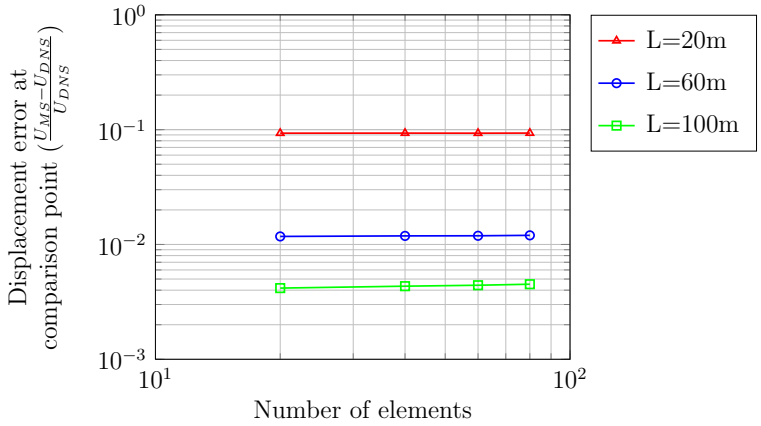

Figure 3.13: Multi-scale and FE displacement convergence at the comparison point for the non-proportional load case (case 3)

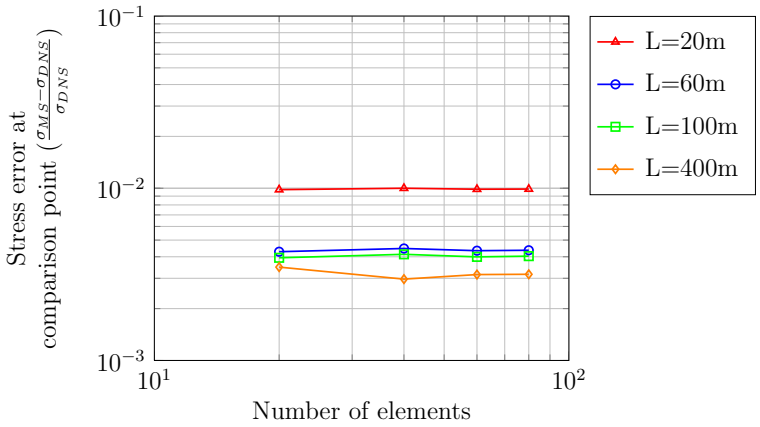

Figure 3.14: Multi-scale and FE stress convergence at the comparison point for the non-proportional load case (case 3)

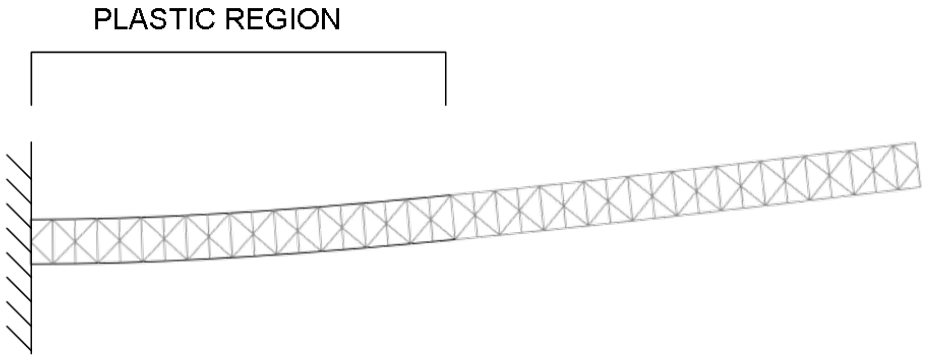

Figure 3.15: Material state for transverse loading, L=20m. Elements with stress greater than yield limit are black; elements with stress under yield limit are grey.

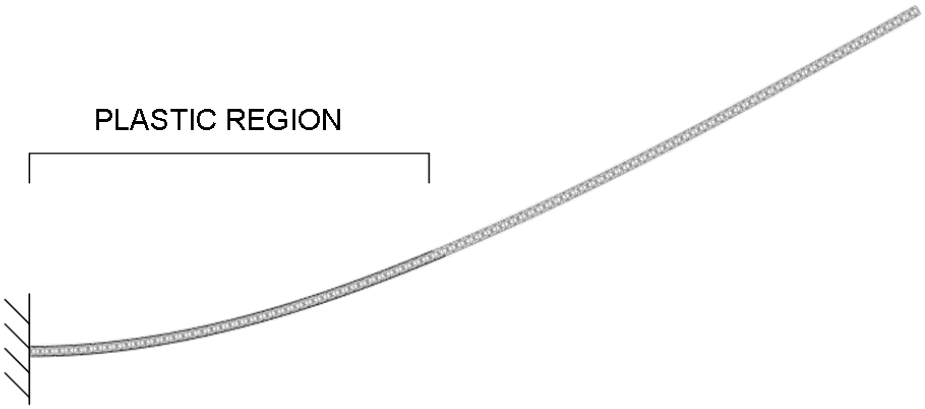

Figure 3.16: Material state for transverse loading, L=100m. Elements with stress greater than yield limit are black; elements with stress under yield limit are grey.

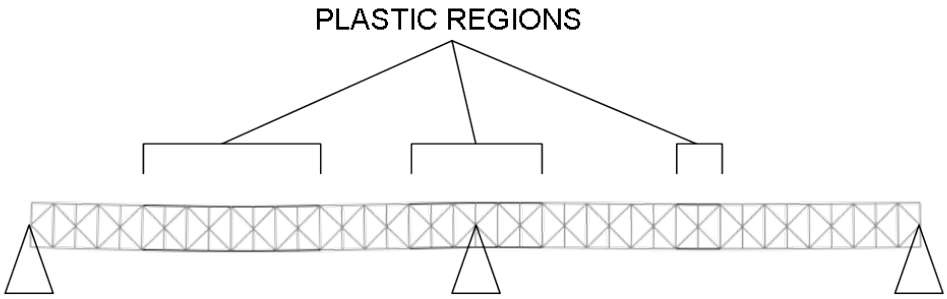

Figure 3.17: Material state for non-proportional load case, L=20m. Elements with stress greater than yield limit are black; elements with stress under yield limit are grey.

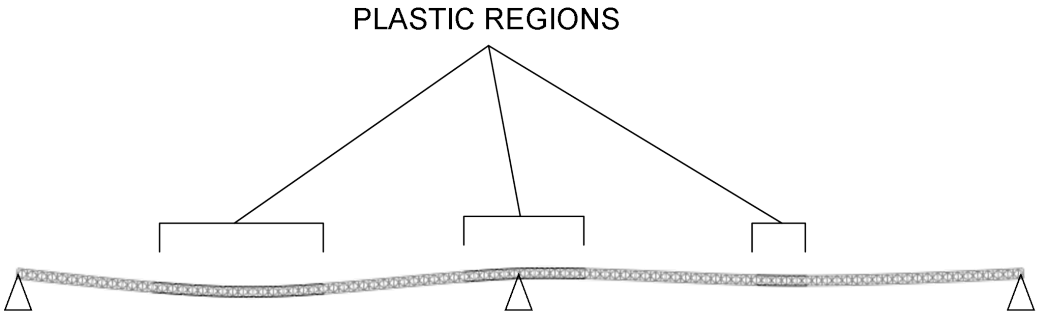

Figure 3.18: Material state for non-proportional load case, L=100m. Elements with stress greater than yield limit are black; elements with stress under yield limit are grey.

cannot be extended to this more general case, are not necessary to construct this extended theory, whereas engineering judgement in determining the scale-bridging operator and the boundary conditions to be used at the small-scale are required not only in this general case but also for the conventional first order theory. Instead of using volumetric averaging to transfer quantities between small and large scales, the small-scale model is augmented with additional degrees of freedom corresponding to the large-scale strains, allowing both the imposition of strains and the recovery of stresses via linear constraint equations. The up-scaling procedure used to recover the stress field in the large-scale model hinges on a generalised Hill's condition, which is not invoked as an assumption but is obtained from general duality principles.

An application of the method to nonlinear truss structures is shown. Multi-scale convergence of this model is discussed for three loading conditions.

The extension of computational homogenisation to structural-to-structural multi-scale models enables new approaches to material and structural modelling problems bridging length scales to be implemented and could allow the rapid creation of multi-scale models using combinations of simple structural elements such as springs, dampers, frictional sliders and thermal expansion elements to represent local behaviour. Where constitutive models are complex, such structural-to-structural multi-scale could be significantly more efficient than continuum multi-scale models

due to dimensional reduction.

We suggest that the computational homogenisation method outlined in this article could be a fruitful approach to modelling problems including marine flexible risers, auxetic materials, honeycomb structures or other impact attenuation materials like foams. Work remains to determine the mathematical conditions for the existence and uniqueness of the multi-scale solution and for multi-scale convergence.

Chapter 4

An enhanced Euler-Bernoulli beam model suitable for large-scale riser analysis

The theoretical work in Chapter 3 provides guidelines on how to carry out a multiscale analysis procedure using numerical models which, at both large and small scale, may be developed using discrete or structural elements, rather than continuum approaches. This work can be directly applied to the modelling of flexible pipes. Flexible pipes are extremely long, slender structures that are most conveniently modelled with beam-type elements at the large scale and have a local structure made of multiple interacting components that is also less suitable for representation using continuum models. In this Chapter, the development of a suitable beam-type element and constitutive model for flexible pipes is described. In the following, attention is directed towards creating a model which can represent the complex nonlinear large-scale behaviour documented for flexible pipes, together with consideration of the small-scale mechanisms that are the ultimate cause of such behaviour.

4.1 Previous work

In his PhD work on modelling of flexible pipes, Ali Bahtui (2008, 2009, 2010) developed a constitutive model to represent the three dimensional nonlinear response

of an unbonded flexible pipe. The general form of the model considers the pipe as a slender structure, represents the state of a pipe section as a set of macroscopic deformation measures, such as axial strain and curvature, and relates them to force and moment resultants such as axial tension and bending moment. Deformation measures are referred to as generalised strains and resultants as generalised stresses.

In this work, it was recognised that the primary cause of nonlinear behaviour under normal operation is the sliding that occurs between the concentric layers of the pipe, and that this is analogous to the slip that occurs between adjacent planes of atoms when a metallic material undergoes plastic deformation. For this reason, the constitutive law proposed is a form of rate-independent hardening plasticity. The inter-layer slip is accompanied by friction, whereby a non-associative type of plasticity was considered. It was considered that the criterion determining slip onset is a function of axial force, the two bending moments and torsion. As it was observed that high internal and/or internal pressures lead to larger hysteresis loops, new generalised stress measures were introduced to isolate the component of internal and external pressures contributing to interlayer contact pressure. This stress resultant was included in the slip-onset function with a tendency to inhibit sliding.

To determine the parameters of the model, a detailed FE model of a flexible pipe was created using 3D continuum elements. This model was used to simulate cyclic axial, bending and torsional loading using the commercial FE program Abaqus/Explicit. Comparisons of the calibrated model with the FE model for cyclic bending are shown in Figure 4.1. Analysis of slip-initiation points occurring under combined loading enables the correct form of the slip-onset function.

The constitutive model described above forms the basis for the large-scale model to be used in the multi-scale approach proposed in this work. In this Chapter, the existing model is described in detail in Section 4.2. Contributions of the current work are presented in following Sections. A new, enhanced algorithmic implementation achieving improved material convergence is described in Section 4.3. In order to use the model in practical riser analysis, new corotational beam finite elements have been developed. Formulations for two and three dimensional elements are presented

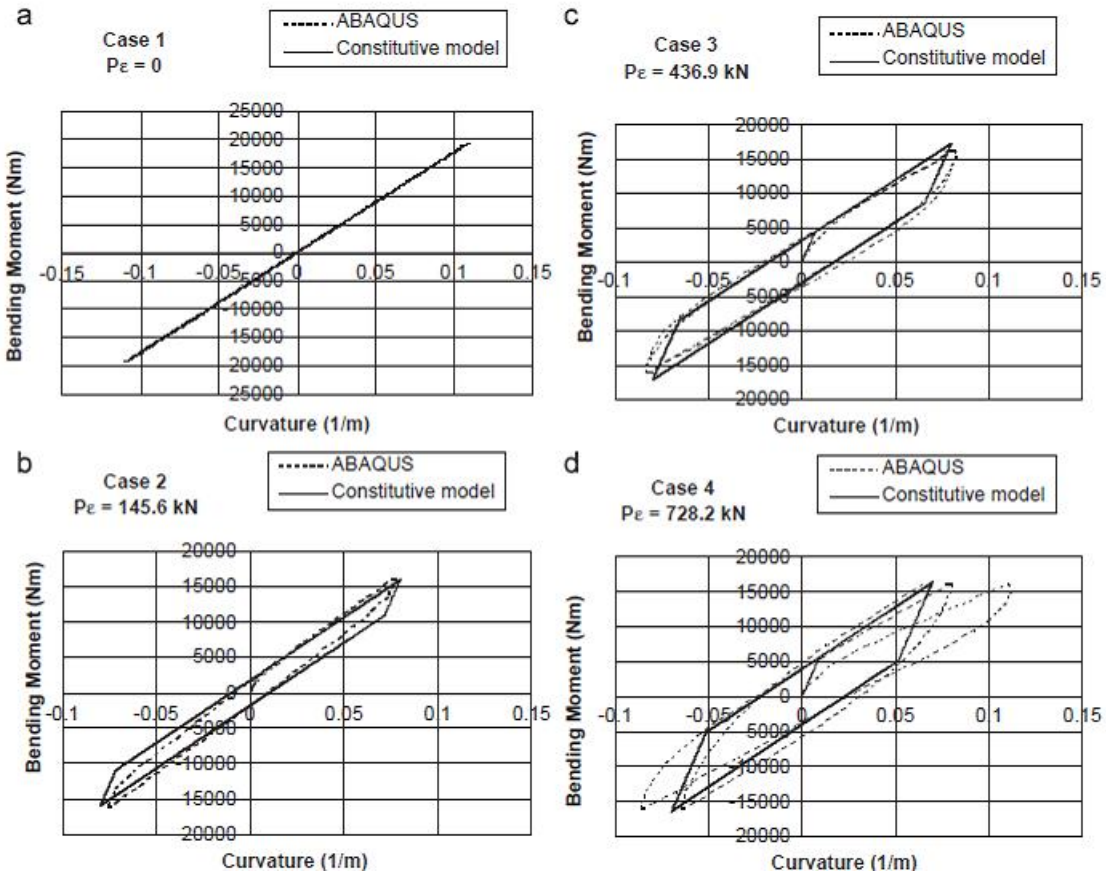

Figure 4.1: Comparison of FE results and constitutive model (Bahtui, 2008)

in Sections 4.4 and 4.5 respectively.

4.2 Large-scale constitutive model for flexible pipes

Development pf the constitutive law was based on the occurrence of hysteresis loops for flexible pipes subjected to cyclic bending. This phenomenon has been noted by many modellers (e.g. Kraincanic and Kebadze (2001); Tan et al. (2007); Witz (1996)). Hysteresis loops are observed to be wider when pipes are under higher pressure. The phenomena is explained by the ability of helical wires to slide relative to adjacent layers when a pipe is subjected to large curvatures,and this relative motion is not fully reversed when the curvature is removed, due to the frictional stick-slip mechanism. Due to the close analogy between the friction-restrained interlaminar slip in a flexible pipe and the microscopic slip between adjacent planes of atoms that is the mechanism for metal plasticity, it is hypothesized that this behaviour can be modelled as a rate-independent elasto-plastic relationship between generalised strains and stresses. Furthermore, it is hypothesized that the conditions at which slip commences involve the force measure that is work conjugate to the interlaminar or radial strain, of which the latter is defined as

$$\varepsilon_r = \frac{u_{INT} - u_{EXT}}{t} \qquad [-] \tag{4.2.1}$$

where u_{INT} and u_{EXT} are the radial displacements of the pressure sheath and of the outermost layers of the flexible pipe and t is the pipe wall thickness. The pressure sheath is the innermost layer of the pipe except for the carcass and is the layer on which internal pressure is applied, because the carcass is permeable to fluids. The complementary generalised strain measure required to characterise the pipe's radial behaviour is the mean radial displacement, defined as

$$u_r = \frac{u_{INT} + u_{EXT}}{2} \qquad [\text{m}] \tag{4.2.2}$$

The following expression can be written for work done by internal and external pressure per unit pipe length:

$$W = 2\pi(P_{INT}u_{INT}R_{INT} - P_{EXT}u_{EXT}R_{EXT}) \tag{4.2.3}$$

where R_{INT} and R_{EXT} are the radii of the pipe layers which carry internal and external pressure, respectively. Substituting expressions (4.2.1) and (4.2.2), Equation (4.2.3) becomes

$$W = P_u u_r + P_\varepsilon \varepsilon_r \tag{4.2.4}$$

Therefore, the internal work-conjugated force measures associated with these generalised strains are:

$$\begin{aligned} P_\varepsilon &= \pi t(P_{INT}R_{INT} + P_{EXT}R_{EXT}) \qquad [\mathrm{N}] \\ P_u &= 2\pi(P_{INT}R_{INT} - P_{EXT}R_{EXT}) \qquad [\mathrm{Nm}^{-1}] \end{aligned} \tag{4.2.5}$$

Hence, for a beam in three dimensions, the following generalised stress and strain measures are defined:

$$\sigma^T = [N \quad M_x \quad M_y \quad T \quad P_u \quad P_\varepsilon] \qquad \varepsilon^T = [\varepsilon_a \quad \chi_x \quad \chi_y \quad \phi \quad u_r \quad \varepsilon_r] \tag{4.2.6}$$

where meaning and units of the components of the vectors are:

N	Axial force	[N]
M_x, M_y	Bending moment	[Nm]
T	Torque	[Nm]
P_u	Radial displacement pressure term	[Nm^{-1}]
P_ε	Radial strain pressure term	[N]

ε_a	Axial strain	[-]
χ_x, χ_y	Curvature	[m^{-1}]
ϕ	Torsion	[m^{-1}]
u_r	Mean radial displacement	[m]
ε_r	Radial strain	[-]

The following non-associative elasto-plastic constitutive relation is then assumed:

$$\begin{cases} \sigma = D(\varepsilon - \varepsilon_s) \\ \dot{\varepsilon}_s = \dot{\lambda}\dfrac{dg}{d\sigma} \\ f(\sigma - \beta) \leq 0, \quad \lambda \geq 0, \quad \lambda f(\sigma - \beta) = 0 \\ \beta = H\varepsilon_s \end{cases} \tag{4.2.7}$$

where ε_s represents the inelastic generalised strains associated with interlayer slip, which will be referred to simply as slip strain, D denotes an elastic stiffness matrix, β is the back stress vector, H is a matrix of kinematic hardening moduli, while the slip-onset function f and slip potential g are defined as follows:

$$f(\sigma - \beta) = \begin{cases} b(N - \beta_1)^2 + c[(M_x - \beta_2)^2 + (M_y - \beta_3)^2] + \\ +d(T - \beta_4) - (P_\varepsilon - \beta_6) - a & \text{if } (N - \beta_1) > 0 \\ -(N - \beta_1) - a & \text{if } (N - \beta_1) \leq 0 \end{cases} \tag{4.2.8}$$

$$g(\sigma - \beta) = \begin{cases} b(N - \beta_1)^2 + c[(M_x - \beta_2)^2 + (M_y - \beta_3)^2] + \\ d(T - \beta_4) & \text{if } (N - \beta_1) > 0 \\ -(N - \beta_1) - a & \text{if } (N - \beta_1) \leq 0 \end{cases} \tag{4.2.9}$$

The linear elastic stiffness matrix is defined as

$$D = \begin{bmatrix} D_{11} & 0 & 0 & 0 & D_{51} & D_{61} \\ & D_{22} & 0 & 0 & 0 & 0 \\ & & D_{22} & 0 & 0 & 0 \\ & & & D_{44} & 0 & 0 \\ & symm. & & & D_{55} & D_{56} \\ & & & & & D_{66} \end{bmatrix} \tag{4.2.10}$$

It is noted that some of the coupling terms are necessary zero on grounds of the symmetries of a flexible pipe: for example, axisymmetric loading cannot cause curvature. The assumption of zero axial-torsional coupling deserves special mention. Due to the inclusion of helical components in flexible pipe structure, axial-torsional coupling is a feature of the behaviour of isolated helical armour layers. However, as this effect induces additional stresses in the wires, composite flexible pipes are designed such that the coupling effects of pairs of contra-wound layers cancel each other out. In the detailed finite element model used, some coupling effects were observed because the requirement for a periodic segment of the structure to be modelled lead to both helical armour layers being given the same pitch length, so that the model length could be minimised. As the observed coupling is an artifact of modelling choices, it will not be included in the constitutive model.

The linear kinematic hardening matrix is assumed not to display coupling between components and not to affect the pressure-related terms, resulting in the following diagonal hardening matrix:

$$H = \begin{bmatrix} H_{11} & 0 & 0 & 0 & 0 & 0 \\ & H_{22} & 0 & 0 & 0 & 0 \\ & & H_{22} & 0 & 0 & 0 \\ & & & H_{44} & 0 & 0 \\ & symm. & & & 0 & 0 \\ & & & & & 0 \end{bmatrix} \tag{4.2.11}$$

4.2.1 Model of slip onset and slip progression

The physical meaning of the criterion used for slip onset and rules for development of slip in the constitutive model described in Section 4.2 can be made more transparent with graphical representations.

The slip-onset criterion (Equation (4.2.9)) is expressed as a function of the generalised stresses. In the work of Bahtui (2008, 2009, 2010), four generalised stresses were considered to contribute to this function: Axial force (N), two bending moments (M_x, M_y) and radial strain pressure (P_ε). The projection of this hypersurface onto $M - P_\varepsilon$, $N - M$ and $N - M - P_\varepsilon$ space are shown in Figures 4.2a, b and c, respectively.

The chosen model is non-associative plasticity, which implies that the slip direction ($\mathbf{m}$) is not equal to the normal of the slip-onset surface ($\mathbf{n}$), or alternatively, not in the direction which gives the fastest reduction in the slip-onset criterion. The slip direction is the derivative of the flow potential function (Equation (4.2.9)) with respect to stress. The flow potential function has no contribution from P_ε. As P_ε is associated only with the radial strain measures in the elastic and hardening laws, this represents the physical fact that a pipe slippage will never cause an increase in layer radial deformation or cause layers to separate.

4.3 Finite-step algorithmic implementation

The governing equations of an inelastic material model do not permit a closed-form solution to be found. The usual procedure for an elasto-plastic rate-independent

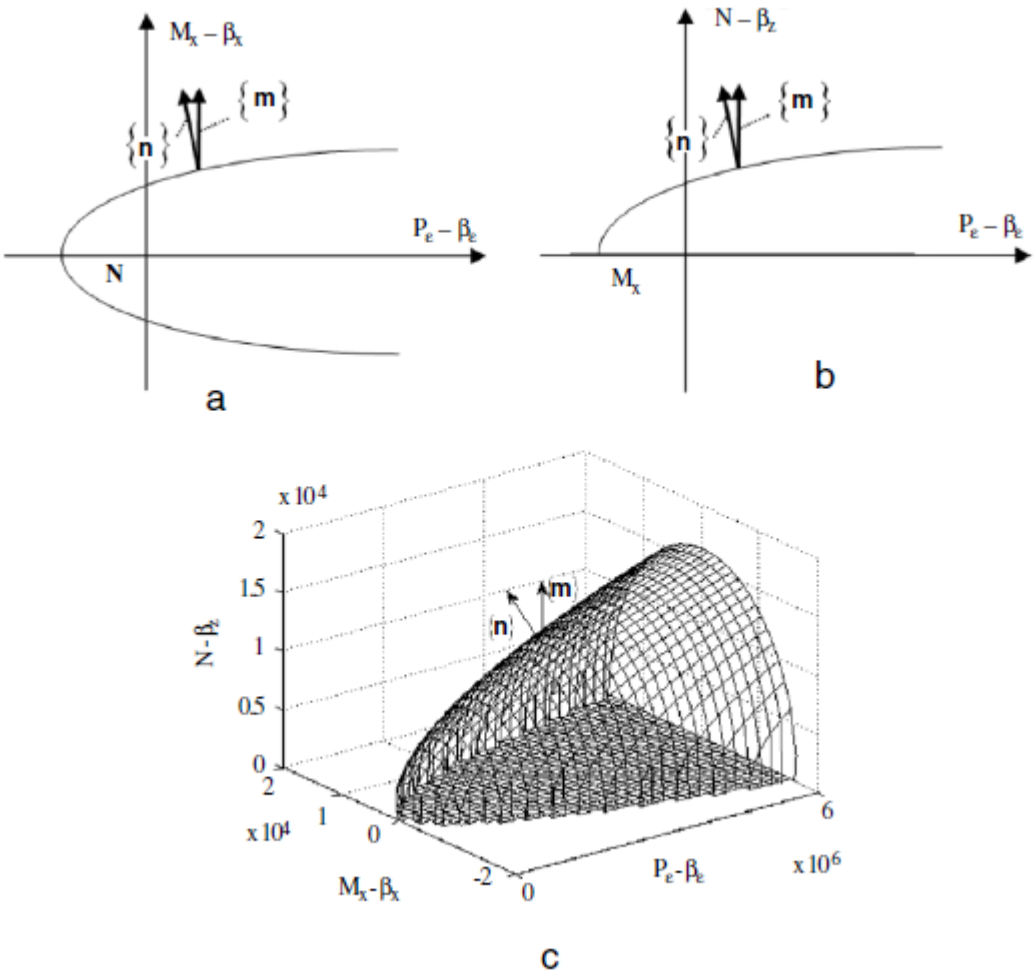

Figure 4.2: a) Projection of slip-onset surface in $M - P_\varepsilon$ space b) Projection of slip-onset surface in $N - P_\varepsilon$ space c) 3D slip-onset surface

material model is a strain-driven return-mapping algorithm.

In this Section, such an algorithm is developed for the numerical integration of a rate-independent non-associative plasticity material model, with kinematic hardening such as that proposed in Section 4.2. The algorithm is an example of a backward Euler return mapping algorithm, a common algorithm for the time-integration of constitutive relations involving rate-independent inelastic behaviour. A return-mapping algorithm is a two-step procedure used to compute the stresses, plastic strains and internal variables at a material point given the values of these variables at the start of the increment and the strain increment for the interval. The first step (predictor step) involves fixing the values of plastic strain and internal variables and calculating the stress increment as if the strain increment were purely elastic. The stress thus calculated is referred to as the trial stress. The yield function is computed using the trial stress (other variables being fixed at their initial state). If the yield limit is not exceeded, the trial state is accepted as the material state at the end of the increment; if not, a "plastic corrector" must be added to the trial state variables to compute the final state (the second, or corrector step). This involves integration of the plastic flow rate equation (as well as any hardening rate and internal variable evolution equations) and ensuring that the yield function for the final state is exactly zero. Numerical integration uses a first-order Euler method, which has explicit, implicit and mixed forms, depending on whether variables at the start, end or a linear combination of the two are used to calculate the integral. In the backward Euler return-mapping algorithms, the implicit method is used.

In distinction to standard methods, this method described here requires the solution of two rather than one equations using an iterative loop. This required modifying the algorithm previously developed by Bahtui (2008) and resulted in improved convergence of the material under a range of load conditions. The convergence of the material algorithm was tested under different trial stress states using an initially unstrained material state. Different combinations of axial strain, curvature and radial strain pressure were selected for the strain increment. The generalised stresses corresponding to these strains (using the model parameters determined by Bahtui (2008)) are detailed in Table 4.1. In all cases, where a "high" value for axial force

LOAD CASES			
Case	Radial strain pressure [N]	Axial force [N]	Bending moment [Nm]
Low P case 1	3320	9962	0
Low P case 2	3551	112	730
Low P case 3	3320	9962	730
Zero P case 1	7	11244	0
Zero P case 2	42	132	730
Zero P case 3	0	11350	730
High P case 1	358920	108880	0
High P case 2	361477	130	7296
High P case 3	358920	108879	7296
YIELD STATES FOR LOAD CASES (UNDER UNIAXIAL LOADING)			
Case		Axial force [N]	Bending moment [Nm]
Low P case 1		5260	380
Low P case 2		5440	393
Low P case 3		5260	380
Zero P case 1		241	17
Zero P case 2		592	43
Zero P case 3		0	0
High P case 1		54690	3950
High P case 2		54885	3964
High P case 3		54690	3950

Table 4.1: Convergence test cases

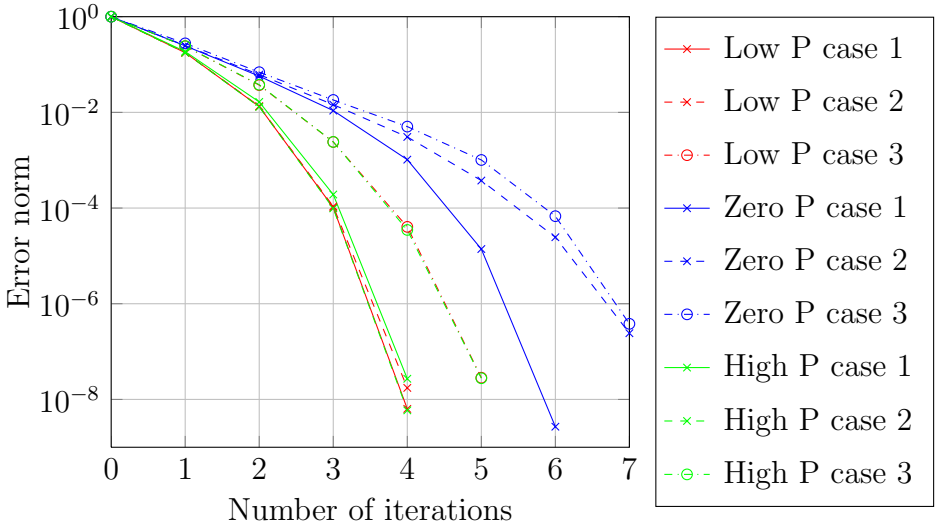

Figure 4.3: Convergence of material algorithm

or bending moment is used, the value used is much greater the value that would cause slip onset under uniaxial loading (see Table 4.1). Low rather than zero values are used for the axial stress to avoid stress states involving axial compression. Convergence with number of material iterations in terms of the norm $\|R(U)\|$ (see Equation (4.3.37)) for the nine generalised trial stresses is given in Figure 4.3.

Convergence was found to be rapid and robust, although poorer for cases with low radial strain pressure. The details and derivation of the algorithm are presented below.

Given a material state at pseudo-time t described by a vector of strains ε^t, a vector of internal state variables (plastic strains in this case) ε_p^t and a strain increment vector $\Delta\varepsilon$, a trial elastic state is calculated by holding the plastic strain constant:

$$\begin{aligned}
\varepsilon^{t+1} &= \varepsilon^t + \Delta\varepsilon \\
\varepsilon_{s,TR}^{t+1} &= \varepsilon_s^t \\
\beta_{TR}^{t+1} &= H\varepsilon_{s,TR} \\
\sigma_{TR}^{t+1} &= E(\varepsilon^{t+1} - \varepsilon_{s,TR}^{t+1})
\end{aligned} \tag{4.3.12}$$

If $f(\sigma_{TR}^{t+1} - \beta_{TR}^{t+1}) \leq 0$ then the trial state is admissible, that is, within the elastic domain specified by the yield function f. If $f(\sigma_{TR}^{t+1} - \beta_{TR}^{t+1}) > 0$ then the quantity of plastic strain increment must be determined such that the final material state lies just within the elastic region. This implies that

$$f(\sigma^{t+1} - \beta^{t+1}) = 0 \tag{4.3.13}$$

The final stress state is expressed in terms of the trial stress state and the plastic strain increment:

$$\begin{aligned} \sigma^{t+1} &= D(\varepsilon^{t+1} - \varepsilon_s^{t+1}) = \\ &= D(\varepsilon^{t+1} - \varepsilon_s^{t}) - D(\varepsilon_s^{t+1} - \varepsilon_s^{t}) = \\ &= \sigma_{TR}^{t+1} - D\Delta\varepsilon_s \end{aligned} \tag{4.3.14}$$

where the $t+1$ superscript is henceforth dropped to simplify the notation.

The finite step evaluation of ε_s is obtained by approximating Equation (4.2.7b) as follows:

$$\Delta\varepsilon_s = \Delta\lambda \frac{\partial g}{\partial \sigma} \tag{4.3.15}$$

Combining Equation (4.3.14) with the discrete non-associative plastic flow rule (Equation (4.3.15)) gives

$$\sigma = \sigma_{TR} - \Delta\lambda D \frac{\partial g}{\partial \sigma} \tag{4.3.16}$$

Defining the relative stress τ as $\tau = \sigma - \beta$, Equation (4.3.16) becomes

$$\tau + \beta = \tau_{TR} + \beta_{TR} - \Delta\lambda D\frac{\partial g}{\partial \sigma} \tag{4.3.17}$$

Including the hardening law (Equation 4.2.7) gives

$$\begin{aligned}
\tau &= \tau_{TR} + H\Delta\varepsilon_s - \Delta D\frac{\partial g}{\partial \sigma} = && (4.3.18)\\
&= \tau_{TR} - H\Delta\lambda D\frac{\partial g}{\partial \sigma} - \Delta\lambda D\frac{\partial g}{\partial \sigma} = \\
&= \tau_{TR} - \Delta\lambda(D+H)\frac{\partial g}{\partial \tau} && (4.3.19)\\
\tau &- \tau_{TR} + \Delta\lambda(D+H)\frac{\partial g}{\partial \tau} = 0 && (4.3.20)
\end{aligned}$$

For convenience, both sides are premultiplied by the constant term $(D+H)^{-1}$ and a residual vector q can be introduced:

$$q(\Delta\lambda, \tau) = (D+H)^{-1}(\tau - \tau_{TR}) + \Delta\lambda\frac{\partial g}{\partial \tau} \tag{4.3.21}$$

Solution of the constrained evolution problem consists of finding the solution to this equation, subject to the yield function constraint (Equation (4.3.13)):

$$\boxed{\begin{array}{c} \textit{SOLVE SIMULTANEOUSLY} \\ q(\Delta\lambda, \tau) = (D+H)^{-1}(\tau - \tau^{TR}) + \Delta\lambda\dfrac{\partial g}{\partial \tau} = 0 \\ f(\tau) = 0 \end{array}}$$

This can be solved by using a coupled Newton-Raphson process using the residual vector $R = [q \quad f]^T$ and solution vector $U = [\tau \quad \Delta\lambda]^T$. The kth iteration provides the following update formula

$$R(U^{k+1}) = 0 \approx R(U^k) + \frac{dR(U^k)}{dU}(U^{k+1} - U^k) = R(U^k) + K^k(U^{k+1} - U^k) \tag{4.3.22}$$

which leads to the linear system:

$$K^k(U^{k+1} - U^k) = -R(U^k) \tag{4.3.23}$$

where the iteration matrix is given by

$$K = \begin{bmatrix} \frac{dq}{d\tau} & \frac{dq}{d(\Delta\lambda)} \\ \frac{df}{d\tau} & \frac{df}{d(\Delta\lambda)} \end{bmatrix} \tag{4.3.24}$$

Denoting

$$n = \frac{\partial f}{\partial \tau} \tag{4.3.25}$$

$$m = \frac{\partial g}{\partial \tau} \tag{4.3.26}$$

$$D^H = D + H \tag{4.3.27}$$

the derivatives in Equation (4.3.24) are given by:

$$\begin{aligned} \frac{dq}{d\tau} &= G^{-1} \\ \frac{dq}{d(\Delta\lambda)} &= \frac{\partial g}{\partial \tau} = m \\ \frac{df}{d\tau} &= n \\ \frac{df}{d(\Delta\lambda)} &= 0 \end{aligned} \tag{4.3.28}$$

where it has been set that:

$$G = [(D^H)^{-1} + \Delta\lambda \frac{\partial^2 g}{\partial \tau^2}]^{-1} \tag{4.3.29}$$

System (4.3.23) can therefore be written as follows:

$$\begin{bmatrix} G^{-1} & m \\ n & 0 \end{bmatrix} \begin{bmatrix} d\tau^k \\ d\Delta\lambda^k \end{bmatrix} = - \begin{bmatrix} e^k \\ f^k \end{bmatrix} \tag{4.3.30}$$

where $d\tau^k = \tau^{k+1} - \tau^k$ and $d\Delta\lambda^k = \Delta\lambda^{k+1} - \Delta\lambda^k$. Writing the equations separately:

$$\begin{aligned} G^{-1}d\tau^k + m \cdot d\Delta\lambda^k &= -e^k \\ n \cdot d\tau^k &= -f^k \end{aligned} \tag{4.3.31}$$

Therefore

$$d\tau^k = G(-e^k - m \cdot d\Delta\lambda^k) \tag{4.3.32}$$

Substituting in the second equation gives

$$nG(-e^k - m \ \cdot d\Delta\lambda^k) - n \cdot Ge^k - n \cdot (Gm)d\Delta\lambda^k = -f^k \tag{4.3.33}$$

leading to:

$$d\Delta\lambda^k = \frac{f^k - n \cdot Ge^k}{n \cdot Gm} \tag{4.3.34}$$

Therefore the two Newton-Raphson increments are found using the equations

$$d\tau = G(-e^k - m \cdot d\Delta\lambda^k) \tag{4.3.35}$$

$$d\Delta\lambda^k = \frac{f^k - n \cdot Ge^k}{n \cdot Gm} \tag{4.3.36}$$

giving the algorithm:

INITIALISE:

$$\begin{aligned} k &:= 0 \\ \tau^{k=0} &:= \tau_{TR} \\ \Delta\lambda^{k=0} &:= 0 \\ n^{k=0} &:= n(\tau_{TR}) \\ m^{k=0} &:= m(\tau_{TR}) \\ R(U^0) &\rightarrow \begin{bmatrix} (D+H)^{-1}(\tau^0 - \tau_{TR}) + \Delta\lambda \frac{\partial g}{\partial \tau} \\ f(\tau^0) \end{bmatrix} \end{aligned} \tag{4.3.37}$$

DO WHILE $\|R(U^k)\| < TOL$

$$\begin{aligned} k &\rightarrow k+1 \\ f &\rightarrow f(\tau^k) \\ n &\rightarrow n(\tau^k) \\ m &\rightarrow m(\tau^k) \\ G &\rightarrow \left((D^H)^{-1} + \Delta\lambda \frac{\partial^2 g}{\partial \tau^2} \right)^{-1} \\ e^k &\rightarrow (D^H)^{-1}(\tau^k - \tau^{TR}) + \Delta\lambda^k m \end{aligned}$$

FIND INCREMENTS

$$\begin{aligned} \Delta\tau^k &= G(-e^k - m \cdot d\Delta\lambda^k) \\ d\Delta\lambda^k &= \frac{f^k - n \cdot Ge^k}{n \cdot Gm} \end{aligned}$$

UPDATE

$$\Delta\lambda^{k+1} = \Delta\lambda^k + d\Delta\lambda^k$$
$$\tau^{k+1} = \tau^k + d\tau^k$$

RECALCULATE RESIDUAL FOR NEXT STEP

$$R(U^{k+1}) \rightarrow \begin{bmatrix} (D+H)^{-1}(\tau^{k+1} - \tau_{TR}) + \Delta\lambda\frac{\partial g}{\partial \tau} \\ f(\tau^{k+1}) \end{bmatrix}$$

END DO

4.3.1 Calculation of the consistent tangent

Taking the elasticity relation evaluated at the end of the time increment:

$$\sigma_{n+1} = D(\varepsilon_{n+1} - \varepsilon_{n+1,s}) \tag{4.3.38}$$

Differentiating this by the total strain at the end of the increment gives:

$$\delta\sigma_{n+1} = D(\delta\varepsilon_{n+1} - \frac{d\varepsilon_{n+1,s}}{d\varepsilon_{n+1}}\delta\varepsilon_{n+1}) \tag{4.3.39}$$

The differential form of the slip rule is obtained using the chain rule:

$$\delta\varepsilon_s = \delta\Delta\lambda\frac{\partial g}{\partial\sigma} + \Delta\lambda\delta\left(\frac{\partial g}{\partial\sigma}\right) = \delta\Delta\lambda\cdot m + \Delta\lambda\frac{\partial^2 g}{\partial\sigma^2}\delta\sigma_{n+1} + \Delta\lambda\frac{\partial^2 g}{\partial\sigma\partial\beta}\delta\beta_{n+1} \tag{4.3.40}$$

The differential form of the hardening law is

$$\delta\beta_{n+1} = H\delta\varepsilon_{n+1,s} \tag{4.3.41}$$

Noting that:

$$\frac{\partial^2 g}{\partial \sigma \partial \beta} = -\frac{\partial^2 g}{\partial \sigma^2} \tag{4.3.42}$$

Combining Equations (4.3.40) and (4.3.41), gives

$$H^{-1}\delta\beta_{n+1} = \delta\Delta\lambda \cdot m + \Delta\lambda\frac{\partial^2 g}{\partial \sigma^2}\delta\sigma_{n+1} + \Delta\lambda\frac{\partial^2 g}{\partial \sigma \partial \beta}\delta\beta_{n+1} \tag{4.3.43}$$

and, using Equation (4.3.42) and rearranging gives an equation incorporating the slip rule and hardening relation:

$$-\Delta\lambda\frac{\partial^2 g}{\partial \sigma^2}\delta\sigma_{n+1} + \left[H^{-1} + \Delta\lambda\frac{\partial^2 g}{\partial \sigma^2}\right]\delta\beta_{n+1} = \delta\Delta\lambda \cdot m \tag{4.3.44}$$

Substituting Equation (4.3.40) into Equation (4.3.38) and premultiplying by D^{-1} results in a second equation combining the slip rule and the equilibrium equation:

$$D^{-1}\delta\sigma_{n+1} = \delta\varepsilon_{n+1} - \delta\Delta\lambda m - \Delta\lambda\frac{\partial^2 g}{\partial \sigma^2}\delta\sigma_{n+1} - \Delta\lambda\frac{\partial^2 g}{\partial \sigma \partial \beta}\delta\beta_{n+1} \tag{4.3.45}$$

Rearranging Equation (4.3.45) gives:

$$\left[D^{-1} + \Delta\lambda\frac{\partial^2 g}{\partial \sigma^2}\right]\delta\sigma_{n+1} + \Delta\lambda\frac{\partial^2 g}{\partial \sigma \partial \beta}\delta\beta_{n+1} = \delta\varepsilon_{n+1} - \delta\Delta\lambda m \tag{4.3.46}$$

Equations (4.3.46) and (4.3.44) can be expressed in matrix form as:

$$\begin{bmatrix} D^{-1} + \Delta\lambda\dfrac{\partial^2 g}{\partial \sigma^2} & -\Delta\lambda\dfrac{\partial^2 g}{\partial \sigma^2} \\ -\Delta\lambda\dfrac{\partial^2 g}{\partial \sigma^2} & H^{-1} + \Delta\lambda\dfrac{\partial^2 g}{\partial \sigma^2} \end{bmatrix} \begin{bmatrix} \delta\sigma_{n+1} \\ \delta\beta_{n+1} \end{bmatrix} = \begin{bmatrix} \delta\varepsilon_{n+1} - \delta\Delta\lambda m \\ \delta\Delta\lambda \cdot m \end{bmatrix} \tag{4.3.47}$$

Inverting the above relation allow expressions for $\delta\sigma_{n+1}$ and $\delta\beta_{n+1}$ to be written as:

$$\begin{aligned}\delta\sigma_{n+1} &= D\delta\varepsilon_{n+1} - \Delta\lambda DQF^{-}1D\ \delta\varepsilon_{n+1} + \Delta\lambda\delta\Delta\lambda DQF^{-1}(D+H)m - \delta\Delta\lambda Dm \\ \delta\beta_{n+1} &= \Delta\lambda HQF^{-1}D\delta\varepsilon_{n+1} - \Delta\lambda\delta\Delta\lambda HQF^{-1}(D+H)m + \delta\Delta\lambda Hm \end{aligned} \tag{4.3.48}$$

Where

$$Q = \frac{\partial^2 g}{\partial\sigma^2}$$

A final relation that relates the elastic stress and back-stress increments is the consistency condition that requires that $\dot{f}(\sigma_{n+1}, \beta_{n+1}) = 0$ at the end of the plastic increment (Simo and Hughes, 1998). This implies that

$$(\delta\sigma_{n+1} - \delta\beta_{n+1}) \cdot n = 0 \tag{4.3.49}$$

The above relation, when applied to Equation 4.3.48, completed the formulation. The slip parameter $\Delta\lambda$ can be determined as

$$\Delta\lambda = \frac{(D - \Delta\lambda(D+H)QF^{-1}D)d\varepsilon_{n+1} \cdot n}{((D+H) - \Delta\lambda(D+H)QF^{-1}(D+H))m \cdot n} \tag{4.3.50}$$

while the consistent tangent operator is

$$\begin{aligned}\frac{\partial\sigma_{n+1}}{\partial\varepsilon_{n+1}} &= (D - \Delta\lambda DZD) - \\ &\frac{((D - \Delta\lambda DZ(D+H))m \otimes (D - \Delta\lambda DZ(D+H))n}{((D+H) - \Delta\lambda(D+H)Z(D+H))m \cdot n}\end{aligned} \tag{4.3.51}$$

4.4 2D corotational element formulation

Two implementations of the constitutive model described in Section 4.2 were carried out, one in a two-dimensional beam element and the second in a three-dimensional beam element.

The 2D element is a two-node Euler-Bernoulli planar beam element enhanced with additional pressure-related generalised strains and stresses. The formulation without these pressure-related terms has already been presented in Section 3.2.1. Here we focus only on the modifications required to accommodate the pressure terms.

A natural way to introduce the new generalised stresses and strains is by introducing new degrees of freedom at the element nodes. It was chosen to introduce one degree of freedom representing the radial displacement of the outer layer and one degree of freedom representing the radial displacement of the pressure sheath. These degrees of freedom are work-conjugate with the internal and external pressures. This method allows variation of external pressure to considered in the element response and allows radial displacement boundary conditions to be imposed, reflecting the constrictions present at end connections and bend limiters.

Recalling Equations (4.2.3) and (4.2.4), the work done by external and internal pressure can now be expressed in two forms:

$$W = 2\pi(P_{INT}u_{INT}R_{INT} - P_{EXT}u_{EXT}R_{EXT}) \tag{4.4.52}$$

and

$$W = P_u u_r + P_\varepsilon \varepsilon_r \tag{4.4.53}$$

If the constitutive relation is formulated in terms of u_r, ε_r, P_u and P_ε, yet the element degrees of freedom and forces are u_{INT}, u_{EXT}, P_{INT} and P_{EXT} then, firstly, u_r and ε_r must be computed from u_{INT} and u_{EXT} by introducing new shape functions for

the element, and, secondly, element internal forces in terms of P_u and P_ε must be converted into P_{INT} and P_{EXT} such that equilibrium can be assessed by the global solver.

The first modification is acheived by introducing the following linear shape functions relating the radial degrees of freedom with the radial generalised strains present in the constitutive model:

$$\begin{bmatrix} u_r \\ \varepsilon_r \end{bmatrix} = B^*(x) = \frac{1}{L} \begin{bmatrix} 0.25(1-x) & 0.25(1-x) & 0.25x & 0.25x \\ \dfrac{0.5(1-x)}{t} & \dfrac{0.5(1-x)}{t} & -\dfrac{0.5x}{t} & -\dfrac{0.5x}{t} \end{bmatrix} \begin{bmatrix} U^1_{INT} \\ U^1_{EXT} \\ U^2_{INT} \\ U^2_{EXT} \end{bmatrix} \quad (4.4.54)$$

where the superscript indicates the node number the degree of freedom is associated with, L is the element length, x is the distance along the pipe axis and t is the pipe thickness, defined as the difference between the radii of the pressure sheath and the outer layer.

The second modification is achieved by equating the force terms in Equations (4.4.52) and (4.4.53), resulting in the following equations:

$$P_u = 2\pi(P_{INT}R_{INT} - P_{EXT}R_{EXT}) \quad (4.4.55)$$

$$P_\varepsilon = \pi t(P_{INT}R_{INT} + P_{EXT}R_{EXT}) \quad (4.4.56)$$

4.4.1 Element convergence study

A convergence study was carried out on the two dimensional pipe element. In this study, a single element is tested. The element is initially straight, with one node being pinned and the other being simply supported. The element is subjected to combinations of pressure, axial force and bending moment. The parameters of the constitutive model are the same as used in the constitutive convergence study (Section 4.3). Axial force is applied by creating a point load on the simply supported node. Bending moment is applied by creating two equal and opposite point moments

LOAD CASES				
Case	Radial strain pressure [N]	Radial displacement pressure [Nm^{-1}]	Axial force [N]	Bending Moment [Nm]
A1	0	0	300000	0
A2	0	0	0	20000
A3	0	0	300000	20000
B1	14560	0	300000	0
B2	14560	0	0	20000
B3	14560	0	300000	20000
C1	463930	0	300000	0
C2	463930	0	0	20000
C3	463930	0	300000	20000
D1	225466	1.656×10^7	300000	0
D2	225466	1.656×10^7	0	20000
D3	225466	1.656×10^7	300000	20000

Table 4.2: Load cases for 2D element convergence study

on the two nodes. For consistency with the riser simulation (Section 4.6), pressure is applied in a separate, initial step. The magnitudes of the radial strain pressure in load cases A1-3, B1-3 and C1-3 correspond to external pressures of 0, 1 and 30 MPa. The magnitude of the radial strain pressure and radial displacement pressure for load cases D1-3 correspond to an external pressure of 30 MPa and an internal pressure of 0.75 MPa, the same as used for the riser analysis in Section 4.6. The combinations of loading investigated in this study are listed in Table 4.2.

Simulations were carried out using the Abaqus solver and the Fortran subroutine implementing the two-dimensional pipe element. Element convergence in the second load step only was in investigated, as convergence in the pressure loading step is achieved after one iteration in all cases. The size of the initial load increment is set to be equal to the total load in all cases, and cutbacks in increment size during the analyses are not allowed. The change in the error norm with iteration number for these load cases is shown in Figure 4.4. Error norm is defined as the ratio of maximum residual force in the element to average residual force, or the ratio of maximum residual moment to average moment, whichever is greater.

From Figure 4.4, the same general trends as for convergence of the constitutive algorithm (Section 4.3) can be seen, in that convergence is faster when radial strain

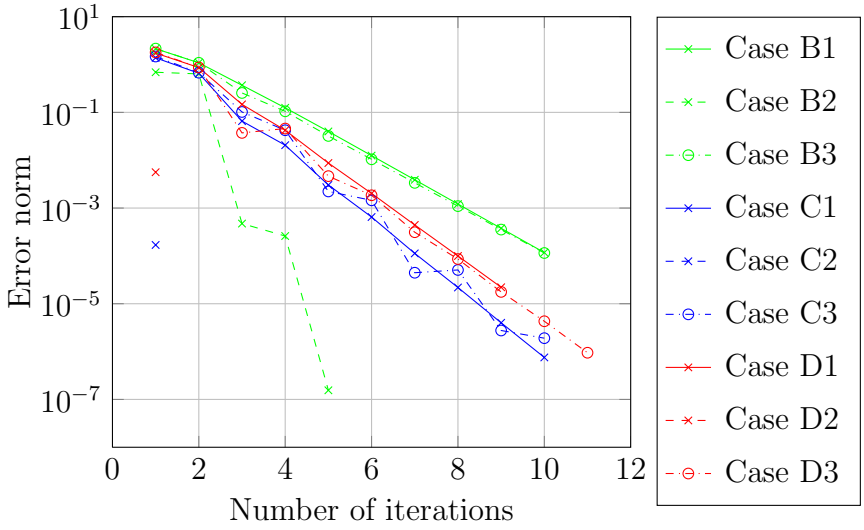

Figure 4.4: Convergence of 2D pipe element

pressure is higher (comparing cases B1-3 with cases C1-3) and that the addition of significant radial displacement pressure (cases D1-3) further improves convergence. The element did not converge at all for zero pressure load cases (cases A1-3), which are not represented in Figure 4.4. Some tests with low radial strain pressures (not presented) did converge, but required multiple cutbacks in the increment size. In general, convergence is fairly slow - the straight lines shown in Figure4.4 indicate that convergence is linear, not quadratic, as the ratio between residuals at successive interations tends to a constant value. It is noted that convergence lines for cases in which both axial force and bending moment are applied may be "jagged" (load cases C3 and D3), which is a consequence of the requirement for the Abaqus solver to resolve two field residuals simultaneously, which are associated with greatly different stiffness values. For load cases involving pressure and bending only (cases B2, C2 and D2), the solution is either accepted after the first iteration (cases C2 and D2) or fast (case B2), which is a consequence of the low bending stiffness.

From this study, it is concluded that the element is usable, but not robust at low values of radial strain pressure. This study did not test the effectiveness of the corotational formulation as the element investigated did not undergo large rigid-body displacements or rotations. This is left for future developments.

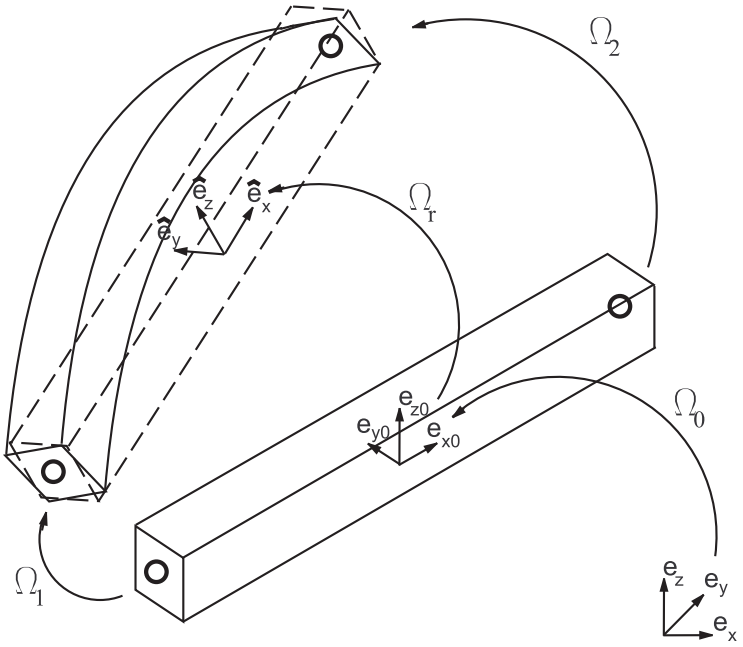

Figure 4.5: 3D corotional beam formulation: 2 configurations (initial and deformed), 3 coordinate systems (global, $\mathbf{e}_i$, initial, $\mathbf{e}_{i0}$ and local, $\hat{\mathbf{e}}_i$) and 4 rotations ($\mathbf{\Omega}_1$, $\mathbf{\Omega}_2$, $\mathbf{\Omega}_0$ and $\mathbf{\Omega}_T$) are used in the formulation

4.5 3D corotational formulation

In this Section the formulation of a 3D corotational beam element enhanced with pressure terms is described.

4.5.1 Geometry and coordinate systems

Finite deformation geometry

Two body configurations, initial and current, and three coordinate systems, global, initial and local are used. The basis vectors of these are denoted as $\mathbf{e}_i$, $\mathbf{e}_{i0}$ and $\hat{\mathbf{e}}_i$, respectively. To transform between local and global coordinate systems, the 3x3 tensor $\mathbf{T}^*$ is used, such that, if vector $\mathbf{v}$ has components v_j in the global system, it has components v'_i in the local system given by $v'_i = T^*_{ij} v_j$. The components of $\mathbf{T}^*$ are given by $T^*_{ij} = \hat{\mathbf{e}}_i \cdot \mathbf{e}_j$.

It is noted that, when written in matrix form, any (passive[1]) transformation matrix is the transpose of the matrix representation of the corresponding (active[2]) rotation tensor. $\mathbf{T}^*$ transforms a vector in the global system to the vector in the local system, $\mathbf{\Omega}_r$ rotates a unit vector in the initial system to the corresponding unit vector in the local system, $\mathbf{\Omega}_0$ rotates a unit vector in the global system to the corresponding unit vector in the initial system, and $\mathbf{\Omega}^*$ rotates a unit vector in the global system to the corresponding unit vector in the local system. It then results that $\mathbf{T}^* = (\mathbf{\Omega}^*)^T$, $\mathbf{\Omega}^* = \mathbf{\Omega}_r\mathbf{\Omega}_0$, and hence, $\mathbf{T}^* = \mathbf{\Omega}_0^T\mathbf{\Omega}_r^T$.

The beam element presented in Edmans et al. (2009) is a two-noded Euler-Bernoulli type element using Hermite shape functions. In addition to the standard six rotational and translational degrees of freedom at each node, the displacements of the internal and external pipe radii are also included. Nodal rotations in finite element software are typically represented as "pseudo-vectors" at the nodes. Each pseudovector represents a three-dimensional rotation with a single unit vector along the axis around which the single equivalent rotation takes place, multiplied by the magnitude of the rotation around this axis in radians. The following numbering convention is used:

$\hat{\mathbf{u}}_{1-3}$	Translational DOFs in the global system for node 1
$\hat{\mathbf{u}}_{4-6}$	Components of pseudovector representing the rotation at node 1
$\hat{\mathbf{u}}_{7-8}$	Radial displacement of pipe inner (7) and outer (8) surfaces at node 1
$\hat{\mathbf{u}}_{9-11}$	Translational DOFs in the global system for node 2
$\hat{\mathbf{u}}_{12-14}$	Components of pseudovector representing the rotation at node 2
$\hat{\mathbf{u}}_{15-16}$	Radial displacement of pipe inner (7) and outer (8) surfaces at node 2

[1]For a vector $\mathbf{v}$ a passive transformation matrix $\mathbf{T}$ transforms the components of $\mathbf{v}$ with respect to the orthonormal basis vector set $\mathbf{e}_i^a$ into the components with respect to a second orthonormal basis $\mathbf{e}_i^b$. This is referred to by some authors as an *alias rotation.*

[2]An active rotation tensor $\mathbf{\Omega}$ premultiplying unit vector $\mathbf{e}_i^a$ results in the corresponding rotated vector $\mathbf{e}_i^b$. This is referred to by some authors as an *alibi rotation.*

The radial degrees of freedom are decoupled geometrically but coupled in the constitutive relation to the standard degrees of freedom. Details of the constitutive model used with this element are given in Section 4.2.

Computing the initial and current local triads, $\mathbf{e}_{i0}$ and $\hat{\mathbf{e}}_i$

The initial local 3-axis $\mathbf{e}_{30}$ is defined as parallel to $(\mathbf{x}^2(0) - \mathbf{x}^1(0))$; similarly, the current local 3-axis is parallel to $(\mathbf{x}^2(t) - \mathbf{x}^1(t))$. The initial local 2-axis $\mathbf{e}_{20}$ is defined as $\mathbf{e}_3 \times \mathbf{e}_{30}$ when $\mathbf{e}_3 \neq \mathbf{e}_{30}$. The initial local 1-axis $\mathbf{e}_{10}$ then follows as $\mathbf{e}_{20} \times \mathbf{e}_{30}$.

Expressions for the current local triad are written in terms of the nodal rotations, which can be collected into two pseudo-vectors expressed in terms of the beam's degrees of freedom:

$$\mathbf{\Phi}_1 = \begin{pmatrix} u_4 \\ u_5 \\ u_6 \end{pmatrix} \qquad \mathbf{\Phi}_2 = \begin{pmatrix} u_{12} \\ u_{13} \\ u_{14} \end{pmatrix} \tag{4.5.57}$$

Using the standard Rodrigues formula (see, for example, Crisfield (1997)), these can be expressed as direction cosine matrices $\mathbf{\Omega}_1(\mathbf{\Phi}_1)$ and $\mathbf{\Omega}_2(\mathbf{\Phi}_2)$. We assume an initially straight beam, i.e. $\mathbf{e}_{i0} = \mathbf{e}^1_{i0} = \mathbf{e}^2_{i0}$. In addition to the three element vector triads already defined, we introduce two "nodal" triads at the beam nodes in the deformed configuration, with vectors corresponding to the tangent to the beam axis at that node (in the deformed configuration), and the associated normals and binormals. The nodal triads in the current configuration are therefore the products $\mathbf{\Omega}_1(\mathbf{\Phi}_1)\mathbf{e}_{j0}$ and $\mathbf{\Omega}_2(\mathbf{\Phi}_2)\mathbf{e}_{j0}$, which give the six nodal vectors for the deformed configuration: $\hat{\mathbf{e}}^1_1$, $\hat{\mathbf{e}}^1_2$ and $\hat{\mathbf{e}}^1_3$ at node 1, and $\hat{\mathbf{e}}^2_1$, $\hat{\mathbf{e}}^2_2$ and $\hat{\mathbf{e}}^2_3$ at node 2. To find the component of the deformed vector $\hat{\mathbf{e}}_2$, the components of $\hat{\mathbf{e}}^1_2$ and $\hat{\mathbf{e}}^2_2$ that lie in the plane to which $\hat{\mathbf{e}}_3$ is a normal, are calculated. $\hat{\mathbf{e}}_2$ is then the normalised sum of the two resulting in-plane vectors. Given that $\hat{\mathbf{e}}_3$ is the normalised vector from the first to the second node represented, as before, as

$$\hat{\mathbf{e}}_3 = \frac{\mathbf{x}^2 - \mathbf{x}^1 + \mathbf{u}^2 - \mathbf{u}^1}{\|\mathbf{x}^2 - \mathbf{x}^1 + \mathbf{u}^2 - \mathbf{u}^1\|} \tag{4.5.58}$$

then

$$\hat{\mathbf{e}}_2 = \frac{(\mathbf{I} - \hat{\mathbf{e}}_3 \otimes \hat{\mathbf{e}}_3)(\boldsymbol{\Omega}_1 + \boldsymbol{\Omega}_2)\mathbf{e}_{20}}{\| \cdot \|} \tag{4.5.59}$$

to ensure that the triad is orthonormal, we do not use a similar projection for $\hat{\mathbf{e}}_1$, but rather define $\hat{\mathbf{e}}_1$ as the product $\hat{\mathbf{e}}_1 = \hat{\mathbf{e}}_2 \times \hat{\mathbf{e}}_3$.

4.5.2 Calculating the local displacements

As shown in the figure, a general deformation can be decomposed into a rigid body rototranslation, an axial stretch and a superimposed bending. In this example, the local displacement $\hat{\mathbf{u}}$ at node 2 is axial only. To obtain the local displacements, we note that rigid body motions do not give rise to internal forces. Therefore we choose the beam midpoint as the point of zero local diplacement and subtract the global displacement of this point from the nodal displacements. This eliminates displacements caused by rigid body translations. Secondly, we subtract the components of the displacement that are caused solely by the rigid body rotation around the midpoint. Finally, the resulting "local" displacements are transformed into the local system.

Defining the positions of the nodes relative to the beam midpoint (in the global system) as

$$\mathbf{x}^{\mathbf{1}}_{\mathbf{rel}} = \mathbf{x}^{\mathbf{1}} - \mathbf{x}_{\mathbf{mid}}$$
$$\mathbf{x}^{\mathbf{2}}_{\mathbf{rel}} = \mathbf{x}^{\mathbf{2}} - \mathbf{x}_{\mathbf{mid}}$$

the local displacements are

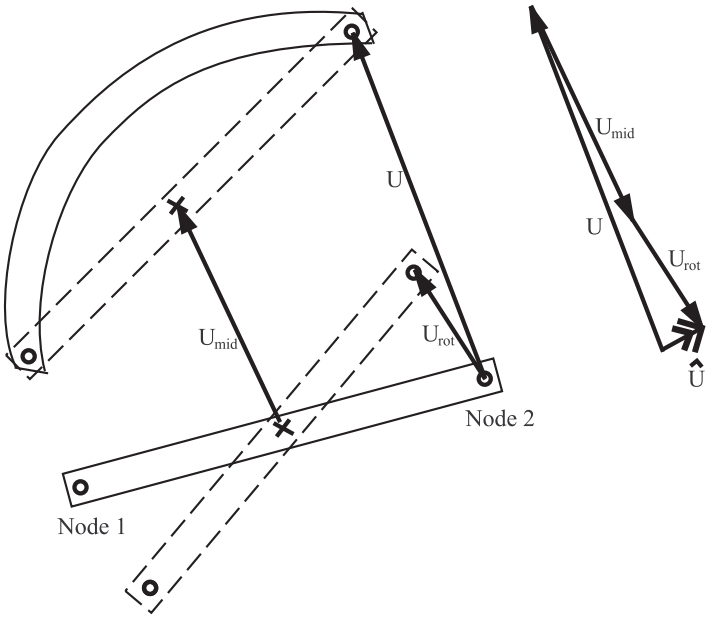

Figure 4.6: A deformation composed of a rigid body rototranslation, an axial stretch and a superimposed bending. In this example, the local displacement $\hat{\mathbf{u}}$ at node 2 is axial only

$$\hat{\mathbf{u}} = \mathbf{u} - \mathbf{u_{mid}} - \mathbf{u_{rot}}$$

This is shown schematically in Fig. 4.5.2.

The local displacement vector $\mathbf{u}'$ expressed in the local system is therefore:

$$\hat{\mathbf{u}}' = \mathbf{T}\hat{\mathbf{u}} = \mathbf{T}(\mathbf{u} - \mathbf{u_{mid}} - \mathbf{u_{rot}}) \tag{4.5.60}$$

where

$$\mathbf{u}_{mid} = 0.5 \begin{pmatrix} \mathbf{u}_1 + \mathbf{u}_2 \\ 0 \\ 0 \\ \mathbf{u}_1 + \mathbf{u}_2 \\ 0 \\ 0 \end{pmatrix} = 0.5 \begin{pmatrix} \mathbf{I_3} & 0 & 0 & \mathbf{I_3} & 0 & 0 \\ 0 & 0 & 0 & 0 & 0 & 0 \\ 0 & 0 & 0 & 0 & 0 & 0 \\ \mathbf{I_3} & 0 & 0 & \mathbf{I_3} & 0 & 0 \\ 0 & 0 & 0 & 0 & 0 & 0 \\ 0 & 0 & 0 & 0 & 0 & 0 \end{pmatrix} \begin{pmatrix} \mathbf{u_1} \\ \mathbf{\Phi_1} \\ \mathbf{w_1} \\ \mathbf{u_2} \\ \mathbf{\Phi_2} \\ \mathbf{w_2} \end{pmatrix} = 0.5\mathbf{I_0} \begin{pmatrix} \mathbf{u_1} \\ \mathbf{\Phi_1} \\ \mathbf{w_1} \\ \mathbf{u_2} \\ \mathbf{\Phi_2} \\ \mathbf{w_2} \end{pmatrix} \tag{4.5.61}$$

and

$$\begin{cases} (\mathbf{u_{rot}})_{1-3} = \mathbf{\Omega}_r \mathbf{x}^1_{rel} - \mathbf{x}^1_{rel} = (\mathbf{\Omega}_r - \mathbf{I})\mathbf{x}^1_{rel} \\ (\mathbf{u_{rot}})_{4-6} = \mathbf{\Phi}_r(\mathbf{\Omega}_r) \\ (\mathbf{u_{rot}})_{9-11} = \mathbf{\Omega}_r \mathbf{x}^2_{rel} - \mathbf{x}^2_{rel} = (\mathbf{\Omega}_r - \mathbf{I})\mathbf{x}^2_{rel} \\ (\mathbf{u_{rot}})_{12-14} = \mathbf{\Phi}_r(\mathbf{\Omega}_r) \end{cases}$$

or, in detail,

$$\begin{pmatrix} \hat{\mathbf{u}}'_1 \\ \hat{\mathbf{\Phi}}'_1 \\ \hat{\mathbf{w}}'_1 \\ \hat{\mathbf{u}}'_2 \\ \hat{\mathbf{\Phi}}'_2 \\ \hat{\mathbf{w}}'_2 \end{pmatrix} = \begin{pmatrix} \mathbf{T}^* & 0 & 0 & 0 & 0 & 0 \\ 0 & \mathbf{T}^* & 0 & 0 & 0 & 0 \\ 0 & 0 & \mathbf{I_2} & 0 & 0 & 0 \\ 0 & 0 & 0 & \mathbf{T}^* & 0 & 0 \\ 0 & 0 & 0 & 0 & \mathbf{T}^* & 0 \\ 0 & 0 & 0 & 0 & 0 & \mathbf{I_2} \end{pmatrix} \left[\begin{pmatrix} \mathbf{u_1} \\ \mathbf{\Phi}_1 \\ \mathbf{w_1} \\ \mathbf{u_2} \\ \mathbf{\Phi_2} \\ \mathbf{w_2} \end{pmatrix} - 0.5\mathbf{I_0} \begin{pmatrix} \mathbf{u_1} \\ \mathbf{\Phi_1} \\ \mathbf{w_1} \\ \mathbf{u_2} \\ \mathbf{\Phi_2} \\ \mathbf{w_2} \end{pmatrix} - \begin{pmatrix} (\mathbf{\Omega}_r - \mathbf{I})\mathbf{x}_{rel} \\ \mathbf{\Phi}_r(\mathbf{\Omega}_r) \\ \mathbf{0} \\ (\mathbf{\Omega}_r - \mathbf{I})\mathbf{x}_{rel} \\ \mathbf{\Phi}_r(\mathbf{\Omega}_r) \\ \mathbf{0} \end{pmatrix} \right] \tag{4.5.62}$$

4.5.3 Formulation

From the definition of local displacements, we next develop the equations of equilibrium, resulting in the global external force vector $\mathbf{F}_{ext}$ and global tangent stiffness

matrix $\mathbf{K}$, as required for the finite element solution procedure.

Using Equation (4.5.60) and taking the variation of $\hat{\mathbf{u}}'$:

$$\begin{aligned}\delta\hat{\mathbf{u}}' = \delta(\mathbf{T}\hat{\mathbf{u}}) = \mathbf{T}\delta\hat{\mathbf{u}} + \delta\mathbf{T}\ \hat{\mathbf{u}} = \mathbf{T}\mathbf{A}\delta\mathbf{u} + \mathbf{H}\hat{\mathbf{u}}\ \delta\mathbf{u} = \\ = (\mathbf{T}\mathbf{A} + \mathbf{H}\hat{\mathbf{u}})\delta\mathbf{u} = \boldsymbol{\Theta}\ \delta\mathbf{u}\end{aligned} \tag{4.5.63}$$

where the third-order tensor $\mathbf{H}$ is such that $\delta\mathbf{T} = \mathbf{H}\ \delta\mathbf{u}$, and the second order tensor $\mathbf{A}$ is such that $\delta\hat{\mathbf{u}} = \mathbf{A}\ \delta\mathbf{u}$.

The weak form of the equation of equilibrium is

$$\delta W_{int} - \delta W_{int} = 0$$

The internal virtual internal work δW_{int} is found by defining a convenient strain measure defined in terms of the local displacements in the local system $\hat{\boldsymbol{\epsilon}} = \hat{\boldsymbol{\epsilon}}(\hat{\mathbf{u}}')$:

$$\delta W_{int} = \int_0^l \hat{\boldsymbol{\sigma}}' \cdot \delta\hat{\boldsymbol{\epsilon}}'(\hat{\mathbf{u}}')\ dl$$

noting that all quantites in the integrand are both "local" and "in the local coordinate system". The small strain formulation implies local geometrical linearity, hence

$$\begin{aligned}\delta W_{int} = \int_0^l \hat{\boldsymbol{\sigma}}' \cdot \delta(\hat{\mathbf{B}}\hat{\mathbf{u}}')\ dl = \int_0^l \hat{\boldsymbol{\sigma}}' \cdot \hat{\mathbf{B}}\ \delta\hat{\mathbf{u}}'\ dl = \int_0^l (\hat{\mathbf{B}}^T\hat{\boldsymbol{\sigma}}') \cdot \delta\hat{\mathbf{u}}'\ dl \\ = \int_0^l (\hat{\mathbf{B}}^T\hat{\boldsymbol{\sigma}}')\ \ dl \cdot \delta\hat{\mathbf{u}}'\end{aligned}$$

where $\mathbf{B}$ is a mapping represented by a 6x16 matrix containing terms linear (for bending and radial strains) and independent (axial and torsional strains) of the distance along the beam. Using the following definition of local forces,

$$\hat{\mathbf{F}}'_{int} = \int_0^l (\hat{\mathbf{B}}^T \hat{\boldsymbol{\sigma}}')dl$$

then the internal work is:

$$\delta W_{int} = \hat{\mathbf{F}}'_{int} \cdot \delta\hat{\mathbf{u}}' = \mathbf{F}_{int} \cdot \delta\mathbf{u} \tag{4.5.64}$$

Virtual external work is given by

$$\delta W_{ext} = \hat{\mathbf{F}}'_{ext} \cdot \delta\hat{\mathbf{u}}' = \mathbf{F}_{ext} \cdot \delta\mathbf{u} \tag{4.5.65}$$

Using Equation (4.5.63), this becomes:

$$\begin{aligned} \delta W_{ext} &= \hat{\mathbf{F}}'_{ext} \cdot \boldsymbol{\Theta}\ \delta\mathbf{u} \\ &= \boldsymbol{\Theta}^T \hat{\mathbf{F}}'_{ext} \cdot \delta\mathbf{u} \end{aligned}$$

where the full expression for $\boldsymbol{\Theta}$ is reported in Appendix B. Thus, the global external and internal force vectors are:

$$\boxed{\mathbf{F}_{ext} = \boldsymbol{\Theta}^T \hat{\mathbf{F}}'_{ext} \qquad \mathbf{F}_{int} = \boldsymbol{\Theta}^T \hat{\mathbf{F}}'_{int}} \tag{4.5.66}$$

These equations show how the global internal and external forces required for the global FE solution procedure can be calculated from the local forces. The tangent stiffness matrix is found by taking the variation of the internal force vector:

$$\begin{aligned}\delta\mathbf{F}_{int} &= \delta\boldsymbol{\Theta}^T\hat{\mathbf{F}}'_{int} + \boldsymbol{\Theta}^T\delta\hat{\mathbf{F}}'_{int} \\ &= \delta[(\mathbf{TA} + \mathbf{H}\hat{\mathbf{u}})^T]\hat{\mathbf{F}}'_{int} + \boldsymbol{\Theta}^T\hat{\mathbf{K}}\delta\hat{\mathbf{u}}' \\ &= [\delta\mathbf{TA} + \mathbf{T}\delta\mathbf{A} + \mathbf{H}\delta\hat{\mathbf{u}} + \delta\mathbf{H}\hat{\mathbf{u}}]\hat{\mathbf{F}}'_{int} + \boldsymbol{\Theta}^T\hat{\mathbf{K}}\boldsymbol{\Theta}\delta\mathbf{u} \qquad (4.5.67)\end{aligned}$$

Evaluation this requires the higher order tensors $\mathbf{T}$, $\mathbf{A}$ and $\mathbf{H}$ to be found, full expressions for which are reported in Appendix B.

4.5.4 Comments

This derivation is similar in many respects to that presented by Crisfield (1997) and described in Section 2.4.3, though the developed form of the equations are different. One difference is that the deformed element triad in this development is derived from the mean of projection of the deformed nodal triads, rather than a curvilinear interpolation. This is in fact suggested by Crisfield as a permissible simplification for low curvatures (Crisfield, 1997, p. 225).

Secondly, this derivation takes local displacements to be measured from the midpoint of the line connecting the deformed positions of the two nodes.

4.6 Results from large-scale modelling

The capabilities of the model to perform practical large-scale analysis were tested by simulating a flexible pipe used as a riser to transport fluids between the seabed and a floating vessel. Realistic dimensions and displacements are used, and the riser is subjected to typical loadings and boundary conditions. Parameters used for the model were taken from the work of Bahtui (2008), which were obtained from calibration with FE model. The purpose of this test is to demonstrate the capability of the new element to be used in an analysis with large displacements and rotations and to show the effects of nonlinearities in the model formulation.

The analysis presented in this Section is two-dimensional, using two-dimensional modified beam elements (using the two-dimensional corotational formulation de-

D_{11}	2.5 x 10^8 N	D_{13}	1.28 x 10^8 N
D_{14}	-5.88 x 10^6 Nm^{-1}	D_{22}	6.08 x 10^5 Nm^2
D_{33}	4.38 x 10^9 Nm^{-2}	D_{34}	-1.36 x 10^8 Nm^{-1}
D_{44}	1.52 x 10^7N	H_{11}	7.3 x 10^7 N
H_{22}	2.5 x 10^5 Nm^2	a	0
b	1.2 x 10^{-4}	c	2.3 x 10^{-2} m^{-1}
Inner diameter	96 mm		
Outer diameter	116 mm		
Pipe weight (inc. buoyancy)	490 N/m		

Table 4.3: Large-scale model parameters

scribed by Urthaler and Reddy (2005) and a version of the constitutive model in which out-of-plane curvature and pipe torsion are ignored). This was done because a similar simulation carried out with three-dimensional elements failed to converge when used in the analysis described below. This is discussed in Section 4.6.2.

4.6.1 Quasi-static riser analysis

A simple test case was simulated, consisting of a riser in catenary configuration subject to imposed periodic vertical and lateral displacement at the top node, representing wave action on the vessel. Seabed interaction is handled by preventing vertical motion of nodes on the seabed. A constant 30 MPa internal pressure was considered. For the external pressure an average constant value of 0.75 MPa was considered. The analysis chosen is static (inertia-free). 12 elements were used to model the riser. Parameters used for the beam elements are given in Table 4.3.

The initial configuration of the riser and imposed displacement loading is shown in Figures 4.7 and 4.8. The analysis procedure comprised of a pressurisation step followed by a weight application step. This was followed by a full cycle of combined lateral and vertical imposed displacement. As shown in Figure 4.6, the displacement of the top node starts at zero, increases in the positive horizontal direction during pressure loading and progresses in a full anti-clockwise elliptical cycle in the cyclic loading step. Vertical and horizontal displacement are applied as sinusoidal functions, rather than ramp functions of step time to impose a more realistic displacement cycle on the top node. The amplitude of vertical and horizontal displacement

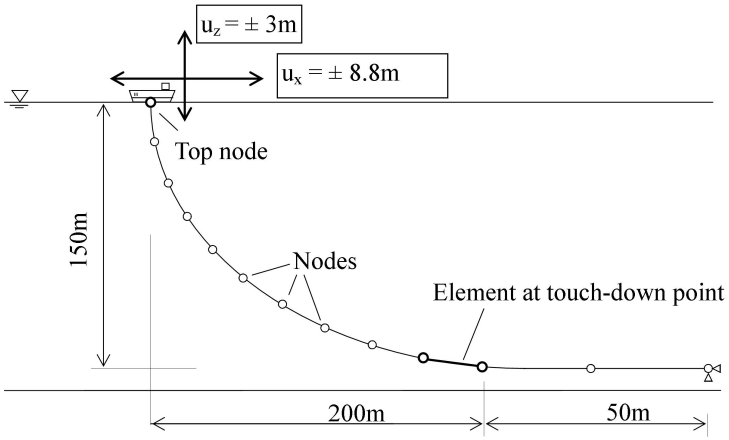

Figure 4.7: Catenary configuration

BOUNDARY CONDITIONS
Final node: Pinned
Seabed nodes: Vertical motion constrained
Top node: Pinned/imposed vertical and horizontal displacement

Table 4.4: Model constraints

cycles was 3m and 9m, respectively, with the horizontal displacement cycle leading by 8 degrees. Selected results are shown in Figures 4.9, 4.10 and 4.11. Figure 4.9 shows the bending-moment curvature relationship in the final element before the touchdown point. It can be seen that high values of bending curvature are achieved and the element's behaviour shows a clear hysteresis loop that appears to be stable. Figures 4.10 shows the variation of vertical reaction force with vertical displacement at the top node. Negative values of the reaction force indicate that the effect of the riser is to tend to pull the support down. The mean value of the reaction force is negative due to the riser's weight. Figure 4.11 shows the variation of horizontal reaction force with horizontal displacement at the top node. Positive values of the horizontal reaction force indicate that the effect of the riser is to attempt to pull the support right (with reference to Figure 4.6). It can be seen that both the vertical and horizontal reaction forces are at a minimum when the top node is at its most extreme positive vertical and horizontal displacement. This can be attributed to the reduction of tension in the riser due to the large horizontal displacement at this point as the riser is closer to its minimum energy configuration i.e. vertical.

LOAD STEP	LOAD
1	a) Application of external pressure (0.75 MPa). b) Application of internal pressure (30 MPa).
2	Application of weight
3	a) Application of imposed vertical displacement at function of step time: $u_z = 3.0\sin(2\pi t)$. b) Application of imposed horizontal displacement at function of step time: $u_z = 1.2\cos(2\pi t) + 8.8\sin(2\pi t)$ (see Figure 4.8). Horizontal displacement leads.

Table 4.5: Loading

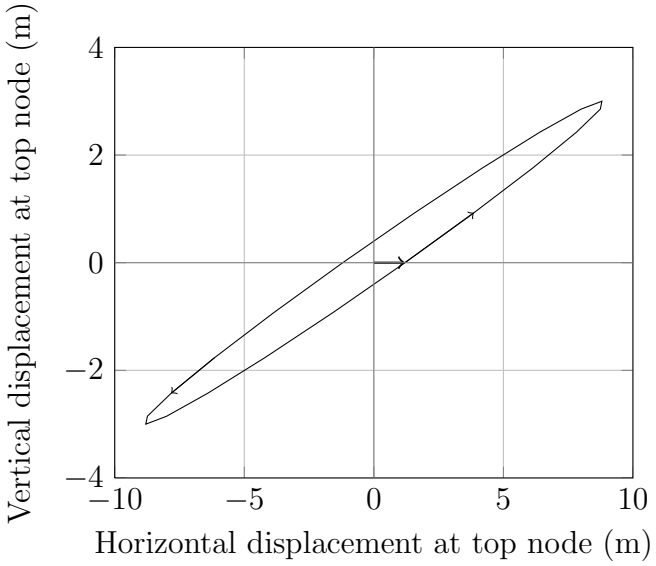

Figure 4.8: Applied displacement cycle

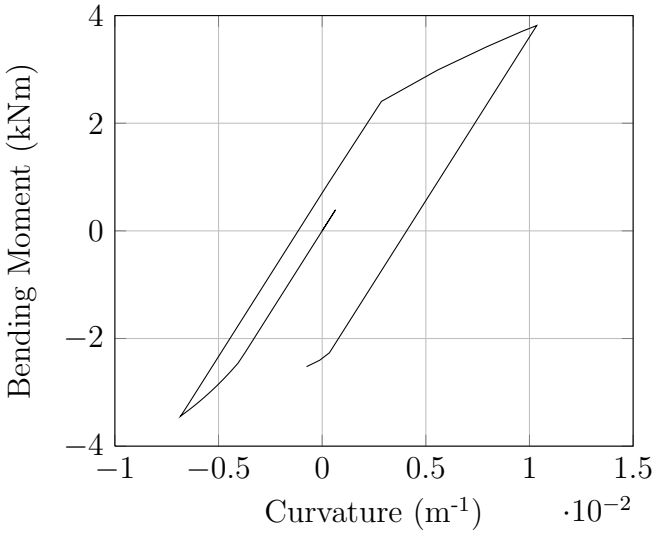

Figure 4.9: Variation of bending moment with curvature at last element before touchdown point over displacement cycle

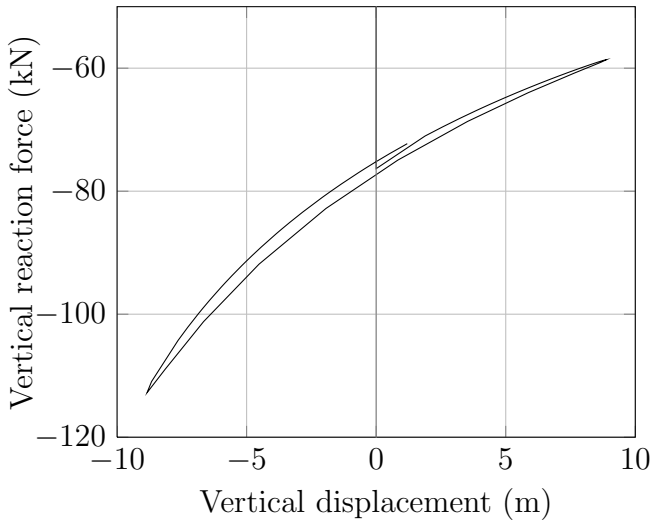

Figure 4.10: Force-displacement plot for vertical motion at top node

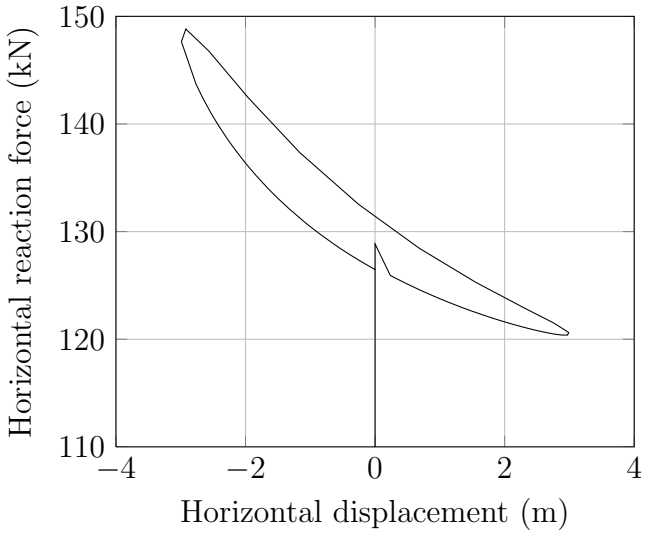

Figure 4.11: Force-displacement plot for horizontal motion at top node

4.6.2 Convergence problems

It was not possible to use three-dimensional beam elements in the constitutive model as convergence could not be achieved when used in the test case described above, although convergence was achieved if smaller values of displacement were imposed on the top node. The cause of this failure does not seem to be the constitutive algorithm, which was found to give good convergence properties when investigated using the load combinations used in the test case (axial force, bending and radial strain pressure) as shown in Figure 4.3. Instead, it seems likely, because convergence was achieved when small total displacements were applied to the element, that lack of convergence is due to an error in the "geometric" part of tangent matrix developed for the element in the corotational formulation. This could be addressed by review of the derivations in Section 4.5 and Appendix B as well as checking the coding in the Fortran implementation.

For this reason, the two-dimensional beam element was used instead. Convergence properties for this element are demonstrated in Section 4.4.1

Chapter 5

Detailed finite-element model

In this Chapter, the development of a general-purpose finite element model for prediction of component stresses and overall behavioural response for flexible pipes is presented. The general modelling approach is based on previous work by Bahtui (2008), which is summarised in Section 5.1, in which a detailed three-dimensional finite element model was created using continuum elements. For this project, a new model was created using shell finite elements. The new model and its implementation are described (Section 5.2), including details on contact modelling (Section 5.2.1), boundary conditions (Section 5.2.2) and simulation options (Section 5.2.3). Numerical results obtained using this model are then reported in Section 5.3. In this section, a sensitivity study is carried out on the contact modelling method (Section 5.3.1) and the effect of boundary conditions on bending simulations is demonstrated (Section 5.3.2). The results of a verification study for stresses under axisymmetric loading is presented (Section 5.3.3). Stress results for this study for the internal pressure load case are shown in Figure 5.1. Finally, plots describing the pipe response under various load combinations are given (Section 5.4). By providing the relations between the six generalised stress and strain measures employed for the large scale model described in Chapter 4, these results provide the information used in Chapter 7 to determine the parameters of the large-scale model in the context of the proposed sequential multi-scale analysis.

5.1 Previous work

The finite element model developed by Bahtui (2008) described in Section 2.4.2 showed that useful results on the mechanical response of flexible pipes can be obtained using finite-element-based modelling methods. The advantage of using such models is that the behaviour can be investigated without introducing unnecessary assumptions about the kinematics or deformation of internal components which may not be possible to justify with available test data. However, several aspects of the model implementation and results limited its utility as an analysis or verification tool. The use of an explicit time-stepping method meant that is it not guaranteed that equilibrium is satisfied in solutions. The model used 3D continuum elements throughout which are prone to display shear-locking effects.

Results presented for the model Bahtui (2008, Figs. 5.3, 5.4, 5.6, 5.11) showed that the contact pressure between layers was uneven and concentrated in bands spaced regularly along the pipe axis. Consequently, the stress field in components was not uniform under axisymmetric loading, which is not physically realistic.

Futhermore, a form of boundary conditions were used that forced all nodes on the end section to remain in the same plane during deformation. This leads to boundary effects such as increased local stresses at the model end sections due to the increased local curvatures (aggravated by any element locking effects). This is not an accurate representation of what happens in practice, because at arbitrarily located flexible pipe sections far from end connections, the tensile armour wires are free to slide relative to underlying components. Also, as was discussed in Chapter 3, uniform boundary conditions are generally ineffective in multiscale homogenisation while periodic boundary conditions are recommended. However, it should be noted that use of uniform displacement boundary condition can be more effective than periodic boundary conditions in the vicinity of the real boundaries of the large-scale model where (macro-) displacements are prescribed and, as a result, stress concentrations can occur. Furthermore, the use of periodic boundary conditions in three-dimensional structural computational homogenisation has been shown to require considerably more solution time than solving the same problem with uniform displacement boundary conditions, a result which was found to be independent of

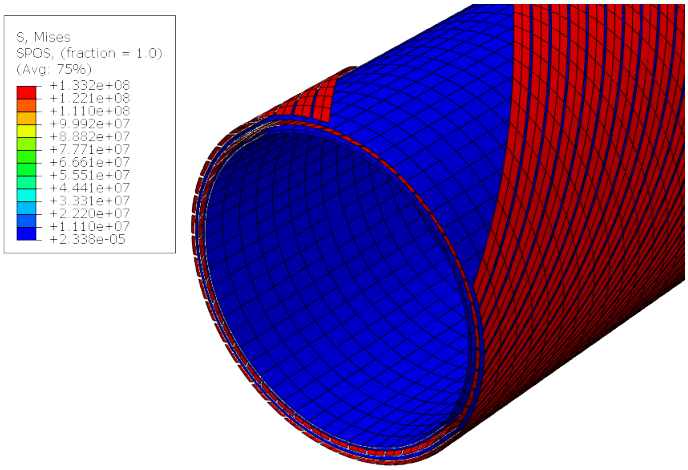

Figure 5.1: Von Mises stress resulting from internal pressure load case

the solution method used (Fritzen and Böhlke, 2010).

5.2 Detailed model

The detailed model was created using the finite element package ABAQUS 6.9. All physically distinct layers of the pipe and the armour wires were considered as separate entities. Unlike previous work (Alfano et al., 2009; Bahtui, 2008) where linear 3D solid elements had been used, in this work all components were modelled with linear shell elements with surface-to-surface frictional contact between all components. The pressure armour and carcass layers of a flexible pipe are self-interlocking strips with complex sections; for this reason, these layers were modelled as equivalent, orthotropic homogenous cylinders with appropriate constants. Details of the material, dimensions and arrangement of constituent layers are given in Table 5.1. Material properties are reported in Table 5.2. Figure 5.2 shows part of the finite-element model in which the elements of the outer layer and some of the outer tensile armour wires have been removed.

The length of the modelled pipe section is equal to one pitch length of the helical armour wires (0.868). As described in Chapter 3, in a homogenisation analysis, only one small scale model (RVE) is analysed to characterise the behaviour at many points in the large-scale model. When analysing periodic structures or media

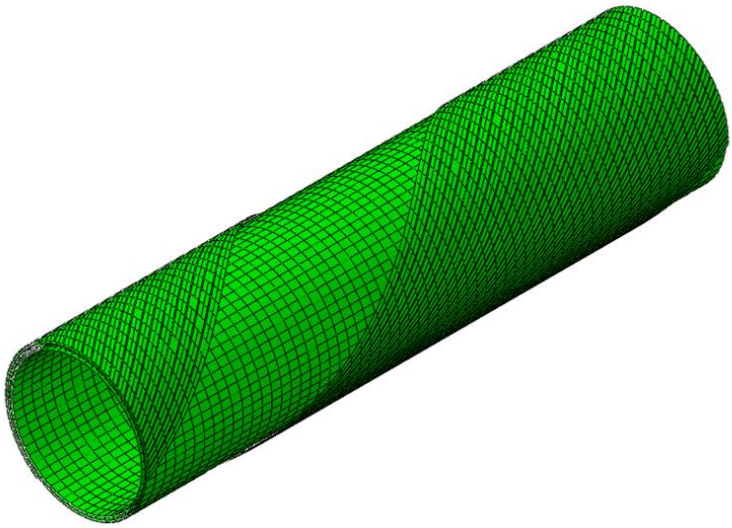

Figure 5.2: Detailed finite element model (outer layer and some wires removed)

with homogenisation methods, specifying an RVE corresponding to one periodically repeating cell of the real structure gives the most accurate results, as the RVE referred to by material points in the large-scale model corresponds exactly to the real structure at that point, if material points in the large-scale model are arranged in a periodic array with the appropriate spacing. This is the case in the multi-scale model proposed here. It is noted that, in real flexible pipes, the pitch length of armour wires in different layers is often designed to be different in order to minimize axial-torsional coupling behaviour. The use of equal pitch lengths for both layers is a simplification that greatly reduces the length of the repeating section to be modelled in the proposed multi-scale analysis.

Frictional contact interactions were implemented between all radially adjacent components, using a surface-to-surface method. Lateral contact interactions between adjacent helical armour wires were not accounted for as they do not occur in usual situations, as noted by McIver (1995). As for the contact formulation, a "hard" pressure-overclosure relation was used, enforced by a penalty method. A constant Coulomb friction coefficient of 0.16 was used throughout. The model used a total of 32 000 nodes. A total of 508 000 equations were required to be solved in the model, including 314 000 equations introduced by the Lagrange multiplier

Layer	Inner radius (mm)	Thickness (mm)	Material model	Material
Carcass	95.9	1.4	3D Orthotropic	Equivalent Layer
Pressure sheath[(1)]	97.3	2	Isotropic	Polyethylene
Tensile armour[(2)]	99.3	4	Isotropic	Carbon Steel
Anti-wear layer	103.3	1.75	Isotropic	Polylethylene
Tensile armour[(3)]	105.05	4	Isotropic	Carbon Steel
External sheath	109.05	7.15	Isotropic	Polyethylene
[(1)]For deep water applications, a pressure armour layer, consisting of a self-interlocking metal strip is typically also included. This was omitted from the model for ease of comparison. [(2)]Inner armour wires: number=46, wire width=12.5mm. [(3)]Outer armour wires: number=48, wire width=12.2mm.				

Table 5.1: Dimensions and materials of components of detailed flexible pipe model. The modelled length of pipe was 868mm.

Material	Stiffness (GPa)	Poisson's Ratio
Equivalent layer	E_1=150 (hoop)	ν_{12}=0.3
	E_2=12.4 (axial)	ν_{13}=0.0
	E_3=10	ν_{23}=0.0
	G_{12}=10	
	G_{13}=10	
	G_{23}=10	
Carbon Steel	E=210	ν=0.3
Polyethylene	E=0.35	ν=0.4

Table 5.2: Material properties

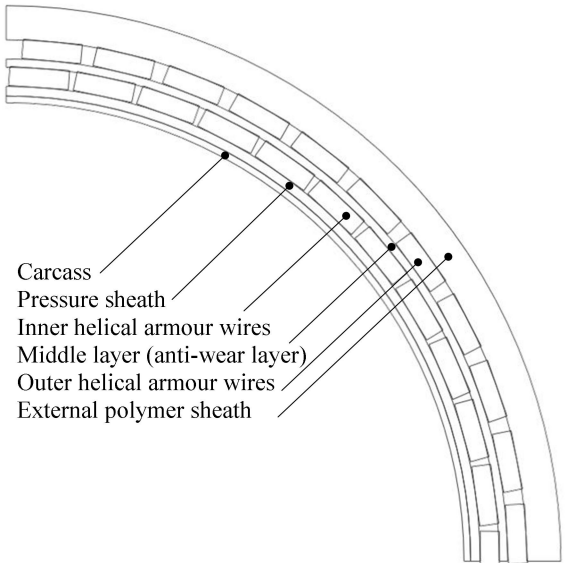

Figure 5.3: Detailed model cross-section

required to implement the contact constraints.

Unlike previous work (Alfano et al., 2009; Bahtui, 2008), in which an explicit dynamics solution scheme was used, the model was executed using an implicit static solver, ensuring that equilibrium was achieved after each load increment.

5.2.1 Modelling pipe radial behaviour

Modelling pipe components with standard shell-type finite elements assuming zero through-thickness strain in their formulation was found to result in the model displaying axial and radial stiffness values that deviated significantly from those predicted by the reference analytical model in cases with negligible inter-layer slip. Furthermore, these stiffness values were also sensitive to the initial contact overclosure/separation distance. This can be explained by the fact that absence of an accurate representation of the through-thickness shell stiffness and inter-layer interface stiffness leads to inaccuracies in predicted displacements, not only in the radial but also in the axial direction due to the static indeterminacy of the problem in the radial direction. The problem is statically indeterminate in the radial direction because knowledge of the internal and external pressure is not sufficient to determine the displacements and stresses in the pipe components because components

are unbonded and the inequalities that describe the normal contact interactions between components do not give explicit force-displacement relations, requiring iterative methods to solve. For both helical and cylindrical components, axial and radial behaviour is coupled, and thus the structure is statically indeterminate in the axial direction as well. Radial displacement determines the hoop stress in a cylindrical layer or axial stress in a helical wire that develops in response to loading, which are fundamental to how the structure carries the load.

This can be remedied by enforcing the no-penetration condition using a penalty method in which the penalty stiffness approximately accounts for the true radial stiffness of the layers. In this way, the penalty stiffness value compensates for the zero compliance of the shell in the out-of-thickness direction.

In fact, de Sousa et al. (2010) use a method to determine the contact stiffness k_C which, when implemented in a surface-to-surface contact formulation, results in the following expression:

$$k_C = \frac{k_1 k_2}{k_1 + k_2} = \frac{2E_1 E_2}{(E_1 h_2 + E_2 h_1)} \qquad [\mathrm{Nm}^{-3}] \tag{5.2.1}$$

where subscripts 1 and 2 stand for the two layers on either side of the contact interface, E_i is the Young's Modulus of the material in the ith layer, h_i is the thickness of the ith layer and k_i is defined as

$$k_i = \frac{P}{\Delta u_n} = \frac{2E_i}{h_i} \qquad [\mathrm{Nm}^{-3}] \tag{5.2.2}$$

where P is the inter-layer pressure and Δu_n is the normal (i.e. radial) interpenetration. In the reference, de Sousa et al. (2010), do not provide details of how their expression is derived, but their procedure is in fact consistent with the previously mentioned idea of transferring the radial compliance of pipe components to the enforcement of the contact conditions if E_i is considered as an approximate value for the material stiffness E_n in the normal direction. However, selection of the appropriate normal stiffness is dependent on an assessment of the kinematic restrictions

present at the material surfaces in contact (Figure 5.4). The limiting cases of no constraint and full constraint on the strain in the tangential direction are considered below, for a linear elastic isotropic material.

Considering first the case where the material at the interface surface is free to expand in the two tangential directions, using the reference system of Figure 5.4, the generalised plane stress condition $\sigma_{xx} = \sigma_{yy} = \sigma_{xy} = 0$ holds, and the normal stiffness can be expressed as $E_n = \sigma_{zz}/\varepsilon_{zz} = E$, where E is the Young's Modulus of the material. In the second case, where lateral expansion is restricted near the point of contact, the generalised plane strain condition $\varepsilon_{xx} = \varepsilon_{yy} = \varepsilon_{xy} = 0$ holds, and it is easy to verify that

$$E_n = \frac{\sigma_{zz}}{\varepsilon_{zz}} = \frac{E(1-\nu)}{(1+\nu)(1-2\nu)} \tag{5.2.3}$$

The difference between the normal stiffness in the two limiting conditions is a function of the Poisson's ratio only. Using the Poisson's ratio for steel, 0.3, the appropriate normal stiffness for the generalised plane stress condition is 74.3% the value required to model the normal stiffness in the generalised plane strain condition; in the case of the polymer layers with ratio 0.4, this proportion drops to 46.7%. As each interface involves the interaction between a stiff material and a compliant material, the Possion's ratio of the more compliant layer has a greater influence on the normal stiffness. The normal stiffness parameter strongly influences the accuracy of pressure and axial loading simulations because of the significant static indeterminancy in the radial direction.

It is suggested that an intermediate value between the two extreme cases is chosen for modelling. Numerical results showing the sensitivity of the model to this contact stiffness are reported in Section 5.3.1.

5.2.2 Boundary conditions

In order for the detailed finite element model to be used as part of a consistent multi-scale procedure, simulations must be carried out in accordance with the theo-

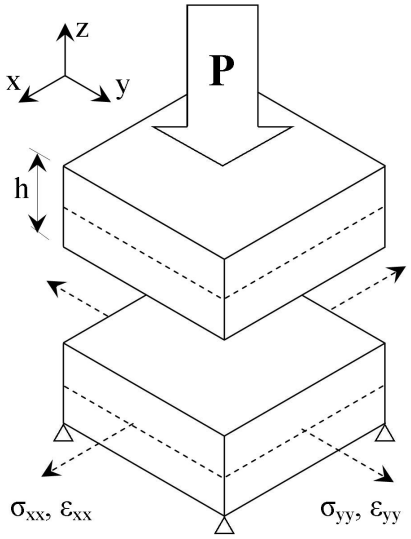

Figure 5.4: Transverse stress/strain conditions at contact region

retical framework of computational homogenisation. In Section 3.1, the formulation of the conventional computational homogenisation problem was presented, and it was shown that, when macroscopic equivalent stresses and strains were defined as the volumetric averages of the corresponding measures, Equation (3.1.7) describes a condition that the boundary displacements on the RVE must satisfy. In order that the stress and strain representations in the large-scale flexible pipe model are unbiased averages of small-scale stresses and strains, this restriction will be respected when carrying out simulations on the detailed finite element model, despite the use of different measures at the different scales. The restriction on boundary conditions represented by this condition does not fully specify the boundary conditions to be applied when solving the microscopic problem; standard choices include uniform displacement (zero fluctuation field on boundaries), periodic and uniform traction.

It has been shown by several authors (Hazanov and Huet (1994), Perić et al. (2011)) that use of uniform displacement boundary conditions will result in "stiffer" local material response than use of periodic boundary conditions, which will in turn give a stiffer response than uniform traction boundary conditions.

In this work, both uniform displacement and periodic boundary conditions have been implemented for the part of the displacement field directly associated with the first four components of the generalised strain vector in Equation (3.1.7). Traction

boundary conditions were applied for the pressure related terms.

Regarding uniform displacement boundary conditions, flexible pipe simulations are often carried out using the restriction that all points on a pipe end section must remain in plane throughout the analysis (referred to hereafter as fixed-in-plane boundary conditions, or FIP in abbreviation) (Alfano et al., 2009; Bahtui, 2008; de Sousa et al., 2010). This condition is straightforward to implement, but is inherently limited in its accuracy, as relative motions between adjacent components at the boundary sections is set to zero. This leads to a locally overstiff response and high stress concentrations towards the pipe ends. Furthermore, as the nonlinear response of the pipe occurs due to the mechanism of interlaminar slip, restricting slip at the boundary will not correctly model the relative motion unless a long section of pipe is modelled, which is computationally expensive.

To apply periodic boundary conditions, it is required that each of the generalised strains computed in the macroscopic model can be imposed on the detailed model in an average sense, without causing nonphysical bias in the stress and strain fields due to location of constraints, while maintaining periodicity of displacement between the two end sections in a sense appropriate to the applied action. To achieve this, the following set of linear constraint equations was generated relating the degrees of freedom of each pair of nodes on the end planes having the same position on the cross-section. The equations link the nodes to a dummy node with degrees of freedom $(U^x_{n,d}, U^y_{n,d}, U^z_{n,d}, \Phi^x_{n,d}, \Phi^y_{n,d}, \Phi^z_{n,d})$, see Figure 5.5 and Equation (5.2.4):

$$\begin{cases} U^x_{n,left} - U^x_{n,right} &= U^x_{n,d} \\ U^y_{n,left} - U^y_{n,right} &= U^y_{n,d} \\ U^z_{n,left} - U^z_{n,right} &= U^z_{n,d} \\ \Phi^x_{n,left} - \Phi^x_{n,right} &= \Phi^x_{n,d} \\ \Phi^y_{n,left} - \Phi^y_{n,right} &= \Phi^y_{n,d} \\ \Phi^z_{n,left} - \Phi^z_{n,right} &= \Phi^z_{n,d} \end{cases} \quad \forall \text{ end nodes n} \tag{5.2.4}$$

One dummy node per each pair of end nodes is placed on a dummy cross-section separated from the physical model. The degrees of freedom of the dummy nodes are

then rigidly constrained to those of a control node C located at their centre using the following rigid body constraint (Equation 5.2.5)

$$\begin{cases} \mathbf{U}_{n,d} &= \mathbf{U}_c + \mathbf{R}(\mathbf{\Phi}_c)(\mathbf{x}_{n,d} - \mathbf{x}_c) \\ \mathbf{\Phi}_{n,d} &= \mathbf{\Phi}_c \end{cases} \quad \forall \text{ dummy nodes n} \tag{5.2.5}$$

where $\mathbf{R}(\mathbf{\Phi}_C)$ is the rotation matrix corresponding to the control node rotation pseudovector $\mathbf{\Phi}_C$, and $\mathbf{x}_{n,d}$ and $\mathbf{x}_C$ denote the position vectors of the dummy and control nodes, respectively. This constraint forces the dummy nodes to remain in the dummy plane and follow the displacement and rotations of the control node. Imposing displacements and rotations on the control node allows the generalised strains of the macroscopic model to be imposed, using the relations

$$\begin{array}{lll} u_C^x = 0 & u_C^y = 0 & u_C^z = \varepsilon_z l \\ \Phi_C^x = \chi_x l & \Phi_C^y = \chi_y l & \Phi_C^z = \chi_z l \end{array}$$

As discussed in Section 3.1.2 of Chapter 3, macroscopic generalised stresses can be recovered from the model from the reaction forces and moment at the control node. These equations are incorporated into the solution procedure by degree-of-freedom elimination in the global stiffness matrix.

5.2.3 Viscous stabilisation of relative rigid body modes

A further computational problem is that the model is comprised of multiple separate parts, held together only by friction, which can only develop once contact is established. This leads to the presence of rigid body modes in the solution. In practical simulations, external and/or internal pressure will often be applied, which presses the layers into contact. However, convergence is greatly assisted by the inclusion of viscous damping in the contact interactions, applied to both normal and tangential motion at the surfaces. The damping value was generated automatically be the program, then scaled down by a factor of 10. it was subsequently shown that varying this scaling factor does not influence the results.

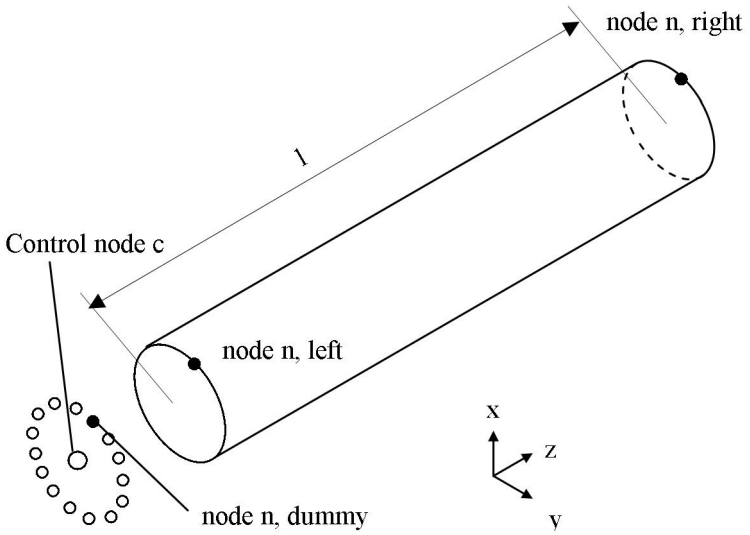

Figure 5.5: Periodic boundary conditions

5.2.4 Computation time

Using contact methods within a nonlinear finite element procedure is often computationally expensive, because contact forces and their distribution are dependent on the deformed configuration of the interacting surfaces and *vice versa*, which requires that several iterations are required to achieve convergence at the contact surface. In this process, contact conditions (whether the surfaces are in contact or not, whether the surfaces are sliding tangentially) change in discrete jumps, leading to step changes in the model's global stiffness matrix. This causes difficulties for gradient-based solvers (such as the Newton-Raphson method) that are used to solve the system of equations of the model. In this model, this is particularly onerous because of the multiple layers of double-sided contact present.

For this model, all simulations were carried out in parallel on a computer cluster. each simulation used two dual-core 1.8 GHz processors (4 processors in total) using 8MB of RAM.

Some representative run times are presented in Table 5.2.4. It is evident that the use of periodic boundary conditions in bending simulations greatly increases the simulation time required.

A higher degree of parallelisation could have be used to reduce run-times; how-

Loading	Amplitude	Boundary Condition	Run-time
Axial extension	0.1%	f.i.p.	1h 30m
Axial extension	0.1%	Periodic	1 h
Pressurised bending, monotonic	0.23 m^{-1}	f.i.p.	6.2h
Pressurised bending, half-cycle	$\pm$0.23 m^{-1}	Periodic	164.6h
Pressurised bending ,full-cycle	$\pm$0.23 m^{-1}	Periodic	174.2h

Table 5.3: Representative run-times

ever, achieving this was not a priority of the investigation.

5.3 Numerical results and verification

5.3.1 Effect of interface stiffness for axisymmetric loading

To investigate the influence of the interface stiffness, models were tested under two conditions: internal pressure P of 3 MPa and imposed axial strain ε_z of 0.1%, under periodic boundary conditions. The resulting axial reaction force N and mean radial displacement u_r were recorded for each condition, enabling the calculation of four stiffness coefficients from ratios of loading and response measures. Models were run using a "hard" pressure-overclosure relationship enforced by a penalty method with (1) the default penalty stiffness chosen by the program and (2) using penalty stiffness calculated for each pair of interacting surfaces using Equation (5.2.1), adopting for E_n either the value E or that given by Equation (5.2.3) to investigate the effects of using different kinematic assumptions to calculate the normal stiffness, as discussed in Section 5.2.1.

Although validation of the model via comparison of its results with those of experimental tests would be most reliable, detailed experimental results in terms of global stiffness and local stresses are not generally available in the published literature. Therefore, in order to appreciate the significance of using appropriate values for the interface stiffness coefficients used in the contact formulation, comparisons were made with the linear analytical model presented by Bahtui (2008). The essential aspects of this model that are relevant for such a comparison are that inter-layer slippage or separation are not included, and that the effect of the Poisson's ratio

coupling radial and axial deformation is accounted for in the polymer layers, where it is most influential on radial behaviour. As the analytical model used fixed-in-plane boundary conditions, the FE models were analysed under fixed-in-plane conditions too.

Differences in results between the finite-element model and the analytical model are expected, but for relatively small values of applied axial strain or pressure reasonably close agreement is expected. Denoting by c_{FE} and c_{an} the generic stiffness coefficients determined with the FE model and Bahtui's analytical formulation, respectively, the differences Δc reported in percentages in the tables below are calculated as $\Delta c = 100\,(c_{FE} - c_{an})/c_{FE}$.

In Table 5.4 the differences between the results of the FE and the analytical model in terms of stiffness are reported, showing that using the default penalty stiffness for the contact formulation leads to highly inaccurate results. This fact supports the arguments presented in Section 5.2.1 that the static indeterminacy of the problem in the radial direction makes the correct representation of the element and inter-layer radial stiffness values crucial to the accuracy of the results and that, consequently, the lack of though-thickness stiffness in the shell elements must be compensated by the stiffness used in the contact formulation.

Tables 5.5 and 5.6 confirm that by using values of the interface stiffness determined vie Equations (5.2.1) and (5.2.2), and assuming for E_n the value given by Equation (5.2.3) (i.e. the transversally constrained case), the numerical results are much closer to the analytical ones, as expected. All stiffness coefficients except those relating axial response to pressure are smaller than those predicted by the analytical model, with a maximum difference of 22%. This can be explained by the additional compliance in the FE model due to the small but non-negligible inter-layer slip.

Simulations were also run to investigate the influence of the assumption of lateral constraints when calculating the appropriate normal stiffness for interlaminar contact. To this end, each model was run using in one case the in-plane constraint assumption (IPC), i.e. determining E_n via Equation (5.2.3), and in another case the in-plane unconstrained assumption (IPU) leading to $E_n = E$. From the results shown in Tables 5.7 and 5.8 it can be seen that the constrained assumption leads to

Stiffness measure	Definition	Difference
Axial stiffness	N/ε_z	+843%
Radial response to axial	N/u_r	+1660%
Axial response to pressure	P/ε_z	+2657%
Radial stiffness	P/u_r	+2488%

Table 5.4: Differences in stiffness coefficients as compared with analytical model (described in Bahtui (2008)), without stiffness correction. All stiffness coefficients are evaluated in situations where the model ends are free to move axially.

Stiffness measure	Unit	$\varepsilon = 0.01\%$	$\varepsilon = 0.02\%$	$\varepsilon = 0.1\%$
Axial stiffness	MN	247.9	248.1	249.0
Radial response to axial	MNm^{-1}	-2341.9	-2353.6	-2384.2
		P = 0.3 MPa	P = 0.6 MPa	P =3 MPa
Axial response to pressure	MNm^{-2}	-5131.7	-5146.7	-5221.9
Radial stiffness	GNm^{-3}	21.4	21.5	21.7

Table 5.5: Stiffness values, with stiffness correction, using the value of E_n from Equation (5.2.3).

stiffer behaviour, as expected, except for the axial response to pressure.

5.3.2 Effect of boundary conditions on bending behaviour

The effectiveness of the detailed shell model may be evaluated by considering end effects, stress and slip distributions. The models were tested under bending by applying internal pressure of 3 MPa and external pressure of 2.34 MPa, followed by an imposed curvature of 0.234 m^{-1}. When fixed-in-plane boundary conditions are used, the nodes on each end plane of the model were forced to rotate around the plane centre using rigid body constraints, ensuring that all end nodes remain

Stiffness measure	$\varepsilon = 0.01\%$	$\varepsilon = 0.02\%$	$\varepsilon = 0.1\%$
Axial stiffness	-22.0%	-21.9%	-21.5%
Radial response to axial	-18.8%	-18.2%	-16.7%
	P = 0.3 MPa	P = 0.6 MPa	P =3 MPa
Axial response to pressure	+0.2%	+0.5%	+2.0%
Radial stiffness	-7.7%	-7.3%	-6.3%

Table 5.6: Differences in stiffness coefficients as compared with analytical model (described in Bahtui (2008)), with stiffness correction, using the value of E_n from Equation (5.2.3).

Stiffness measure	Unit	Value (IPC)	Value (IPU)	Difference (IPC-IPU)/IPU
Axial stiffness	MN	249.0	240.9	+3.3%
Radial response to axial	MNm^{-1}	-2384.2	-2289	+4.0%
Axial response to pressure	MNm^{-2}	-5221.9	-5221.9	0.0%
Radial stiffness	GNm^{-3}	21.7	20.891	+3.7%

Table 5.7: Difference in stiffness coefficients using penalty stiffness values calculated using in-plane constrained (IPC) (Equation (5.2.3)) and in-plane unconstrained (IPU).

Stiffness measure	Difference (IPC)	Difference (IPU)
Axial stiffness	-21.5 %	-25.5%
Radial response to axial	-16.7%	-21.5%
Axial response to pressure	+2.0%	+2.0%
Radial stiffness	-6.3%	-10.5%

Table 5.8: Difference in stiffness coefficients compared to analytical model, IPC and IPU conditions compared

in plane throughout the bending. When periodic boundary conditions are used, a rotation is applied to the control node only, in accordance with Equations (5.2.5) and (5.2.4).

The following results show the differences between models using periodic and fixed-in-plane boundary conditions for otherwise identical 0.868m pipe models undergoing bending. Comparisons are made for the global bending moment-curvature relationship (Figures 5.6 and 5.7), the stress distributions (Figures 5.8-5.12) and the slip fields (Figures 5.13, 5.14). Comparisons are also made for the axial stresses occurring at specific points on one armour wire over a bending cycle (Figures 5.15 and 5.16). Axial stress in these plots are reported for the inner (Figure 5.15) and outer (Figure 5.15) surfaces of a wire. The circumferential location of the evaluation point was as the extrados of the bend, and the axial location was one quarter of the pipe length from the end section, removing the influence of end effects.

Figure 5.6 shows that use of both periodic and fixed-in-plane boundary conditions leads to almost bilinear behaviour in bending. In the initial part the response is effectively linear and characterised by negligible inter-layer slip. After the onset of slipping, the stiffness rapidly decreases, quickly reaching an asymptotic value. How-

ever, use of fixed-in-plane boundary conditions gave a much stiffer initial response. Increasing curvature beyond 0.03 m^{-1} causes a sharp reduction to the less stiff response. When periodic boundary conditions are used, this transition occurs later and is less marked. It is noted that at large curvatures, the values of the tangent bending stiffness of the two models are almost the same (the model with periodic boundary conditions is 6.5% less stiff). Figure 5.8 shows that lower and more uniform stresses are predicted for the carcass layer when periodic boundary conditions are used. Figures 5.9 and 5.11 show generally lower stresses in the helical wires developing when using periodic boundary conditions, for the same imposed curvature. Figures 5.10 and 5.12 show more uniform stress fields and less pronounced end effects in the middle and outer polymer layer when using periodic boundary conditions.

Evaluating axial slip fields shows that significant slip occurs between the carcass and pressure sheath if fixed-in-plane boundary conditions are used, but not if periodic boundary conditions are used (Figure 5.13), in which case the slip is uniformly zero. The influence of end-effects on slippage between the inner helical armour layer is apparent in Figure 5.14, with all significant slip concentrated in the central 50% of the model. This effect is reversed when periodic boundary conditions are used, showing increased slip at the pipe ends. It was noted that this was accompanied by variation in the pipe section ovalisation during bending[1] from 0.000577 at the midsection to 0.0378 at the end sections.

Summarising, the results show that use of periodic boundary conditions for testing a finite element-based flexible pipe model undergoing bending gives a more correct description of the relative movement of internal components, specifically more even slip distributions and significantly less pronounced end effects. This clearly suggests the use of such a model is more appropriate for an analysis of local stresses. Using periodic boundary conditions rather than fixed-in-plane boundary conditions improves results significantly.

The stress data from Figures 5.15 and 5.16 seem to indicates that stress on

[1]Defined as $(D_{max} - D_{min})/(D_{max} + D_{min})$, where D_{max} and D_{min} are the maximum and minimum pipe diameters (API, 1998).

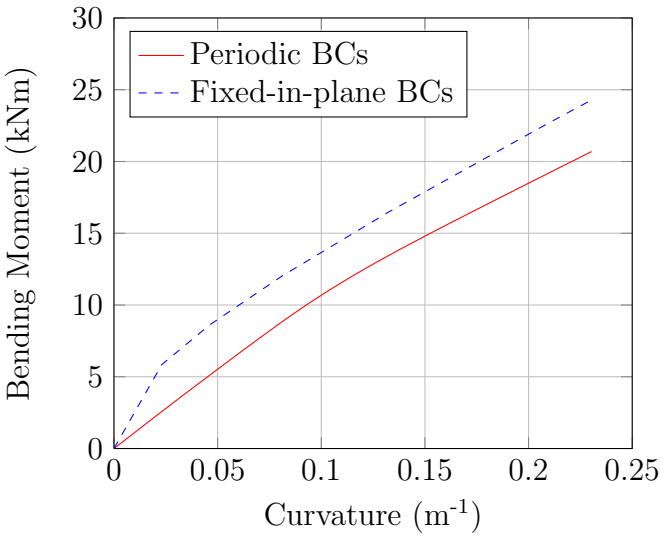

Figure 5.6: Bending moment-curvature relationship for two identical 0.868m models run with fixed-in-plane and periodic boundary conditions. Initial tangent calculated from first data point of each model.

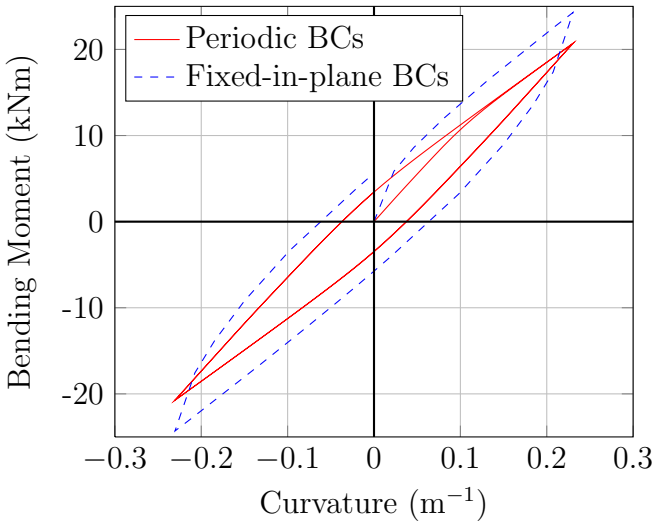

Figure 5.7: Bending hysteresis using a) Periodic boundary conditions and b) Fixed-in-plane boundary conditions

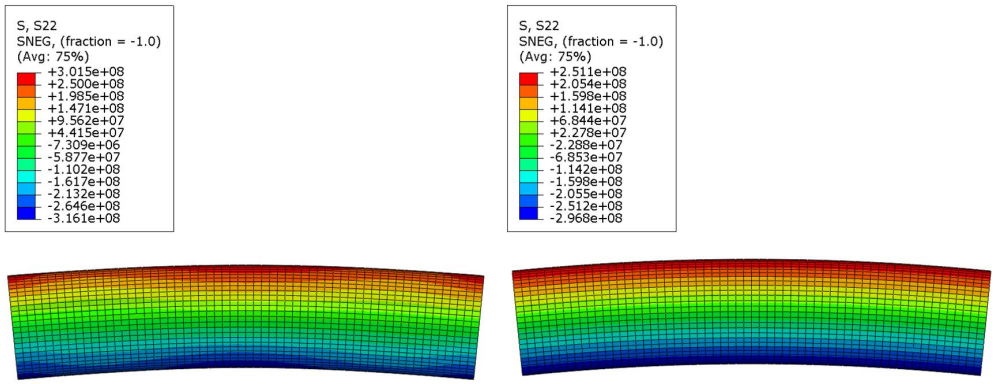

Figure 5.8: Axial stress on carcass layer using (a) Fixed-in-plane BCs, (b) Periodic BCs

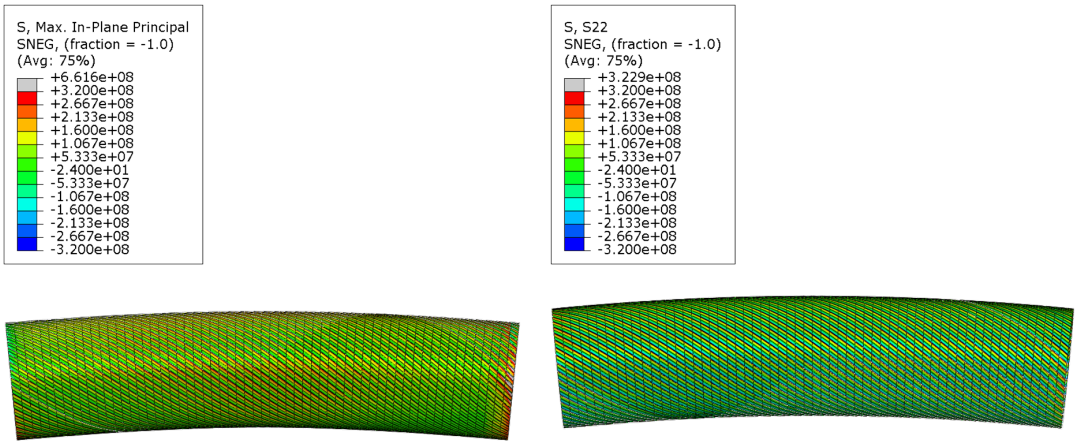

Figure 5.9: Maximum principal stress on inner helical armour wires using (a) Fixed-in-plane BCs, (b) Periodic BCs

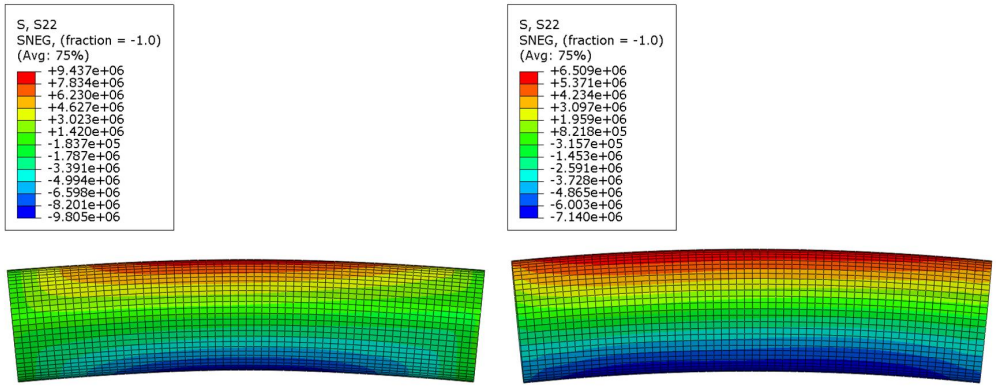

Figure 5.10: Axial stress on middle layer using (a) Fixed-in-plane BCs, (b) Periodic BCs

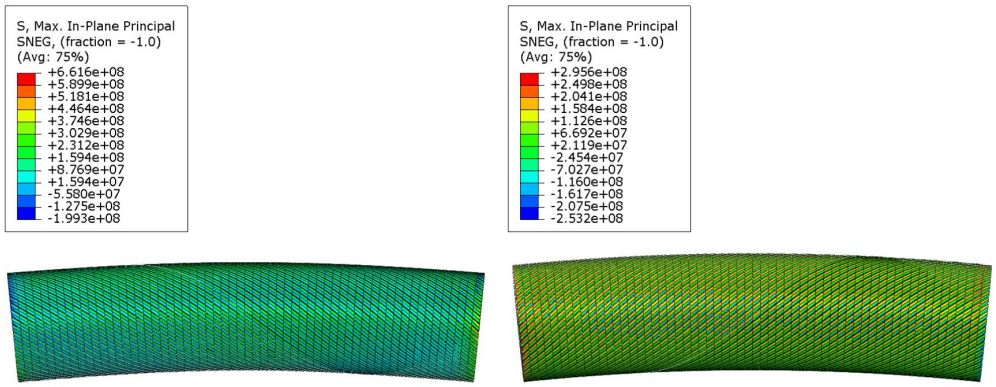

Figure 5.11: Maximum principal stress on outer helical armour wires using (a) Fixed-in-plane BCs, (b) Periodic BCs

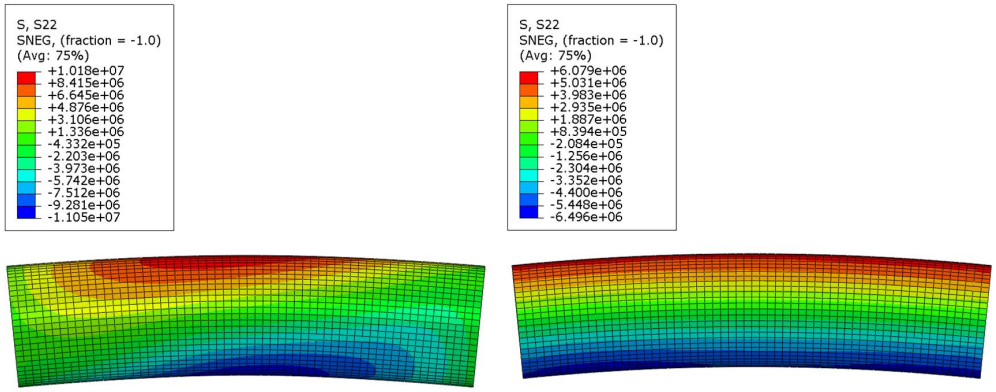

Figure 5.12: Axial stress on outer layer using (a) Fixed-in-plane BCs, (b) Periodic BCs

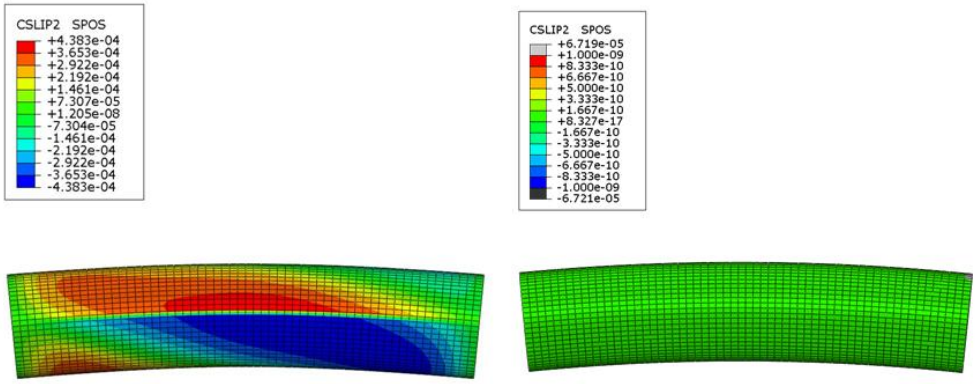

Figure 5.13: Axial slip between carcass layer and pressure sheath using (a) Fixed-in-plane BCs, (b) Periodic BCs

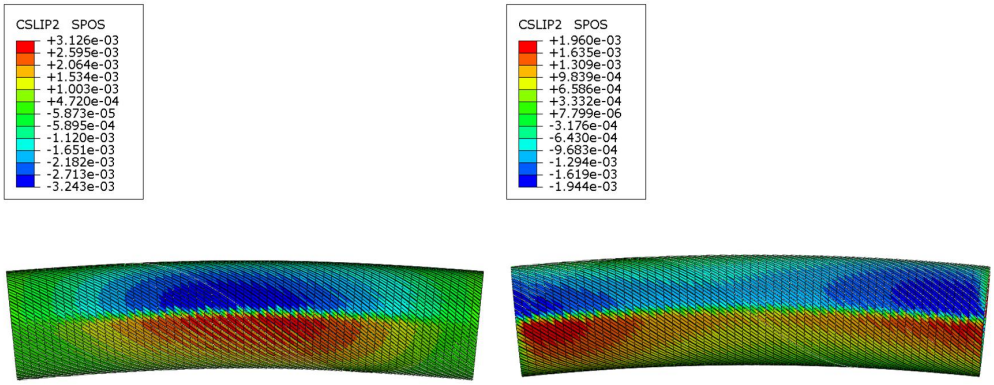

Figure 5.14: Axial slip between inner helical armour and middle anti-wear layer using (a) Fixed-in-plane BCs, (b) Periodic BCs

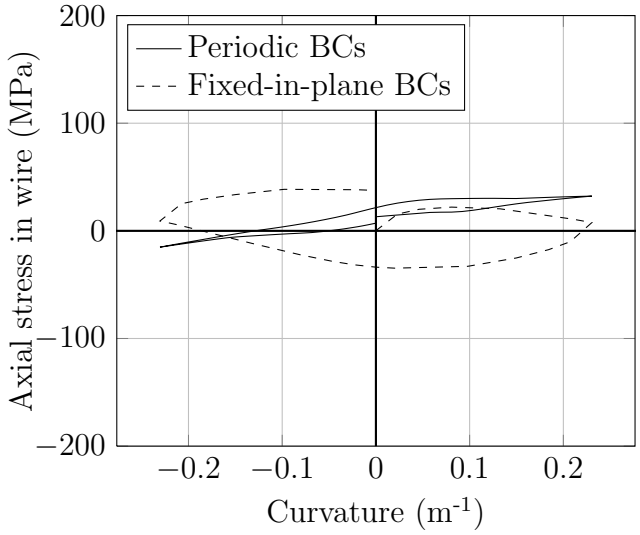

Figure 5.15: Variation of stress on outer tensile armour along wire (inner surface of wire)

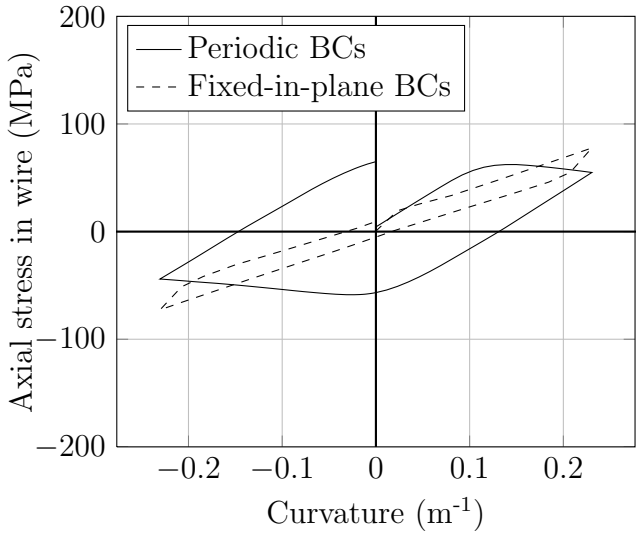

Figure 5.16: Variation of stress on outer tensile armour along wire (outer surface of wire)

the outer surface of the wire has a greater magnitude at the evaluation point and stress on the inner surface has a smaller magnitude when using periodic boundary conditions.

5.3.3 Detailed stress results and verification

A further set of simulations were carried out using the detailed model. These load cases represented axisymmetric loading situations with various types of boundary conditions applied to the pipe ends.

Comparisons were carried out for the following load cases:

1. Axial strain (ε=0.205%). Axial strain is imposed on the model by applying an imposed displacement to the control node (for the finite element model) or by fixing one end and imposing a displacement on the other end (comparison model). No pressure load were applied. A plot of von Mises stress is shown in Figure 5.17, and results are compared in Table 5.9.

2. Internal pressure (P_{INT}=3.45 MPa). Pressure loading is applied to the pressure sheath, while the model is restrained from contracting axially. A plot of von Mises stress is shown in Figure 5.18, and results are compared in Table

5.10.

3. External pressure (P_{EXT}=6.41 MPa). Pressure is applied to the outer sheath, while the model is restrained from contracting axially. A plot of von Mises stress is shown in Figure 5.19, and results are compared in Table 5.11.

The stress results in the components of the detailed model were recorded and compared to those calculated using analytical models. For these simulation, a second analytical model, developed by Richards and Andronicou (1997) is used to generate results for comparison. This model has the capability to simulate bonded and unbonded pipes; for these comparisons, the unbonded option was used. All comparison simulations were carried out using a model with an identical geometrical description of pipe components and identical material properties. The data presented in Tables 5.9, 5.10 and 5.11 show firstly the absolute values of stresses in the finite element and comparison models and, secondly, the relative differences between the finite element model and the two reference models, differences being reported relative to the finite element model, as in Section 5.3.1. It should be noted that neither of the comparison models calculated the bending stress in helical wires. In order to extract data suitable for comparison, stresses presented for the finite element model are averages of the stresses on the interior and exterior surfaces of the wires, at the point of comparison. This eliminated any local bending component from the finite element results.
In Tables 5.9, 5.10 and 5.11, "Ref. model 1" is an abbreviation for the model described by Bahtui (2008) and "Ref. model 2" denoted the model described by Richards and Andronicou (1997).

5.4 Full behavioural response

In this Section, the axial, flexural and torsional response of the detailed model is presented in graphical form. Periodic boundary conditions are used for all simulations. As the influence of internal and external pressure is of particular interest, results are presented for combined bending/pressure loading (Section 5.4.1 and combined axial/pressure loading (Section 5.4.2). Instead of investigating the effects of internal

a)

Layer (Stress component)	Values (MPa)		
	FEA	Ref. model 1	Ref. model 2
Inner Tensile Armour (Axial)	142	158	154
Outer Tensile Armour (Axial)	124	146	131
Carcass (Axial)	19	19	n/a
Carcass (Hoop)	-241	-250	-250
Layer (Stress component)		Differences	
		Ref. model 1	Ref. model 2
Inner Tensile Armour (Axial)		11%	8%
Outer Tensile Armour (Axial)		17%	6%
Carcass (Axial)		0%	n/a
Carcass (Hoop)		4%	4%

b)

K_1= 247 MNm^{-1}	9%	2%
K_2=2347 MNm^{-1}	19%	0%

Table 5.9: Axial tension load case: a) Component stresses b) Pipe stiffness results

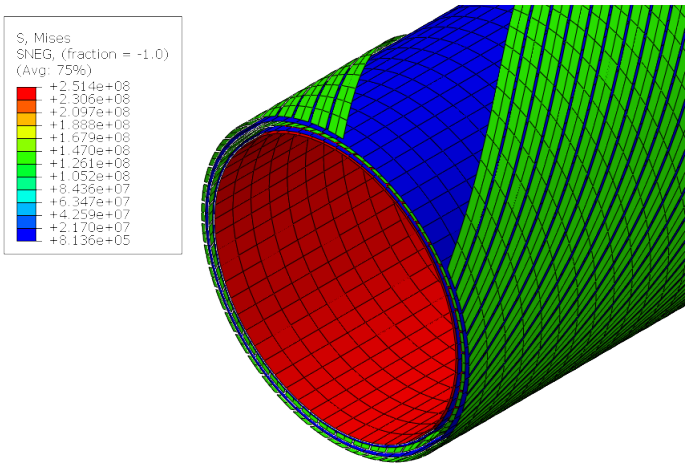

Figure 5.17: Von Mises stress resulting from axial tension load case

a)

Layer (Stress component)	Values (MPa)		
	FEA	Ref. model 1	Ref. model 2
Inner Tensile Armour (Axial)	131	139	131
Outer Tensile Armour (Axial)	126	141	136
Layer (Stress component)		Differences	
		Ref. model 1	Ref. model 1
Inner Tensile Armour (Axial)		6%	0
Outer Tensile Armour (Axial)		12%	8%
b)			
K_3=21.7 GNm^{-3}		23%	17%

Table 5.10: Burst/internal pressure load case: a) Component stresses b) Pipe stiffness results

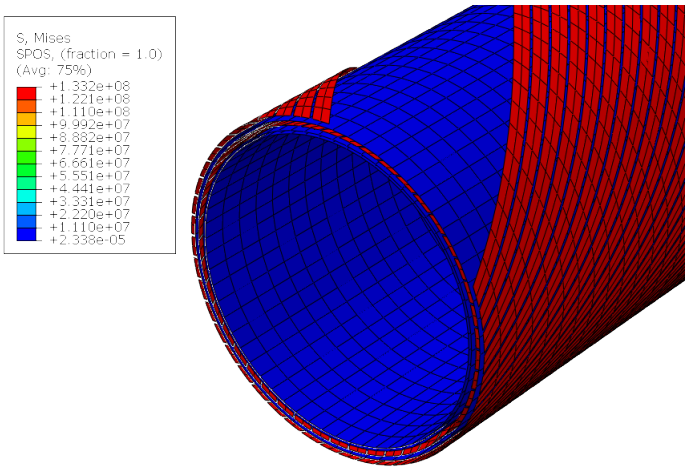

Figure 5.18: Von Mises stress resulting from internal pressure load case

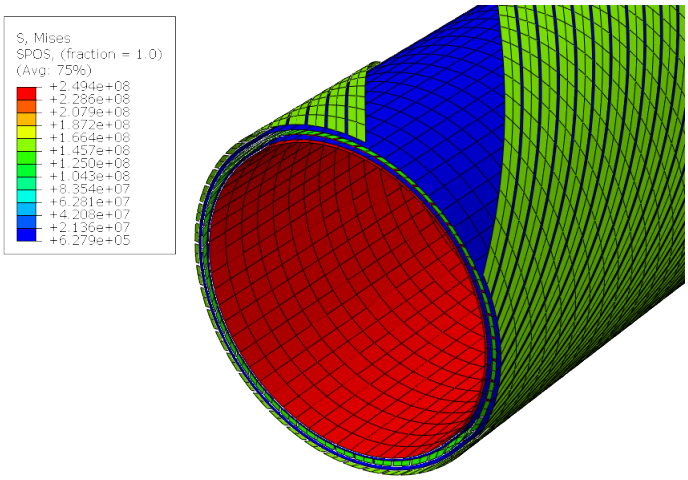

Figure 5.19: Von Mises stress resulting from external pressure load case

a)

Layer (Stress component)	Values (MPa)		
	FEA	Ref. model 1	Ref. model 2
Inner Tensile Armour (Axial)	-126	-109	-126
Outer Tensile Armour (Axial)	-148	-111	-142
Carcass (Axial)	-6.3	-6.3	n/a
Carcass (Hoop)	-252	-254	-256
Layer (Stress component)		Differences	
		Ref. model 1	Ref. model 2
Inner Tensile Armour (Axial)		13%	0
Outer Tensile Armour (Axial)		25%	4%
Carcass (Axial)		0	n/a
Carcass (Hoop)		1%	2%

b)

K_3=33.0 GNm^{-3}	19%	5%

Table 5.11: Radial external pressure load case: a) Component stresses b) Pipe stiffness results

and external pressure separately, the equivalent pressures P_ε and P_u are defined as the actions which cause radial strain and mean radial expansion, respectively (full explanation is provided in Chapter 4), and it is the effect of these actions which is investigated below. The measures u_r and ε_r refer to mean radial displacement and radial strain, respectively.

5.4.1 Bending simulations

In the bending simulations, the model was subject to both imposed curvature and radial strain pressure (P_ε), in a two step simulation. In the first step, a combination of internal and external pressure was applied to the pipe such that the radial displacement pressure (P_u) was zero. In the second step, a prescribed rotation was imposed on the control node, which enforced relative rotation of the end planes of the pipe via the periodic boundary conditions, as described in Section 5.2.2. In both steps, the pipe was not restrained in the axial direction, thus ensuring that the net axial force in the pipe section was zero.

Figure 5.20 shows that increasing P_ε increases the initial bending stiffness of the pipe; however, the slip initiation point or final stiffness is not systematically affected. The pressure-dependence of the initial stiffness cannot be accounted for

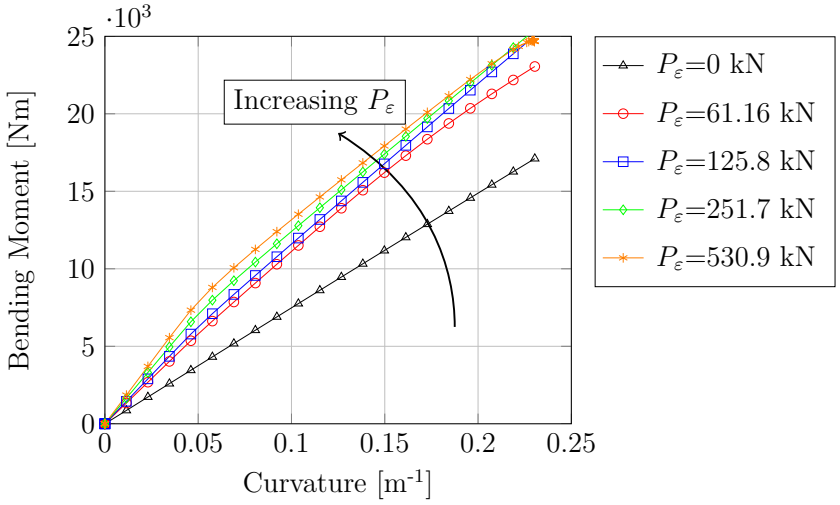

Figure 5.20: Bending moment vs. bending curvature for different initially applied P_ε. $M_y = 0$ throughout.

by the linear model $M_y = D_{22}\chi_x$ assumed in the beam constitutive model. Neither can the phenomenon be accounted for by the addition of pressure coupling terms as was proposed for the axial response because this would predict increase in M_x that is uniform for all values of curvature[2]. A plausible conclusion for these findings is that the bending behaviour is better represented by an elasto-plastic material model with zero yield limit and a nonlinear harding law. This would represent the condition that the tensile armour wires in the pipe slip even at very low curvatures and are not effectively prevented from slipping by radial contact interations. The implementation of this modification is left to future work.

The flexible pipe model was not in torsional balance, due to the requirement the the pitch length of all helical wires equal the length of the model. Torque reaction was therefore observed (Figure 5.21).

Radial strain was discovered to increase with pipe curvature (Figure 5.22. To obtain representative values of radial strain for the model, differences in radial displacement between nodes of the pressure sheath and corresponding nodes of the outer layer were divided by their initial separation. This was calculated for four pairs of nodes (equally spaced around the circumference) and then averaged. The

[2]Assuming that ε_r is not a function of curvature. This is true for the curvature in the initial region that is relevant for initial stiffness calculations (see later graph).

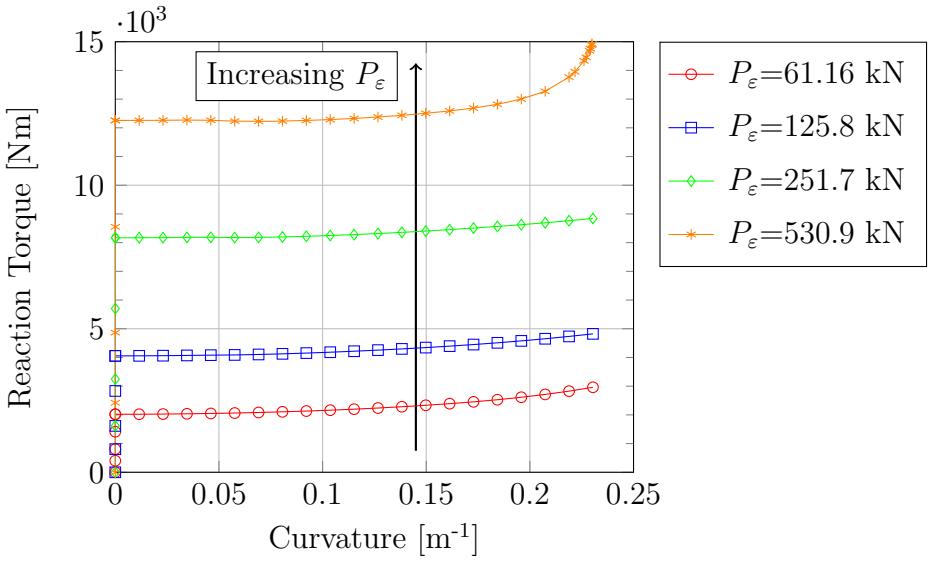

Figure 5.21: Torque-bending coupling for different initially applied P_ε

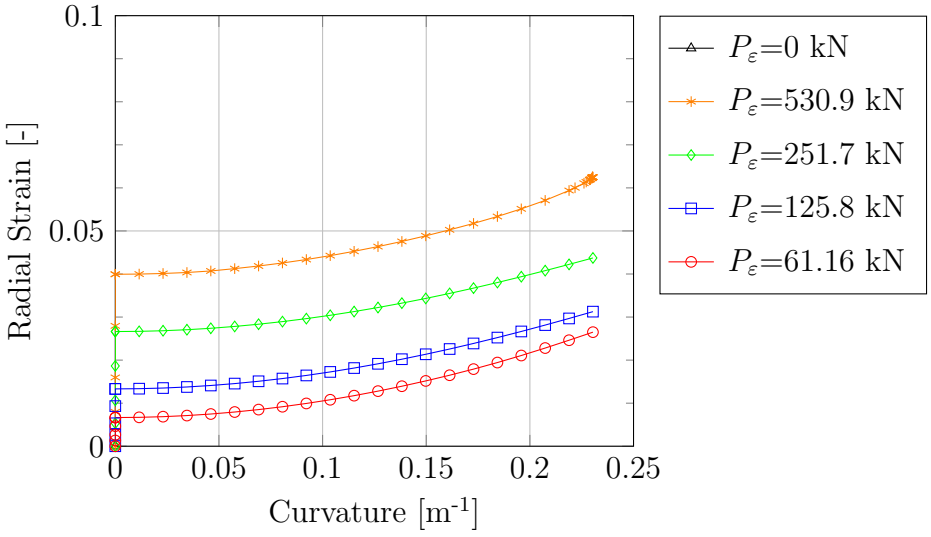

Figure 5.22: Radial strain vs. bending curvature for different initially applied P_ε

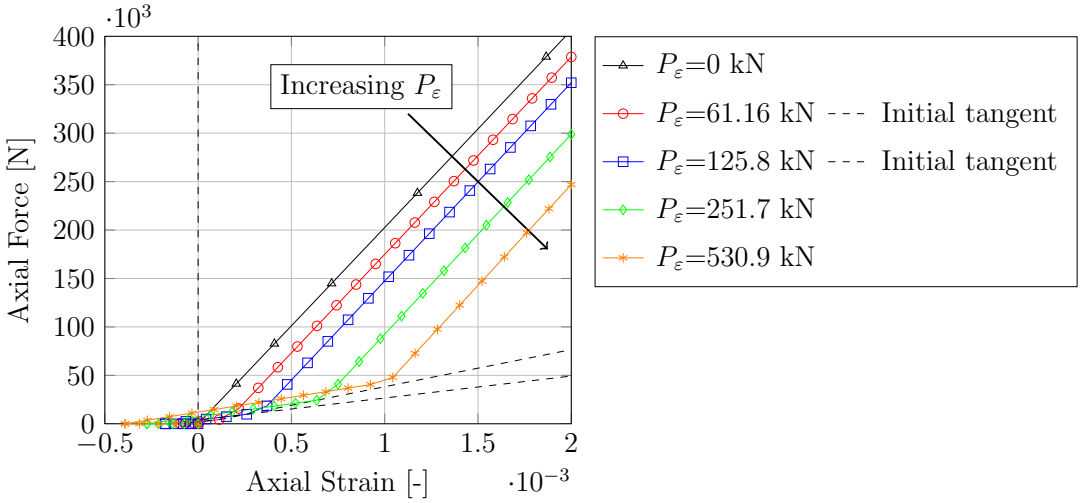

Figure 5.23: Axial force vs. axial strain for different initially applied P_ε

node pairs chosen for evaluation were located in the central cross-sectional plane of the pipe, in order that the radial displacement recorded (defined in a fixed cylindrical coordinate system) does not differ from radial displacement defined relative to the axis of the bent pipe. It is noted that radial strain development under bending in opposite in sign for pairs of points located at the intrados and extrados of the bend, but the averaged trend is an increase in radial strain with pipe bending. This may be associated with the increasing ovalisation of the pipe section that is evident at higher curvatures, which may cause pipe layers to squeeze more tightly together, in regions of the pipe distant from the lines of extrados and intrados.

As for all radial response results, results were averaged from results at four equally spaced points around the pipe circumference, at the cross-sectional plane halfway along the pipe length.

5.4.2 Axial simulations

In these simulations, pressure loading was applied first while the pipe was allowed to contract axially. Following this, the axial extension was imposed. The model showed the phenomenon of the separation of the carcass from the other layers under high P_ε, causing axial stiffness to be reduced until sufficient axial extension had been imposed to bring the carcass back into contact again (Figure 5.23). This phenomenon is not

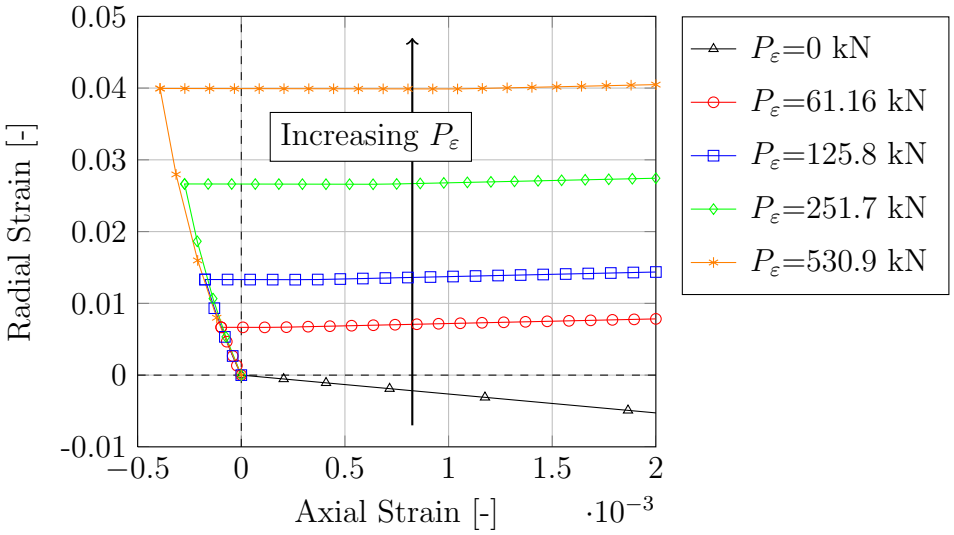

Figure 5.24: Radial strain vs. axial strain for different initially applied P_ε

represented in the large-scale pipe model, and therefore additional modifications to the model are proposed to incorporate it in the existing framework (Section 6).

This result is similar to that obtained by McIver (1995, Fig. 9), who noted that the results from his analytical model predicted a much lower axial stiffness if the pipe was in compression because two layers (the pressure armour and first helical armour layer in this case) separated from each other in this condition.

The radial response to axial extension (Figures 5.24, 5.25) shows that radial strain increases with pressure, but is then not altered by the application of axial load. As the nodes in the end planes are able to contract radially without constraint there are no barrelling-type end effects. It should be noted that the accuracy of the results may be limited by the lack of a transverse Possion effect in the layers of the model because of the shell elements and contact implementation used. In a physical pipe, this effect would causes reduction in the radial thickness of components in response to axial strain.

In a further set of axial simulations, internal pressure instead of P_ε was applied (Figure 5.27). It is noted that, in terms of P_u and P_ε these simulations applied low to moderate P_ε, but high P_u. The lack of a pressure armour layer in the pipe model lead to very high axial strains being displayed in the pressure load step. In the second step, in which prescribed axial displacement was imposed on the control node, large

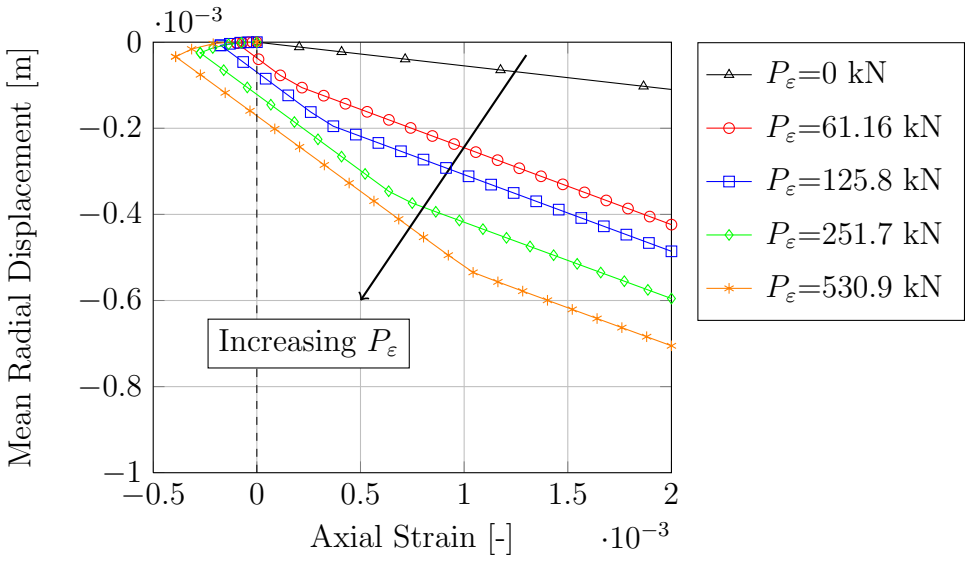

Figure 5.25: Mean radial displacement vs. axial strain for different initially applied P_ε

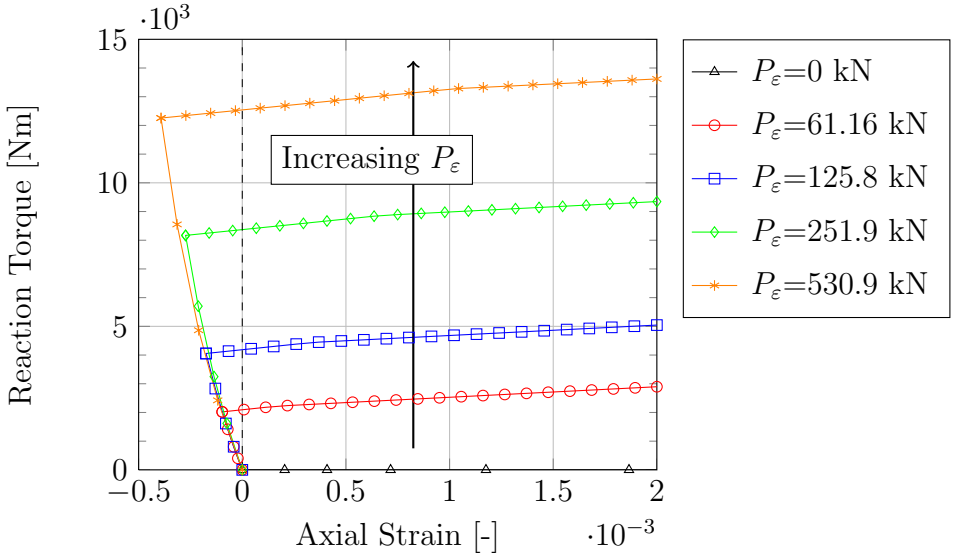

Figure 5.26: Reaction torque v. axial strain for different initially applied P_ε. M_x=M_y=0 throughout.

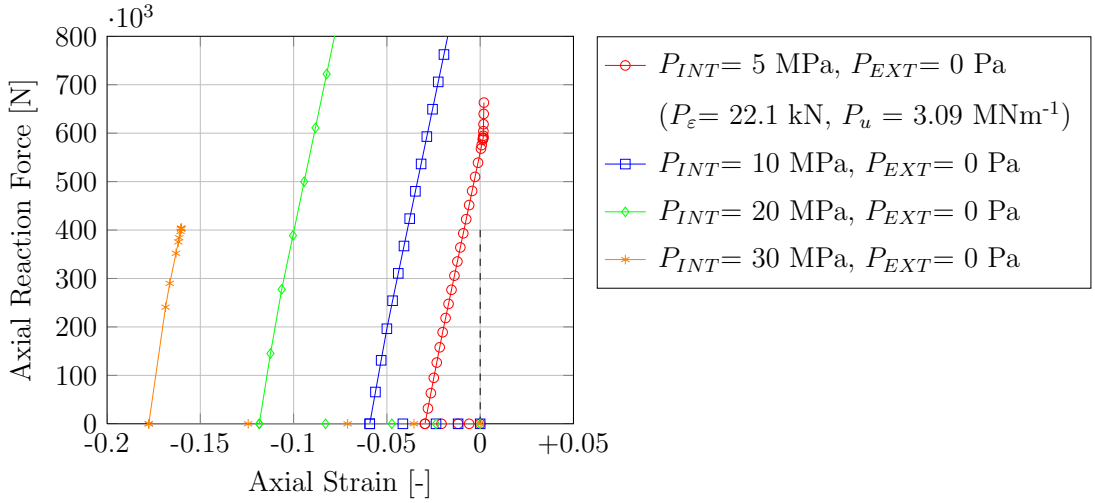

Figure 5.27: Axial reaction force vs. axial strain for different initially applied P_{INT}

values of axial force were obtained as the axial reaction force. In most cases positive axial strain could not be reached as the simulations did not complete. Comparing results to those in Figure 5.23, where radial strain pressure was applied, it can be seen that, in both simulations, axial stiffness is not affected by pressure, but axial force is. In distinction to the results in Figure 5.23, axial stiffness under internal pressure loading is roughly 10 times higher. Furthermore, a carcass reattachment effect may also be present for P_{INT}=5 MPa. This does not become manifest until positive axial strain is attained.

5.4.3 Pressure simulations

Application of radial strain pressure (Figure 5.29) and radial displacement pressure (Figure 5.30) alone show that there is a positive linear relationship between each generalised stress and its associated generalised strain and a negative linear coupling effect with the other pressure-related term.

The data from Figure 5.30 show the axial reaction force resulting from application of radial displacement pressure to a pipe model with ends restrained from translating axially. These data allow the axial-pressure coupling in the flexible pipe to be determined.

Due to the axial-torsional coupling introduced by making the pitch length of

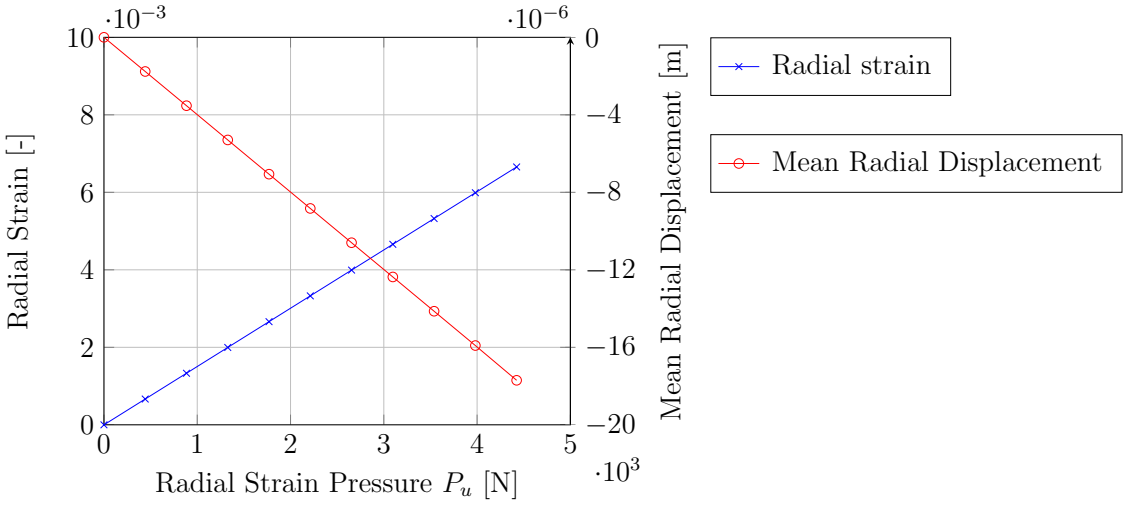

Figure 5.28: Radial strain and mean radial displacement resulting from applied P_ε. P_u=0

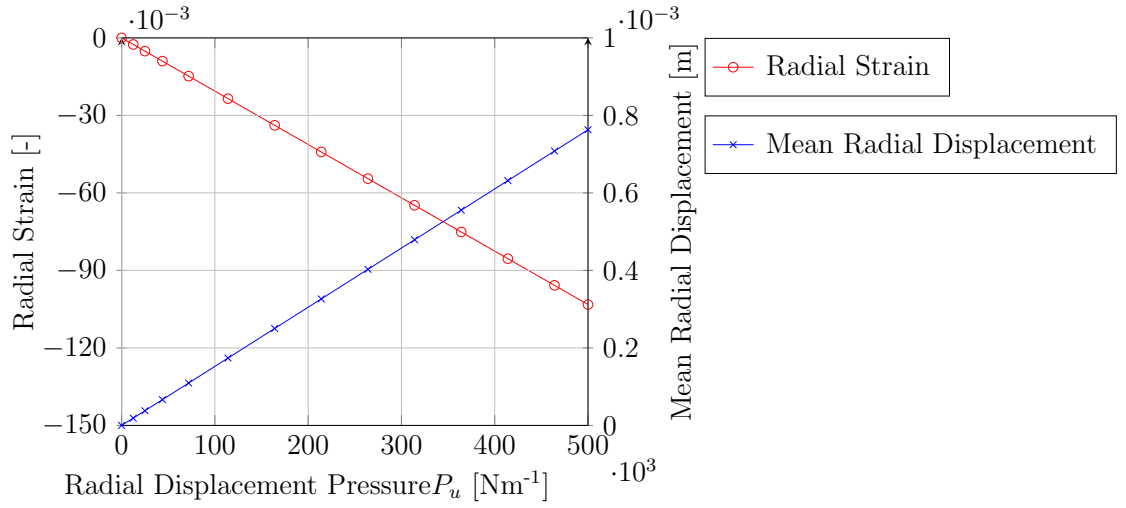

Figure 5.29: Radial strain and mean radial displacement resulting from applied P_u. P_ε=0

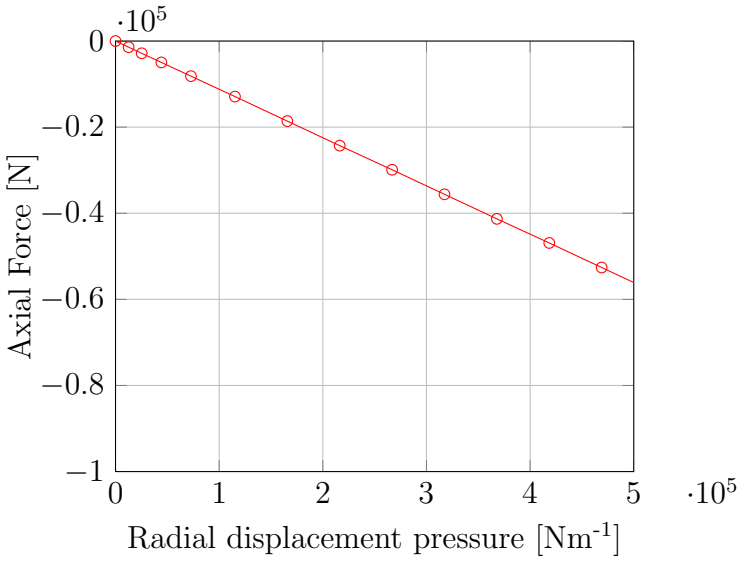

Figure 5.30: Response to radial displacement pressure. M_x, M_y=0

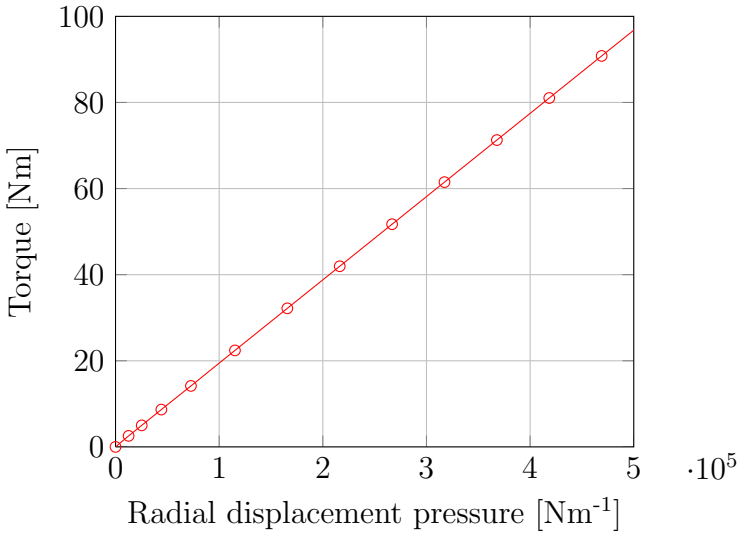

Figure 5.31: Reaction torque vs. radial displacement pressure. $P_\varepsilon = 0$

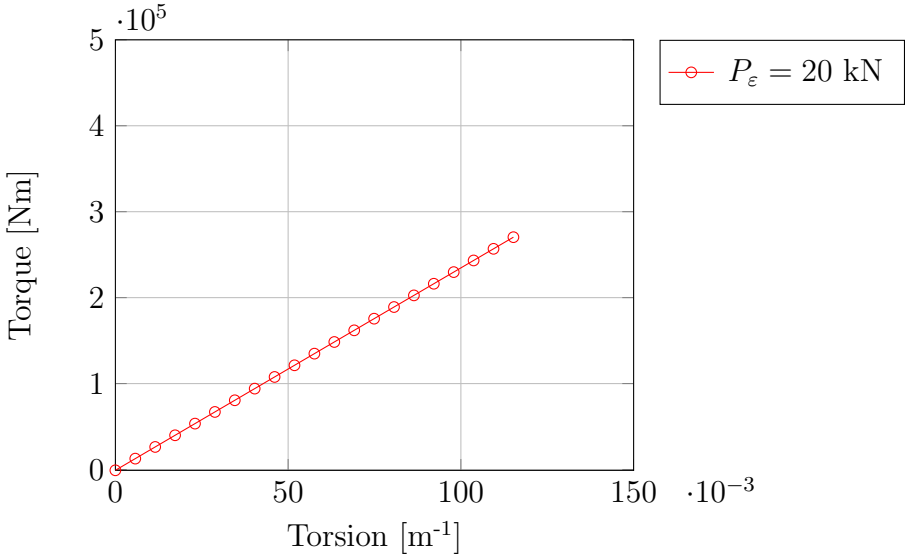

Figure 5.32: Torque reaction vs. applied torsion. P_ε=20 kN.

both tensile armour wires equal, the application of radial displacement pressure also results in a torque reaction (Figure 5.31). This result does not occur in real flexible pipes as pipes are designed to be torsional balanced by selection of the wire lay angles.

5.4.4 Torsion simulations

To determine the torsional response of the model, simulations were carried out in which radial strain pressure was applied in the first load step, allowing the ends to expand axially, before applying a rotation to the control node in the second step.

Application of torsion to the model (Figures 5.32, 5.33, 5.34 and 5.35) shows that torque tends to separate the layers. Torque was applied in only one direction in this simulation. Torsion in flexible pipes is avoided if possible because it is known to cause either layer separation or inter-layer squeezing, depending on the direction of the applied torque, because the alternating direction of winding of the tensile wires causes them to respond in opposite directions. Layer separation is of concern because it can lead to birdcaging and squeezing is avoided because it causes additional stress in components.

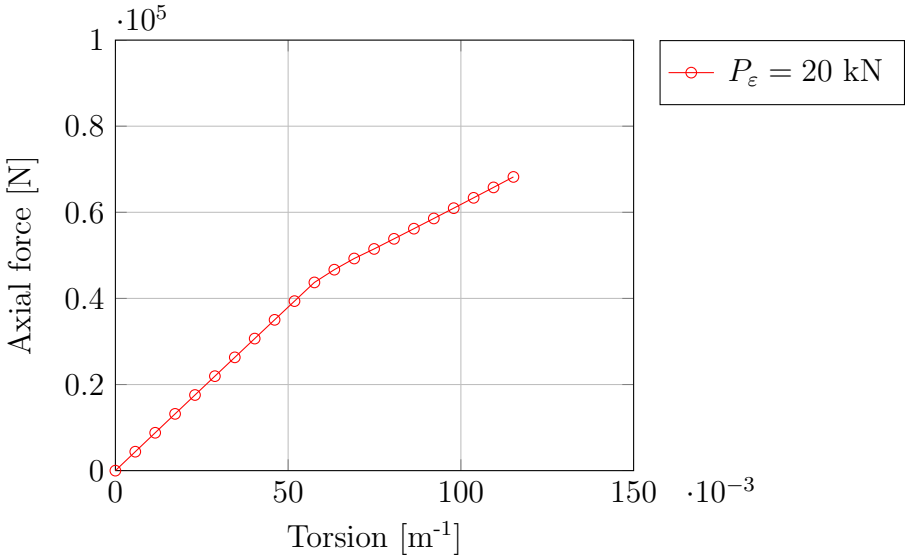

Figure 5.33: Axial reaction force vs. applied torsion. $P_\varepsilon = 20kN$

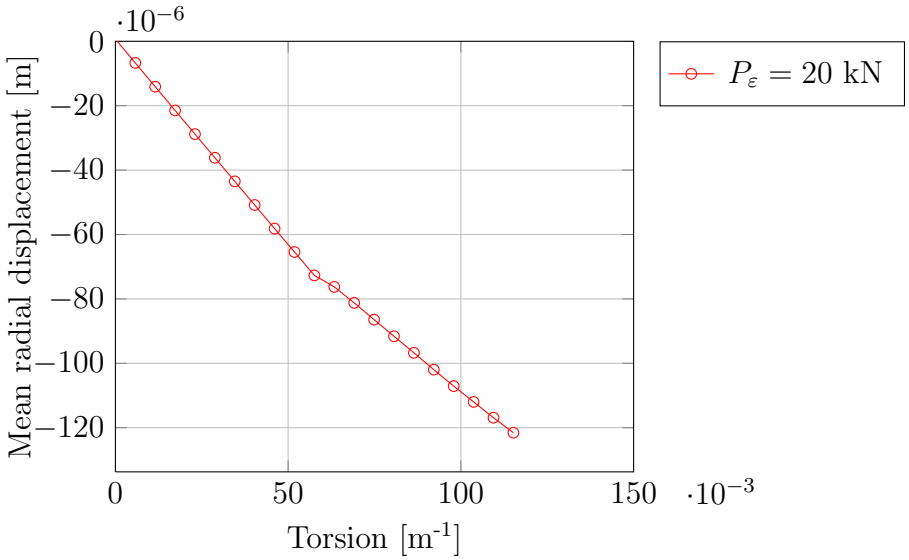

Figure 5.34: Mean radial displacement vs. applied torsion. P_ε=20 kN

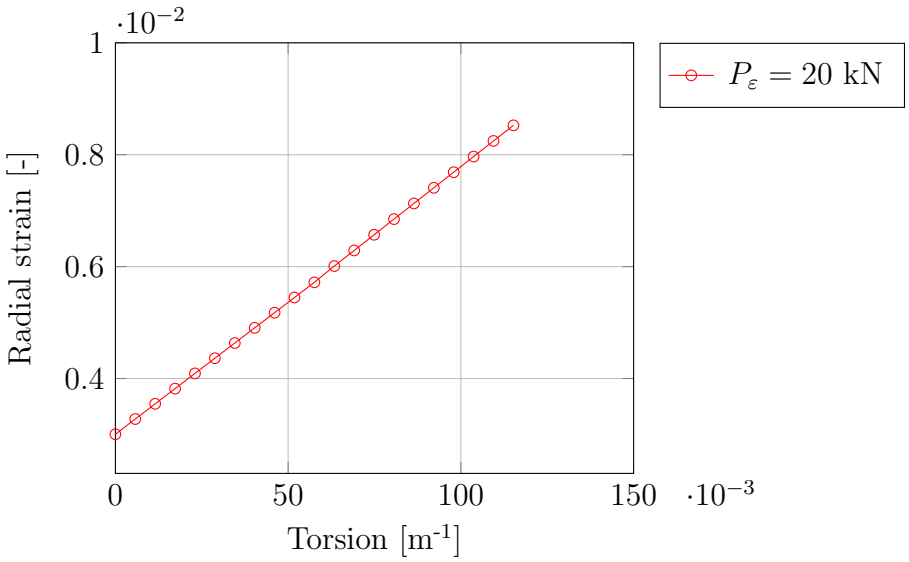

Figure 5.35: Radial strain vs. applied torsion. P_ε= 20 kN

5.5 Discussion of results

In this Chapter, a finite element model of a flexible pipe has been described. Simulations carried out on this model were carried out and the model's predictions of the pipe response have been presented and compared to the predictions of two analytical models used for flexible pipes.

Several valuable results have been obtained from simulations carried out using the model. Firstly, when subjected to tension, internal and external pressure loads, the axial and radial displacement response of the model is fairly close to that predicted by analytical models (Sections 5.2.1 and 5.2.3). Secondly, in the process of model verification, an important improvement was made to the model by softening the pressure-overclosure relationship used to compute radial contact between layers, and by deriving physically appropriate values of contact stiffness to use such that the normal compliance of components is re-introduced into the model (Sections 5.1.1 and 5.2.1). Thirdly, the influence of the boundary conditions used on the model ends for bending simulations was investigated and it was found that using periodic boundary conditions (as described in Section 5.1.2) significantly reduced the bending stiffness predicted by the pipe. Examination of the stresses occurring in pipe components showed that use of periodic boundary conditions significantly

reduced (but did not entirely eliminate spurious end effects, suggesting that use of such boundary conditions gives more accurate stress predictions for bending simulations. However, it is not clear whether use of such boundary boundary will lead to lower predictions of stress in the tensile armour wires, considered over a full cycle of bending (Figures 5.15 and 5.16). Finally, a range of investigations have been carried out on the model, applying axial displacement, curvature, torsion, internal and external pressure, corresponding to the generalised stresses defined for the constitutive model described in Chapter 4.1. The resulting load-response plots (Figures 5.20 to 5.35) have allowed the effect of carcass separation to be identified (Figure 5.23). The effects of of radial strain pressure on the pipe's bending moment-curvature response (Figure 5.21) shows that bending stiffness is indeed increased by radial strain pressure, as assumed in the constitutive model, but shows a saturation effect at high values of radial strain pressure which the constitutive model cannot account for. Other load-response plots are broadly inline with physical intuition, but validation against test data has not been shown.

Results obtained from these simulations have highlighted several important issues involved in the finite element modelling of flexible pipes and progress has been made in incorporating experience gained into an improved model. However, the accuracy of the model has not yet been satisfactorily shown by comparison with test data. Two important issues, the physical realism of the boundary condition choice and the ability of the mode to accurately predict the deformed shape of tensile armour wires in bending (both of which are important for accurate fatigue analysis of flexible risers) remain unresolved and would benefit from further attention in any future work.

Several aspects of the verification procedure described limit the extent to which this finite element model can be considered verified; firstly, the comparisons were made with analytical models that are simpler in terms of the number of degrees of freedom included in the model and more restricted in the deformation phenomena that can be represented (such as ovalisation of cylindrical layers, frictional sliding of tensile armour wires and rotation of armour wires around their own axes). Secondly, it was not possible to compare stress results resulting from pipe bending as the ref-

erence analytical models do not analyse pipe bending. Clearly, it would be desirable to compare the model response and component stresses with full scale instrumented tests, but this was not possible within the project scope and budget limitations. Instead, validation against the analytical models was suggested by the project sponsor, Lloyd's Register, given that these models have previously given good results when compared with data from manufacturers.

Chapter 6

Modification for carcass modelling

The results from the detailed model presented in Chapter 5 give a more reliable and precise description of flexible pipe behavior than the finite element model used previously, compared with the results obtained by Bahtui (2008). Inspection of the plots generated for the pipe's behavioural response seems to show that much of the pipe's behaviour can be captured by a linear coupled model as proposed in Chapter 4. However, one major discrepancy is the axial response to axial loading is nonlinear (Figure 5.23), which is associated with separation of the carcass from the other pipe layers. It is believed that this phenomenon could occur in practice under certain combinations of pressure and axial loading, but this effect cannot be reproduced using the large-scale model describe in Chapter 4. Hence, in this Chapter, to improve large-scale flexible pipe modelling, a new modification to the constitutive model used in the large-scale model will be developed in which carcass detachment is accounted for.

6.1 Carcass modification

As a consequence of the analysis of axial results described in Section 5.4.2, a new method is proposed for modelling the carcass separation phenomenon in the constitutive model. It is assumed that the constitutive model represents the behaviour of the pipe without the carcass, i.e. in the condition where the carcass has separated from the other layers and does not affect the behaviour of the remainder of the pipe.

The effect of the carcass is reduced to an internal pressure applied to the pressure sheath, in addition to hydrostatic pressure, representing the contact force exerted by the carcass. This contact force is only applied if the radial displacement of the pressure sheath is negative. If the displacement is negative, the ultimate effect of this contact pressure is to increase the stiffness of the pipe, as is demonstrated in the following developments. In this Section, the appropriate modification to the stiffness matrix for this case will be derived. The contribution of the carcass to the axial stiffness is also accounted for in the derivation.

The radial displacement of the pressure sheath can be described using the generalised strains of the constitutive model as

$$u_i = u_r + \varepsilon_r \frac{t}{2} \tag{6.1.1}$$

where t is the wall thickness of the composite pipe, defined as the difference between the mean radius of the pressure sheath and the mean radius of the outer layer. If the carcass and pressure sheath are in contact, the carcass will also experience a radial deformation equal to u_i. If this radial displacement is imposed on the carcass (modelled as an orthotropic linear elastic cylinder), the contact force exerted by the cylinder back onto the pressure sheath can be calculated from equilibrium of a cylindrical segment of the carcass.

The constitutive equations for the pipe, excluding the carcass layer, and omitting the bending terms (i.e. limiting the analysis to axisymmetric loading) are as follows:

$$\begin{cases} D_{11}\varepsilon_a + D_{15}u_r + D_{16}\varepsilon_r &= N \\ D_{51}\varepsilon_a + D_{55}u_r + D_{56}\varepsilon_r &= P_u \\ D_{61}\varepsilon_a + D_{65}u_r + D_{66}\varepsilon_r &= P_\varepsilon \end{cases} \tag{6.1.2}$$

The constitutive equations for the carcass alone can be expressed as

$$\begin{cases} \tilde{D}_{11}\tilde{\varepsilon} + \tilde{D}_{12}\tilde{u}_{rc} = \tilde{N} \\ \tilde{D}_{21}\tilde{\varepsilon} + \tilde{D}_{22}\tilde{u}_{rc} = \tilde{P} \end{cases} \tag{6.1.3}$$

where $\tilde{P}$ is a generalised radial stress that is work conjugate to the carcass radial displacement $\tilde{u}_{rc}$. In the following, a tilde (˜) is used to identify quantities relating to the carcass layer alone, whereby $\tilde{N}$ is the axial force acting on the carcass, while $\tilde{\varepsilon}$ and $\tilde{u}_{rc}$ are the axial strain and radial displacement of the carcass, respectively. It is noted that the work per unit length of pipe performed by the resultants $\tilde{N}$ and $\tilde{P}$ acting on the carcass layer alone, for the virtual displacements ($\delta\varepsilon$, δu_{rc}) is $\delta W = \tilde{N}\delta\varepsilon + \tilde{P}\delta u_{rc}$. This implies that the dimensions of $\tilde{P}$ are FL^{-1}.

The contact pressure P_c is defined as the pressure that the carcass exerts on the rest of the pipe, and conversely, the pressure the rest of the pipe exerts on the carcass. Its sign is positive if the carcass and rest of the pipe are in contact and zero otherwise. $\tilde{P}$ is related to the contact pressure using the following relation:

$$\tilde{P} = -P_c 2\pi R_c \tag{6.1.4}$$

where R_c is the radius of the carcass. The negative sign indicates that P_c (as experienced by the carcass) acts radially inwards. In the equations in this Section, only the instance of P_c which acts on the carcass will be considered, and hence it will always be considered as the magnitude of a force acting radially inwards. If the carcass if attached (i.e. the condition $u_r + \frac{t}{2} < 0$ is satisfied) then the following conditions apply for the composite structure:

$$\begin{cases} \varepsilon = \tilde{\varepsilon} & \text{(Compatibility)} \\ \left.\begin{array}{l} N^{TOT} = N + \tilde{N} \\ P_{INT}^{TOT} = P_{INT}^{F} + P_c \end{array}\right] & \text{(Equilibrium)} \end{cases} \tag{6.1.5}$$

where P_{INT}^{F} is the internal fluid pressure while P_{EXT}^{TOT} and P_{INT}^{TOT} are the total pressure acting externally and internally on the pipe without the carcass. The following

condition holds for radial displacements:

$$\tilde{u}_{rc} = u_r + \frac{t}{2}\varepsilon_r + \frac{P_c}{k} = u_r + \frac{t}{2}\varepsilon_r - \frac{\tilde{P}}{2\pi R_{INT} k} \tag{6.1.6}$$

so that, setting $C = 1/(2\pi R_{INT} k)$, one has

$$\tilde{u}_{rc} = u_r + \frac{t}{2}\varepsilon_r - C\tilde{P} \tag{6.1.7}$$

where k is the penalty stiffness used to implement the contact interaction between the carcass and pressure sheath. This modification is necessary for consistency with the contact model used in the detailed model, as described in Section 5. The generalised stresses P_u and P_ε in the pipe, as defined in Equation 4.2.5 of Section 4.2 (replacing P_{INT} with P_{TOT}^{INT}), are a function of the internal and external pressures applied to the pressure sheath (the innermost layer, excluding the carcass) and the outer sheath. The radial equilibrium equation above expresses the fact that the effective internal pressure acting on the pressure sheath is the sum of the internal fluid pressure and the contact pressure exerted by the carcass. This is because the carcass is permeable to the internal fluid.

Notice also that the fluid pressure does not strictly act on the entire surface of the pressure sheath, as the actual contact area between the carcass and pressure sheath (which can be defined and in principle determined in a micromechanical description of contact) should be excluded. However, we assume this area to be negligible with respect to the total area using the same assumption made in soil mechanics to define "effective stresses". Also, this is consistent with the small-scale FE analysis conducted in Chapter 5.

Hence, when the carcass is separated, the pressure-related stress resultants in the constitutive model are calculated from the internal and external pressures as follows:

$$
\begin{aligned}
P_u &= 2\pi(P^F_{INT}R_{INT} - P_{EXT}R_{EXT}) \\
P_\varepsilon &= \pi t(P^F_{INT}R_{INT} + P_{EXT}R_{EXT})
\end{aligned} \tag{6.1.8}
$$

With the increase in internal pressure from the carcass contact pressure, the equations become:

$$
\begin{aligned}
P_u &= 2\pi((P^F_{INT} + P_c)R_{INT} - P_{EXT}R_{EXT}) \\
&= 2\pi(P^F_{INT}R_{INT} + P_cR_{INT} - P_{EXT}R_{EXT}) \\
&= 2\pi(P^F_{INT}R_{INT} - P_{EXT}R_{EXT}) + 2\pi P_cR_{INT} \qquad (6.1.9a) \\
P_\varepsilon &= \pi t((P^F_{INT} + P_c)R_{INT} + P_{EXT}R_{EXT}) \\
&= \pi t(P^F_{INT}R_{INT} + P_cR_{INT} + P_{EXT}R_{EXT}) \\
&= \pi t(P^F_{INT}R_{INT} + P_{EXT}R_{EXT}) + \pi tP_cR_{INT} \qquad (6.1.9b)
\end{aligned}
$$

which can be expressed in more compact form as

$$
\begin{cases}
P_u = P^F_u + \tilde{P}_u \\
P_\varepsilon = P^F_\varepsilon + \tilde{P}_\varepsilon
\end{cases} \tag{6.1.10}
$$

where the superscript F indicted the contribution from internal fluid pressure rather than carcass pressure and

$$
\begin{aligned}
\tilde{P}_u &= -\tilde{P} \\
\tilde{P}_\varepsilon &= -\frac{t}{2}\tilde{P}
\end{aligned} \tag{6.1.11}
$$

using the expression for $\tilde{P}$ from Equation 6.1.4. Combining Equations 6.1.3 and 6.1.7 and rearranging such that all $\tilde{P}$ terms are on the left side gives

$$\begin{bmatrix} 1 & C\tilde{D}_{12} \\ 0 & 1+C\tilde{D}_{22} \end{bmatrix} \begin{bmatrix} \tilde{N} \\ \tilde{P} \end{bmatrix} = \begin{bmatrix} \tilde{D}_{11} & \tilde{D}_{12} & \frac{t}{2}\tilde{D}_{12} \\ \tilde{D}_{21} & \tilde{D}_{22} & \frac{t}{2}\tilde{D}_{22} \end{bmatrix} \begin{bmatrix} \tilde{\varepsilon} \\ u_r \\ \varepsilon_r \end{bmatrix} \tag{6.1.12}$$

By premultiplying both sides by the inverse of the first matrix on the left hand side, the following explicit relation is obtained relating the loads on the carcass to the generalised strains of the model without the carcass:

$$\begin{bmatrix} \tilde{N} \\ \tilde{P} \end{bmatrix} = \begin{bmatrix} \tilde{D}_{11}+\gamma\tilde{D}_{21} & \tilde{D}_{12}+\gamma\tilde{D}_{22} & \frac{t}{2}(\tilde{D}_{12}+\gamma\tilde{D}_{22}) \\ \beta\tilde{D}_{21} & \beta\tilde{D}_{22} & \frac{t}{2}\beta\tilde{D}_{22} \end{bmatrix} \begin{bmatrix} \tilde{\varepsilon} \\ u_r \\ \varepsilon_r \end{bmatrix} \tag{6.1.13}$$

noting that $\tilde{\varepsilon} = \varepsilon$ and the factors β and γ are defined by

$$\beta = \frac{1}{1+C\tilde{D}_{22}} \qquad \gamma = -\frac{C\tilde{D}_{12}}{1+C\tilde{D}_{22}} \tag{6.1.14}$$

Since, from Equation 6.1.13, $\tilde{P}$ can also be expressed in terms of the generalised strains of the pipe as

$$\tilde{P} = \beta\tilde{D}_{21}\varepsilon + \beta\tilde{D}_{22}u_r + \frac{t}{2}\beta\tilde{D}_{22}\varepsilon_r \tag{6.1.15}$$

then

$$\tilde{P}_u = -\beta\tilde{D}_{21}\varepsilon - \beta\tilde{D}_{22}u_r - \frac{t}{2}\beta\tilde{D}_{22}\varepsilon_r \tag{6.1.16}$$

$$\tilde{P}_\varepsilon = -\frac{t}{2}\beta\tilde{D}_{21} - \frac{t}{2}\beta\tilde{D}_{22}u_r - \frac{t^2}{4}\beta\tilde{D}_{22}\varepsilon_r \tag{6.1.17}$$

This allows the equilibrium equations of the composite structure (Equation 6.1.5) to be expressed in terms of N^{TOT}, P_u^F and P_ε^F:

$$\begin{cases} N_{TOT} = N + \tilde{N} \\ P_u^F = P_u - \tilde{P}_u \\ P_\varepsilon^F = P_\varepsilon - \tilde{P}_\varepsilon \end{cases} \tag{6.1.18}$$

Substituting Equations 6.1.2, 6.1.13 and 6.1.17 into Equation 6.1.18 allows the stiffness matrix of the composite structure to be written as

$$\begin{bmatrix} N \\ P_u^F \\ P_\varepsilon^F \end{bmatrix} = \left(\begin{vmatrix} D_{11} & D_{15} & D_{16} \\ D_{51} & D_{55} & D_{56} \\ D_{61} & D_{65} & D_{66} \end{vmatrix} + \begin{vmatrix} \tilde{D}_{11} + \gamma\tilde{D}_{21} & \tilde{D}_{12} + \gamma\tilde{D}_{22} & \frac{t}{2}(\tilde{D}_{12} + \gamma\tilde{D}_{22}) \\ \beta\tilde{D}_{21} & \beta\tilde{D}_{22} & \frac{t}{2}\beta\tilde{D}_{22} \\ \frac{t}{2}\beta\tilde{D}_{21} & \frac{t}{2}\beta\tilde{D}_{22} & \frac{t^2}{4}\beta\tilde{D}_{22} \end{vmatrix} \right) \tag{6.1.19}$$

where the first part of the stiffness matrix represents the contribution of all layers except the carcass and the second part represents the contribution of the carcass, modified by the interlaminar penalty stiffness. Using the definitions of β and γ it can be shown that the stiffness is symmetric.

The coefficients $\tilde{D}_{11}$, $\tilde{D}_{12}$ and $\tilde{D}_{22}$ are derived using the material properties of the orthotropic carcass layer. The plane stress relations between stress and strain in a plane stress orthotropic material are

$$\begin{bmatrix} \varepsilon_a \\ \varepsilon_h \end{bmatrix} = \begin{bmatrix} \frac{1}{E_a} & -\frac{\nu_{ah}}{E_h} \\ -\frac{\nu_{ha}}{E_a} & \frac{1}{E_h} \end{bmatrix} \begin{bmatrix} \sigma_a \\ \sigma_h \end{bmatrix} \tag{6.1.20}$$

where the subscripts a and h denote components in the axial and hoop directions, respectively. The stresses are derived from consideration of equilibrium with external forces:

$$\sigma_a = \frac{\tilde{N}}{2\pi R_{INT} t_c} \qquad \text{and} \qquad \sigma_h = -\frac{R_{INT} P_c}{t_c} = \frac{\tilde{P}}{2\pi t_c} \tag{6.1.21}$$

where t_c is the thickness of the carcass.

Substituting Equation (6.1.21) into Equation (6.1.20) leads to

$$\begin{aligned}\tilde{\varepsilon} = \varepsilon_a &= \frac{1}{2\pi R_{INT} t_c E_a}\tilde{N} - \frac{\nu_{ah}}{2\pi t_c E_h}\tilde{P} \\ \tilde{u}_{rc} = \varepsilon_h R_{INT} &= -\frac{\nu_{ha}}{2\pi t_c E_a}\tilde{N} + \frac{R_{INT}}{2\pi t_c E_h}\tilde{P}\end{aligned} \tag{6.1.22}$$

Expressed in matrix form, this becomes

$$\begin{bmatrix}\tilde{\varepsilon} \\ \tilde{u}_{rc}\end{bmatrix} = \frac{1}{2\pi R_{INT} t_c}\begin{bmatrix}\frac{1}{E_a} & -\frac{\nu_{ah}}{E_h}R_{INT} \\ -\frac{\nu_{ha}}{E_a}R_{INT} & \frac{R_{INT}^2}{E_h}\end{bmatrix}\begin{bmatrix}\tilde{N} \\ \tilde{P}\end{bmatrix} \tag{6.1.23}$$

Inverting this relation gives:

$$\begin{bmatrix}\tilde{N} \\ \tilde{P}\end{bmatrix} = \frac{2\pi t_c}{R_{INT}(1-\nu_{ha}\nu_{ah})}\begin{bmatrix}E_a R_{INT}^2 & E_a \nu_{ah} R_{INT} \\ E_h \nu_{ha} R_{INT} & E_h\end{bmatrix}\begin{bmatrix}\tilde{\varepsilon} \\ \tilde{u}_{rc}\end{bmatrix} \tag{6.1.24}$$

Equation (6.1.24) is formally identical to Equation (6.1.3), which allows the coefficients $\tilde{D}_{11}$, $\tilde{D}_{12}$ and $\tilde{D}_{22}$ to be identified as

$$\begin{aligned}\tilde{D}_{11} &= \frac{2\pi R_{INT} t_c E_a}{(1-\nu_{ha}\nu_{ah})} \\ \tilde{D}_{12} &= \frac{2\pi t_c E_a \nu_{ah}}{(1-\nu_{ha}\nu_{ah})} \\ \tilde{D}_{21} &= \frac{2\pi t_c E_h \nu_{ha}}{(1-\nu_{ha}\nu_{ah})} \\ \tilde{D}_{22} &= \frac{2\pi t_c E_h}{R_{INT}(1-\nu_{ha}\nu_{ah})}\end{aligned} \tag{6.1.25}$$

It is noted that the following relation holds for the orthotropic material parameters:

$$\frac{\nu_{ah}}{E_h} = \frac{\nu_{ha}}{E_a} \tag{6.1.26}$$

This implies that $\tilde{D}_{12} = \tilde{D}_{21}$.

In the case in which the carcass is separated, the following conditions apply

$$\begin{cases} \tilde{\varepsilon} = \varepsilon_a & \text{(Compatibility)} \\ \tilde{P} = 0 & \text{(Carcass unaffected by fluid pressure)} \\ P_{INT}^{TOT} = P_{INT}^{F} & \\ P_{EXT}^{TOT} = P_{EXT}^{F} & \\ N^{TOT} = N + \tilde{N} & \text{(Axial equilibrium)} \end{cases}$$

Thus the proposed model changes the initial elastic stiffness as follows

$$D^* = \begin{pmatrix} D_{11} & 0 & D_{15} & D_{16} \\ 0 & D_{22} & 0 & 0 \\ D_{51} & 0 & D_{55} & D_{56} \\ D_{61} & 0 & D_{65} & D_{66} \end{pmatrix} + h(-(u_r + \frac{t}{2}\varepsilon_r)) \begin{pmatrix} \tilde{D}_{11} + \gamma\tilde{D}_{21} & 0 & \beta\tilde{D}_{21} & \frac{t}{2}\beta\tilde{D}_{21} \\ 0 & 0 & 0 & 0 \\ \beta\tilde{D}_{21} & 0 & \beta\tilde{D}_{22} & \frac{t}{2}\beta\tilde{D}_{22} \\ \frac{t}{2}\beta\tilde{D}_{21} & 0 & \frac{t}{2}\beta\tilde{D}_{22} & \frac{t^2}{4}\beta\tilde{D}_{22} \end{pmatrix} \tag{6.1.27}$$

where $h(\cdot)$ is the Heaviside step function:

$$h(x) = \begin{cases} 0 & x < 0 \\ 1 & x \geq 0 \end{cases} \tag{6.1.28}$$

The stress becomes

$$\sigma = D^*(\varepsilon - \varepsilon_p) \tag{6.1.29}$$

6.2 Concluding remarks

In this Chapter, the phenomenon of carcass separation observed in results obtained when applying axial tension to the detailed finite element model (Section 5.3.2), is incorporated into the constitutive model developed for the beam element (Section 4.2) by introducing a conditional modification to the elastic stiffness matrix. This modification is derived using expressions for the compatibility and equilibrium of two concentric cylinders, alternatively in or out of contact together with definitions of the radial generalised stresses and strain (Section 4.2). For consistency with the finite element model, the modification takes into account the softened pressure-overclosure relationship used to compute contact interactions described in Section 5.1.1. The modification developed has the advantage that no additional parameters need be included in the constitutive model.

In the following chapter, the results of simulations carried out on the small-scale finite element model shall be used to determine the parameters of the constitutive model that best represent the behaviour of the flexible pipe under consideration. To enable the constitutive model to better represent the behaviour of the flexible pipe, the only simulations in which carcass separation does not occur shall be used to determine the parameters; once this is complete, the stiffness modification will be computed and the modifed constitutive model shall be used to predict the axial force-displacement behaviour of the pipe, the results of which shall then be checked against those from the finite element model.

Chapter 7

Parameter identification for a sequential multi-scale analysis

The final part of the sequential computational homogenisation procedure presented in this work is the determination of the parameters of the large-scale model from results data obtained from a large set of simulations carried out on the small-scale model. In this Chapter, calculations used to obtain these parameters will be described, and all parameters determined will be listed.

Using the simulation results obtained for the finite element model (Section 5.4), it becomes possible to obtain estimates of the most appropriate values for the parameters of the large-scale model (Chapter 5). The use of periodic boundary conditions and use of the control node method for obtaining stress resultants ensures that this procedure implements a sequential structural-to-structural multi-scale analysis as described in Chapter 3.

In accordance with the constitutive model used in the large-scale model, three sets of parameters need to be determined. The parameters of the initial elastic stiffness matrix are derived in Section 7.1. The parameters a, b and c used in the slip onset function are obtained by determining slip onset points in Section 7.2. The linear hardening coefficients used to describe post-slip behaviour are derived in Section 7.3. Parameters are derived for the flexible pipe in the state in which the carcass is separated from the other layers. In order to correct for the increase in axial stiffness due to carcass reattachment, the model described in Chapter 6 is

used. Parameters for this model are calculated in Section 7.4.

7.1 Identification of elastic moduli

In this Section, the simulation data shall be used to determine the initial stiffness matrix. As the aim is to fit the data to a symmetric, linear elastic model, data from simulations where layer separation occurs will be disregarded, with the exception of the situation where the carcass layer separates under axial-pressure loading. With regard to this situation, the initial stiffness coefficients will be determined for the case where the carcass is separated. This requires that carcass separation occurs in all the simulation data used for parameter determination.

For a first simulation, where P_u^1 and P_ε^1 are applied and axial strain ε_a is prescribed to be zero, the following two equations apply:

$$D_{55}u_r^1 + D_{56}\varepsilon_r^1 = P_u^1 \tag{7.1.1a}$$

$$D_{65}u_r^1 + D_{66}\varepsilon_r^2 = P_\varepsilon^1 \tag{7.1.1b}$$

where u_r^1 and ε_r^1 are the mean radial displacement and radial strain obtained in the small-scale FE analysis under the loads P_u^1 and P_ε^1.

A second simulation is carried out with P_u^2 and P_ε^2 applied:

$$D_{55}u_r^2 + D_{56}\varepsilon_r^2 = P_u^2 \tag{7.1.2a}$$

$$D_{65}u_r^2 + D_{66}\varepsilon_r^2 = P_\varepsilon^2 \tag{7.1.2b}$$

The coefficients may be found by solving the system of equations

Loading	u_r (mm)	ε_r (-)
$P_u^1 = 2.638 MNm^{-1}, P_\varepsilon^1 = 69.58$ kN	0.2135	9.362×10^{-3}
$P_u^2 = 3.088 MNm^{-1}, P_\varepsilon^2 = 22.12$ kN	0.2740	2.059×10^{-3}

Table 7.1: Simulations to obtain pressure coefficients

$$\begin{bmatrix} u_r^1 & \varepsilon_r^1 & 0 & 0 \\ 0 & 0 & u_r^1 & \varepsilon_r^1 \\ u_r^2 & \varepsilon_r^2 & 0 & 0 \\ 0 & 0 & u_r^2 & \varepsilon_r^2 \end{bmatrix} \begin{bmatrix} D_{55} \\ D_{56} \\ D_{65} \\ D_{66} \end{bmatrix} = \begin{bmatrix} P_u^1 \\ P_\varepsilon^1 \\ P_u^2 \\ P_\varepsilon^2 \end{bmatrix} \tag{7.1.3}$$

whose solution provides D_{55}, D_{56}, D_{65} and D_{66}. Applying $P_u^1 = 2.638$ MNm^{-1}, $P_\varepsilon^1 = 69.58$ kN, $P_u^2 = 3.088$ MNm^{-1} and $P_\varepsilon^2 = 22.12$ kN, the radial displacements and strains obtained in the small-scale FE analysis are reported in Table 7.1 and result in the following values:

$$D_{55} = 1.0972 \times 10^{10} \text{ Nm}^{-2}$$
$$D_{56} = 2.9692 \times 10^{7} \text{ Nm}^{-1}$$
$$D_{65} = 2.9359 \times 10^{7} \text{ Nm}^{-1}$$
$$D_{66} = 6.7408 \times 10^{6} \text{ N}$$

Due to the assumed symmetry of the elasticity matrix, the coefficients D_{56} and D_{65} are set to

$$D_{56} = D_{65} = \frac{2.9692 + 2.9359}{2} \times 10^7 = 2.95255 \times 10^7 \text{Nm}^{-1}$$

The coefficients D_{15} and D_{16} may be determined by considering the axial reaction force in the above simulations. As the axial strain ε_a is zero, the following equations

apply:

$$\begin{aligned} D_{15}u_r^1 + D_{16}\varepsilon_r^1 &= N^1 \\ D_{15}u_r^2 + D_{16}\varepsilon_r^2 &= N^2 \end{aligned} \tag{7.1.4}$$

Therefore, the coefficients may be found by solving the following set of equations

$$\begin{bmatrix} u_r^1 & \varepsilon_r^1 \\ u_r^2 & \varepsilon_r^2 \end{bmatrix} \begin{bmatrix} D_{15} \\ D_{16} \end{bmatrix} = \begin{bmatrix} N^1 \\ N^2 \end{bmatrix} \tag{7.1.5}$$

The computed reactions in the small-scale simulations were $N^1 = 473.1$ kN and $N^2 = 551.2$ kN, which results in the following coefficients:

$$\begin{aligned} D_{15} = D_{51} &= 1.9715 \times 10^9 \text{ Nm}^{-1} \\ D_{16} = D_{61} &= 5.6367 \times 10^6 \text{ N} \end{aligned}$$

In accordance with the symmetry of the proposed elastic model, it will be assumed that $D_{51} = D_{15}$ and $D_{61} = D_{16}$.

To determine D_{11}, a third simulation is conducted with $P_u^3 = P_u^2$, $P_\varepsilon^3 = P_\varepsilon^2$ and with the ends free to contract (i.e. $N = 0$ while $\varepsilon_a \neq 0$). In this situation, the following equation for the axial force applies:

$$D_{11}\varepsilon_a^3 + D_{15}u_r^3 + D_{16}\varepsilon_r^3 = N = 0 \tag{7.1.6}$$

which allows D_{11} to be calculated as follows:

$$D_{11} = -(D_{15}u_r + D_{16}\varepsilon_r)/\varepsilon_z \tag{7.1.7}$$

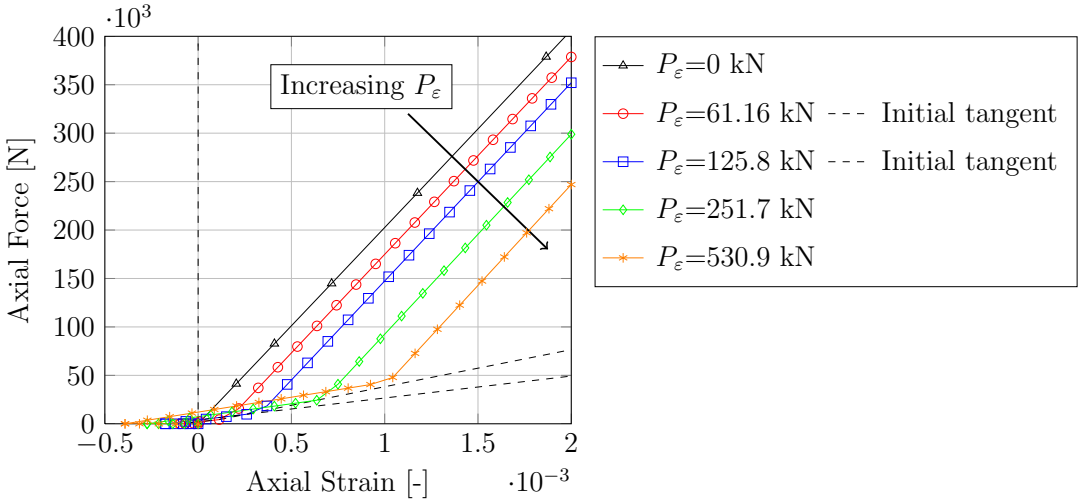

Figure 7.1: Axial force vs. axial strain for different initially applied P_ε (plot reproduced from Section 5.3.2).

The resulting values from the simulation were $\varepsilon_a^3 = 4.221\%$, $u_r^3 = 7.793$ mm and $\varepsilon_r^3 = 3.895 \times 10^{-3}$, which results in

$$D_{11} = 3.7353 \times 10^8 \text{ N} \tag{7.1.8}$$

For reasons of symmetry, pressure loading does not cause bending moments and D_{25} and D_{26} (and by symmetry of the elastic stiffness matrix, D_{52} and D_{62}) are thus equal to zero. Therefore D_{22} can be obtained from the data in Figure 5.20 by using values of bending moment and curvature after the first increment of bending only. The size of the initial curvature increment is equal in all of these bending simulations.

7.2 Identification of the parameters of the slip onset function

From Figure 5.23 no slip point is found and the slip function is proposed to be a function of bending moment and curvature alone, and thus the coefficient b is set to zero. The tangent bending stiffness values as a function of curvature (derived from

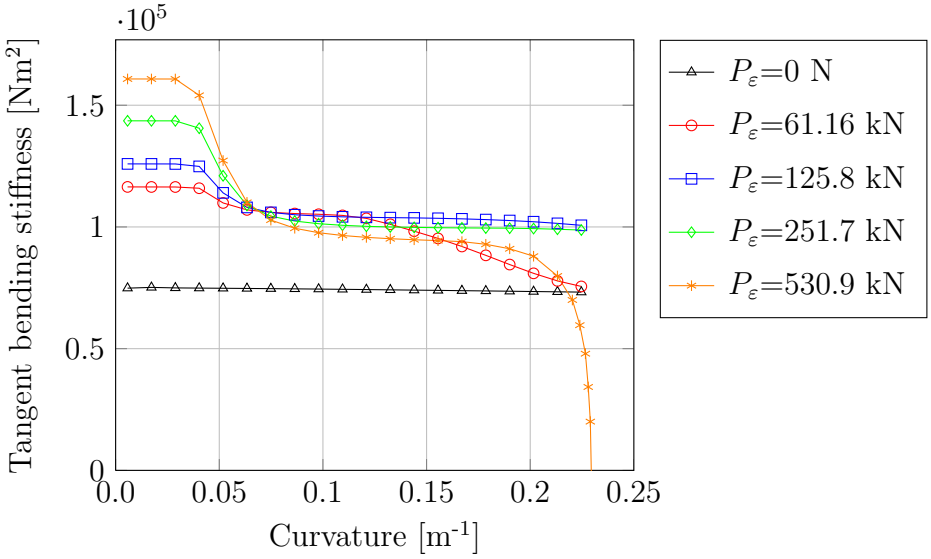

Figure 7.2: Tangent bending stiffness

Figure 5.20) are presented in Figure 7.2.

It can be determined from Figure 7.2 that slip occurs at a roughly constant curvature in all cases. There is a noticeable transition region where bending stiffness decreases at a decreasing rate until the final bending stiffness is attained. The coefficient c can be determined from the slip-onset function $cM^2 - P_\varepsilon = 0$. Averaging results for the four pressures simulations, this results in a value of c of 5.392×10^{-3} $N^{-1}m^{-2}$. It is also noted that, for the simulation with $P_\varepsilon = 530.9kN$, bending stiffness decreases to zero and the simulation terminates immediately before the curvature step is completed. This indicates loss of structural stability under bending. From inspection of the final deformed shape, it can be seen that this failure is associated with high section ovalisation which tends to cause axisymmetric collapse of the pipe.

It is further noted that the hypothesis of a constant pre- and post-slip bending stiffness appears to be approximately valid, apart from the cases P_ε= 530.9 kN (where the model showed difficulty converging at large curvatures) and P_ε= 61.19 kN.

7.3 Identification of the kinematic hardening coefficients

As no slip point can be found in axial simulations, H_{11} is set to zero.

From taking the average of the post-slip gradients in the bending moment-curvature gradients presented in Figure 5.20, the hardening parameter H_{22} can be estimated using the following relation for the tangent stiffness in linear hardening elasticity:

$$\frac{dM}{d\chi} = \frac{D_{22}H_{22}}{D_{22}+H_{22}} \implies H_{22} = \frac{\frac{dM}{d\chi}D_{22}}{D_{22}-\frac{dM}{d\chi}}$$

Averaging the hardening coefficients for all curves in Figure 5.20 gives H_{22}=8.06 $\times$ 10^5 Nm^2.

7.4 Modification for attached or detached carcass

It is recalled from the axial force simulations (results shown in Figures 5.23 and 7.1 and Section 5.3.2), that the axial stiffness of the model abruptly changes at points which were found correspond to the separation of carcass layer from the remaining layers of the FE model. In Chapter 6, a modification of the constitutive model is proposed based on an analytical derivation of the critical conditions and consequences for the axial stiffness of the model of such a separation. In this Section, the modification to the axial stiffness due to the effects of the carcass is calculated using parameters of the constitutive model identified earlier in this Chapter, according to the derivation presented in Chapter 6.

The stiffness coefficients of the carcass layer are:

$$\tilde{D}_{11} = \frac{2\pi R t_c E_a}{(1 - \nu_{ha}\nu_{ah})} = 1.0606 \times 10^7$$
$$\tilde{D}_{12} = \frac{2\pi t_c E_a \nu_{ah}}{(1 - \nu_{ha}\nu_{ah})} = 3.2968 \times 10^7$$
$$\tilde{D}_{21} = \frac{2\pi t_c E_h \nu_{ha}}{(1 - \nu_{ha}\nu_{ah})} = 3.2968 \times 10^7$$
$$\tilde{D}_{22} = \frac{2\pi t_c E_h}{(1 - \nu_{ha}\nu_{ah})} = 1.3294 \times 10^9$$

The parameters C, β and γ are

$$C = \frac{1}{2\pi R_{INT} k} = 4.8227 \times 10^{-12}$$
$$\beta = \frac{1}{1 + C\tilde{D}_{22}} = 0.99363$$
$$\gamma = -\frac{C\tilde{D}_{12}}{1 + C\tilde{D}_{22}} = -1.5798 \times 10^{-4}$$

The addition to the stiffness matrix is then

$$D_{WITHC} = \begin{pmatrix} 1.0601 & 0 & 3.2758 & 0.0022931 \\ 0 & 0 & 0 & 0 \\ 3.2758 & 0 & 132.09 & 0.093058 \\ 0.0022931 & 0 & 0.093058 & 0.000064726 \end{pmatrix} \times 10^7$$

Predictions of axial behaviour for $P_\varepsilon = 61.18$ kN using the modified stiffness matrix and the detailed FE model are shown in Figure 7.3.

These results show that the linear model predicts axial forces well up to the point the carcass meets the other layers. However, even using the modification to account for carcass separation the linear model does not predict axial stresses past this point well. This requires that the carcass separation model be re-examined and the FE model further investigated to discover the cause and mechanism of the large increase in axial stiffness.

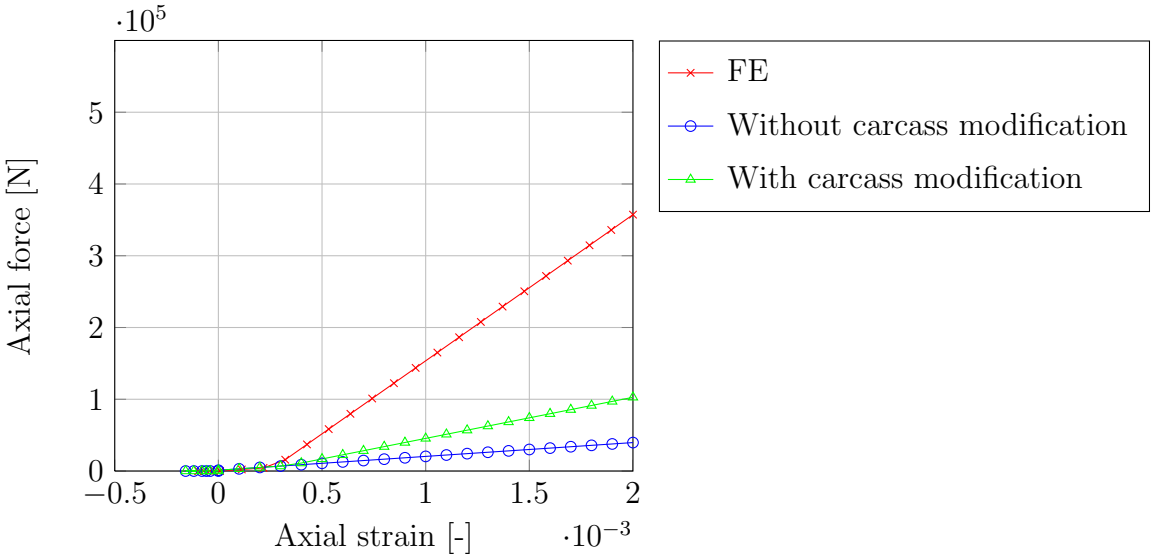

Figure 7.3: Predictions of axial force from generalised strain data

7.5 Summary of model parameters

The model coefficients determined are presented in full in Table 7.4:

Parameter	Value		Parameter	Value	
D_{11}	3.7353×10^8	N	H_{11}	0.0×10^0	Nm^2
D_{22}	1.1528×10^5	Nm^{-2}		.	
D_{15}	1.9715×10^9	Nm^{-1}	H_{22}	8.06×10^5	Nm^2
D_{16}	5.6367×10^6	N		.	
D_{55}	1.0972×10^{10}	Nm^{-2}		.	
D_{56}	2.9526×10^7	Nm^{-1}	R_{INT}	9.73×10^{-2}	m
D_{66}	6.7408×10^6	N	R_{EXT}	1.162×10^{-2}	m
b	0.0		R_c	9.94×10^{-2}	m
c	5.392	$N^{-1}m^{-2}$		.	

Figure 7.4: Model parameters

Chapter 8

Conclusions

8.1 Key findings

In this work, a multi-scale method for the mechanical simulation of flexible pipes is presented, drawing on existing large- and small-scale modelling techniques used for flexible pipes, and on multi-scale techniques in computational mechanics.

A general framework is developed for computational homogenisation where models at both scales are comprised of structural elements (Chapter 3). By using general, abstract spaces of displacement, strain, stress and forces and duality principles, it is shown how the concepts and procedures of the first-order computational homogenisation method may be generalised including that of the Hill-Mandel principle of macro-homogeneity and method for imposing and recovering generalised stresses and strains from the small-scale model. The solution of a nonlinear truss problem is demonstrated using a coupled homogenisation approach based on these principles. Good multi-scale convergence results are shown. This framework is novel, of general applicability and allows the creation of a wider range of multi-scale models than was previously possible using spatial averaging techniques.

Using the above methods, a sequential multi-scale analysis of flexible pipes is proposed and carried out, which requires definition of a large-scale model and a small-scale model, and determination of the parameters of the large-scale model using simulation data from the small-scale model.

For the large-scale model, the nonlinear constitutive model developed by Bahtui

(2008) is implemented in a user-defined element subroutine (coded in FORTRAN) such that it can be used with the commercial finite element program Abaqus (Chapter 4). A robust constitutive solver for this plasticity model was developed (Section 4.3) and the algorithm was shown to have good convergence properties for processing various combined generalised stress states in the pipe. To enable the formulation to be used in a beam where large displacements occur, an existing two-dimensional corotational formulation is included in the coding. A new three-dimensional corotational formulation was also developed (Section 4.5 and Appendix B), which makes possible the use of beam elements in a three-dimensional riser simulations so that multiaxial loading and torsion may be analysed.

A detailed finite element model of a flexible pipe has been developed (Chapter 5). This model is based on shell elements and computes contact interactions between all components in the pipe. The model incorporates recent developments in contact modelling that reduce some of the limitations in using shell elements by using a penalty method for enforcing normal contact constraints that represent the true layer compliance. The model uses an implicit solution procedure. The main innovation is the use of periodic boundary conditions imposed with a "control node" and linear constraint equations. This follows standard practice in composites modelling. To enable the rapid creation of parameterised flexible pipe models of arbitrary component dimensions and internal arrangement, a Python script was written that automates the model creation steps in Abaqus/CAE.

The model is validated against two flexible pipe analytical models for axial, internal pressure and external pressure and found to give fairly close results in terms of bulk response and component stresses. Bending results using this technique show reduced end effects (which are an artificial result of an over-constrained model) due to the use of periodic boundary conditions. It is shown that boundary condition choice affects not only component stresses but also initial bending stiffness and energy loss through hysteresis. Contour plots of component stress, contact pressure and tangential slip between components are shown to be significantly smoother than results from previous finite element models of flexible pipes. A full set of results are obtained using the model for a pipe under axial, bending, torsion and pressure

loading. Radial displacement and radial strain results show that the model captures the radial response of a pipe in a qualitatively realistic way.

It was discovered that, under combined pressure and axial loading, a sudden and significant increase in the axial stiffness was observed to occur at axial strain levels that varied with the pressure. The physical mechanism for this increase was discovered to be due to the carcass separating from the other layers in the initial pressurisation step. The carcass then re-attaches to the other layers when sufficient axial loading is applied to the pipe, a phenomenon which may occur in practice in operating regimes of high internal pressure, low external pressure and low tension. In Chapter 6, an analytical derivation of this increase in axial stiffness is presented.

In Chapter 7, data from simulations using the detailed model are used to derive parameters of the large scale model. In distinction to the work of Bahtui (2008), no reduction in axial stiffness is observed at high axial strain and thus axial loading is concluded not to cause interlaminar sliding. It is likely that this difference in results is a consequence in the different boundary conditions used. The bending response appears to indicate that initial bending stiffness of a flexible pipe varies with the effective pressure. It is suggested that a better way to represent the pipe response would be to use a purely plastic material model, in which yielding occurs even for very small curvatures, and to model the hardening response as a nonlinear relationship dependent on the pressure.

8.2 Future work

Several avenues for future investigation arising from this work can be identified. Potential applications of the structural-to-structural computational homogenisation procedure include the creation of multi-scale models of auxetic materials and honeycomb structures. A further possibility is the creation of intuitive multi-scale models for materials and structures consisting of a variety of structural elements (such as springs, dampers and frictional sliders) at the small scale. This framework would allow such models to be quickly investigated and modified.

For further work of finite-element-based modelling of flexible pipe, suggestions

can be made regarding both the large and small-scale models.

The large-scale model could be made more complete by the addition of a mass matrix. It is proposed that the corotational beam element could be used with the buoyancy and external load relations developed by Yazdchi and Crisfield (2005). Use of a mixed finite element method (as used in Flexcom) to improve convergence is of theoretical and practical interest.

The results of the detailed finite element analyses in this work suggest that there is scope for improvement in the constitutive models used in large-scale models of flexible pipes. Formulation of new constitutive models should make full use of all available test data to understand the phenomena and mechanisms that occur in practice.

Regarding the detailed FE model, as an alternative to the use of shell elements to model helical wires, the use of beam elements (as used by de Sousa et al. (2010)) could be investigated. In this case, attention would need to be paid to accurate representation of the wire cross-section when computing contact interactions. Such elements would not "lie flat" on the supporting cylindrical surface, and this inaccuracy in discretisation could lead to anomalies and inaccuracies. However, computations may be faster and, depending on the wire's cross-sectional aspect ratio, this may be a better structural model of the wire. It is the author's contention that implicit FE methods, despite causing convergence difficulties, are more promising than explicit methods for investigating the component stresses arising in a flexible pipe.

The multi-scale procedure may also be carried out as a nested analysis, in which generalised stresses and the material tangent are obtained by direct simulation using the detailed model, for each integration point, for each iteration in the analysis. The computational cost could be minimised by storing the last converged deformed configuration of the detailed model in restart files, meaning that the latest strain increments can be applied to the detailed model instead of the entire strain. Similarly, the use of very short FE models (as used by Leroy et al. (2010)) in this context can be investigated. Efforts could be made to reduce run times for the detailed model by using reduced integration shell elements and improved parallelisation.

No convergence study was carried out on the mesh used for the detailed finite

element model, as the initially proposed discretisation caused simulations to have fairly long run-times and refining the mesh further was not practically feasible. However with increased computing power and a more effective FE model this could be done. It seems likely that the most critical feature that could require improved discretisation to model accurately is the bending stresses and lateral displacements of the tensile armour wires under pipe bending.

Finally, it should be noted that comparison with test results is essential to validate the multi-scale model such that it can be used as a reliable tool for pipeline analysis. Test data used for comparison would need to include results for the stresses in the tensile wires, and if possible, the local bending stresses in the wires, as well as bending moment-curvature data under different values of internal pressure.

In summary, the approach presented in this work seems promising though there remains considerable scope for analysts and experimental investigators to develop and calibrate reliable multi-scale finite element models for flexible pipes.

Bibliography

Addessi, D., Sacco, E., Paolone, A., 2010. Cosserat model for periodic masonry deduced by nonlinear homogenization. European Journal of Mechanics, A/Solids 29, 724–737.

Alfano, G., Bahtui, A., Bahai, H., 2009. Numerical derivation of constitutive models for unbonded flexible risers. International Journal of Mechanical Science .

Amieur, M., Hazanov, S., Huet, C., 1995. Numerical and experimental assesment of the size and boundary conditions effects for the overall properties of granular composite bodies smaller than the representative volume, in: Parker, D., England, A. (Eds.), IAUTAM Symposium on Anisotropy, Inhomogeneity and Nonlinearity in Solid Mechanics, Kluwer Academic Publishers, Dordrecht. pp. 149–154.

API, 1998, 1998. Recommended Practice for Flexible Pipe. Technical Report 17B. American Petroleum Institute. 1220 L Street N.W., Washington D.C. 20005.

Bahai, H., Hosseini-Khordkheili, S.A., 2008. Nonlinear dynamic analysis of flexible riser structures, in: Proceedings of the ASME 2008 27th International Conference on Offshore, Ocean and Arctic Engineering. OMAE2008-58014.

Bahtui, A., 2008. Development of a Constitutive Model to Simulate Unbonded Flexible Riser Pipe Elements. Ph.D. thesis. Brunel Univ,ersity, UK.

Bahtui, A., Alfano, G., Bahai, H., 2009. Numerical and analytical modelling of unbonded flexible risers. Journal of Offshore Mechanics and Arctic Engineering-Transactions of the ASME 131, 1–14.

Bahtui, A., Alfano, G., Bahai, H., Hosseini-Kordkheili, S.A., 2010. On the multi-scale computation of un-bonded flexible risers. Engineering Structures 32, 2287–2299.

Bai, Y., Bai, Q., 2005. Subsea Pipelines and Risers. Elsevier Ltd.

Bathe, K.J., Almeida, C., 1980. A simple and effective pipe elbow element: Linear analysis. Journal of Applied Mechanics 47, 93–100.

Bathe, K.J., Almeida, C., Ho, L., 1983. A simple and effective pipe elbow element: Some nonlinear capabilities. Computers and Structures 17, 659–667.

Belytschko, T., Liu, W.K., Moran, B., 2000. Nonlinear Finite Elements for Continua and Structures. John Wiley and Sons, Ltd.

Bergan, P.G., Mollestad, E., Sandsmark, N., 1985. Non-linear and dynamic response analysis for floating offshore structures. Eng. Comput. 2, 13–20.

Buannic, N., Cartraud, P., 2001. Higher-order effective modeling of periodic heterogenous beams. I. asymptotic expansion method. International Journal of Solids and Structures 38, 7139–7161.

Coenen, E., Kouznetsova, V., Geers, M., 2010. Computational homogenization for heterogeneous thin sheets. International Journal for Numerical Methods in Engineering 83, 1180–1205.

Costello, G.A., 1977. Large deflections of helical spring due to bending. Journal of the Engineering Mechanics Division 103, 481–487. Technical Note, American Society of Civil Engineers.

Crisfield, M., 1997. Non-linear Finite Element Analysis of Solids and Structures. volume 2: Advanced Topics. John Wiley and Sons.

Crisfield, M., Moita, G., 1996. A unified corotational framework for solids, shells and beams. International Journal for Solids and Structures 33, 2969–2992.

Custódio, A.B., Vaz, M.A., 2002. A nonlinear formulation for the axisymmetric response of umbilical cables and flexible pipes. Applied Ocean Research 24, 21–29.

da Silveira, L., de Arruda Martins, C., 2005. A numerical method to solve the three-dimensional static problem of a riser with bending stiffness, in: Proceedings of the International Conference on Offshore Mechanics and Arctic Engineering, Halkidiki,Greece. pp. 297–307. OMAE2005-67130, summary of validation with Orcaflex is available at http://www.orcina .com/SoftwareProducts/OrcaFlex/-Validation/index.php, Detailed Validation case 99/103.

de Sousa, J.R.M., Viero, P., Magluta, C., Roitman, N., 2010. An experimental and numerical study on the axial compression response of flexible pipes, in: Proceedings of the ASME 2010 29th International Conference on Offshore, Ocean and Arctic Engineering. OMAE2010-20856.

Edmans, B., Alfano, G., Bahai, H., 2010a. Multiscale finite element modelling of flexible marine risers, in: Proceedings of the 10th International Conference on Computational Plasticity (COMPLAS X).

Edmans, B., Alfano, G., Bahai, H., 2010b. Multiscale modelling of flexible risers with nonlinear homogenisation, in: Proceedings of the ASME 2010 29th International Conference on Ocean, Offshore and Arctic Engineering. OMAE2010-21020.

Felippa, C.A., Chung, J.S., 1981. Nonlinear static analysis of deep ocean mining pipe. Transactions of the ASME: Journal of Energy Resources Technology 103, 11–25.

Féret, J., Leroy, J.M., Estrier, P., 1995. Calculation of stresses and slips in flexible armour layers with layers interaction, in: Proceedings of the International Conference on Offshore Mechanics and Arctic Engineering, pp. 469–474.

Féret, J.J., Bournazel, C.L., 1987. Calculation of stresses and slip in structural layers of unbonded flexible pipes. Journal of Offshore Mechanics and Arctic Engineering 109, 263–269.

Feyel, F., Chaboche, J.L., 2000. FE^2 multiscale approach for modelling the elastoviscoplastic behaviour of long fibre SiC/Ti composite materials. Computer Methods in Applied Mechanics and Engineering 183, 309–330.

Fish, J., Shek, K., 2000. Multiscale analysis of composite materials and structures. Composites Science and Technology 60, 2547–2556.

Flexcom, 2011, 2011. Flexcom data sheet. MCS Kenny.

Fritzen, F., Böhlke, T., 2010. Influence of the type of boundary conditions on the numerical properties of unit cell problems. Technische Mechanik 30, 254–363.

Geers, M., Coenen, E., Kouznetsova, V., 2007. Multi-scale computational homogenisation of thin sheets. Modelling and Simulation in Materials Science and Engineering 15, 393–404.

Geers, M., Kouznetsova, V., Brekelmans, W., 2002. Multi-scale constitutive modelling of heterogenous materials with a gradient-enhanced computational homogenisation scheme. International Journal for Numerical Method in Engineering 54, 1235–1260.

Ghosh, S., Lee, K., Moorthy, S., 1995. Multiple scale analysis of heterogeneous elastic structures using homogenization theory and voronoi cell finite element method. Int. J. Solids Structures 32, 27–62.

Goto, Y., Okamoto, T., Araki, M., Fuku, T., 1987. Analytical study of the mechanical strength of flexible pipes. J. Offshore Mech. and Arctic Engg. 109, 249–253.

Guedes, J., Kikuchi, N., 1990. Preprocessing and postprocessing for materials based on the homogenization method with adaptive finite element methods. Computer Methods in Applied Mechanics and Engineering 83, 143–198.

Harte, A.M., McNamara, J.F., 1989. Three-dimensional analytical simulation of flexible pipe wall structure, in: Proceedings of the 8th International Conference on Offshore Mechanics and Arctic Engineering, pp. 477–482.

Harte, A.M., McNamara, J.F., 1993. Modeling procedures for the stress analysis of flexible pipe cross-sections. Journal of Offshore Mechanics and Arctic Engineering 115, 46–51.

Hashin, Z., 1983. Analysis of composite materials - a survey. Journal of Applied Mechanics 50, 481–505.

Hassani, B., Hinton, E., 1998. A review of homogenization and topology optimization: I- homogenization theory for media with periodic microstructures. Computers and Structures 69, 707–717.

Hazanov, S., Amieur, M., 1995. On overall properties of elastic heterogeneous bodies smaller then the representative volume. Int. J. Engrg. Sci. 33, 1289–1301.

Hazanov, S., Huet, C., 1994. Order relationships for boundary conditions in heterogenous bodies smaller than the representative volume. J. Mech. Phys. Solids 42, 1995–2011.

Hill, R., 1963. Elastic properties of reinforced solids: some theoretical principles. J. Mech. Phys. Solids 11, 357–372.

Hill, R., 1972. On constitutive macro-variables for heterogeneous solids at finite strain. Proc. R. Soc. London, Ser. A 11, 131–147.

Hosseini-Khordkheili, S., Bahai, H., 2008. Non-linear finite element analysis of flexible risers in presence of buoyancy force and seabed interaction boundary condition. Arch. Appl. Mech. 78, 765–774.

Hsiao, K.M., Horng, H.J., Chen, Y.R., 1987. A corotational procedure that handles large rotations of spatial beam structures. Computers and Structures 27, 769–781.

Kaczmarczyk, Ł., Pearce, C., Bićanić, N., de Souza Neto, E., 2010. Numerical multiscale solution strategy for fracturing heterogeneous materials. Computer Methods in Applied Mechanics and Engineering 199, 1100–1113.

Knapp, R.H., 1979. Derivation of a new stiffness matrix for helically armoured cables considering tension and torsion. International Journal for Numerical Methods in Engineering 14, 415–529.

Kraincanic, I., Kebadze, E., 2001. Slip initiation and progression in helical armouring layers of unbonded flexible pipes and its effect on pipe bending behaviour. Journal of Strain Analysis 36, 265–275.

Lanteigne, J., 1985. Theoretical estimation of the response of helically armoured cables to tension, torsion and bending. Journal of Applied Mechanics 52, 423–432.

Larsson, F., Runesson, K., Saroukhani, S., Vafadari, R., 2011. Computational homogenization based on a weak format of micro-periodicity for rve-problems. Computer Methods in Applied Mechanics and Engineering 200, 11–26.

Le Corre, V., Probyn, I., 2009. Validation of a 3-dimensional finite element analysis model of a deep-water steel tube umbilical in combined tension and cyclic bending, in: Proceedings of the International Conference on Offshore Mechanics and Arctic Engineering, Honolulu, Hawaii.

Leroy, J.M., Estrier, P., 2001. Calculation of stresses and slips in helical layers of dynamically bent flexible pipes. Oil and Gas Science and Technology - Rev. IFP 56, 545–554.

Leroy, J.M., Estrier, P., et al, T.P., 2010. Stress assesment in armour layers of flexible risers, in: Proceedings of the ASME 2010 29th International Conference on Offshore, Ocean and Arctic Engineering. OMAE2010-20932.

Løtveit, S.A., Often, O., 1990. Increased reliability through a unified analysis tool for bonded and non-bonded pipes. Advances in subsea pipeline engineering & technology, Society for Underwater Technology Conference Aspect 90 24, 79–110. Utrecht.

Love, A.E.H., 1944. A Treatise on the Mathematical Theory of Elasticity. Dover, New York. 4 edition.

Low, Y., Langley, R., 2006. A comparison of time domain and frequency domain approaches for the fully coupled analysis of deepwater floating systems, in: Proceedings of the International Conference on Offshore Mechanics and Arctic Engineering, Hamburg, Germany.

Marfia, S., Sacco, E., 2012. Multiscale damage contact-friction model for periodic masonry walls. Computer Methods in Applied Mechanics and Engineering 205-208, 189–203.

Matsui, K., Terada, K., Yuge, K., 2004. Two-scale finite element analysis of heterogenous solids with periodic microstructure. Computers and Structures 82, 593–606.

McIver, D., 1992. A method of modelling the detailed component and overall structural behaviour of flexible pipe sections, in: MARINFLEX92, Proc. 1st European Conference on Flexible Pipes, Umbilicals and Marine Cables. London.

McIver, D.B., 1995. A method for modelling the detailed component and overall structural behaviour of flexible pipe sections. Engineering Structures 17, 254–266.

McNamara, J.F., Lane, M., 1984. Practical modeling for articulated risers and loading columns. Transactions of the ASME: Journal of Energy Resources Technology 106, 444–450.

Merino, H.E.M., de Sousa, J.R.M., Magluta, C., Roitman, N., 2010. Numerical and experimental study of a flexible pipe under torsion, in: Proceedings of the ASME 2010 29th International Conference on Offshore, Ocean and Arctic Engineering. OMAE2010-20902.

Michel, J.C., Moulinec, H., Suquet, P., 1999. Effective properties of composite materials with periodic microstructure: a computational approach. Comput. Methods Appl. Mech. Engrg. 172, 109–143.

O'Brien, P.J., McNamara, J.F., Grealish, F., 1991. Extreme bending and torsional responses of flexible pipelines, in: Proceedings of the ASME 11th International

Offshore Mechanics and Arctic Engineering Symposium, Calgary, Canada. pp. 319–324.

de Oliveira, J., Goto, Y., Okamoto, T., 1985. Theoretical and methodological approaches to flexible pipe design and application, in: Offshore Technology Conference, OTC 5021, Houston, TX, USA. pp. 517–526.

Oliveira, J., Pinho-da-Cruz, J., Teixeira-Dias, F., 2009. Asymptotic homogenisation in linear elasticity. Computational Materials Science 45, 1073–1096.

Orcina Ltd., 2010, . OrcaFlex Manual. Version 9.5a.

Out, J.M.M., von Morgen, B.J., 1997. Slippage of helical reinforcing on a bent cylinder. Engineering Structures 19, 507–515.

Palmer, A.C., King, R.A., 2008. Subsea Pipeline Engineering. PennWell Corporation.

Perić, D., De Souza Neto, E., Somer, D., Dettmer, W., 2009. On computational procedures for multiscale analysis of heterogeneous solids: Variational basis and fe implementation, in: Computational Plasticity X - Fundamentals and Applications.

Perić, D., de Souza Neto, E.A., Feijóo, R.A., Partovi, M., Molina, A.J.C., 2011. On micro-to-macro transitions for multi-scale analysis of non-linear heterogeneous materials: unified variational basis and finite element implementation. International Journal for Numerical Methods in Engineering 87, 149–170.

Provasi, R., de Arruda Martins, C., 2010. A finite macro-element for cylindrical layer modelling, in: Proceedings of the ASME 2010 29th International Conference on Ocean, Offshore and Arctic Engineering, Shanghai, China. OMAE2010-20379.

Provasi, R., de Arruda Martins, C., 2011. A three-dimensional curved beam element for helical components modelling, in: Proceedings of the ASME 2011 30th International Conference on Ocean, Offshore and Arctic Engineering, Rotterdam, Netherlands. OMAE2011-49133.

Ramos, Jr., R., de Arruda Martins, C., Pesce, C.P., 2008. A case study on the axial-torsional behaviour of flexible pipes, in: Proceedings of the ASME 2008 27th International Conference on Offshore, Ocean and Arctic Engineering. OMAE2008-57514.

Richards, D., Andronicou, A., 1997. Verification of flexible risers and flowlines for offshore applications, in: The OCS Technology Group International Conference of Floating Production Systems, Stavanger, Norway.

Risa, A., 2011. Finite element analysis of marine umbilical. Master's thesis. Department of Marine Structures, NTNU, Trondheim, Norway.

Royal Dutch Shell plc, 1976. Development and Onshore Testing of a 4 inch ID 10,000 psi Coflexip Flexible Flowline. Technical Report EP.47 194. Shell Internationale Petroleum Maatschappij B. V. (EP/29).

Sævik, S., 1993. A finite element model for predicting stresses and slip in a flexible pipe armouring tendons. Computers and Structures 46, 219–230.

Sævik, S., 2010. Comparison between theoretical and experimental flexible pipe bending stresses, in: Proceedings of the ASME 2010 29th International Conference on Offshore, Ocean and Arctic Engineering. OMAE2010-20352.

Sævik, S., Giertsen, E., Olsen, G., 1998. A new method for calculating stresses in flexible pipe tensile armours, in: Proceedings of the ASME 1998 17th International Conference on Offshore, Ocean and Arctic Engineering, Lisboa.

Samadikhah, K., Larsson, R., Bazooyar, F., Bolton, K., 2012. Continuum-molecular modelling of graphene. Computational Materials Science 53, 37–43.

Simo, J., Hughes, T., 1998. Computational Inelasticity. Springer Verlag.

Smith, C., Grima, J., Evans, K., 2000. Novel mechanism for generating auxetic behaviour in reticulated foams: Missing rib foam model. Acta Materialia 48, 4349–4356.

Suquet, P., Marigo, J.J., Mialon, P., Michel, J.C., 1987. Plasticity and homogenization: An example of prediction of the limit loads of a periodic heterogeneous structure. [plasticite et homogeneisation: Un exemple de prevision des charges limites d'une structure heterogene periodique.]. Journal de mecanique theorique et appliquee 6, 47–75.

Tan, Z., Case, M., Sheldrake, T., 2005. Higher order effects on bending of helical armor wire inside an unbonded flexible pipe, in: Proceedings of the 24th Conference on Offshore Mechanics and Arctic Engineering, pp. 447–455. OMAE2005-67106.

Tan, Z., Quiggin, P., Sheldrake, T., 2007. Time domain simulation of the 3D bending hysteresis behaviour of an unbonded flexible riser, in: Proceedings of the 26th International Conference on Offshore Mechanics and Arctic Engineering. OMAE2007-29315.

Terada, K., Hori, M., Kyoya, T., Kikuchi, N., 2000. Simulation of the multi-scale convergence in computational homogenization approaches. International Journal of Solids and Structures 37, 2285–2311.

Terada, K., Kikuchi, N., 2001. A class of general algorithms for multi-scale analyses of heterogenous media. Comput. Methods Appl. Mech. Engrg. 190, 5427–5464.

Tollenaere, H. andCaillerie, D., 1998. Continuous modeling of lattice structures by homogenization. Advances in Engineering Software 29, 699–705.

Urthaler, Y., Reddy, J., 2005. A corotational finite element formulation for the analysis of planar beams. Communications in Numerical Methods in Engineering 21, 553–570.

Van Der Sluis, O., Schreurs, P., Brekelmans, W., Meijer, H., 2000. Overall behaviour of heterogeneous elastoviscoplastic materials: Effect of microstructural modelling. Mechanics of Materials 32, 449–462.

Vaz, M.A., Rizzo, N.A.S., 2011. A finite element model for flexible pipe armour wire instability. Marine Structures 24, 275–291.

von Morgen, B., . Analysis of flexible pipe: Bending of cylinder with helical reinforcing. Technical Report 88.03.OS.2492. Faculteit der Werktuigbouwkunde en Maritieme Techniek, TU Delft.

Witz, J., Tan, Z., 1992a. On the axial-torsional structural behaviour of flexible pipes, umbilicals and marine cables. Marine Structures 5, 205–227.

Witz, J., Tan, Z., 1992b. On the flexural structural behaviour of flexible risers, umbilicals and marine cable. Marine Structures 5, 229–249.

Witz, J.A., 1996. A case study in the cross-section analysis of flexible risers. Marine Structures 9, 885–904.

Witz, J.A., Tan, Z., 1995. Rotary bending of marine cables and umbilicals. Engineering Structures 17, 267–275.

Yazdchi, M., 2005. Buoyancy potential conserving technique for dynamic analysis of flexible marine pipes and risers. International Journal for Numerical Methods in Engineering 63, 2040–2067.

Yazdchi, M., Crisfield, M., 2002a. Non-linear dynamic behaviour of flexible marine pipes and risers. International Journal for Numerical Methods in Engineering 54, 1265–1308.

Yazdchi, M., Crisfield, M., 2002b. Non-linear dynamic behaviour of flexible marine pipes and risers. International Journal for Numerical Methods in Engineering 54, 1265–1308.

Yuan, Z., Fish, J., 2007. Towards realisation of computational homogenisation in practise. International Journal for Numerical Methods in Engineering 73, 361–380.

Appendix A

Software for flexible pipe analysis

Coflexip, NKT Engineering, Wellstream

Relevant industry standards:

- API RP 17B, "Recommended Practice for Flexible Pipe", 1988.
- Bureau Veritas, "Non-Bonded Flexible Steel Pipes used as Flow-Lines".
- Veritec, "Guidelines for Flexible Pipes", 1987.
- Det Norske Veritas, "Rules for Certification of Flexible Risers and Pipes", 1994.
- MCS International, "Specification for Unbonded Flexible Pipe", JIP Doc. No: 5-4-012/SP01, Rev. 5, January, 1996.
- MCS International, "Recommended Practice for Unbonded Flexible Pipe", JIP Doc. No: 5-4-029/RP01, Rev. 2, October, 1995.

Name	Institution	References	Notes
Bflex	Marintek	Sævik et al. (1998)	Stresses and fatigue in tensile and pressure armour layers, local analysis only
Caflex/Eflex	Institut Français du Pétrole	Féret and Bournazel (1987)	Stress assessment in cross-sections
FENRIS		Bergan et al. (1985)	General purpose nonlinear FE code used with linear bar elements, fully nonlinear formulation
Flex-Able		McIver (1995)	Stress analysis of sections
Flexcom-3D	MCS Kenny		Nonlinear FE, for general offshore systems, time-domain and frequency domain, hybrid beam elements
Flexpipe		Løtveit and Often (1990)	
Orcaflex	Orcina Ltd.	(Orcina Ltd., 2010)	Global analysis program, time domain (see **2.5**)
RIFLEX	Marintek		Static and linearised dynamic analysis of risers, bar and beam finite elements, time domain analysis
STA Catenary	Stewart Technology Associates		2D global static analysis program
Zenriser (formerly Flexriser)	Zentech International Inc.		Finite differences, 3D global dynamic analysis program

Table A.1: Commercial software used for flexible pipe analysis

Appendix B

Tangent matrix derivation for 3D corotational formulation

In this Appendix, the tangent matrix for the 3D corotational formulation described in Section 4.5 is derived. Nomenclature follows that used in the above Section.

The tangent stiffness matrix is found by taking the variation of the internal force vector:

$$\begin{aligned}\delta\mathbf{F}_{int} &= \delta\boldsymbol{\Theta}^T\hat{\mathbf{F}}'_{int} + \boldsymbol{\Theta}^T\delta\hat{\mathbf{F}}'_{int} \\ &= \delta[(\mathbf{TA} + \mathbf{H}\hat{\mathbf{u}})^T]\hat{\mathbf{F}}'_{int} + \boldsymbol{\Theta}^T\hat{\mathbf{K}}\delta\hat{\mathbf{u}}' \\ &= [\delta\mathbf{TA} + \mathbf{T}\delta\mathbf{A} + \mathbf{H}\delta\hat{\mathbf{u}} + \delta\mathbf{H}\hat{\mathbf{u}}]\hat{\mathbf{F}}'_{int} + \boldsymbol{\Theta}^T\hat{\mathbf{K}}\boldsymbol{\Theta}\delta\mathbf{u} \qquad \text{(B.0.1)}\end{aligned}$$

Next, the following derivatives are introduced:

$$\mathbf{H} = \frac{\partial\mathbf{T}}{\partial\mathbf{u}} \qquad \Rightarrow \delta\mathbf{T} = \mathbf{H}\ \delta\mathbf{u} \qquad \text{(B.0.2a)}$$

$$\boldsymbol{\Lambda} = \frac{\partial\mathbf{A}}{\partial\mathbf{u}} \qquad \Rightarrow \delta\mathbf{A} = \boldsymbol{\Lambda}\ \delta\mathbf{u} \qquad \text{(B.0.2b)}$$

$$\boldsymbol{\Gamma} = \frac{\partial\mathbf{H}}{\partial\mathbf{u}} \qquad \Rightarrow \delta\mathbf{H} = \boldsymbol{\Gamma}\ \delta\mathbf{u} \qquad \text{(B.0.2c)}$$

It is noted that $\mathbf{H}$ and $\boldsymbol{\Lambda}$ are third-order tensors, and $\boldsymbol{\Gamma}$ is a fourth-order tensor. Therefore,

$$\delta\mathbf{F}_{int} = [(\mathbf{H}\delta\mathbf{u})\mathbf{A} + \mathbf{T}(\mathbf{\Lambda}\delta\mathbf{u}) + \mathbf{H}(\mathbf{A}\delta\mathbf{u}) + (\mathbf{\Gamma}\delta\mathbf{u})\hat{\mathbf{u}}]\hat{\mathbf{F}}'_{int} + \mathbf{\Theta}^T\hat{\mathbf{K}}\mathbf{\Theta}\delta\mathbf{u} \tag{B.0.3}$$

To manipulate this expression algebraically, we express the left hand side terms in indical notation:

$$[(\mathbf{H}\delta\mathbf{u})\mathbf{A}]_{ij} = \mathbf{H}_{ikl}\delta\mathbf{u}_l\mathbf{A}_{kj} = (\mathbf{H}_{ikl}\mathbf{A}_{kj})\delta\mathbf{u}_l \tag{B.0.4a}$$

$$[\mathbf{T}(\mathbf{\Lambda}\delta\mathbf{u})]_{ij} = \mathbf{T}_{ik}\mathbf{\Lambda}_{kjl}\delta\mathbf{u}_l = (\mathbf{T}_{ik}\mathbf{\Lambda}_{kjl})\delta\mathbf{u}_l \tag{B.0.4b}$$

$$[\mathbf{H}(\mathbf{A}\delta\mathbf{u})]_{ij} = \mathbf{H}_{ijk}(\mathbf{A}_{kl}\delta\mathbf{u}_l) = (\mathbf{H}_{ijk}\mathbf{A}_{kl})\delta\mathbf{u}_l \tag{B.0.4c}$$

$$[(\mathbf{\Gamma}\delta\mathbf{u})\hat{\mathbf{u}}]_{ij} = \mathbf{\Gamma}_{ijlk}\delta\mathbf{u}_k\hat{\mathbf{u}}_l = (\mathbf{\Gamma}_{ijlk}\hat{\mathbf{u}}_l)\delta\mathbf{u}_k \tag{B.0.4d}$$

We now define the operations for tensors $\mathbf{X}$ and $\mathbf{Y}$ such that:

$$(\mathbf{X}\odot\mathbf{Y})_{ijk} \stackrel{def}{=} \mathbf{X}_{ikj}\mathbf{Y}_k \qquad \text{for } O(\mathbf{X})=3,\ O(\mathbf{Y})=1 \tag{B.0.5a}$$

$$(\mathbf{X}\oplus\mathbf{Y})_{ijk} \stackrel{def}{=} \mathbf{X}_{ilk}\mathbf{Y}_{lj} \qquad \text{for } O(\mathbf{X})=3,\ O(\mathbf{Y})=2 \tag{B.0.5b}$$

$$(\mathbf{X}\oslash\mathbf{Y})_{ijk} \stackrel{def}{=} \mathbf{X}_{ijlk}\mathbf{Y}_l \qquad \text{for } O(\mathbf{X})=4,\ O(\mathbf{Y})=1 \tag{B.0.5c}$$

$$(\mathbf{XY})_{12\cdots(n-1)(n+1)\cdots z} \stackrel{def}{=} \mathbf{X}_{12\cdots n}\mathbf{Y}_{n\cdots z} \qquad \text{for } O(\mathbf{X})>1,\ O(\mathbf{Y})>1 \tag{B.0.5d}$$

This allows the terms to expressed more compactly as:

$$(\mathbf{H}_{ikl}\mathbf{A}_{kj})\delta\mathbf{u}_l = (\mathbf{H}\oplus\mathbf{A})_{ijl}\ \delta\mathbf{u}_l = (\mathbf{H}\oplus\mathbf{A})\delta\mathbf{u} \tag{B.0.6a}$$

$$(\mathbf{T}_{ik}\mathbf{\Lambda}_{kjl})\delta\mathbf{u}_l = (\mathbf{T}\mathbf{\Lambda})_{ijl}\delta\mathbf{u}_l = (\mathbf{T}\mathbf{\Lambda})\delta\mathbf{u} \tag{B.0.6b}$$

$$(\mathbf{H}_{ijk}\mathbf{A}_{kl})\delta\mathbf{u}_l = (\mathbf{H}\mathbf{A})_{ijl}\delta\mathbf{u}_l = (\mathbf{H}\mathbf{A})\delta\mathbf{u} \tag{B.0.6c}$$

$$(\mathbf{\Gamma}_{ijlk}\hat{\mathbf{u}}_l)\delta\mathbf{u}_k = (\mathbf{\Gamma}\oslash\hat{\mathbf{u}})_{ijk}\ \delta\mathbf{u}_k = (\mathbf{\Gamma}\oslash\hat{\mathbf{u}})\delta\mathbf{u} \tag{B.0.6d}$$

The internal force vector then becomes:

$$\begin{aligned}\delta\mathbf{F}_{int} &= [(\mathbf{H}\oplus\mathbf{A}+\mathbf{T}\boldsymbol{\Lambda}+\mathbf{H}\mathbf{A}+\boldsymbol{\Gamma}\oslash\hat{\mathbf{u}})\delta\mathbf{u}]^T\hat{\mathbf{F}}'_{int}+\boldsymbol{\Theta}^T\hat{\mathbf{K}}\boldsymbol{\Theta}\ \delta\mathbf{u}\\ &= [\mathbf{B}\delta\mathbf{u}]^T\hat{\mathbf{F}}'_{int}+\boldsymbol{\Theta}^T\hat{\mathbf{K}}\boldsymbol{\Theta}\ \delta\mathbf{u}\end{aligned} \tag{B.0.7}$$

Defining the transpose of a third-order tensor as

$$(\mathbf{A})^T_{ijk}\overset{def}{=}\mathbf{A}_{jik}$$

then

$$\begin{aligned}[(\mathbf{B}\delta\mathbf{u})^T]_{ij} &= (\mathbf{B}\delta\mathbf{u})_{ji}=\mathbf{B}_{jik}\delta\mathbf{u}_k=\mathbf{B}^T\delta\mathbf{u}\\ [(\mathbf{B}\delta\mathbf{u})^T\hat{\mathbf{F}}'_{int}]_i &= \mathbf{B}_{jik}\delta\mathbf{u}_k(\hat{\mathbf{F}}'_{int})_j=(\mathbf{B}_{jik}(\hat{\mathbf{F}}'_{int})_j)\delta\mathbf{u}_k\\ \delta\mathbf{F}_{int} &= (\mathbf{B}^T\odot\hat{\mathbf{F}}'_{int})\delta\mathbf{u}_k+\boldsymbol{\Theta}^T\hat{\mathbf{K}}\boldsymbol{\Theta}\ \delta\mathbf{u}\\ \mathbf{K} &= \frac{\partial\mathbf{F}_{int}}{\partial\mathbf{u}}=(\mathbf{B}^T\odot\hat{\mathbf{F}}'_{int})+\boldsymbol{\Theta}^T\hat{\mathbf{K}}\boldsymbol{\Theta}\end{aligned} \tag{B.0.8}$$

$$\boxed{\mathbf{K}=((\mathbf{H}\oplus\mathbf{A}+\mathbf{T}\boldsymbol{\Lambda}+\mathbf{H}\mathbf{A}+\boldsymbol{\Gamma}\oslash\hat{\mathbf{u}})^T\odot\hat{\mathbf{F}}'_{int})+\boldsymbol{\Theta}^T\hat{\mathbf{K}}\boldsymbol{\Theta}} \tag{B.0.9}$$

Therefore, in the following, we will develop expressions for the tensors $\mathbf{T}$, $\mathbf{A}$, $\mathbf{H}$, $\boldsymbol{\Lambda}$ and $\boldsymbol{\Gamma}$.

B.1 Incremental displacement matrix $\mathbf{A}=\mathbb{QMAT}$

The matrix $\mathbf{A}$ is defined by the relation $\delta\hat{\mathbf{u}}=\mathbf{A}\delta\mathbf{u}$. Using Equation (4.5.60) and taking the variation of $\hat{\mathbf{u}}$,

$$\delta\hat{\mathbf{u}}_k=\delta(\mathbf{u}-\mathbf{u}_{mid}-\mathbf{u}_{rot})_k=\delta\mathbf{u}_k-(\delta\mathbf{u}_{mid})_k-(\delta\mathbf{u}_{rot})_k \tag{B.1.10}$$

From Equation (4.5.62) follows:

$$\delta(\mathbf{u}_{mid})_k = 0.5(\mathbf{I_0})_{kj}\delta\mathbf{u}_j \tag{B.1.11a}$$

$$\delta(\mathbf{u}_{rot})_k = \begin{pmatrix} \delta((\mathbf{\Omega}_r - \mathbf{I})(\mathbf{x_1} - \mathbf{x_{mid}})) \\ \delta(\mathbf{\Phi}_r(\mathbf{\Omega}_r)) \\ \mathbf{0} \\ \delta((\mathbf{\Omega}_r - \mathbf{I})(\mathbf{x_2} - \mathbf{x_{mid}})) \\ \delta(\mathbf{\Phi}_r(\mathbf{\Omega}_r)) \\ \mathbf{0} \end{pmatrix} = \begin{pmatrix} \delta\mathbf{\Omega}_r\mathbf{x_{rel}} \\ \delta\mathbf{\Phi}_r(\mathbf{\Omega}_r) \\ \mathbf{0} \\ \delta\mathbf{\Omega}_r\mathbf{x_{rel}} \\ \delta\mathbf{\Phi}_r(\mathbf{\Omega}_r) \\ \mathbf{0} \end{pmatrix} = \mathbb{DUROT}\ \delta\mathbf{u} \tag{B.1.11b}$$

where $\mathbf{\Phi}_r$ is the *elemental* rotation pseudo-vector associated with the rotation from the initial to the current configuration; $\mathbf{\Omega}_r$ being the corresponding direction cosine matrix for the rotation. The variations of the quantities $\mathbf{\Omega}_r = \mathbf{\Omega}_r(\hat{\mathbf{u}})$ and $\mathbf{\Phi}_r = \mathbf{\Phi}_r(\mathbf{\Omega}_r(\hat{\mathbf{u}}))$ are evaluated using the chain rule

$$\delta\mathbf{\Omega}_r = \sum_m \frac{\partial\mathbf{\Omega}_r}{\partial\hat{\mathbf{e}}_m}\frac{\partial\hat{\mathbf{e}}_m}{\partial\mathbf{u}}\delta\mathbf{u} \qquad \frac{\partial\mathbf{\Omega}_r}{\partial\mathbf{u}} = \mathbb{DOMU} = \mathbb{INTER}\cdot\mathbb{INTER2}$$

$$\delta\mathbf{\Phi}_r = \sum_m \frac{\partial\mathbf{\Phi}_r}{\partial\mathbf{\Omega}_r}\frac{\partial\mathbf{\Omega}_r}{\partial\hat{\mathbf{e}}_m}\frac{\partial\hat{\mathbf{e}}_m}{\partial\mathbf{u}}\delta\mathbf{u}_j \qquad \frac{\partial\mathbf{\Phi}}{\partial\mathbf{u}} = \mathbb{DPHI}$$

or, in component form:

$$\delta\mathbf{\Omega} = \frac{\partial\mathbf{\Omega}_{kl}}{\partial(\hat{\mathbf{e}}_m)_n}\frac{\partial(\hat{\mathbf{e}}_m)_n}{\partial\mathbf{u}_j}\delta\mathbf{u}_j \tag{B.1.12}$$

$$\delta\mathbf{\Phi} = \frac{\partial\mathbf{\Phi}_i}{\partial\mathbf{\Omega}_{kl}}\frac{\partial\mathbf{\Omega}_r}{\partial(\hat{\mathbf{e}}_m)_n}\frac{\partial(\hat{\mathbf{e}}_m)_n}{\partial\mathbf{u}_j}\delta\mathbf{u}_j \tag{B.1.13}$$

B.1.1 Partial derivative of ê by u

Expressing the vectors $\hat{\mathbf{e}}_i$ as components in the global system and computing the derivative:

$$\frac{\partial(\hat{\mathbf{e}}_m \cdot \mathbf{e}_n)}{\partial \mathbf{u}_j} = \frac{\partial \mathbf{T}_{mn}}{\partial \mathbf{u}_j} = \mathbf{H}_{mnj} \tag{B.1.14}$$

B.1.2 Partial derivative of $\mathbf{\Omega}_r$ by $\hat{\mathbf{e}}$

Once the local triad has been determined, the rotation matrix can then be found using $(\mathbf{\Omega}_r)_{ij} = (\hat{\mathbf{e}}_j \cdot \mathbf{e}_{i0})$. It is noted that this matrix is in the *initial* system. The elemental rotation vector $\mathbf{\Phi}_r(\mathbf{\Omega}_r)$ is calculated using the equations for θ and $\mathbf{n}$ listed in section 4. To compute the partial derivative with repect to the local triad (whose components are given in the global system), the $\mathbf{\Omega}_r$ matrix is first converted into the global system, then differentiated.

$$\begin{aligned}
\mathbf{\Omega}_{kl} &= (\mathbf{e}_k \cdot \mathbf{e}_{h0})(\hat{\mathbf{e}}_m \cdot \mathbf{e}_{h0})(\mathbf{e}_l \cdot \mathbf{e}_{m0}) \\
\delta\mathbf{\Omega}_{kl} &= (\mathbf{e}_k \cdot \mathbf{e}_{h0})((\hat{\mathbf{e}}_m + \delta\hat{\mathbf{e}}_m) \cdot \mathbf{e}_{h0})(\mathbf{e}_l \cdot \mathbf{e}_{m0}) - (\mathbf{e}_k \cdot \mathbf{e}_{h0})(\hat{\mathbf{e}}_m \cdot \mathbf{e}_{h0})(\mathbf{e}_l \cdot \mathbf{e}_{m0}) \\
&= (\mathbf{e}_k \cdot \mathbf{e}_{h0})(\delta\hat{\mathbf{e}}_m \cdot \mathbf{e}_{h0})(\mathbf{e}_l \cdot \mathbf{e}_{m0}) \\
&= [(\mathbf{e}_k \cdot \mathbf{e}_{h0})(\mathbf{e}_l \cdot \mathbf{e}_{m0})\mathbf{e}_{h0}] \cdot \delta\hat{\mathbf{e}}_m
\end{aligned}$$

so

$$\frac{\partial \mathbf{\Omega}_{kl}}{\partial \hat{\mathbf{e}}_m} = (\mathbf{e}_k \cdot \mathbf{e}_{h0})(\mathbf{e}_l \cdot \mathbf{e}_{m0})\mathbf{e}_{h0}$$

or, in component form:

$$\begin{aligned}
\left(\frac{\partial \mathbf{\Omega}_{kl}}{\partial \hat{\mathbf{e}}_m}\right)_n &= ((\mathbf{e}_k \cdot \mathbf{e}_{h0})(\mathbf{e}_l \cdot \mathbf{e}_{m0})\mathbf{e}_{h0}) \cdot \mathbf{e}_n \\
&= (\mathbf{e}_k \cdot \mathbf{e}_{h0})(\mathbf{e}_l \cdot \mathbf{e}_{m0})(\mathbf{e}_{h0} \cdot \mathbf{e}_n)
\end{aligned} \tag{B.1.15}$$

B.1.3 Partial derivative of $\mathbf{\Phi}_r$ by $\mathbf{\Omega}_r$

This partial derivative is derived by normalising the rotation vector $\Phi_i = \theta n_i$ and the standard formulae for converting the "Euler axis and angle"' representation of a rotation to the direction cosine matrix:

$$\frac{\partial \mathbf{\Phi}_i}{\partial \mathbf{\Omega}_{kl}} = \frac{\partial \theta}{\partial \mathbf{\Omega}_{kl}} n_i + \frac{\partial n_i}{\partial \mathbf{\Omega}_{kl}} \theta = \mathbb{G}1 \cdot n_i + \mathbb{G}2 \cdot \mathbb{TWIST} \tag{B.1.16}$$

and, from the Rodrigues relationships,

$$\theta = \text{acos}\ ((0.5(\mathbf{\Omega}_{11} + \mathbf{\Omega}_{22} + \mathbf{\Omega}_{33} - 1)) = \mathbb{TWIST} \tag{B.1.17}$$

$$n_i = -\frac{\varepsilon_{ikl}\mathbf{\Omega}_{kl}}{2\ \sin\ \theta} \tag{B.1.18}$$

so

$$\begin{aligned} \frac{\partial n_i}{\partial \mathbf{\Omega}_{kl}} &= \frac{(2\ \sin\ \theta)(\varepsilon_{ikl}) + \varepsilon_{ipq}\mathbf{\Omega}_{pq}\ 2\ \cos\ \theta \frac{\partial \theta}{\partial \mathbf{\Omega}_{kl}}}{4\ \sin^2\ \theta} \\ \frac{\partial n_i}{\partial \mathbf{\Omega}_{kl}} &= \frac{-\varepsilon_{ikl} \sin\ \theta + \varepsilon_{ipq}\mathbf{\Omega}_{pq} \cos\ \theta \frac{\partial \theta}{\partial \mathbf{\Omega}_{kl}}}{2\ \sin^2\ \theta} = \mathbb{G}2 \end{aligned} \tag{B.1.19}$$

while

$$\frac{\partial \theta}{\partial \mathbf{\Omega}_{kl}} = \frac{-0.5\ \delta_{kl}}{\sqrt{1 - (\frac{tr(\mathbf{\Omega})-1}{2})^2}} = \mathbb{G}1 \tag{B.1.20}$$

If the element rotations are zero, these equations become singular. In this case, the derivative $\frac{\partial \mathbf{\Phi}_i}{\partial \mathbf{\Omega}_{kl}}$ is calcuated using the small rotation approximation to the rotation matrix

$$\begin{aligned} \mathbf{\Omega}_r(\mathbf{\Phi}_r) &= \mathbf{I} + \mathbf{S}(\mathbf{\Phi}_r) \\ \mathbf{\Phi}_i &= 0.5\varepsilon_{kil}\mathbf{\Omega}_{kl} \end{aligned} \tag{B.1.21}$$

where $\mathbf{S}(\cdot)$ is the skew-symmetric matrix formed from the vector argument.

This results in

$$\frac{\partial \mathbf{\Phi}_i}{\partial \mathbf{\Omega}_{kl}} = 0.5\varepsilon_{kil} = -0.5\varepsilon_{ikl} \tag{B.1.22}$$

Rearranging **5.1**, **5.2** for the code, we have:

$$\mathbb{INTER} = (\mathbf{e}_{k0} \cdot \mathbf{e}_h)(\mathbf{e}_{h0} \cdot \mathbf{e}_n)$$
$$\mathbb{INTER2} = (\mathbf{e}_{l0} \cdot \mathbf{e}_m)\mathbf{H}_{mnj}$$

$$\mathbb{QMAT} = \mathbf{I} - 0.5\mathbf{I}_0 - \mathbb{DUROT}$$
$$\mathbb{DUROT} = \begin{pmatrix} \mathbb{DOMU} \cdot \mathbb{XX}1 \\ \mathbb{DPHI} \\ \mathbf{0} \\ \mathbb{DOMU} \cdot \mathbb{XX}2 \\ \mathbb{DPHI} \\ \mathbf{0} \end{pmatrix}$$

B.2 Evaluation of T, H, H* and H**

Noting that the "degrees of freedom" 16x16 transformation matrix $\mathbf{T}$ is composed of the "coordinate" transformation matrix $\mathbf{T}^*$, the derivative of $\mathbf{T}$ can be found by calculating the reduced 3x3x16 $\mathbf{H}^*$ tensor:

$$\mathbf{H}^* = \frac{\partial \mathbf{T}^*}{\partial \mathbf{u}} \qquad H^*_{ijk} = \frac{\partial(\hat{\mathbf{e}}_3 \cdot \mathbf{e}_j)}{\partial u_k} \tag{B.2.23}$$

and then assembling. Recalling the definitions of the vectors $\hat{\mathbf{e}}_i$ from Equation (4.5.58),

$$\begin{aligned}
\hat{\mathbf{e}}_3 &= \frac{\mathbf{x}^2 - \mathbf{x}^1 + \mathbf{u}^2 - \mathbf{u}^1}{\|\mathbf{x}^2 - \mathbf{x}^1 + \mathbf{u}^2 - \mathbf{u}^1\|} \\
(\hat{\mathbf{e}}_3 \cdot \mathbf{e}_j) &= \frac{x_j^2 - x_j^1 + u_j^2 - u_j^1}{\|\mathbf{x}^2 - \mathbf{x}^1 + \mathbf{u}^2 - \mathbf{u}^1\|} = \frac{\tilde{x}_j(u)}{\| \tilde{\mathbf{x}}(u) \|} \\
\mathbf{H}^*_{3jk} = \frac{\partial(\hat{\mathbf{e}}_3 \cdot \mathbf{e}_j)}{\partial u_k} &= \frac{\| \tilde{\mathbf{x}} \| \tilde{x}_{j,k} - \tilde{x}_j \| \tilde{\mathbf{x}} \|_{,k}}{\| \tilde{\mathbf{x}} \|^2}
\end{aligned} \tag{B.2.24}$$

$$\frac{\partial \tilde{x}_j}{\partial u_k} = \begin{cases} -\delta_{jk} & k = 1,2,3 \\ +\delta_{j(k-7)} & k = 9,10,11 \\ 0 & \text{otherwise} \end{cases} \qquad \frac{\partial \| \tilde{\mathbf{x}} \|}{\partial u_k} = \begin{cases} \frac{-\tilde{x}_k}{\|\tilde{\mathbf{x}}\|} & k = 1,2,3 \\ \frac{+\tilde{x}_k}{\|\tilde{\mathbf{x}}\|} & k = 9,10,11 \\ 0 & \text{otherwise} \end{cases} \tag{B.2.25}$$

$$\mathbf{H}^*_{3jk} = \begin{cases} \frac{-\delta_{jk}}{\mathbb{ELEN}} + \frac{\tilde{x}_j \tilde{x}_k}{\mathbb{ELEN}^3} & k = 1,2,3 \\ \frac{+\delta_{jk}}{\mathbb{ELEN}} - \frac{\tilde{x}_j \tilde{x}_k}{\mathbb{ELEN}^3} & k = 9,10,11 \end{cases}$$

$$\mathbf{H}^*_{3jk} = \begin{cases} \frac{-\delta_{jk}}{\mathbb{ELEN}} + \frac{(\hat{e}_3)_j (\hat{e}_3)_k}{\mathbb{ELEN}} & k = 1,2,3 \\ \frac{+\delta_{jk}}{\mathbb{ELEN}} - \frac{(\hat{e}_3)_j (\hat{e}_3)_k}{\mathbb{ELEN}} & k = 9,10,11 \end{cases} \tag{B.2.26}$$

For the second basis vector, using Equation. (4.5.59):

$$\begin{aligned}
\hat{\mathbf{e}}_2 &= \frac{(\mathbf{I} - \hat{\mathbf{e}}_3 \otimes \hat{\mathbf{e}}_3)(\boldsymbol{\Omega}_1 + \boldsymbol{\Omega}_2)\mathbf{e}_{20}}{\| \cdot \|} \\
(\hat{\mathbf{e}}_2)_j &= \frac{(\delta_{jl} - (\hat{\mathbf{e}}_3)_j (\hat{\mathbf{e}}_3)_l)((\boldsymbol{\Omega}_1)_{lm} + (\boldsymbol{\Omega}_2)_{lm})(\mathbf{e}_{20})_m}{\| \cdot \|}
\end{aligned} \tag{B.2.27}$$

Noting that the derivative of a unit vector $\frac{\mathbf{v}}{\|\mathbf{v}\|}$ is given by

$$\frac{\partial}{\partial u_k} \left(\frac{v_j}{\|\mathbf{v}\|} \right) = \frac{\|\mathbf{v}\|^2 \frac{\partial v_j}{\partial u_k} - v_j v_p \frac{\partial v_p}{\partial u_k}}{\|\mathbf{v}\|^3} \tag{B.2.28}$$

then, if the corresponding unnormed vector is the numerator of Equation (B.2.27),

$$\mathbf{v} = (\delta_{jl} - (\hat{\mathbf{e}}_3)_j(\hat{\mathbf{e}}_3)_l)((\mathbf{\Omega}_1)_{lm} + (\mathbf{\Omega}_2)_{lm})(\mathbf{e}_{20})_m \tag{B.2.29}$$

and the derivative of the unnormed vector is

$$\frac{\partial v_j}{\partial u_k} = (\mathbf{e}_{20})_m \left[\frac{\partial (\mathbf{I} - \hat{\mathbf{e}}_3 \otimes \hat{\mathbf{e}}_3)_{jl}}{\partial u_k} (\mathbf{\Omega}_1 + \mathbf{\Omega}_2)_{lm} + (\mathbf{I} - \hat{\mathbf{e}}_3 \otimes \hat{\mathbf{e}}_3)_{jl} \left(\frac{\partial (\mathbf{\Omega}_1)_{lm}}{\partial u_k} + \frac{\partial (\mathbf{\Omega}_2)_{lm}}{\partial u_k} \right) \right] \tag{B.2.30}$$

Then $\mathbf{H}^*_{2jk}$ is equal to Equation (B.2.28) with the substitutions from Equations (B.2.29) and (B.2.30).

The derivative of the nodal rotation matrix $\mathbf{\Omega}_1$ is:

$$\frac{\partial (\mathbf{\Omega}_1)_{lm}}{\partial u_k} = \frac{\partial (\mathbf{\Omega}_1)_{lm}}{\partial (\mathbf{\Phi}_1)_s} \frac{\partial (\mathbf{\Phi}_1)_s}{\partial u_k} \tag{B.2.31}$$

$$\frac{\partial \mathbf{\Omega}_1}{\partial \mathbf{\Phi}_1} = \frac{\partial}{\partial \mathbf{\Phi}_1} (\mathbf{I} + \frac{\sin\theta_1}{\theta_1} \mathbf{S}(\mathbf{\Phi}_1) + \frac{1 - \cos\theta_1}{\theta_1^2} \mathbf{S}(\mathbf{\Phi}_1)\mathbf{S}(\mathbf{\Phi}_1)) = \frac{\partial}{\partial \mathbf{\Phi}_1} (\mathbf{I} + \mathbf{\Omega}_1^A + \mathbf{\Omega}_1^B) \tag{B.2.32}$$

The derivatives comprising Equation (B.2.32) are given by

$$\frac{\partial \mathbf{\Omega}_1^A}{\partial (\mathbf{\Phi}_1)_i} = \frac{\theta_1 \cos\theta_1 \frac{\partial \theta_1}{\partial (\mathbf{\Phi}_1)_i} - \sin\theta_1 \frac{\partial \theta_1}{\partial (\mathbf{\Phi}_1)_i}}{\theta_1^2} \mathbf{S}(\mathbf{\Phi}_1) + \frac{\sin\theta_1}{\theta_1} \frac{\partial \mathbf{S}(\mathbf{\Phi}_1)}{\partial \mathbf{\Phi}_1} = \mathbb{DOMM1A} \tag{B.2.33}$$

$$\frac{\partial \theta_1}{\partial (\mathbf{\Phi}_1)_i} = \frac{(\mathbf{\Phi}_1)_i}{\theta_1} \tag{B.2.34}$$

$$\frac{\partial S_{ik}(\mathbf{\Phi}_1)}{\partial (\mathbf{\Phi}_1)_l} = -\varepsilon_{ikl} \tag{B.2.35}$$

and

$$\frac{\partial \mathbf{\Omega}_1^B}{\partial \mathbf{\Phi}_1} = \frac{\theta_1^2 \sin\theta_1 \frac{\partial \theta}{\partial \mathbf{\Phi}_1} - 2\theta_1(1-\cos\theta)\frac{\partial \theta_1}{\partial \mathbf{\Phi}_1}}{\theta_1^4}\mathbf{S}(\mathbf{\Phi}_1)\mathbf{S}(\mathbf{\Phi}_1) + \frac{1-\cos\theta_1}{\theta_1^2}\frac{\partial}{\partial \mathbf{\Phi}_1}(\mathbf{S}(\mathbf{\Phi}_1)\mathbf{S}(\mathbf{\Phi}_1)) = \mathbb{DOM}1\mathbb{B} \quad \text{(B.2.36)}$$

Using the definition

$$\mathbf{Z}_{ijlm} = \varepsilon_{ijk}\varepsilon_{klm} = \det\begin{bmatrix} \delta_{ik} & \delta_{il} & \delta_{im} \\ \delta_{jk} & \delta_{jl} & \delta_{jm} \\ \delta_{kk} & \delta_{kl} & \delta_{km} \end{bmatrix} \quad \text{(B.2.37)}$$

then

$$\begin{aligned} \frac{\partial}{\partial(\mathbf{\Phi}_1)_n}(\mathbf{S}(\mathbf{\Phi}_1)_{ik}\mathbf{S}(\mathbf{\Phi}_1)_{km}) &= \varepsilon_{ijk}(\mathbf{\Phi}_1)_j\varepsilon_{klm}(\mathbf{\Phi}_1)_l \\ &= \frac{\partial}{\partial(\mathbf{\Phi}_1)_n}((\varepsilon_{ijk}\varepsilon_{klm})(\mathbf{\Phi}_1)_j(\mathbf{\Phi}_1)_l) = \mathbf{Z}_{ijlm}\frac{\partial}{\partial(\mathbf{\Phi}_1)_n}\left[(\mathbf{\Phi}_1)_j(\mathbf{\Phi}_1)_l\right] \\ &= \mathbf{Z}_{ijlm}\left[(\mathbf{\Phi}_1)_l\delta_{jn} + (\mathbf{\Phi}_1)_j\delta_{ln}\right] \quad \text{(B.2.38)} \end{aligned}$$

Finally,

$$\frac{\partial(\mathbf{\Phi}_1)_l}{\partial u_k} = \begin{cases} \delta_{k(l+3)} & k = 4,5,6 \\ 0 & \text{otherwise} \end{cases} \qquad \frac{\partial(\mathbf{\Phi}_2)_l}{\partial u_k} = \begin{cases} \delta_{k(l+11)} & k = 12,13,14 \\ 0 & \text{otherwise} \end{cases} \quad \text{(B.2.39)}$$

For the case of zero rotation, the derivative $\frac{\partial \mathbf{\Omega}_1}{\partial \mathbf{\Phi}_1}$ is evaluated using the small rotation approximation for the rotation matrix

$$\mathbf{\Omega}_1(\mathbf{\Phi}_1) = \mathbf{I} + \mathbf{S}(\mathbf{\Phi}_1) \quad \text{(B.2.40)}$$

leading to

$$\frac{\partial \mathbf{\Omega}_{ij}}{\partial \mathbf{\Phi}_k} = \varepsilon_{ikj} = -\varepsilon_{ijk} \tag{B.2.41}$$

By replacing the subscript "1' 'with "2" on $\mathbf{\Omega}$, Equations (B.2.31)-(B.2.41) can also be used for calculating $\frac{\partial(\mathbf{\Omega}_2)_{lm}}{\partial u_k}$.

The derivative of the projector matrix $(\mathbf{I} - \hat{\mathbf{e}}_3 \otimes \hat{\mathbf{e}}_3)$ is[1] :

$$\frac{\partial(\mathbf{I} - \hat{\mathbf{e}}_3 \otimes \hat{\mathbf{e}}_3)_{jl}}{\partial u_k} = -\frac{\partial((\hat{\mathbf{e}}_3)_j(\hat{\mathbf{e}}_3))_l}{\partial u_k} = -\frac{(\hat{\mathbf{e}}_3)_j}{\partial u_k}(\hat{\mathbf{e}}_3)_l - (\hat{\mathbf{e}}_3)_j\frac{(\hat{\mathbf{e}}_3)_l}{\partial u_k} = \\ - \mathbf{H}^*_{3jk}(\hat{\mathbf{e}}_3)_l - (\hat{\mathbf{e}}_3)_j\mathbf{H}^*_{3lk} \tag{B.2.42}$$

For the third basis vector:

$$\hat{\mathbf{e}}_1 = \hat{\mathbf{e}}_2 \times \hat{\mathbf{e}}_3$$

$$\frac{\partial(\hat{\mathbf{e}}_1)_i}{\partial u_n} = \varepsilon_{ijk}\frac{\partial(\hat{\mathbf{e}}_2)_j}{\partial u_n}(\hat{\mathbf{e}}_3)_k + \varepsilon_{ipq}(\hat{\mathbf{e}}_2)_p\frac{\partial(\hat{\mathbf{e}}_3)_q}{\partial u_n} = \varepsilon_{ijk}\mathbf{H}^*_{2jn}(\hat{\mathbf{e}}_3)_k + \varepsilon_{ipq}(\hat{\mathbf{e}}_2)_p\mathbf{H}^*_{3qn} \tag{B.2.43}$$

Considering how the coordinate transformation matrix $\mathbf{T}^*$ is derived, it can be seen that it is dependent on the translational degrees of freedom only.

The full 16x16x16 tensor $\mathbf{H}$ is

[1] This derivative makes use of the Rodrigues formula for $\mathbf{\Omega}_1(\mathbf{\Phi}_1)$, where $\theta_1 = \| \mathbf{\Phi}_1 \|$ and $\mathbf{S}(\mathbf{\Phi}_1)$ is the skew-symmetric matrix with components $\mathbf{S}_{ik} = \varepsilon_{ilk}\mathbf{\Phi}_l$

$$\mathbf{H}_{1:16,1:16,k} = \begin{pmatrix} H^*_{1:3,1:3,k} & 0 & 0 & 0 & 0 & 0 \\ 0 & H^*_{1:3,1:3,k} & 0 & 0 & 0 & 0 \\ 0 & 0 & 0_{2x2} & 0 & 0 & 0 \\ 0 & 0 & 0 & H^*_{1:3,1:3,k} & 0 & 0 \\ 0 & 0 & 0 & 0 & H^*_{1:3,1:3,k} & 0 \\ 0 & 0 & 0 & 0 & 0 & 0_{2x2} \end{pmatrix}_k \tag{B.2.44}$$

B.3 Derivation of geometric tangent matrix

Correct evaluation of the global external force vector requires knowledge of the tensor $\mathbf{\Lambda}_{ijk} = \frac{\partial \mathbf{A}_{ij}}{\partial \mathbf{u}_k}$ (Equation (B.0.2b)). Also, for optimal convergence, the correct nonlinear corotational tangent stiffness matrix (Equation (B.0.9)) should be used. If Equation (4.5.62), (B.1.10), (B.1.11a), (B.1.11b), (B.1.12) and (B.1.13) are used to write $\mathbf{A}$ as

$$\mathbf{A}_{kj} = \mathbf{I} - 0.5\mathbf{I}_0 - \begin{pmatrix} \frac{\partial \mathbf{\Omega}_r}{\partial \hat{\mathbf{e}}} \frac{\partial \hat{\mathbf{e}}}{\partial \mathbf{u}} (\mathbf{x}_1 - \mathbf{x}_{mid}) \\ \frac{\partial \mathbf{\Phi}_r}{\partial \mathbf{\Omega}_r} \frac{\partial \mathbf{\Omega}_r}{\partial \hat{\mathbf{e}}} \frac{\partial \hat{\mathbf{e}}}{\partial \mathbf{u}} \\ \mathbf{0} \\ \frac{\partial \mathbf{\Omega}_r}{\partial \hat{\mathbf{e}}} \frac{\partial \hat{\mathbf{e}}}{\partial \mathbf{u}} (\mathbf{x}_2 - \mathbf{x}_{mid}) \\ \frac{\partial \mathbf{\Phi}_r}{\partial \mathbf{\Omega}_r} \frac{\partial \mathbf{\Omega}_r}{\partial \hat{\mathbf{e}}} \frac{\partial \hat{\mathbf{e}}}{\partial \mathbf{u}} \\ \mathbf{0} \end{pmatrix} \tag{B.3.45}$$

then

$$\frac{\partial \mathbf{A}_{kj}}{u_n} = \frac{\partial}{\mathbf{u}_n}\begin{pmatrix} \frac{\partial \mathbf{\Omega}_r}{\partial \hat{\mathbf{e}}}\frac{\partial \hat{\mathbf{e}}}{\partial \mathbf{u}}(\mathbf{x}_1 - \mathbf{x}_{mid}) \\ \frac{\partial \mathbf{\Phi}_r}{\partial \mathbf{\Omega}_r}\frac{\partial \mathbf{\Omega}_r}{\partial \hat{\mathbf{e}}}\frac{\partial \hat{\mathbf{e}}}{\partial \mathbf{u}} \\ \mathbf{0} \\ \frac{\partial \mathbf{\Omega}_r}{\partial \hat{\mathbf{e}}}\frac{\partial \hat{\mathbf{e}}}{\partial \mathbf{u}}(\mathbf{x}_2 - \mathbf{x}_{mid}) \\ \frac{\partial \mathbf{\Phi}_r}{\partial \mathbf{\Omega}_r}\frac{\partial \mathbf{\Omega}_r}{\partial \hat{\mathbf{e}}}\frac{\partial \hat{\mathbf{e}}}{\partial \mathbf{u}} \\ \mathbf{0} \end{pmatrix} \tag{B.3.46}$$

The first row of this matrix is

$$\begin{aligned} \frac{\partial}{\partial \mathbf{u}}(\frac{\partial \mathbf{\Omega}_r}{\partial \hat{\mathbf{e}}}\frac{\partial \hat{\mathbf{e}}}{\partial \mathbf{u}})(\mathbf{x}_1 - \mathbf{x}_{mid}) &= \frac{\partial \mathbf{\Omega}_{kl}}{\partial (\hat{\mathbf{e}}_p)_q}\frac{\partial}{\partial u_n}(\frac{\partial (\hat{\mathbf{e}_p})_q}{\partial u_m})((\mathbf{x}_1)_m - (\mathbf{x}_{mid})_m) \\ &= \frac{\partial \mathbf{\Omega}_{kl}}{\partial (\hat{\mathbf{e}}_p)_q}\mathbf{\Gamma}_{pqmn}((\mathbf{x}_1)_m - (\mathbf{x}_{mid})_m) \end{aligned} \tag{B.3.47}$$

Similarly, the fourth row of Equation (B.3.46) becomes

$$\frac{\partial \mathbf{\Omega}_{kl}}{\partial (\hat{\mathbf{e}}_p)_q}\mathbf{\Gamma}_{pqmn}((\mathbf{x}_2)_m - (\mathbf{x}_{mid})_m) \tag{B.3.48}$$

The derivatives of the second and fifth row are

$$\frac{\partial}{\partial u_n}(\frac{\partial \mathbf{\Phi}_i}{\partial \mathbf{\Omega}_{kl}}\frac{\partial \mathbf{\Omega}_{kl}}{\partial (\hat{\mathbf{e}}_p)_q}\frac{\partial (\hat{\mathbf{e}}_p)_q}{\partial u_m}) = \frac{\partial \mathbf{\Omega}_{kl}}{\partial (\hat{\mathbf{e}}_p)_q}\left[\frac{\partial}{\partial u_n}(\frac{\partial \mathbf{\Phi}_i}{\partial \mathbf{\Omega}_{kl}})\frac{\partial (\hat{\mathbf{e}}_p)_q}{\partial u_m} + \frac{\partial \mathbf{\Phi}_i}{\partial \mathbf{\Omega}_{kl}}\mathbf{\Gamma}_{pqmn}\right] \tag{B.3.49}$$

where

$$\begin{aligned} \frac{\partial}{\partial u_n}(\frac{\partial \mathbf{\Phi}_i}{\partial \mathbf{\Omega}_{kl}}) &= \frac{\partial}{\partial u_n}(\frac{\partial \theta}{\partial \mathbf{\Omega}_{kl}}n_i + \frac{\partial n_i}{\partial \mathbf{\Omega}_{kl}}\theta) \\ &= \frac{\partial}{\partial u_n}(\frac{\partial \theta}{\partial \mathbf{\Omega}_{kl}})n_i + \frac{\partial \theta}{\partial \mathbf{\Omega}_{kl}}\frac{\partial n_i}{\partial u_n} + \frac{\partial}{\partial u_n}(\frac{\partial n_i}{\partial \mathbf{\Omega}_{kl}})\theta + \frac{\partial n_i}{\partial \mathbf{\Omega}_{kl}}\frac{\partial \theta}{\partial u_n} \\ &= \mathbf{W}n_i + \frac{\partial \theta}{\partial \mathbf{\Omega}_{kl}}\mathbf{X} + \mathbf{Y}\theta + \frac{\partial n_i}{\partial \mathbf{\Omega}_{kl}}\mathbf{Z} \end{aligned} \tag{B.3.50}$$

With $\mathbf{W}$, $\mathbf{X}$, $\mathbf{Y}$ and $\mathbf{Z}$ being given by

$$\mathbf{W} = \frac{\partial}{\partial u_n}\left(\frac{\partial \theta}{\partial \mathbf{\Omega}_{kl}}\right) = -0.5\delta_{kl}\frac{\partial}{\partial u_n}\left(\left[1-\left(\frac{tr(\mathbf{\Omega}_{kl})-1}{2}\right)^2\right]^{-0.5}\right)$$
$$= 0.25\delta_{kl}\left[1-\left(\frac{tr(\mathbf{\Omega}_{kl})-1}{2}\right)^2\right]^{-1.5}(tr(\mathbf{\Omega}_{kl})-1)\frac{\partial(tr(\mathbf{\Omega}_{kl}))}{\partial u_n} \quad \text{(B.3.51)}$$

$$\frac{\partial(tr(\mathbf{\Omega}_{kl}))}{\partial u_n} = \delta_{kl}\frac{\partial \mathbf{\Omega}_{kl}}{\partial u_n} = \delta_{kl}\frac{\partial \mathbf{\Omega}_{kl}}{\partial(\hat{\mathbf{e}}_p)_q}\frac{\partial(\hat{\mathbf{e}}_p)_q}{\partial u_n} \quad \text{(B.3.52)}$$

$$\mathbf{X} = \frac{\partial n_i}{\partial u_n} = \frac{\partial n_i}{\partial \mathbf{\Omega}_{pq}}\frac{\partial \mathbf{\Omega}_{pq}}{\partial(\hat{\mathbf{e}}_r)_s}\frac{\partial(\hat{\mathbf{e}}_r)_s}{\partial u_n} \quad \text{(B.3.53)}$$

$$\mathbf{Z} = \frac{\partial \theta}{\partial \mathbf{u}_n} = \frac{\partial \theta}{\partial \mathbf{\Omega}_{pq}}\frac{\partial \mathbf{\Omega}_{pq}}{\partial(\hat{\mathbf{e}}_r)_s}\frac{\partial(\hat{\mathbf{e}}_r)_s}{\partial u_n} \quad \text{(B.3.54)}$$

The unknown terms in the above equations for (B.3.49) are $\frac{\partial n_i}{\partial \mathbf{\Omega}_{kl}}$ and $\frac{\partial}{\partial u_n}\left(\frac{\partial n_i}{\partial \mathbf{\Omega}_{kl}}\right)$.

$$\frac{\partial n_i}{\partial \mathbf{\Omega}_{kl}} = \frac{-\varepsilon_{ikl}\sin\theta + \varepsilon_{ipq}\mathbf{\Omega}_{pq}\cos\theta\frac{\partial\theta}{\partial \mathbf{\Omega}_{kl}}}{2\sin^2\theta} \quad \text{(B.3.55)}$$

$$\mathbf{Y} = \frac{\partial}{\partial u_n}\left(\frac{\partial n_i}{\partial \mathbf{\Omega}_{kl}}\right) = \frac{-\varepsilon_{ikl}\cos\theta\frac{\partial\theta}{\partial u_n}}{2\sin^2\theta} + \frac{\varepsilon_{ipq}\frac{\partial \mathbf{\Omega}_{pq}}{\partial u_n}\cos\theta\frac{\partial\theta}{\partial \mathbf{\Omega}_{kl}}}{2\sin^2\theta}$$
$$-\frac{\varepsilon_{ipq}\mathbf{\Omega}_{pq}\sin\theta\frac{\partial\theta}{\partial u_n}\frac{\partial\theta}{\partial \Omega_{kl}}}{2\sin^2\theta} + \frac{\varepsilon_{ipq}\mathbf{\Omega}_{pq}\cos\theta\frac{\partial}{\partial u_n}\left(\frac{\partial\theta}{\partial \mathbf{\Omega}_{kl}}\right)}{2\sin^2\theta}$$
$$+\frac{\left(\varepsilon_{ikl}\sin\theta - \varepsilon_{ipq}\mathbf{\Omega}_{pq}\cos\theta\frac{\partial\theta}{\partial \mathbf{\Omega}_{kl}}\right)\frac{\partial\theta}{\partial u_l}}{\sin^2\theta\tan\theta}$$

$$= \frac{-\varepsilon_{ikl}\cos\theta\ \mathbf{Z}(n)}{2\sin^2\theta} + \frac{\varepsilon_{ipq}\frac{\partial \mathbf{\Omega}_{pq}}{\partial(\hat{\mathbf{e}}_y)_z}\mathbf{H}^*_{yzn}\cos\theta\frac{\partial\theta}{\partial \mathbf{\Omega}_{kl}}}{2\sin^2\theta}$$
$$-\frac{\varepsilon_{ipq}\mathbf{\Omega}_{pq}\sin\theta\ \mathbf{Z}(n)\frac{\partial\theta}{\partial \Omega_{kl}}}{2\sin^2\theta} + \frac{\varepsilon_{ipq}\mathbf{\Omega}_{pq}\cos\theta\ \mathbf{W}(k,l,n)}{2\sin^2\theta}$$
$$+\frac{\left(\varepsilon_{ikl}\sin\theta - \varepsilon_{ipq}\mathbf{\Omega}_{pq}\cos\theta\frac{\partial\theta}{\partial \mathbf{\Omega}_{kl}}\right)\mathbf{Z}(l)}{\sin^2\theta\tan\theta} \quad \text{(B.3.56)}$$

The only remaining unknown that is required to calculate $\mathbf{\Lambda}$ is $\mathbf{\Gamma}$.

B.3.1 Evaluating $\mathbf{\Gamma}_{3jkl}$

$$\mathbf{\Gamma} = \frac{\partial \mathbf{H}}{\partial \mathbf{u}}$$

Recognising the only nonzero elements of $\mathbf{H}$ are contained within $\mathbf{H}^*$, only the 3x3x16x16 sub-tensor

$$\mathbf{\Gamma}^* = \frac{\partial \mathbf{H}^*}{\partial \mathbf{u}} \tag{B.3.57}$$

must be calculated; the full tensor will be assembled afterwards. From Equation (B.2.24),

$$\begin{aligned}
\mathbf{H}^*_{3jk} &= \frac{\partial(\hat{\mathbf{e}}_3 \cdot \mathbf{e}_j)}{\partial u_k} = \frac{\parallel \tilde{\mathbf{x}} \parallel \tilde{x}_{j,k} - \tilde{x}_j \parallel \tilde{\mathbf{x}} \parallel_{,k}}{\parallel \tilde{\mathbf{x}} \parallel^2} \\
\mathbf{\Gamma}^*_{3jkl} &= \frac{\partial \mathbf{H}^{**}_{3jk}}{\partial u_l} \\
\mathbf{\Gamma}^*_{3jkl} &= \frac{\|\tilde{\mathbf{x}}\|^2 \frac{\partial \mathbf{N}}{\partial u_l} - \mathbf{N}(2\|\tilde{\mathbf{x}}\| \frac{\partial \|\tilde{\mathbf{x}}\|}{\partial u_l})}{\|\tilde{\mathbf{x}}\|^4} \\
&= \begin{cases} \frac{\frac{\partial \mathbf{N}}{\partial u_l}}{\|\tilde{\mathbf{x}}\|^2} - \frac{2\mathbf{N}\tilde{x}_l}{\|\tilde{\mathbf{x}}\|^4} & l = 1,2,3 \\ \frac{\frac{\partial \mathbf{N}}{\partial u_l}}{\|\tilde{\mathbf{x}}\|^2} + \frac{2\mathbf{N}\tilde{x}_l}{\|\tilde{\mathbf{x}}\|^4} & l = 9,10,11 \\ 0 & \text{otherwise} \end{cases}
\end{aligned} \tag{B.3.58}$$

where $\mathbf{N}$ is the numerator of Equation (B.2.24)

$$\mathbf{N} = \|\tilde{\mathbf{x}}\|\tilde{x}_{j,k} - \tilde{x}_j\|\tilde{\mathbf{x}}\|_{,k} \tag{B.3.59}$$

$$\frac{\partial \mathbf{N}}{\partial u_l} = \frac{\partial \|\tilde{\mathbf{x}}\|}{\partial u_l}\tilde{x}_{j,k} + \|\tilde{\mathbf{x}}\|\frac{\partial}{\partial u_l}(\tilde{x}_{j,k}) - \frac{\partial \tilde{x}_j}{\partial u_l}\|\tilde{\mathbf{x}}\|_{,k} - \tilde{x}_j\frac{\partial}{\partial u_l}(\|\tilde{\mathbf{x}}\|_{,k}) \tag{B.3.60}$$

the only unknown terms in the final equation are:

$$\frac{\partial}{\partial u_l}(\tilde{x}_{j,k}) = 0 \tag{B.3.61}$$

$$\frac{\partial}{\partial u_l}(\|\tilde{\mathbf{x}}\|_{,k}) = \begin{cases} \frac{\partial}{\partial u_l}\left(\frac{-\tilde{x}_k}{\|\tilde{\mathbf{x}}\|}\right) & k = 1,2,3 \\ \frac{\partial}{\partial u_l}\left(\frac{\tilde{x}_k}{\|\tilde{\mathbf{x}}\|}\right) & k = 7,8,9 \\ 0 & \text{otherwise} \end{cases}$$

$$= \begin{cases} \mathbf{H}^*_{3kl} & k = 1,2,3 \\ -\mathbf{H}^*_{3kl} & k = 9,10,11 \\ 0 & \text{otherwise} \end{cases} \tag{B.3.62}$$

B.3.2 Evaluating $\mathbf{\Gamma}_{2jkl}$

Letting $\mathbf{v}$ be the numerator of the normed vector expression of $(\hat{\mathbf{e}}_2)_j$ (Equation (B.2.27)),

$$\mathbf{v} = (\delta_{jk} - (\hat{\mathbf{e}}_3)_j(\hat{\mathbf{e}}_3)_k)((\mathbf{\Omega}_1)_{kl} + (\mathbf{\Omega}_2)_{kl})(\mathbf{e}_{20})_l \tag{B.3.63}$$

along with its derivative (Equation (B.2.30)) and the expression for the derivative of its norm (Equation (B.2.28)), then

$$
\begin{aligned}
\boldsymbol{\Gamma}^{*}_{2jkl} = \frac{\partial \mathbf{H}^{**}_{2jk}}{\partial u_l} &= \frac{\partial}{\partial u_l}\left(\frac{\partial}{\partial u_k}\left(\frac{v_j}{\|\mathbf{v}\|}\right)\right) \\
&= \frac{\partial}{\partial u_l}\left(\frac{\partial}{\partial u_k}\left(\frac{(\delta_{jl}-(\hat{\mathbf{e}}_3)_j(\hat{\mathbf{e}}_3)_l)((\boldsymbol{\Omega}_1)_{lm}+(\boldsymbol{\Omega}_2)_{lm})(\mathbf{e}_{20})_m}{\|\cdot\|}\right)\right) \\
&= \frac{\partial}{\partial u_l}\left(\frac{\|\mathbf{v}\|^2\frac{\partial v_j}{\partial u_k}-v_jv_p\frac{\partial v_p}{\partial u_k}}{\|\mathbf{v}\|^3}\right) \\
&= \frac{\|\mathbf{v}\|^3\frac{\partial}{\partial u_l}(\|\mathbf{v}\|^2\frac{\partial v_j}{\partial u_k}-v_jv_p\frac{\partial v_p}{\partial u_k})-3\|\mathbf{v}\|^2\frac{\partial\|\mathbf{v}\|}{\partial u_l}(\|\mathbf{v}\|^2\frac{\partial v_j}{\partial u_k}-v_jv_p\frac{\partial v_p}{\partial u_k})}{\|\mathbf{v}\|^6} \\
&= \frac{\|\mathbf{v}\|(2\|\mathbf{v}\|\frac{\partial\|\mathbf{v}\|}{\partial u_l}\frac{\partial v_j}{\partial u_k}+\|\mathbf{v}\|^2\frac{\partial^2 v_j}{\partial u_l\partial u_k}-\frac{\partial v_j}{\partial u_l}v_p\frac{\partial v_p}{\partial u_k}-v_j\frac{\partial v_p}{\partial u_l}\frac{\partial v_p}{\partial u_k}-v_jv_p\frac{\partial^2 v_p}{\partial u_k\partial u_l})}{\|\mathbf{v}\|^4} \\
&\quad -\frac{3\frac{\partial\|\mathbf{v}\|}{\partial u_l}(\|\mathbf{v}\|^2\frac{\partial v_j}{\partial u_k}-v_jv_p\frac{\partial v_p}{\partial u_k})}{\|\mathbf{v}\|^4}
\end{aligned}
\tag{B.3.64}
$$

$$
\begin{aligned}
&= \frac{\|\mathbf{v}\|\left[2\|\mathbf{v}\|\left(\frac{v_z\frac{\partial v_z}{\partial u_n}}{\|\mathbf{v}\|}\right)\frac{\partial v_j}{\partial u_k}+\|\mathbf{v}\|^2\frac{\partial^2 v_j}{\partial u_l\partial u_k}-\frac{\partial v_j}{\partial u_l}v_p\frac{\partial v_p}{\partial u_k}-v_j\frac{\partial v_p}{\partial u_l}\frac{\partial v_p}{\partial u_k}-v_jv_p\frac{\partial^2 v_p}{\partial u_k\partial u_l}\right]}{\|\mathbf{v}\|^4} \\
&\quad -\frac{3\left(\frac{v_z\frac{\partial v_z}{\partial u_l}}{\|\mathbf{v}\|}\right)(\|\mathbf{v}\|^2\frac{\partial v_j}{\partial u_k}-v_jv_p\frac{\partial v_p}{\partial u_k})}{\|\mathbf{v}\|^4} \\
&= \frac{2\ v_z\frac{\partial v_z}{\partial u_n}\frac{\partial v_j}{\partial u_k}+\|\mathbf{v}\|^2\frac{\partial^2 v_j}{\partial u_l\partial u_k}-\frac{\partial v_j}{\partial u_l}v_p\frac{\partial v_p}{\partial u_k}-v_j\frac{\partial v_p}{\partial u_l}\frac{\partial v_p}{\partial u_k}-v_jv_p\frac{\partial^2 v_p}{\partial u_k\partial u_l}}{\|\mathbf{v}\|^3} \\
&\quad -\frac{3v_z\frac{\partial v_z}{\partial u_l}\left(\|\mathbf{v}\|^2\frac{\partial v_j}{\partial u_k}-v_jv_p\frac{\partial v_p}{\partial u_k}\right)}{\|\mathbf{v}\|^5}
\end{aligned}
$$

Noting that

$$
\frac{\partial\|\mathbf{v}\|}{\partial u_n} = \frac{v_z\frac{\partial v_z}{\partial u_n}}{\|\mathbf{v}\|} \tag{B.3.65}
$$

$$\frac{\partial^2 v_j}{\partial u_k \partial u_n} = (e_{20})_m \left[\frac{\partial^2 (\mathbf{I} - \hat{\mathbf{e}}_3 \otimes \hat{\mathbf{e}}_3)_{jl}}{\partial u_k \, \partial u_n} (\boldsymbol{\Omega}_1 + \boldsymbol{\Omega}_2)_{lm} \right] + (e_{20})_m \left[\frac{\partial (\mathbf{I} - \hat{\mathbf{e}}_3 \otimes \hat{\mathbf{e}}_3)_{jl}}{\partial u_k} \left(\frac{\partial (\boldsymbol{\Omega}_1)_{lm}}{\partial u_n} + \frac{\partial (\boldsymbol{\Omega}_2)_{lm}}{\partial u_n} \right) \right] + (e_{20})_m \left[\frac{\partial (\mathbf{I} - \hat{\mathbf{e}}_3 \otimes \hat{\mathbf{e}}_3)_{jl}}{\partial u_n} \left(\frac{\partial (\boldsymbol{\Omega}_1)_{lm}}{\partial u_k} + \frac{\partial (\boldsymbol{\Omega}_2)_{lm}}{\partial u_k} \right) + (\mathbf{I} - \hat{\mathbf{e}}_3 \otimes \hat{\mathbf{e}}_3)_{jl} \left(\frac{\partial^2 (\boldsymbol{\Omega}_1)_{lm}}{\partial u_k \partial u_n} + \frac{\partial^2 (\boldsymbol{\Omega}_2)_{lm}}{\partial u_k \partial u_n} \right) \right] \tag{B.3.66}$$

where

$$\begin{aligned} \frac{\partial^2 (\mathbf{I} - \hat{\mathbf{e}}_3 \otimes \hat{\mathbf{e}}_3)_{jl}}{\partial u_k \, \partial u_n} &= \frac{\partial}{\partial u_n} (\mathbf{H}^*_{3jk} (\hat{\mathbf{e}}_3)_l - (\hat{\mathbf{e}}_3)_j \mathbf{H}^*_{3lk}) \\ &= \boldsymbol{\Gamma}^*_{3jkn} (\hat{\mathbf{e}}_3)_l + \mathbf{H}^*_{3jk} \mathbf{H}^*_{3ln} - \mathbf{H}^*_{3jn} \mathbf{H}^*_{3lk} - \boldsymbol{\Gamma}^*_{3lkn} (\hat{\mathbf{e}}_3)_j \end{aligned} \tag{B.3.67}$$

and

$$\begin{aligned} \frac{\partial^2 (\boldsymbol{\Omega}_1)_{lm}}{\partial u_k \partial u_n} &= \frac{\partial^2 (\boldsymbol{\Omega}_1)_{lm}}{\partial (\boldsymbol{\Phi}_1)_s \, \partial u_n} \frac{\partial (\boldsymbol{\Phi}_1)_s}{\partial u_k} \\ &= \frac{\partial}{\partial u_n} \left(\frac{\partial \boldsymbol{\Omega}^A_1}{\partial (\boldsymbol{\Phi}_1)_s} + \frac{\partial \boldsymbol{\Omega}^B_1}{\partial (\boldsymbol{\Phi}_1)_s} \right) \frac{\partial (\boldsymbol{\Phi}_1)_s}{\partial u_k} \\ &= \frac{\partial}{\partial (\boldsymbol{\Phi}_1)_z} \left(\frac{\partial \boldsymbol{\Omega}^A_1}{\partial (\boldsymbol{\Phi}_1)_s} + \frac{\partial \boldsymbol{\Omega}^B_1}{\partial (\boldsymbol{\Phi}_1)_s} \right) \frac{\partial (\boldsymbol{\Phi}_1)_z}{\partial u_n} \frac{\partial (\boldsymbol{\Phi}_1)_s}{\partial u_k} \end{aligned} \tag{B.3.68}$$

with the component

$$\begin{aligned}
\frac{\partial^2(\mathbf{\Omega}_1^A)_{lm}}{\partial(\mathbf{\Phi}_1)_i\partial(\mathbf{\Phi}_1)_z} &= \frac{\theta_1\cos\theta_1\frac{\partial\theta_1}{\partial(\mathbf{\Phi}_1)_i}-\sin\theta_1\frac{\partial\theta_1}{\partial(\mathbf{\Phi}_1)_i}}{\theta_1^2}\frac{\partial\mathbf{S}_{lm}(\mathbf{\Phi}_1)}{\partial(\mathbf{\Phi}_1)_z}+\dots \\
&\quad+\mathbf{S}_{lm}(\mathbf{\Phi}_1)\left(\frac{\theta_1^2\mathbf{P}_1-2\theta_1\frac{\partial\theta_1}{\partial(\mathbf{\Phi}_1)_z}(\theta_1\cos\theta_1\frac{\partial\theta_1}{\partial(\mathbf{\Phi}_1)_i}-\sin\theta_1\frac{\partial\theta_1}{\partial(\mathbf{\Phi}_1)_i})}{\theta_1^4}\right)+\dots \\
&\quad+\left(\frac{\theta_1\cos\theta_1\frac{\partial\theta_1}{\partial(\mathbf{\Phi}_1)_z}-\sin\theta_1\frac{\partial\theta_1}{\partial(\mathbf{\Phi}_1)_z}}{\theta_1^2}\right)\frac{\partial\mathbf{S}_{lm}(\mathbf{\Phi}_1)}{\partial(\mathbf{\Phi}_1)_i} \\
&= -\varepsilon_{lmz}\left(\frac{(\mathbf{\Phi}_1)_i(\theta_1\cos\theta_1-\sin\theta_1)}{\theta_1^3}\right)+\left(\frac{\theta_1^3\mathbf{P}_1-2(\mathbf{\Phi}_1)_z(\mathbf{\Phi}_1)_i(\theta_1\cos\theta_1-\sin\theta_1)}{\theta_1^5}\right)\mathbf{S}_{lm}(\mathbf{\Phi}_1) \\
&\quad-\varepsilon_{lmi}\left(\frac{(\mathbf{\Phi}_1)_z(\theta_1\cos\theta_1-\sin\theta_1)}{\theta_1^3}\right)+\frac{\sin\theta_1}{\theta_1}\frac{\partial^2\mathbf{S}_{lm}(\mathbf{\Phi}_1)}{\partial(\mathbf{\Phi}_1)_i\partial(\mathbf{\Phi}_1)_z} \qquad \text{(B.3.69)}
\end{aligned}$$

noting that

$$\frac{\partial^2\mathbf{S}_{lm}(\mathbf{\Phi}_1)}{\partial(\mathbf{\Phi}_1)_i\partial(\mathbf{\Phi}_1)_z}=0$$

and

$$\begin{aligned}
\mathbf{P}_1 &= \frac{\partial\theta_1}{\partial(\mathbf{\Phi}_1)_z}\cos\theta_1\frac{\partial\theta_1}{\partial(\mathbf{\Phi}_1)_i}-\theta_1\frac{\partial\theta_1}{\partial(\mathbf{\Phi}_1)_i}\sin\theta_1\frac{\partial\theta_1}{\partial(\mathbf{\Phi}_1)_z}+\theta_1\cos\theta_1\frac{\partial^2\theta_1}{\partial(\mathbf{\Phi}_1)_i\partial(\mathbf{\Phi}_1)_z}-\dots \\
&\quad-\cos\theta_1\frac{\partial\theta_1}{\partial(\mathbf{\Phi}_1)_z}\frac{\partial\theta_1}{\partial(\mathbf{\Phi}_1)_i}-\sin\theta_1\frac{\partial^2\theta_1}{\partial(\mathbf{\Phi}_1)_z\partial(\mathbf{\Phi}_1)_i} \\
&= -\theta_1\frac{\partial\theta_1}{\partial(\mathbf{\Phi}_1)_i}\sin\theta_1\frac{\partial\theta_1}{\partial(\mathbf{\Phi}_1)_z}+(\theta_1\cos\theta_1-\sin\theta_1)\frac{\partial^2\theta_1}{\partial(\mathbf{\Phi}_1)_z\partial(\mathbf{\Phi}_1)_i} \qquad \text{(B.3.70)}
\end{aligned}$$

which contains the term

$$\frac{\partial^2\theta_1}{\partial(\mathbf{\Phi}_1)_i\partial(\mathbf{\Phi}_2)_z}=\frac{\partial}{\partial(\mathbf{\Phi})_z}\left(\frac{(\mathbf{\Phi}_1)_i}{\theta_1}\right)=\frac{\theta_1^2\delta_{iz}-(\mathbf{\Phi}_1)_i(\mathbf{\Phi}_1)_z}{\theta_1^3} \qquad \text{(B.3.71)}$$

The second component of Equation (B.3.68) is

$$\begin{aligned}\frac{\partial^2(\mathbf{\Omega}_1^B)_{lm}}{\partial(\mathbf{\Phi})_i\partial(\mathbf{\Phi})_z} &= \mathbf{P}_2\mathbf{S}_{ly}(\mathbf{\Phi}_1)\mathbf{S}_{ym}(\mathbf{\Phi}_1)+ \\ &2\frac{\partial\theta_1}{\partial(\mathbf{\Phi}_1)_i}\left(\frac{\theta_1^2\sin\theta_1-2\theta_1(1-\cos\theta_1)}{\theta_1^4}\right)\frac{\partial\mathbf{S}_{ly}(\mathbf{\Phi}_1)}{\partial(\mathbf{\Phi}_1)_z}\mathbf{S}_{ym}(\mathbf{\Phi}_1)+ \\ &+\left(\frac{1-\cos\theta_1}{\theta_1^2}\right)\frac{\partial^2}{\partial(\mathbf{\Phi}_1)_i\partial(\mathbf{\Phi}_1)_z}(\mathbf{S}_{ly}(\mathbf{\Phi}_1)\mathbf{S}_{ym}(\mathbf{\Phi}_1))+ \\ &+\frac{\partial\theta_1}{\partial(\mathbf{\Phi}_1)_z}\left(\frac{\theta_1^2\sin\theta_1-2\theta_1(1-\cos\theta_1)}{\theta_1^4}\right)\frac{\partial}{\partial(\mathbf{\Phi}_1)_i}(\mathbf{S}_{ly}(\mathbf{\Phi}_1)\mathbf{S}_{ym}(\mathbf{\Phi}_1)) \quad \text{(B.3.72)}\end{aligned}$$

$$\begin{aligned}&= \mathbf{P}_2\mathbf{S}_{ly}(\mathbf{\Phi}_1)\mathbf{S}_{ym}(\mathbf{\Phi}_1) \\ &-2\varepsilon_{lyz}(\mathbf{\Phi}_1)_i\left(\frac{\theta_1\sin\theta_1-2(1-\cos\theta_1)}{\theta_1^4}\right)\mathbf{S}_{ym}(\mathbf{\Phi}_1)+ \\ &+\left(\frac{1-\cos\theta_1}{\theta_1^2}\right)(\varepsilon_{lyi}\varepsilon_{ymz}+\varepsilon_{lyz}\varepsilon_{ymi})+ \\ &-(\mathbf{\Phi}_1)_z\left(\frac{\theta_1\sin\theta_1-2(1-\cos\theta_1)}{\theta_1^4}\right)(\varepsilon_{lyi}\mathbf{S}_{ym}(\mathbf{\Phi}_1)+\varepsilon_{ymi}\mathbf{S}_{ly}(\mathbf{\Phi}_1)) \quad \text{(B.3.73)}\end{aligned}$$

containing the term

$$\begin{aligned}\mathbf{P}_2 &= \frac{\theta_1^4\mathbf{P}_3-4\theta_1^3\frac{\partial\theta_1}{\partial(\mathbf{\Phi}_1)_z}(\theta_1^2\sin\theta_1\frac{\partial\theta_1}{\partial(\mathbf{\Phi}_1)_i}-2\theta_1(1-\cos\theta_1)\frac{\partial\theta_1}{\partial(\mathbf{\Phi}_1)_i})}{\theta_1^8} \\ &= \frac{\theta_1^2\mathbf{P}_3-4(\mathbf{\Phi}_1)_z(\mathbf{\Phi}_1)_i(\theta_1\sin\theta_1-2+2\cos\theta_1)}{\theta_1^6} \quad \text{(B.3.74)}\end{aligned}$$

which itself contains the term

$$\begin{aligned}\mathbf{P}_3 = 2\theta_1 \frac{\partial\theta_1}{\partial(\mathbf{\Phi}_1)_z}\sin\theta_1\frac{\partial\theta_1}{\partial(\mathbf{\Phi}_1)_i} + \theta_1^2\cos\theta_1\frac{\partial\theta_1}{\partial(\mathbf{\Phi}_1)_z}\frac{\partial\theta_1}{\partial(\mathbf{\Phi}_1)_i} + \\ \theta_1^2\sin\theta_1\frac{\partial^2\theta_1}{\partial(\mathbf{\Phi}_1)_z\partial(\mathbf{\Phi}_1)_i} - (2-2(\cos\theta_1-\theta_1\sin\theta_1))\frac{\partial\theta_1}{\partial(\mathbf{\Phi}_1)_z}\frac{\partial\theta_1}{\partial(\mathbf{\Phi}_1)_i} - \\ 2\theta_1(1-\cos\theta_1)\frac{\partial^2\theta_1}{\partial(\mathbf{\Phi}_1)_i\partial(\mathbf{\Phi}_1)_z} \\ = \frac{\partial\theta_1}{\partial(\mathbf{\Phi}_1)_z}\frac{\partial\theta_1}{\partial(\mathbf{\Phi}_1)_i}\left[2\theta_1\sin\theta_1+\theta_1^2\cos\theta_1-(2-2(\cos\theta_1-\theta_1\sin\theta_1))\right] \\ + \frac{\partial^2\theta_1}{\partial(\mathbf{\Phi}_1)_z\partial(\mathbf{\Phi}_1)_i}\left[\theta_1^2\sin\theta_1-2\theta_1(1-\cos\theta_1)\right]\end{aligned}$$

$$\begin{aligned}= \frac{\partial\theta_1}{\partial(\mathbf{\Phi}_1)_z}\frac{\partial\theta_1}{\partial(\mathbf{\Phi}_1)_i}\left[\theta_1^2\cos\theta_1+2\cos\theta_1-2\right] \\ + \frac{\partial^2\theta_1}{\partial(\mathbf{\Phi}_1)_z\partial(\mathbf{\Phi}_1)_i}\left[\theta_1^2\sin\theta_1-2\theta_1+2\theta_1\cos\theta_1\right] \quad \text{(B.3.75)}\end{aligned}$$

The final part of the second component of Equation (B.3.68) is given by

$$\begin{aligned}\frac{\partial^2(\mathbf{S}_{ly}(\mathbf{\Phi}_1)\mathbf{S}_{ym}(\mathbf{\Phi}_1))}{\partial(\mathbf{\Phi}_1)_i(\mathbf{\Phi}_1)_z} &= \frac{\partial}{\partial(\mathbf{\Phi}_1)_z}\left[\frac{\partial\mathbf{S}_{ly}(\mathbf{\Phi}_1)}{\partial(\mathbf{\Phi}_1)_i}\mathbf{S}_{ym}(\mathbf{\Phi}_1)+\mathbf{S}_{ly}(\mathbf{\Phi}_1)\frac{\partial\mathbf{S}_{ym}(\mathbf{\Phi}_1)}{\partial(\mathbf{\Phi}_1)_i}\right] \\ &= \frac{\partial}{\partial(\mathbf{\Phi}_1)_z}\left[-\varepsilon_{lyi}\mathbf{S}_{ym}(\mathbf{\Phi}_1)-\mathbf{S}_{ly}(\mathbf{\Phi}_1)\varepsilon_{ymi}\right] \\ &= \varepsilon_{lyi}\varepsilon_{ymz}+\varepsilon_{lyz}\varepsilon_{ymi} \quad \text{(B.3.76)}\end{aligned}$$

In the case of zero rotation, then, instead of equations (B.3.68)-(B.3.76), equation (B.2.41) is substituted into $(\frac{\partial^2(\mathbf{\Omega}_1)_{lm}}{\partial u_k\partial u_n})$, giving:

$$\frac{\partial^2(\mathbf{\Omega}_2)_{lm}}{\partial u_k\partial u_n} = \frac{\partial}{\partial u_n}\left(\frac{\partial\mathbf{\Omega}_{lm}}{\partial(\mathbf{\Phi}_1)_s}\right)\frac{\partial(\mathbf{\Phi}_1)_s}{\partial u_k} = \frac{\partial}{\partial u_n}\left(-\varepsilon_{lms}\right)\frac{\partial(\mathbf{\Phi}_1)_s}{\partial u_k} = 0$$

The second derivatives of the rotations at the second node $(\frac{\partial^2(\mathbf{\Omega}_2)_{lm}}{\partial u_k\partial u_n})$ are calculated in a similar manner.

B.3.3 Evaluation of $\mathbf{\Gamma}_{1jkl}$

$$\begin{aligned}\mathbf{\Gamma}^*_{1jkl} &= \frac{\partial \mathbf{H}^{**}_{1jk}}{\partial u_l} = \frac{\partial}{\partial u_l}(\frac{\partial (\hat{\mathbf{e}}_1)_i}{\partial u_n}) \\ &= \frac{\partial}{\partial u_l}(\varepsilon_{ijk}\mathbf{H}^*_{2jn}(\hat{\mathbf{e}}_3)_k + \varepsilon_{ipq}(\hat{\mathbf{e}}_2)_p\mathbf{H}^*_{3qn}) \\ &= \varepsilon_{ijk}(\mathbf{\Gamma}^*_{2jnl}(\hat{\mathbf{e}}_3)_k + \mathbf{H}^*_{2jn}\mathbf{H}^*_{3kl}) + \varepsilon_{ipq}(\mathbf{H}^*_{2pl}\mathbf{H}^*_{3qn} + (\hat{\mathbf{e}}_2)_p\mathbf{\Gamma}^*_{3qnl}) \end{aligned} \tag{B.3.77}$$

The full 16x16x16x16 tensor $\mathbf{\Gamma}$ is

$$\begin{aligned}\mathbf{\Gamma}_{ijkl} = \mathbf{\Gamma}_{(i+3)(j+3)kl} = \mathbf{\Gamma}_{(i+8)(j+8)kl} = \mathbf{\Gamma}_{(i+11)(j+11)kl} = \mathbf{\Gamma}^*_{ijkl} \\ \mathbf{\Gamma}_{ij(k+8)l} = \mathbf{\Gamma}_{(i+3)(j+3)(k+8)l} = \mathbf{\Gamma}_{(i+8)(j+8)(k+8)l} = \mathbf{\Gamma}_{(i+11)(j+11)(k+8)l} = \mathbf{\Gamma}^*_{ijkl} \\ \text{for } i,j,k = 1,2,3, l = 1,2,\cdots 16 \end{aligned} \tag{B.3.78}$$

Appendix C

Model generator script

Introduction

The following provides usage instructions and partial code listing for the Python script used to generate flexible pipe models in the Abaqus/CAE environment. This code allows the creation of a multi-layer flexible pipe with arbitrary dimensions, layer order, layer type and materials. The code was created using the Abaqus Python Developer Environment (PDE)[1]. The script is used with the menu path **File–>Run Script**... and selecting the script file. Once the model has been generated, a new job must be created and executed as usual. To use the file to create different flexible pipe models, the script file must be edited as described in Section C.

Partial code listing

The following shows the modifiable part of the script file used to generate the standard flexible pipe model used in this project.

[1]Accessed with menu path **File–>Abaqus PDE**...

```
##################################################
#       SHELL-BASED FLEXIBLE PIPE MODEL GENERATOR
##################################################
#
# Version 1.0
# Created by Ben Edmans at Brunel University, London, UK
# 16/02/2012
#
##################################################
from part import *
from material import *
from section import *
from assembly import *
from step import *
from interaction import *
from load import *
from mesh import *
from job import *
from sketch import *
from visualization import *
from connectorBehavior import *
#
##################################################
#       MODIFY CODE IN THIS SECTION ONLY
##################################################
#
# MODEL PARAMETERS
modelname='Model-1'
jobname='Job-1'
#
# MASTER LAYER LIST (INSIDE LAYER FIRST)
innradius=[0.0959e0,0.0973e0,0.0993e0,0.1033e0,0.1055e0,
           0.1095e0]
thck=[0.0014,0.002,0.004,0.00175,0.004,0.00715]
norm=[1e10,3.5e8,2e11,2e11,2e11,2e11]
type=['C','S','W','S','W','S']
mat=['Carcass','HDPE','Steel','HDPE','Steel','HDPE']
width=[0,0,0.0125,0,0.012,0]
lay=[0,0,1,0,-1,0]
number=[0,0,46,0,48,0]
pipelength=0.868
#
#
# FRICTION
friction=0.16
#
# MESH PARAMETERS
nelcircum=60
nellength=30
```

```
nelwires=60
#
# MATERIAL PARAMETERS - POLYMER AND STEEL
#
epolymer=3e8
nupolymer=0.4
esteel=2e11
nusteel=0.3
#
# MATERIAL PARAMETERS - CARCASS
E1=150e9
E2=12.4e9
E3=1e10
nu12=0.3
nu13=0.0
nu23=0.0
G12=1e10
G13=1e10
G23=1e10
#
# BOUNDARY CONDITION CHOICE (P=Periodic, FIP=Fixed-in-plane)
bcc='P'
#
#
# LOADING
#
PINT=30e6
PEXT=23.4e6
#
# DOF CONSTRAINTS ON CONTROL NODE
#
dof1=['FIXED',0]
dof2=['FIXED',0]
dof3=['FIXED',0]
dof4=['FIXED',0]
dof5=['FIXED',0]
dof6=['FIXED',0]
#
#
# FORCES/MOMENTS ON CONTROL NODE
fm1=0
fm2=0
fm3=0
fm4=0
fm5=0
fm6=0
#
##########################################################
...
```

```
[FURTHER CODING]
```

Code beyond this point should not be modified (unless there are problems in execution, see Section C).

Modifying the code

Fundamental layer data are entered in the section marked “Master layer list”. Each entry in the following list gives a value or type designator for a layer. The first value in each list provides data for the innermost layer. Each list must have a number of entries equal to the number of layers in the pipe. Layer dimensions are defined in terms of layer inner radii and layer thicknesses, allowing for initial gaps to be specified. The list “norm” supplies the radial stiffnesses for the layers which is used to calculate penalty stiffnesses for contact interactions, as described elsewhere. The entries in the list “type” must be either “C”, designating the layer is the carcass layer, “W”, designating the layer as comprised of helical wires, or “S”, specifying that the layer is a solid cylindrical sheath.

Three preset material models are supplied, designated “Carcass”, “Steel” and “HDPE”. “Carcass” is a 3D orthotropic linear elastic material; “Steel” and “HDPE” are linear elastic materials. The values used can be easily changed, but the use of new material models requires modification of the code outwith the “control panel” presented above.

The list “width” refers to the chord width of helical wires (measured in the plane of the pipe cross-section). Values are not meaningful for other layers. the list “lay” refers to the lay angle of layers comprised of helical wires. It may take the value 1 or -1. Values for other layers are not meaningful. The list “number” refers to the number of helical wires in the layer. Values for other layers are not meaningful.

Control of discretisation is achieved with the parameters “nelcircum”, the number of elements around the circumference of carcass and solid layers, “nellength”, the number of elements used alond the length of carcass and solid layers and“nelwires”, the number of elements used along the length of helical wires.

This script automatically creates pressure loads on the second layer (“PINT”)

and on the outer layer ("PEXT") and well as forces and moments ("fm") on the control node. In the numbering convention for fm, fm3 is axial force, fm6 is torsion, fm4 and fm5 are bending moments and fm2 and fm3 are transverse shear loading.

Boundary conditions may be applied to the control node. The numbering of the dof lists corresponds to the numbering of the fm parameters. The first entry in the lists must be either "FIXED", if the boundary condition is prescribed, or "FREE" if it is left free. The second entry is the magnitude of the imposed displacement/rotation, which is not meaningful if the first entry is "FREE".

Important notes

Python is an object-orientated language whose commands mirror the operations that may be carried out using the graphical user interface of the Abaqus/CAE environment. Repeated operations can be automated in loops in Python. Using Python scripts is a more convenient but also more limited way of creating models as many low-level operations that can be specified using keywords (in manually generated input files) are not available as Abaqus/CAE operations. Specifically, the options available for specifying nodes are limited. Some nodes in this script are selected using viewport-based *getSequenceFromMask* commands which are known to cause minor stability problems when running the script on different platforms. If this occurs, the author's advice is to perform the missing operations in Abaqus/CAE and copy the new keys (e.g. '[#3]') to the script file.

Loops and conditional statements in Python are controlled by indentation of the code lines: lines with the same indentation are executed at the same level in the nesting hierarchy. Thus, it is important to remove or alter the spaces at the start of each line.

If fixed-in-plane boundary conditions rather than periodic boundary conditions are required, this may be achieved by changing bcc="P" to bcc="FIP" in the above code. However, this will not create the kinematic constraints on the end planes or loads or boundary conditions on control nodes. Currently, these features must be added manually.

The objects created are named in a logical manner. These can be changed by

changing the relevant key (e.g ['Part-1']) to the desired name wherever it occurs in the code.

Appendix D

List of publications

Journal papers

Edmans, B., Alfano, G., Bahai, H., 2012. Nonlinear multi-scale homogenisation with different structural models at different scales. International Journal for Numerical Methods in Engineering. In Press.

Edmans, B., Alfano, G., Bahai, H. A finite element model for local analyses of marine flexible marine pipes. Ocean Engineering. In advanced state of preparation.

Conference papers

Edmans, B., Alfano, G., Bahai, H., 2009. Multiscale modelling of flexible pipes, in: Proceedings of the 17th UK National Conference on Computational Mechanics.

Edmans, B., Alfano, G., Bahai, H., 2010a. Multiscale modelling of flexible pipes with nonlinear homogenisation, in: Proceedings of the ASME 2010 29th International Conference on Ocean, Offshore and Arctic Engineering. OMAE2010-21020.

Edmans, B., Alfano, G., Bahai, H., 2010b. Multiscale finite-element modelling of flexible marine risers, in: Proceedings of the 10th International Conference on Computational Plasticity (COMPLAS X).

Edmans, B., Alfano, G., Bahai, H., 2011. Computational homogenisation

accounting for structural-to-structural scale bridging, in: Proceedings of the 19th UK conference of the Association for Computational Mechanics in Engineering.

Edmans, B., Alfano, G., Bahai, H., 2012. Large-scale analysis and local stress assessment of flexible unbonded pipes using FEA, OMAE2012-84249, in: Proceedings of the ASME 2010 31st International Conference on Ocean, Offshore and Arctic Engineering.

Edmans, B., Alfano, G., Bahai, H., Bahtui, A., Andronicou, L., 2012. Local stress assessment of flexible unbonded pipes using FEA, in: Proceedings of the ASME 2010 31st International Conference on Ocean, Offshore and Arctic Engineering. OMAE2012-84248.